MICROBIAL-MINERAL-TRACE METAL INTERACTIONS IN ARD BIOFILMS

MICROBIAL-MINERAL-TRACE METAL INTERACTIONS IN ACID-ROCK DRAINAGE BIOFILMS: INTEGRATING MACRO-, MICRO-AND MOLECULAR-LEVEL TECHNIQUES TO UNDERSTAND METAL BEHAVIOUR

By
ELIZABETH ANNE HAACK, B.Sc.

A Thesis
Submitted to the School of Graduate Studies
In Partial Fulfilment of the Requirements
for the Degree
Doctor of Philosophy

McMaster University

DOCTOR OF PHILOSOPHY (2004) McMaster University
School of Geography and Geology Hamilton, Ontario

TITLE: Microbial-Mineral-Trace metal interactions in acid rock drainage biofilms: Integrating macro-, micro-, and molecular-level techniques to understand metal behaviour

AUTHOR: Elizabeth Anne Haack, B.Sc. (Trent University)

SUPERVISOR: Professor Lesley A. Warren

NUMBER OF PAGES: xiii, 150

ABSTRACT

In this study a combined field and laboratory approach was used to identify the bio-geochemical processes that control trace metal (Ni, Co, Cr) reactive transport within natural acid rock drainage (ARD) biofilms, over both diel and seasonal timescales. Results indicated that metal (Mn, Ni, Co and Cr) scavenging by these biological solids is stable on a seasonal time frame. Metal scavenging occurs within two key solids, the organic constituents of the biofilm (Ni, Co) and associated biogenic hydrous Mn oxyhydroxides (HMO; Ni, Co and Cr), and not in association with Fe-oxyhydroxy-sulphates which dominate the mineralogy of the biofilm samples by mass. On a diel basis, cycling of HMO and associated trace metal dynamics appear to be contingent on the vertical migration of the biofilm oxic-anoxic boundary, a microbially controlled process.

The reactivity and sorptive capacities of synthetic HMO analogs for Ni were further examined under well-characterized laboratory conditions. Analysis of the local chemical environment of Ni sorbed to HMO by synchrotron-based X-ray absorption spectroscopy was integrated with a bulk geochemical model of the acid-base characteristics of HMO and a theoretical model of the HMO structure. The synergistic use of these techniques allowed unique insight into the structural reactivity of HMO for Ni and is the first study to mechanistically demonstrate why bulk surface complexation models (SCM) are not accurate for HMO metal uptake.

Overall, the results of this thesis highlight the utility of combined field and laboratory investigation to characterize relevant processes for reactive metal transport and underscore the need to: (1) consider microscale microbial-geochemical linkages in geochemical behaviour; (2) use caution when applying results derived from synthetic analogs to interpret natural system behaviour; and (3) examine processes at the appropriate scale e.g. microscale, to evaluate the mechanisms involved in metal reactions with solids.

ACKNOWLDEGEMENTS

I would first like to extend my most sincere thanks to my Ph.D. supervisor, Dr. Lesley A. Warren. You opened the door into the world of biogeochemistry and have offered me every opportunity to succeed. Your never-ending professional and personal support has been the foundation of this process.

I wish to extend thanks to my committee members, Drs. James Smith, Ian Droppo and Brian McCarry, for their professional guidance. I have benefited professionally and personally from the mentorship of many. I would like to expressly thank Dr. Jim Smith again for his advice on numerous applications and documents. Other excellent mentors during my Ph.D. have been Drs. D. Scott Smith, Thomas P. Trainor, and Hok Woo. I also thank Drs. Paulin Coulibaly, Adam Hitchcock, John Lawrence and Jim Britten for guidance in research.

I owe much thanks to many for technical support. Thanks to Pam Collins, Klaus Schultes, Martin Knyf, Marnie Timleck, Bob Harris (University of Guelph), Matthew Newville and Steve Sutton (Advanced Photon Source, Argonne, IL), and the employees at Unisense (Jens, Lars, Lars, and Lars),

This research would not have been possible without financial and support-in-kind from Falconbridge Ltd. Thanks to Shirley Lalonde for XRD analyses. I acknowledge funding for this research from NSERC, CFI and OIT grants to LAW. I am extremely thankful for financial support from NSERC in the form of a PGS-A (2000-2002) and a Julie-Payette Post-Graduate Scholarship (2002-2004). I also acknowledge funding from the Department of Fisheries and Oceans, the Walter Gibbons Memorial Travel Grant, and the McMaster Graduate Students Association.

I would like to extend my most heart-felt thanks to those in my research group: Derek Amores, Tara Nelson, Lisa Melymuk, Corrie Kennedy, and Luc Bernier. Your collective support has been invaluable. Lastly, I would like to thank those that have offered personal support: Richard and Karen Haack, Erin Clark, Keren Brown, Reuben Rasiah and my other close friends from Guelph, Joe Hall, my church community, Bob Bignell, and my community of colleagues at McMaster University. My most sincere thanks go to Valorie Crooks. You are an amazing friend, an excellent scholar, and an exceptional colleague; I look forward to your certain success and to our shared ventures.

TABLE OF CONTENTS

LIST OF FIGURES

LIST OF TABLES

LIST OF ACRONYMS

%LOI ..... Percent Loss on Ignition
ARD..... Acid Rock Drainage
DBL ..... Double Layer Model
EPS .....Extracellular Polysaccharides
ESEM ..... Environmental Scanning Electron Microscopy
EXAFS ..... Extended X-ray Absorption Fine Structure
FOCUS ..... Fully Optimized Continuous pK_a Model
HFO ..... Hydrous Ferric Oxyhydroxides
HMO ..... Hydrous Manganese Oxyhydroxides
MDSEP .....Microwave Digestion Sequential Extraction Protocol
MRB ..... Metal Reducing Bacteria
MUSIC ..... Multi-Site Complexation Model
SCM ..... Surface Complexation Model
SEM ..... Scanning Electron Microscopy
SRB ..... Sulphate Reducing Bacteria
XAFS .....X-ray Absorption Fine Structure
XANES ..... X-ray Absorption Near-Edge Structure
XAS ..... X-ray Absorption Spectroscopy
XRD ..... X-ray Diffractometry

PREFACE

Two chapters of this thesis consist of modified versions of manuscripts: Chapter 1 (Warren, L.A. and Haack, E.A., 2001. Biogeochemical controls on metal behaviour in freshwater environments. *Earth-Science Reviews*. 54: 261-320.) and Chapter 3 (Haack, E.A. and Warren, L.A., 2003. Biofilm Hydrous Manganese Oxyhydroxides and Metal Dynamics in Acid Rock Drainage. *Environmental Science & Technology*. 37: 4138-4147.).

Warren and Haack (2001), a review, was one of the top ten downloaded papers in Earth-Science Reviews in 2001. The contribution of the thesis author to this manuscript was substantial and included independent research and writing of several sections of the larger manuscript; the overall contribution of the thesis author to this manuscript was 40%. Chapter 1 draws on relevant sections of that review appropriate to the scope of the thesis objectives. The second published manuscript (Chapter 3) and results soon to be submitted found in Chapter 2, [Haack, E.A. and L.A. Warren. 2004. Evaluation of sequential extraction scheme alterations to mineralogy of synthetic analogues for acid rock drainage tailings material. Limnology and Oceanography], and Chapter 4 [Haack, E.A., D.S. Smith, T. Trainor and L.A. Warren. 2004. EXAFS investigation of Ni sorption to hydrous manganese oxyhydroxides (HMO); Why surface complexation models do not work for all oxyhydroxide minerals. Proceedings of the National Academy of Science], are the result of research carried out by the thesis author under the supervision of Dr. Lesley A. Warren, in partial fulfillment of a Ph.D. degree. The thesis author carried out all aspects of the research including review of the pertinent literature, field- and laboratory-based data collection, data analysis, and writing of the chapters; Dr. Warren provided guidance and editorial comments throughout. Chapter 4 presents results from collaboration also with Dr. Thomas P. Trainor (University of Alaska, Fairbanks) who provided expertise on synchrotron based-X-ray absorption data collection and data analysis, and Dr. S. Scott Smith (Wilfrid Laurier University) who provided expertise on equilibrium modeling and many discussions on application of the MUSIC model. While Drs. Trainor, Smith and Warren provided guidance, the direction, analysis of the spectroscopic results, interpretation of the modeling results, and writing of this chapter were carried out by the thesis author.

CHAPTER 1: MICROBIAL-MINERAL-TRACE METAL INTERACTIONS IN FRESHWATER ENVIRONMENTS

Reproduced with permission from Warren, L.A., Haack, E.A., 2001. Biogeochemical controls on metal behaviour in freshwater environments. *Earth-Science Reviews*, 54: 261-320. Copyright 2003 Elsevier BV.

1.1. Introduction

Trace metal concentrations in aqueous environments have increased dramatically in the past several decades as a result of anthropogenic inputs. Because of the potential toxicity of these metals to ecosystem and human health, their behaviour within these environments is cause for concern (Beveridge et al., 1995). Regulation, mitigation and remediation of metal-impacted environments are important challenges, since our understanding of the controls on metal behaviour is incomplete (Ledin and Pederson, 1996). What has become increasingly evident from the vast but segregated literature on the broad topic of metals in aquatic environments (spanning the disciplines of biology, chemistry, physics and geology) is the trans-disciplinary nature of the controls on metal cycling. Interdisciplinary studies that have linked the potential influencing parameters across disciplines have shown that the controls on metal behaviour involve complex linkages of biological (principally bacterially driven) and geochemical processes, occurring at both the microscopic and macroscopic scales.

In this introductory chapter, current knowledge of the controls on metal behaviour in freshwater environments is reviewed and hightlighted is the area needing further research: the role of microorganisms in these controlling processes. The first part of the chapter (sections 1.1. to 1.4.) examines the reactivities of important solid fractions for trace metals, in light of the discovery that reactions occurring at solid surfaces play a dominant role in metal partitioning between the solid and solution phases (Jenne, 1968). The controls on surface reactions are outlined, and highlight the biological dimension that must be incorporated into the traditional geochemical paradigm of surface complexation reactions to understand metal cycling in natural environments. The surface chemistry and reactivities of different solid surfaces in natural environments for trace metals are then discussed – focusing on the controlling roles of Fe and Mn oxyhydroxides and bacterial surfaces for the partitioning of metals from solution to the solid phase. While there is great utility in examining the reactivity of these sorbent phases individually, natural environments are heterogeneous and trace metal sequestration in association with composite bacterial-mineral surfaces is more difficult to quantify. Biofilms represent composite bacterial-mineral solids. Biofilms are highly structured microbial

communities of high cell density. Within the biofilm structure, microbial ecology and associated processes of metabolism produce internal geochemical gradients. Further, minerals are precipitated in association with the biofilm structure. A review of the relevant literature reveals gaps in the current understanding of the relative role of biofilms on metal cycling within systems as a whole.

The complexity of metal sorption reactions has led to a number of equilibrium modelling approaches. The model most relevant to this thesis is the Surface Complexation Model (SCM). Historically, this model was built to predict metal sorption at the surface of iron oxide surfaces under varying geochemical conditions (Dzombak and Morel, 1990; Drever, 1997). The challenge for all geochemical models is an accurate representation of the interaction between species in solution and the variably-charged surfaces of important environmental particles, including Fe/Mn oxyhydroxides and bacterial surfaces. The theory behind SCM and the limitations of this model and other geochemical models for our understanding of the processes controlling metal behaviour are outlined in section 1.5.

Bacteria, apart from being important reactive surfaces, impact a number of highly relevant processes for metal dynamics. These include the micro-scale processes of solid-solution partitioning and mineral precipitation/dissolution reactions, and macro-scale system geochemistry (section 1.6.). Again, it is the linkages between these physical, chemical and bacterially-driven processes that are occurring at all scales that need to be delineated and characterized. The development of powerful new analytical and spectroscopic tools that can be used in situ (section 1.7) is providing a means to quantitatively examine these linkages.

The overall objective of this thesis was to elucidate the controls on metal behaviour within biofilms in a metal-impacted Acid Rock Drainage (ARD) environment, at all relevant scales (section 1.9). Biofilms are chosen as the obvious locale to study microbial-mineral-metal interactions because they are highly stratified microbial communities characterized by associated mineral phases and strong internal dynamic geochemical gradients. Metal behaviour is likely significantly impacted by these gradients, even though the gradients occur within the relatively small volume (at the system scale) of the biofilm. ARD environments are created by the weathering and oxidation of pyritic materials, a process that is now accepted to be the result of bacterial catalysis, and are characterized by heterogeneous microbial communities, low pH, and high metal loads. As such, they represent a uniquely suited study site for the elucidation of the biogeochemical controls on trace metal behaviour.

1.2. Surface Chemistry and Reactivity of Natural Materials

1.2.1. Surface Reactions

A foundation of the emerging aquatic metal bio-geochemistry paradigm lies in the discovery that reactions occurring at solid surfaces play a dominant role in determining metal partitioning between the solid and solution phases, and thus, the potential impact of

metals in aqueous environments (Jenne, 1968). Reactions occurring at the interface of solid surfaces with their surrounding aqueous medium occur because solids carry a surface charge in aquatic environments and thus attract counter ions from solution to balance that charge (see Fig. 1.1. for an oxide surface as an illustrative example). The potential for reactions involving metals to occur at solid surfaces arises from (i) the existence of unfulfilled charge requirements of molecules or functional groups (e.g., hydroxyl, carboxyl, phosphoryl) at the solid surface; (ii) the unique properties of water itself that cause it to be a polar molecule; (iii) the presence of solution or dissolved elements that also possess non neutral charges; and (iv) the inherently dynamic nature (strongly driven by biological processes) of aquatic systems that causes constant dis-equilibrium within the system and the impetus for reactions to occur.

The pH value at which a solid surface has a net neutral charge from the binding of H^+ and OH^- ions at surface functional groups is referred to as the point of zero charge, or pH_{zpc} (Stumm and Morgan, 1996). A mineral surface will be positively charged at pH values above and negatively charged at pH values below the pH_{zpc}. Dependent on their respective acid dissociation constants (K_a, often expressed as $pK_a = -\log K_a$), functional groups at a solid surface can become negatively charged through the loss of protons (in response to changes in system chemistry that affect pH, such as surface functional groups buffering pH by donating protons to solution as solution pH values increase). Deprotonated functional groups can act as binding sites for positively charged ions such as metals. Functional groups at mineral surfaces can also become positively charged through binding of protons, and thus act as buffers by accepting protons at lower pH values. Protonated functional groups are capable of binding negatively charged compounds. Functional groups associated with mineral surfaces are often amphoteric and the species (cation or anion) bound at these sites is ultimately dependent on system pH.

In general, any reaction involving an ion in solution and a functional group at a solid surface that results in the formation of a surface complex is referred to as a sorption reaction. Because the surface of the solid is charged, an interfacial potential gradient is created between the solid surface and the bulk solution (see 1.5.2.). Inner sphere complexes are formed when a solute ion from solution moves through the interfacial gradient and forms a covalent bond with a functional group at the surface of the solid. The formation of this type of complex, that involves both chemical and electrostatic forces, is also known as "adsorption" (Stumm and Morgan, 1996). Outer-sphere complexes are formed when a solute ion interacts with the surface purely by electrostatic forces. Solutes sorbed as outer-sphere complexes are more weakly associated to the solid surface than adsorbed solutes, and thus, are more easily re-solubilized.

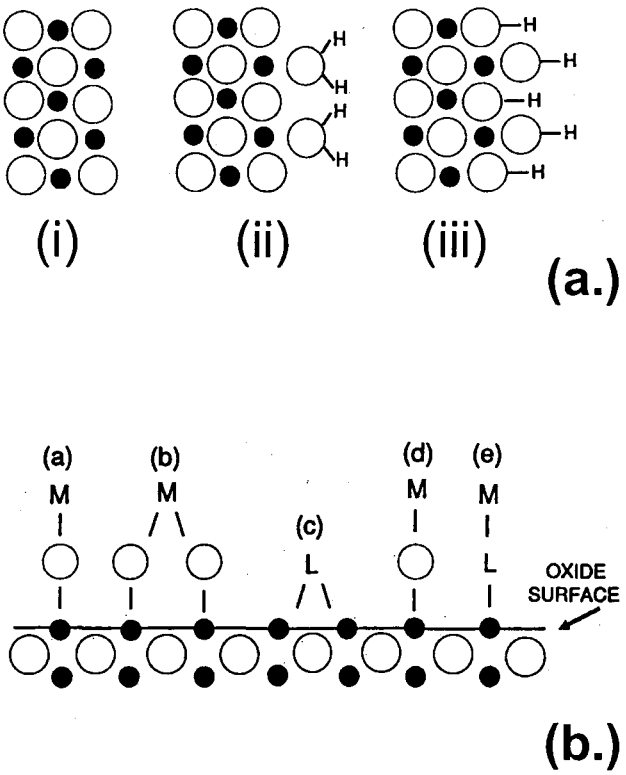

Figure 1.1: (a) A cross section of the surface layer of a metal oxide: •, metal ions and ○, oxygen ions. (i) A dry oxide surface; (ii) in the presence of water, surface metal ions may coordinate H_2O molecules; (iii) dissociative chemosorption leads to a hydroxylated surface. (b) Possible hydrated oxide surface complexation reactions. Oxide surface; •, metal ions and ○, oxygen ions; and solution ions: M, metal ion; L, ligand. The surface hydroxyl group (OH) has a complex-forming O donor atom that can complex a metal ion from the solution (a); two surface O donor atoms can complex one metal ion (b); the underlying metal ion (• e.g., Fe, Mn, Al, Si), can exchange its surface OH group for other ligands (c); the O donor atom can complex a metal-ligand complex (d); or (e) the underlying metal ion can exchange its OH group for a ligand-metal complex (adapted from Warren and Zimmerman, 1993).

1.2.2. Controls on surface reactions

The underlying control on solid surface charge as well as on the speciation of elements within solution is pH. As such, pH dictates cation and anion partitioning between the solid and the solution phases with all the attendant ramifications for geochemical behaviour, e.g., mobility, reactivity, bioavailability, bioaccumulation, and toxicity. pH is commonly thought of as the master variable controlling metal behaviour in aquatic environments.

While pH has an overwhelming dominance in metal dynamics, other factors can also play a substantial role within this framework. The factors that can profoundly affect the snapshot of metal behaviour observed at any given time are, specifically: (i) the physical and chemical properties of an aquatic environment (e.g., ionic strength, redox status, presence of water currents, the location and activity of biota); (ii) the composition of its solution phase (e.g. the types and concentrations of solution species); (iii) the types and densities of solid sorbents and the kinetics of relevant reactions, e.g., the influence of biological activity and temperature (Allard et al., 1987; Sigg, 1997; Westall, 1987; Sheintuch and Rebhun, 1988; Tessier et al., 1989; Johnson, 1990; Warren and Zimmerman, 1994a, 1994b; Warren and Ferris, 1998; Warren et al., 1998; Small et al., 1999, 2000).

Ionic strength affects metal partitioning through two principal mechanisms. The activity of a species in solution is affected by the solution ionic strength. Solutions of higher ionic strength result in decreased activities or effective concentrations of elements for reaction with surface functional groups. Solution ionic strength also affects the thickness of the charge differential zone at the interface between the solid surface and the bulk solution (see Eq. 1.10). The distance to which this zone extends into solution from the solid surface decreases with increased ionic strength. Solutions of higher ionic strength generally result in a decrease in the number of surface complexation reactions occurring between metal species in solution and functional groups at solid surfaces (e.g. Puls et al., 1991; Lores and Pennock, 1998). In particular, outer-sphere complexes (purely electrostatic interaction) are more inhibited at high ionic strength than are inner-sphere complexes.

Redox status impacts the partitioning of metals between the solid and dissolved phase as well as the dominant chemical form of a metal in solution. Redox species of metals that possess more than one possible oxidation state in natural waters are differentially mobile, soluble, toxic and reactive (Ahmann et al., 1994; Losi and Frankenberger, 1997; Newman et al., 1998; Brown et al., 1999; Wang, 2000). Highly charged metals ions, such as Cr(VI) and As (V) tend to exist as oxyanions in solutions at moderate to high pH, and also tend to have a high affinity for biological binding sites and associated toxicity (Bartlett, 1991; Richard and Bourg, 1991; Baruthio, 1992). The redox state of a metal is often impacted by bacterial activity. Bacteria are able to enzymatically reduce toxic metals; the reduction represents a detoxification process (e.g. Hg^{2+} to Hg^{0}; Ogunseitan and Olson, 1991; Saouter et al., 1994). Bacteria also enzymatically reduce metals within mineral phases, such as Fe and Mn oxy-hydroxides. Fe in its oxidized trivalent state, Fe^{3+} readily hydrolyzes and precipitates as an oxyhydroxide solid Fe (III) phase that then subsequently provides a highly reactive and important surface for trace

metal scavenging in aqueous environments. Reduction of Fe^{3+} to divalent Fe^{2+} can be accompanied by dissolution of the solid Fe oxy-hydroxide phase and potential release of any associated metals. Similarly, oxidation and reduction involving Mn will result in solid phase capture or solution release. A significant proportion of the metal reduction occurring within sediments is thought to be a result of such enzymatic processes (Lovley, 1995). All of these redox mediated transformations have differential implications for metal behaviour in aquatic systems.

Beyond the impact of bacteria on the redox state of individual metals, the redox status of the compartments (e.g. water column, sediments) of any given system is directly impacted by the biological community composition and function within those compartments. Biota influence system redox status principally through the two major linked processes of photosynthesis and decomposition that cycle carbon and energy through organic and inorganic states. Biota, therefore, affect both oxygen and proton concentrations. The links between redox and pH become evident when these two processes are considered (Drever, 1997):

$$CO_2 + NO_3^- + PO_4^{3-} + H_2O + H^+ + \text{trace elements} + \text{energy} \rightarrow \text{organic matter} + O_2 \qquad (1.1)$$

Photosynthesis in the presence of either electromagnetic or chemically derived energy drives the above reaction to the right, producing organic/reduced carbon compounds, consuming protons, and producing molecular oxygen. Decomposition of organic matter (oxidation) will drive the reaction to the left. Organic compounds are oxidized through a series of organic intermediates, and potentially back to CO_2. Oxygen is consumed by this process and protons liberated. The exact stoichiometry of the reaction depends on system conditions, the nature of the inorganic (e.g. HCO_3^-, CO_3^{2-}, CO_2) and organic carbon sources (e.g. lactate, pyruvate, succinate), and the microbes involved. It is very important to note that the relative intensities of these reactions, especially photosynthesis, are both diurnally and seasonally correlated. Biological reactions influence system chemistry in a dynamic manner, whether viewed on a daily or on a seasonal basis. The relative impact of these reactions will be determined by both the intensity of the reaction rates, which is a function of biotic density and activity, and by the location of biota in the system. Thus at periods of high biological activity, significant changes in redox or pH may occur in localized areas which can strongly impact metal dynamics within that zone.

1.3. Metal speciation and reactivity

Not all metals are equally reactive, toxic, or available to biota (Hare, 1992). Metals ions dissolved in solution, or complexed to simple dissolved ligands, are thought to be the most available and toxic (Sunda and Lewis, 1978; Luoma, 1983; Martell et al., 1988; Shuttleworth and Unz, 1991; Campbell, 1995). Thus, measurement of total metal ion concentration in solution or as part of a solid matrix is often meaningless for prediction of metal behaviour (Campbell and Tessier, 1989). With regards to reactivity, it is generally observed that different metal ions display differing affinities for surface

binding sites across substrates, and further that not all metals display the same affinities for individual surfaces (e.g. Sauvé et al., 2000). The strength of the metal-sorbent bond is given by a surface complexation/binding constant, K_{SM}^{z+} (where M^{z+} refers to the specific metal of interest). The value of the binding constant has important implications for potential re-release of the metal ion into solution given changes in system chemistry. The greater its surface complex formation constant, the less likely that the metal ions will be desorbed and released to solution, where it is potentially more available, reactive and toxic.

1.4. Important Solids

1.4.1. Fe and Mn oxyhydroxide minerals

To a large extent, mineral surfaces, especially those of Fe oxyhydroxides, have received a large degree of attention in aquatic metal chemistry. This is due to their ubiquitous and abundant nature, as well as their proven geochemical reactivity (Honeyman and Santschi, 1988; Brown et al., 1999). Metals can be incorporated into solid minerals by a number of processes including: inner and outer sphere complexation, coprecipitation (solid solution), and precipitation as discrete oxide or hydroxide precipitates (Martinez and McBride, 1998). There are a number of factors that can influence the extent of metal sorption by any one mineral sorbent type: degree of crystallinity (e.g. Martinez and McBride, 1998), number of defect sites, impurities and/or coprecipitates (Banfield et al., 1997; Webster et al., 1998), surface coatings of organic matter and/or bacteria, and particle size (Brown et al., 1999).

Fe and Mn oxyhydroxides commonly form surface coatings on other types of mineral substrates such as clays and carbonates (e.g. Whitney, 1975; Helios-Rybicka and Forstner, 1986; Warren and Zimmerman, 1993, 1994c; Coston et al., 1995) and thus, whilst their relative mass in a suspended sediment pool may be relatively small, they often dominate the geochemical reactivity of that sediment compartment. The sorptive capacity of Fe oxyhydroxides is extremely well studied relative to other potentially relevant mineral surfaces. Attention is turning increasingly to other minerals, which are also likely to play a role in determining the geochemical behaviour of metals in aquatic environments through their similar characteristics and potentially significant concentrations in certain locales. One such group of minerals is Mn oxyhydroxides.

Mn (III,IV) oxyhydroxides are generally denoted as MnO_x ($1 \leq x \leq 2$) and include oxides, oxyhydroxides and manganates (contain a variety of charge balancing, low valence cations; Tebo et al., 1997). Like Fe oxyhydroxides, Mn oxyhydroxides are also very stable, exhibit low solubility (Stumm and Morgan 1996), and precipitate as very small crystals that are often poorly crystallized or amorphous, (Fortin et al., 1993; Mandernack et al., 1995; Tessier et al. 1996). Mn oxyhydroxides have been shown to be highly effective scavengers of a variety of metals (e.g. Tessier et al., 1996; Fuller and Harvey 2000) and are thought to be potentially more reactive than Fe oxyhydroxides (e.g. Whitney, 1975; Balikungeri and Haerdi, 1988; Bendell-Young and Harvey, 1992; Nelson et al., 1999a.). The higher reactivity imparted to Mn oxyhydroxides compared to Fe oxyhydroxides at pH values relevant to natural environments is related to the pH_{zpc}

values of these minerals. Iron oxyhydroxides (goethite, hematite, ferrihydrite) have pH_{zpc} values ranging from 7.5 to 9.5 (Cornell and Schwertmann, 1996). Practically, this means that sorption of metal ions to iron oxyhydroxides such as ferrihydrite does not occur at pH values below 4 (Dzombak and Morel, 1990). In contrast, Mn oxyhydroxides have much more acidic pH_{zpc} values; values range from less than 2.40 for amorphous manganese oxyhydroxides to 7.2 for more crystalline phases (Murray, 1974; Stumm and Morgan, 1996; Catts and Langmuir, 1986). The more acidic pH_{zpc} values of manganese oxyhydroxides means that significant metal sorption can occur in association with these mineral at pH values as low as 2 (Matocha et al., 2001; Tonkin et al., 2004).

The oxidation of Mn(II) is thought to be a biologically controlled process under circumneutral conditions in most freshwaters (Nealson et al., 1989; Sunda and Kieber, 1994; Emerson, 2000). This is in contrast to the oxidation of Fe(II). Abiotic oxidation of Fe (II) by molecular oxygen occurs rapidly at values above 6 (Cornell and Schwertmann, 1996); experimental rates for the abiotic oxidation of Fe(II) match those measured for Fe(II) oxidation in natural lakes at circumneutral pH values (Tipping et al., 1989), suggesting that microbial catalysis of this reaction plays a minor role in the overall reaction rate. Oxidation of Fe(II) in the absence of catalysis is very slow at pH values below 6; at pH values below 4 the rate is independent of pH (Stumm and Morgan, 1996). Mn(II) is oxidized much more slowly than Fe(II) in the absence of biological material (Davison, 1993). In the absence of catalysts, solutions of Mn(II) at pH 8.4 are stable for at least seven years (Diem and Stumm, 1984). The half-life for the oxidation reaction of Mn(II) to Mn(IV) in natural waters (pH 8, O_2 ~9.0 mg/L, 1μM dissolved Mn) is on the order of 10^3 days (Davison, 1993). This half-life is not reflected in natural lakes where the experimentally observed half-life of this reaction is 1-100 days (Chapnick et al., 1982; Tipping et al., 1984). Little doubt presently exists regarding the role of microbial catalysis in the formation of MnO_2 in most natural environments (Davison, 1993).

1.4.2. Bacteria

Bacteria can have two roles in the cycling of trace metals in natural systems. The first role is as a sorbent phase. Surfaces of bacteria are analogous to mineral surfaces in that they possess surface functional groups that can sorb metals from solution. This role is discussed below. The second is a result of their "live" nature; they show an incredible versatility in metabolic processes and live in many physically and chemically extreme environments. This role is discussed further in Section 1.6.

Surface reactivity and metal binding to bacterial cell walls and exopolymers

There is a growing interest in the use of bacteria as biosorbents for removal of metals from solution as their effectiveness as solid phase sorbents becomes increasingly evident (e.g. Volesky, 1990; Volesky and Holan, 1995; Schiewer and Volesky, 2000). A bacterium's potential sorptive capacity and affinity for various metals is dependent on the types and densities of functional groups associated with the cell. The types and densities of functional groups are in turn affected by the microbe's cell wall composition (gram positive vs. gram negative), metabolic state, and associated extracellular polysaccharides (EPS). Live, metabolically active cells, live non metabolically active cells and dead

intact cell surfaces can all possess different surface reactivities (e.g. Parmar et al., 2000). EPS are highly hydrated fibrous matrices secreted by live organisms that may be found in association with or surrounding various bacterial species (Urrutia, 1997). Structurally, EPS are homo- or heteropolymers of carbohydrates and proteins (Urrutia, 1997).

Bacterial surfaces are indicated amphoteric and to have the ability to bind metals (Doyle et al., 1980). Under most environmental pH conditions, the bacterial cell surfaces carry a net negative charge as a result of negatively charged functional groups in the cell wall (Ferris and Beveridge, 1985). The overall anionic nature of bacterial cells in most aquatic environments is a result of the pk_a values of the carboxyl and phosphoryl groups (4-6 and ~7, respectively) that, in different densities, make up the cell walls of both gram-positive and gram-negative bacteria. Cell surfaces also possess amino groups, which at circumneutral pH are positively charged (pK_a ~9). The relative abundance of these three groups in the cell wall as well as the metal-binding nature of each group, will determine the metal-binding capacity of the cell surface at a given pH. Different surface sites may play a larger role in aquatic environments of low pH versus those at high pH.

Early research on metal binding to bacterial cell walls was focused on reactions occurring specifically at the cell surface of *B. subtilis* (gram positive; Beveridge, 1984). Beveridge and Murray (1976) found that isolated walls of *B. subtilis* complexed substantial amounts of Mg^{2+}, Fe^{3+}, Cu^{2+}, Na^{+}, K^{+}, intermediate amounts of Mn^{2+}, Zn^{2+}, Au^{3+}, Ni^{2+}, small amounts of Hg^{2+}, Sr^{2+}, Pb^{2+} and Ag^{+}, and did not complex Li^{+}, Ba^{2+}, Co^{2+} and Al^{3+} at all. Further, some metals were bound more strongly than others. The metal complexing ability of the cell wall material was later attributed primarily to the carboxyl groups associated with the cell wall structure (Beveridge, 1978; Doyle et al., 1980). Chemical modification of the carboxyl and amino groups of the *B. subtilis* cell wall established the importance of both groups for metal interactions with the surface, with an increase in metal binding capacity observed with the loss of amino groups (Doyle et al., 1980). More recently, Puranik and Paknikar (1999) observed differential metal affinity in association with the gram negative *Citrobacter* strain MCM B-181. When exposed to multi-metal solutions, metals were adsorbed to the biomass preferentially in the order $Co^{2+} < Ni^{2+} < Cd^{2+} < Cu^{2+} < Zn^{2+} < Pb^{2+}$. Philip et al. (2000) showed that Cu (II) binding to *Bacillus polymyxa* surfaces occurred by complex formation with oxygen and nitrogen atoms. Consistent with the earlier work suggesting the importance of carboxylic groups, the results of Philip et al. (2000) suggest that Cu is bound by the carboxyl groups of the peptidoglycan layer and amino sugars or structural proteins.

Overall, the reactions occurring at bacterial surfaces share the same characteristics as those occurring at mineral surfaces. Similarities include that all surface functional groups can play an important role in proton and metal binding to cell walls and that binding affinities and bond strengths vary amongst metals for the same surface sites. For bacteria, however, surface reactivity is made more complex in that the relative importance and density of the functional groups differs between gram-negative and gram-positive bacteria, but also among bacterial species. An important caveat to also consider for metal reactions occurring at bacterial surfaces is that bacteria in natural environments often co-exist in mutually beneficial, highly functionally structured consortia. The

overall geochemical reactivity of such consortia is likely to be considerably different than those of the individual bacterial strains.

1.4.3. Biofilms

There are several possible modes of bacterial existence in aquatic environments: planktonic, biofilms and suspended aggregate - flocs. The existence, dominance and importance of each mode varies among aquatic systems as well as within various compartments (e.g. water column, sediments, pelagic versus littoral) in any given aquatic environment. Typical cell densities in the pelagic zone are on the order of 10^6 mL^{-1}; in biofilms they can reach 10^9 - 10^{11} mL^{-1} (Characklis, 1990). Thus, another factor that must be considered in the potential for bacterial scavenging of metals in aquatic environments is their dynamic, heterogeneous, non-uniform spatial distributions (microcolony structure) and concentrations. Bacterial influence can be relatively minor when considered for a system as a whole, but may play the dominant role in certain locales due to high cell density and associated activity.

Biofilms represent a macroscopic "uber-bacteria". To give perspective on the sheer numbers of bacteria and relative potential for intensity of geochemical effect: the average size of a bacterium is approximately 1-2 μm in length. Bacterial biofilms can extend in physical size up to metres. These biological structures, comprising live and dead cells and organic matrices, represent a highly complex and highly structured environment where the macro structure of the biofilm, created principally by EPS secretion (Neu and Lawrence 1997; Davies et al., 1998; Lawrence et al., 1998a;) helps irrigate the biofilm providing nutrients and removing waste products. Within the biofilm, there is structural and spatial heterogeneity with regards to cell physiological state, phenotype and genotype (Lawrence et al., 1995; Little et al., 1997; de Beer and Schramm., 1999; Ferris et al., 1999; Sternberg et al., 1999). The physical structure of the biofilm is stratified, with the various microbial inhabitants in tightly linked sequential reaction pathways from the biofilm-solution interface to its bottom interface with the substratum (Figure 1.2; Canfield and Des Marais, 1993; Little et al., 1997). Photosynthetic and aerobic organisms are positioned at the biofilm-water interface, while bacteria that decompose organic matter (coupled to the reduction of sulphate, Fe (III) or Mn (III/IV) oxyhydroxides) are more commonly found deeper in the biofilm where anoxic conditions have been created.

Due to the diversity in metabolic function within biofilms, these structures are likely to be characterized by steep, continuously shifting physico-chemical gradients (Lawrence et al., 1995). These geochemical gradients will shift diurnally and over time, reflecting changes in biofilm community composition and activity. Thus, biofilms are biological reactors creating geochemical micro-environments that can differ substantially from the overlying water column. The conditions occurring with biofilms are likely to be highly dynamic reflecting both the diel nature of biological activities as well as the natural aging process that occurs in biofilms or mats. Metal dynamics within biofilms are likely to be substantially different from either the sedimentary or water column compartments, however, the extent of their relative influence on shaping metal cycling as a whole within systems remains largely unknown.

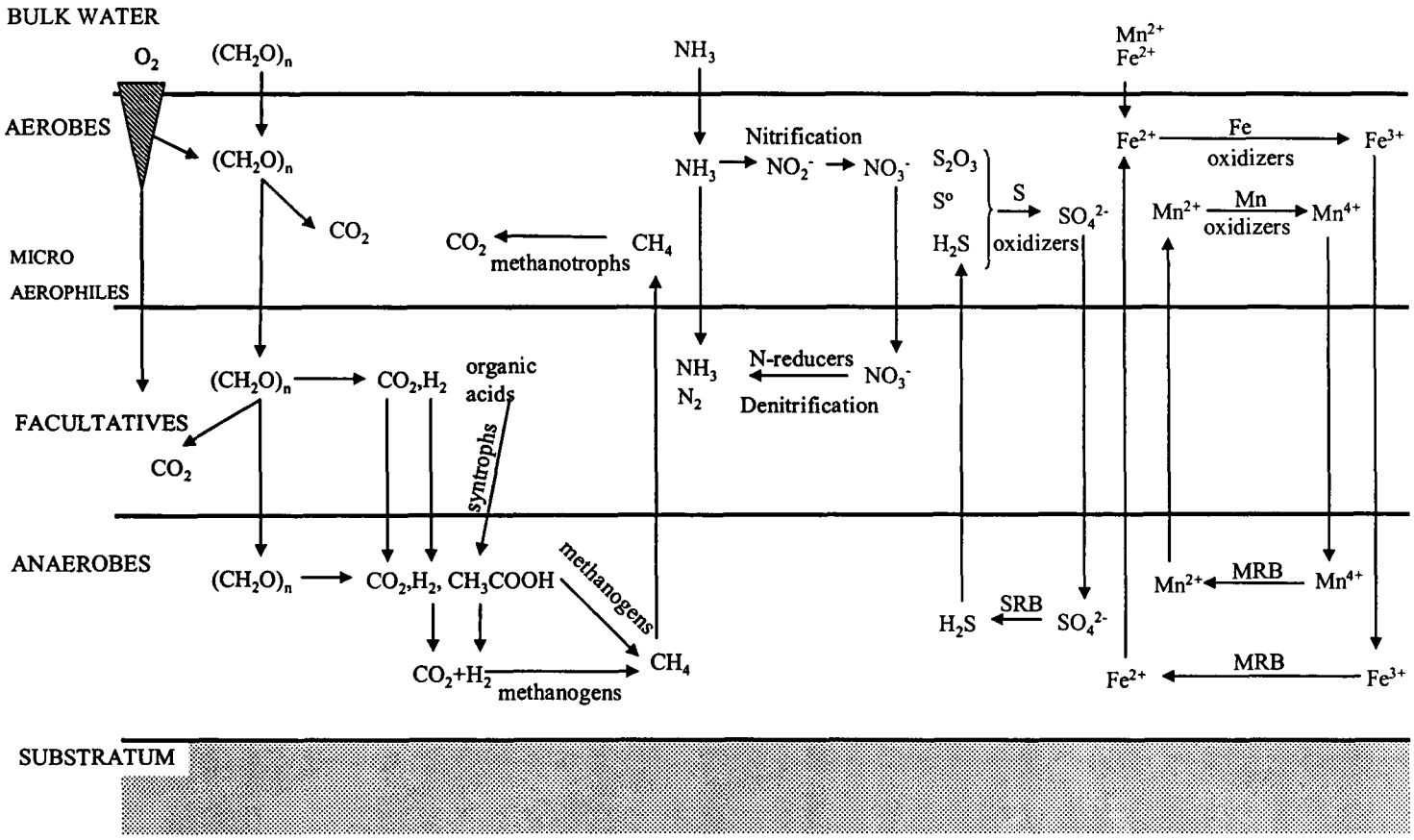

Figure 1.2. Biofilm microbial stratification and resulting geochemical zonation within biofilm consortia (adapted from Little et al., 1997). Microbial function is vertically stratified within the biofilm leading to depth dependent differences in geochemical reactions and conditions within the biofilm. O_2 requirements for growth: aerobe (requiring oxygen), microearophile (requiring O_2 values < atmospheric), facultative (O_2 not required but growth can occur in the presence of O_2), and anaerobe (O_2 is harmful to growth) (Brock, 1984). Other terms defined, see page xii.

1.4.4. Biofilms and Metals: Metal sorption to Composite Solids

Studies examining metal sorption within biofilms have indicated that: 1) metals are highly accumulated in these structures, i.e. concentrations of metals associated with the biofilm can be orders of magnitude greater than respective solution phase concentrations; 2) both minerals formed in association with the biofilm organic matrix and the organic matrix itself are important metal sorbents. Biofilms are essentially composite solids as they are composed of bacterial cells, associated EPS, and minerals. Minerals formed in association with biofilms are commonly referred to as biominerals and have a high reactivity for trace metals. Biogenic minerals are discussed subsequently in more detail (Section 1.6.1). Each of the components of the biofilm structure is characterized by different surface properties (e.g., nature and densities of surface functional groups, and complexing ability; Buffle, 1988). The extent and pattern of metal sequestration within biofilms will thus likely reflect pH and the relative affinity of the metal for the individual solid fractions.

Ferris et al. (1989) carried out one of the early studies on metal capture by biofilms. The results of this study suggested that the amount of metal accumulated in the biofilm was pH-dependent. Aqueous and biofilm-associated metal concentrations from an acidic (pH 3.1) and a circumneutral lake were quantified. Total biofilm associated metal concentrations exceeded respective aqueous metal concentrations in both systems. Metal accumulation was enhanced in the biofilms from the circumneutral lake, by as much as 12 orders of magnitude over those measured in the biofilms from the acidic system. Iron oxyhydroxide precipitates were observed in association with the biofilms in both systems; however the importance of these minerals for metal sequestration likely was significant only in the circumneutral system (pH_{zpc} values for Fe oxyhydroxides range from 7.5-9.5, see section 1.4.1.).

A number of more recent studies have indicated that the mineral fraction of the biofilm is important for metal sequestration. Nelson et al. (1995) examined Pb sorption to a pure biofilms of *Pseudonomas cepia* and found that the presence Fe oxyhydroxides substantially increased Pb sorption to the bioiflm (up to 5 fold over the organic matrix alone). Pb sorption to natural biofilms was examined in a follow-up study (Nelson et al., 1999b). The mineral and organic components of the natural biofilm samples were identified using sequential extraction techniques. Pb sorption to whole biofilm samples was then measured in the laboratory over a range of Pb concentrations. The extent of Pb sorption was found to increase with increased Fe and chemical oxygen demand (i.e. cell growth). Finally, Ferris et al. (1999) quantified the metals bound to the bacterial iron precipitates in a mixed-species biofilm from a subterranean site (pH 7.0-8.0) in Sweden and found that they exceeded dissolved metal concentrations in the overlying water. The iron oxides associated with the biofilm had little long-range crystallinity, and were not found exclusively associated with the bacterial cells but were found throughout the biofilm in association with EPS. The important finding of this study was that the Fe oxide fraction was shown to bind 50-100% of the associated metals (Na, Mn, Zn, Co and Cu).

Other studies of the patterns of metal sequestration within biofilms suggest that the organic matrix of the biofilm (dominantly EPS) acts both as a reactive surface for

metal binding and as a protective mechanism. Enrichment of Zn and Cu in a river biofilm compared to the underlying sediments was attributed to the higher organic matter of the biofilm (Schorer and Eisele, 1997). In river biofilms, made up of microcolonies of 6 to 30 cells surrounded by an outer envelope, the spatial distribution of elements in association with the organic matrix was observed to be element-specific (Lünsdorf et al. 1997). Fe, Mn and Al deposits were all found at the surface of the microcolonies, while only Al penetrated the outer envelope and was detected within the microcolony. None of the elements were detected within the cytoplasm of the cells. Lünsdorf et al., (1997) proposed that the EPS surrounding the cells immobilized Al, likely sheltering the cells against metal toxicity, and that the Fe and Mn were deposited at the microcolony surface through both active and passive processes and may act as energy sources for the cells.

Together, these studies highlight the complexity of predicting metal behaviour in association with natural mixed solids and the need to further evaluate the behaviour of metals associated with biofilms.

1.5. Macroscale Predictive Models

Clearly, metal-sorbent dynamics are complex, reflecting specificity in both the metal(s) involved, as well as the solid surface(s) (i.e., types and densities of surface functional groups are solid dependent). The overwhelming importance of interfacial reactions has driven the development of a variety of modeling approaches. The diversity of models reflects not only the geochemical diversity of surface reactions but also the varying complexity depending on surface type (i.e. mineral or bacterial surface) and solution conditions (e.g. ionic strength).

All geochemically based modelling techniques have as their basis those laws governing coordination reactions in solution; i.e., complexation reactions between ligands and (for this discussion) protons and metal ions, characterized as chemical equilibrium models. The complexities of modelling proton and metal ion binding to heterogeneous sorbents such as bacteria and metal oxides are twofold: (1) bacterial cell walls and metal oxide surfaces are charged so that long-range electrostatic interactions must be accounted for to describe the complexation reactions in a physically meaningful manner; and (2) sorbent-sorbate interactions can not be simply represented by a single type of binding site because of the heterogeneity of functional groups present on the sorbent. Rather, "binding sites" are created purely for modelling convenience and must not be mistaken either to directly represent the actual physical reality of the surface functional groups or to permit interpretation of the surface reactions at the molecular level (Buffle, 1988).

Ideally, geochemical models should address all of the following considerations: (i) How do the electrostatic effects and the ionic strength of a solution affect complexation reactions at the solid-liquid interface? (ii) How penetrable are the sorbents to the sorbate species? (iii) Can we characterize competitive cation binding (e.g proton-metal ion or metal ion -metal ion) to the same sorbent over a wide range of chemical conditions? (iv) How does time affect the establishment of equilibrium partitioning of the sorbent between the solid and liquid phases? In reality, the first two considerations have been, and continue to be, extensively studied while the third consideration is a more recent development, and the last consideration is largely ignored.

1.5.1. Model Type

The model type addresses the complexity of representing the intrinsic heterogeneity of sorbents. Proton binding is thought to occur at a number of independent types of monoprotic sites (≥ 1) distributed randomly on the macromolecular surface. The term "binding site" is a collective term for surface binding sites or functional groups which demonstrate chemical equivalency; i.e. a specific type of carboxylic or hydroxyl group. All binding sites have associated equilibrium constants (pK_a), which when plotted against their abundance ($molkg^{-1}$), yields a pK/affinity spectrum (Leuenberger and Schindler, 1986). There are two model types: discrete and continuous. Discrete and continuous models differ in their representation of the binding sites used to reproduce the experimental acid-base titration data. Discrete models fix the number of binding sites to a (usually small) finite number, and each site is considered to have a unique (or discrete) pK_a value. Overall proton binding to the sorbent is then mathematically described as the linear sum of Langmuir isotherms for each of the individual sites (Borkovek et al., 1996). Isotherms express a relationship between the bulk aqueous phase activity (concentration) of the sorbate and the amount sorbed at a constant temperature (Stumm and Morgan, 1996). Langmuir isotherms are the simplest of adsorption isotherms, assuming a 1:1 stoichiometry at the binding sites. Alternatively, proton binding curves can be mathematically described as a summation of monoprotic ligands (Brassard et al., 1990). In both cases, the solution is numerical rather than analytical, meaning that a set of pK_a values is found through an iterative procedure. The number of peaks in the distribution corresponds to the chosen number of unique binding sites. The number of sites that is chosen is somewhat arbitrary; it is often a choice between the minimum number of sites needed to give a good fit to the experimental data (thus, minimizing the number of model parameters) and the number of sites that the researcher feels gives a better estimation of all the possible sites or of functional groups of the sorbent (Cox et al., 1999).

The continuous model is based on the theory that the sorbent is comprised of an infinite number or monoprotic sites with independent reactivities. Instead of describing overall proton binding as the linear sum of adsorption isotherms for each site, it is alternatively expressed as a continuous function of Langmuir isotherms. Not all these continuous equations can be solved analytically so that continuous models are often simplified to allow for a mathematical solution to the description of sorbent binding sites.

It is very important to note at this time that model-derived binding sites, whether derived from continuous or discrete models, do not directly represent functional groups associated with the sorbent phase. The identity of the "binding sites" can only be inferred by comparison of the binding site pK_a values with pK_a values of model compounds (for example carboxyl and phosphoryl groups for bacterial surfaces). Spectroscopic evidence is needed to link the modelled sites to "real" surface functional groups (Borkovec et al, 1998).

1.5.2. Mechanism: representation of the surface

A fundamental challenge in all geochemical models is how to quantitatively represent the dynamically charged interfacial region that occurs between the solid (e.g.

oxide surfaces, bacterial cell walls) and the bulk solution. Models attempt to account for electrostatic effects by employing a number of hypothetical physical representations that locate either specifically adsorbed ions and/or counter ions in the interfacial region, and as such, quantify the charge at a given pH

Theoretical models of the interfacial region

A complexation reaction between a sorbent functional group (L) and a sorbate (M) at equilibrium is generally represented as:

$$L + M \rightleftharpoons ML \tag{1.2}$$

and the associated equilibrium constant for such a reaction is expressed:

$$K_{LM} = [ML]/[M][L] \tag{1.3}$$

In the case of where a sorbate ion is adsorbed to a charged sorbent, the total energy of adsorption is the sum of short-range chemical (intrinsic), and long-range electrostatic (Coulombic) energy terms (Morel and Hering 1993).

$$\Delta G_{adsorption} = \Delta G_{intrinsic} + \Delta G_{coulombic} \tag{1.4}$$

Eq. 1.4 is the basis of all adsorption models (Morel et al., 1981). The energy contribution of the electrostatic interactions corresponds to the work necessary to bring an aqueous ion, M^{z+}, from the bulk solution through the interfacial potential gradient, Ψ, to the reactive site on the sorbent (Buffle, 1988; Stumm, 1992).

$$-\Delta G_{coulombic} = \ln K_{coulombic}/RT = -\Delta Z\,(-F\Psi/RT) \tag{1.5}$$

where Z is the net change in charge number due to the adsorption reaction, F the Faraday constant, R the ideal gas constant, T the absolute temperature. The "apparent" equilibrium constant for adsorption, is expressed:

$$K_{apparent} = K_{int} \times K_{coulobmic} = K_{int} \exp(-\Delta ZF\Psi/RT) \tag{1.6}$$

The exponential term in Eq. 1.6, $(-ZF\Psi/RT)$, is referred to as the Boltzmann factor and essentially expresses the effect of the interfacial potential at a charged surface. The subscript "int" used in the above expression is short for intrinsic. The intrinsic equilibrium constant, K_{int}, corresponds to K_{ML} from Eq. 1.3. Both are the equilibrium constants for the adsorption reaction at zero net surface charge (Goldberg 1992), i.e. they express the purely chemical bond formed between sorbent and sorbate without an electrostatic component. Analogously, [M] in Eq. 1.3 corresponds to the concentration of the sorbate, M, at the binding site, not in the bulk solution; i.e. the concentration of M accumulated in the interfacial region as affected by the electric potential of the charged sorbent.

$$[M] = [M_{bulk}] \exp(-\Delta ZF\Psi/RT) \tag{1.7}$$

Eq. 1.8 applies if the sorbent in Eq. 7 is a proton (Z=1).

$$pH = pH_{bulk} - 0.434\,(F\Psi/RT) \tag{1.8}$$

The interfacial potential gradient, Ψ, is not a directly measurable parameter. Thus, models of the reactions at the solid-liquid interface must rely on a "best guess" representation of the charge distribution as it occurs between the solid and bulk solution. All models that account explicitly for electrostatic effects must derive an expression relating potential to a measurable (or fitted) parameter. All theoretical models of the

interfacial region (1) relate the interfacial potential to the measured total sorbent charge, (2) involve some knowledge or assumptions about particle geometry and permeability (Dzombak and Morel, 1990; Milne et al., 1995), and (3) describe the accumulation of counter-ions in the interfacial region.

Pure surfaces: The Surface Complexation Model

Sorbents modelled as pure surfaces are variably represented as impenetrable and infinite planes or as impenetrable spheres. In a pure surface, the total particle charge is assumed to be distributed uniformly over the surface (e.g. Bartschat et al., 1992). Electric Double Layer models (EDL) are used to account for electrostatic effects on complexation reactions at these surfaces. EDL models all involve solving the Poisson-Boltzmann Equation, which assumes that electrostatic potential arises from a centrally charged region about which small, mobile ions in the solution arrange themselves in relation to the magnitude of the potential. The equation is composed of two parts, the Poisson equation relating potential to charge density and the Boltzmann distribution of co- and counter-ions in the potential field (Bartschat et al., 1992). Solving both parts of the equation permits description of the spatial distribution of co- and counter-ions in the interfacial region, and yields an expression for the surface potential as a function of distance from the charged surface.

The basic model for metal oxide surfaces is the Surface Complexation Model (SCM). Important to the discussion here is that this model treats the surface of metal oxides as infinite planes and that only one surface site type, described as hydroxyl groups, is considered necessary to explain their acid-base behaviour. The hydroxyl group is modelled as a diprotic acid; the neutral hydroxyl group, $\equiv XOH^0$, can be protonated to form $\equiv XOH_2^+$, or deprotonated to form $\equiv XO^-$, (where $\equiv X$ designates a surface species). Iron oxide surfaces are thus characterized by two discrete pK_a values. Metal ions are also deemed to interact with the hydroxyl functional groups, as either inner or outer-sphere complexes. The relative positioning of the metal ion differs for inner and outer sphere complexes due to the nature of the interaction; metal ions bound as inner sphere complexes are placed close to the surface sites while metal ions bound as outer sphere complexes are placed some specified distance from the surface sites. Because surface complexation reactions result in a change in surface charge, and associated surface potential, EDL models for metal oxide surfaces must consider (i) protonated and hydrolyzed surface species, (ii) surface sites coordinated with major ions of the background electrolyte, and (iii) surface-sorbate complexes (Morel et al., 1981). A discussion of specific EDL models follows.

For infinite planes the Poisson-Boltzmann Equation has an analytical solution derived by Gouy and Chapman (Morel and Hering, 1993). Surface charge is expressed as a function of surface potential:

$$\sigma_P = (8\ \varepsilon\varepsilon_o\ RT\ I)^2 \sinh(\Psi F/2RT) \qquad (1.9)$$

where σ_P is the net total particle charge, ε the dielectric constant of water, ε_o the permeability of free space, and I the ionic strength. Due to thermal motion, counter-ions do not form a plane of countercharge (Stumm and Morgan, 1996), rather, the distribution

of counter-ions, decays exponentially with distance from the charged surface, and is characterized by the "double layer thickness" or Debye length, $1/\kappa$ (nm). For small potentials the thickness of the double layer is linearly related to the ionic strength (Stumm and Morgan, 1996) by:

$$1/\kappa = 0.30\ I^{-1/2} \qquad (1.10)$$

The double layer thickness expresses the distance from the surface over which counter-ions are accumulated and co-ions repelled by the charged surface (Morel and Hering, 1993). The capacitance (farads m^{-2}) is expressed:

$$C = \sigma_P / \Psi = 2.3\ I^{1/2} \qquad (1.11)$$

Referring to Eq. 1.9 through 1.11, consider the acid-base titration of a metal oxide surface (Figure 1.1) at different ionic strengths. The double layer thickness, surface charge, and surface potential are all related to the ionic strength of the solution. As the ionic strength increases, the electric double layer thickness decreases, and the surface charge (considering H^+ to be the only potential-determining ion) increases due to counterion shielding (e.g. at low pH the electrolyte ions shield the positive charge of the surface resulting in less surface-proton repulsion and a greater protonation of the surface; Dzombak and Morel, 1990). At high ionic strength (1.0 M) the double layer is effectively so compressed that the interfacial region is "collapsed". Because there is no longer a differential between sorbate concentration at the surface and in bulk solution, the interfacial potential becomes so infinitesimally small that its value approaches zero. This effect of high ionic strength applies not only to EDL models of pure surfaces, but also to all electrostatic models of the interfacial region.

Double Layer Models

Models of the EDL at charged surfaces either ignore or variously differentiate between the location of potential-determining ions and counterions (for reviews of the individual models see Westall and Holh, 1980; Robertson and Leckie, 1998; Venema et al., 1996; Hayes et al., 1987; Davis and Kent, 1990). However, all models represent these areas by layers between the solid surface and bulk solution. The double layer model (DLM), also referred to as the diffuse layer model, represents the interfacial region with an inner layer comprising the potential determining ions and a second, outer layer of counterions. The simplest model is the constant capacitance model (CCM). This model assumes that the interfacial region can be described by a single constant capacitance, i.e. is characterized by a linear relationship between surface charge and potential (Eq. 1.11). In this case, all potential-determining ions are positioned in a plane directly parallel to the surface. Ions that are not adsorbed to the surface are not considered. As such, the CCM has limited utility; it is applicable only under given chemical conditions. The triple layer model (TLM) represents the interface as a series of three layers (Westall and Holh, 1980). The two layers closest to the surface are constant capacitance layers, and the outermost layer the so-called diffuse layer. Different researchers assign differently sorbed species to each of these layers, i.e. some assign inner sphere complexes, H^+, and OH^- ions to the innermost layer, where the ions experience the same potential, Ψ_0. Species bound as outer sphere complexes are positioned in the second layer and experience a potential of

Ψ_b and co- and counterions are distributed in the diffuse layer according to the potential Ψ_d (Drever, 1997). Other researchers may restrict the innermost layer to H^+ and OH^- ions only, alternatively placing inner-sphere complexes in the second layer and outer-sphere complexes in the diffuse layer (Drever, 1997). These models are all referred to as double layer models (DLM); although not all of them use a double layer to represent the solid liquid interface.

It must be considered that any model assuming a planar surface may be an oversimplification for the representation of metal oxide surfaces in nature, where any defects or three-dimensional aspects of a solid surface modify the local electric double layer (Parks, 1990; Banfield and Hamers, 1997)

1.5.3. Predictive Models and Metal Sorption

In extending models from the description of proton binding to the description of metal ion sorption, two considerations must be addressed. The first is whether or not the binding of the metal occurs at the same site as the protons, i.e. is the binding competitive? The second consideration is the stoichiometry of the metal binding. Monodentate (1:1) and bidentate (1:2) binding of a divalent metal ions are expressed, respectively, as:

$$\equiv XOH + M^{2+} = \equiv XOM^+ + H^+ \quad (1.12)$$

$$2(\equiv XOH) + M^{2+} = (\equiv XO^-)_2M + 2H^+ \quad (1.13)$$

Both monodentate and bidentate binding are illustrated in Fig 1.1. Strictly, not only monodentate and bidentate binding of metal ions should be considered in the models: multidentate binding of the metal ions metals as well as binding of hydrolyzed species (e.g. $CdOH^+$) should also be considered. If monodentate metal ion binding occurs competitively at proton-binding sites, then the maximum number of binding sites for that metal ion corresponds to the maximum number of proton binding sites (assuming all protons can be displaced; Kinniburgh et al., 1999). The total number of metal ions that can be bound decreases if the binding is bi- or multidentate as multiple sites are needed to bind a single metal ion.

The molar exchange ratio, H^+/M^{z+}, expresses the number of protons released from the sorbent as a function of the number of metal ions bound. Non-stoichiometric exchange ratios have been observed experimentally for oxide surfaces (Dzombak and Morel, 1990; Kinniburgh et al., 1998). Exchange ratios for metal ions with metal oxide surfaces vary somewhere between 1.6-2.0 at all pH values and ionic strengths (Benjamin and Leckie, 1981; Dzombak and Morel, 1990; Robertson and Leckie, 1998). Alkaline earth metals give lower exchange ratios; an exchange ratio of ~0.9 was reported by Kinniburgh et al. (1983).

Limitations and Summary

All geochemical models must account for both the inherent physico-chemical complexity of natural sorbents and the limited information content of measurable experimental data (Buffle, 1988). A fundamental limitation of the modelling techniques discussed here is that they are based on potentiometric titrations. Smith et al. (1999) demonstrated that the greatest uncertainty in parameter estimations from acid-base titrations occurred outside of the pH range 4-10 for a sample of natural organic matter.

Although there may be binding sites outside of this range, they are not accessible with glass electrodes. The authors state that it would be necessary to increase the sorbent concentration above levels found in natural waters to reduce these uncertainties. Because of such pH range limitations, potentially very high proton affinity (high pK_a) and very low proton affinity (low pK_a values) are not accessible (Martínez et al. 1998, Kinniburgh et al. 1999). The importance of the model to accurately describe the acid-base behaviour and metal sorption to the solid is clear. Prediction of the fate of metals in natural and complex systems is only as good as the model-derived binding constants, which are only as good as the models developed, which are in turn only as good as the experimental data (Martínez et al, 1998). Further, models that assume equilibrium conditions are certainly simplified representations of natural systems and, as such, are operationally defined.

1.6. Microbial Ecology: Geochemical Implications

The previous sections of this chapter have focused on the interactions between surfaces of important solid phases and metal ions from solution. The focus now turns to bacteria and their role, not as sorbent phases, but as living organisms that impact metal behaviour through their metabolic activity. Metabolic processes include aerobic respiration, nitrification and denitrification, methane oxidation, sulfur oxidation and sulphate reduction, Mn and Fe reduction and oxidation, and methanogenesis (Figure 1.2). Microbes effectively utilize environmental redox pairs to derive energy and or nutrients for their own metabolic needs and for this reason accumulate at redox interfaces. Extracellular enzymes produced by bacteria modify nutrient sources, and the nutrients are brought into the cytoplasm against a concentration gradient by specific transport systems (Nealson and Stahl, 1997). Many bacteria are able to adapt to new environmental conditions through the synthesis of those of enzymes and other cellular components needed for those particular conditions (Holt and Leadbetter, 1992). Because bacteria are able to use electron acceptors other than molecular oxygen for respiration, including carbonate, ferric iron, nitrate, sulphate, and various organic molecules (Holt and Leadbetter, 1992; Nealson and Stahl, 1997) they impact all elemental cycles important in metal behaviour.

Historically, the quantitative understanding of metal behaviour has developed from a strict geochemical perspective. However, the overwhelming importance of bacteria as a key player in determining both metal behaviour and impact, is becoming increasingly evident. Any bacterially promoted changes in either mineral formation or dissolution will likely impact subsequent metal reactions through associated changes in the relative amount of solid surface and associated functional groups available for metal complexation. Bacteria influence these processes through a variety of mechanisms all related to bacterial metabolic processes. Further, bacteria influence these processes at both microscopic (e.g. weathering of mineral surfaces) and macroscopic scales (e.g. geochemistry of the system; Bennett et al., 2000).

1.6.1. Biomineralization: microbially promoted mineral formation

Biomineralization is a process that can occur actively, i.e. "biologically controlled", or passively, i.e. "biologically induced" (Lowenstam, 1981; Bazylinski and Moskowitz, 1997). Bacterial cells that actively control mineralization regulate the precipitation of physiologically essential minerals. Minerals that are not thermodynamically favorable can thus be formed by introducing specific ions either intracellularly or extracellularly in a developed organic framework (e.g. magnetite formation inside magnetosomes; Mann, 1983). Biologically induced or passive biomineralization is the dominant mineralization mechanism among bacteria and results from the interaction between the organism and the external environment. Bacteria promote mineral precipitation principally through their metabolic effects on system geochemistry with respect to saturation state of potential minerals and/or the kinetics of precipitation reactions. Bacterial promotion of mineral formation, often in association with the bacteria cell, is commonly referred to as authigenic mineral or biomineral precipitation. Biomineral formation is widely described for a broad array of mineral types (e.g. carbonates, sulphides, phosphate minerals, Fe and Mn oxides, uraninites; silicates) and over significant geologic timescales, from almost every environment on earth (Sunda and Huntsman, 1987; Beveridge, 1989; Thompson et al., 1990; Ghiorse and Ehrlich, 1992; Southam and Beveridge, 1992; McLean et al., 1996; Mojzsis et al., 1996; Fortin et al., 1997; Konhauser, 1998; Beard and Johnson 1999; Ingebritsen et al., 2000). Biomineralization is currently being evaluated as a potential process that can be harnessed for bioremediation strategies involving solid phase capture of metals and/or radionuclides from contaminated water systems (e.g. Warren et al., 2000) or reduction of metal contaminants (Lovley and Anderson, 2000). Thus biological influence for metal behaviour extends beyond just surface scavenging capacity but also to a direct influence on the types, concentrations and locations of potentially reactive mineral phases.

This bacterial promotion of mineral formation occurs through a variety of geochemical pathways, all ultimately reflecting the inherent thermodynamic constraints on mineral formation. Bacteria cannot change these constraints, they can however, speed up the rate at which those reactions occur, or promote changes in geochemical conditions to those favorable for precipitation to occur, often through influences on redox conditions or pH. For example, microbially mediated metal reduction can lead to precipitation of minerals. Lovley and Phillips (1992) demonstrate that bacterial enzymatic reduction of U(VI) to U(IV) led to rapid epicellular precipitation of uraninite on the bacterial surface. Bacterial oxidation of Mn(II) to Mn(IV) and subsequent precipitation of Mn oxyhydroxides has also been observed (Nealson et al., 1989; Nelson et al., 1999a). Bacteria that deposit Fe (III) and Mn (III,IV) oxyhydroxides in structures outside their cells are ubiquitous and are both gram-positive and gram-negative (Mann, 1990). TEM analyses commonly indicate bacterial cells partially to completely enclosed within iron-rich epicellular matrices or with intracellular precipitates (Konhauser, 1998). Iron precipitates formed on the surface of three viable non metabolically active strains of bacteria (gram negative *Pseudomonas aeruginosa* and gram positive *Bacillus subtilis* and *Bacillus licheniformis*) that varied in their surface characteristics were all identified as

poorly ordered ferrihydrite by selected area electron diffraction (Warren and Ferris, 1998). Ferrihydrite has also been shown to be deposited on the organic remains of dead cells, suggesting that iron mineralization can occur independently of cell morphology, classification, or physiological state (Konhauser, 1998).

Metals bound to the bacterial surface can also be subsequently precipitated through reactions with solution ligands and metabolic waste products such as H_2S, HCO_3^-, CO_3^{2-}, SO_4^{2-}, and OH^- (McLean et al., 1996; Fortin et al., 1997). The precipitates formed generally reflect the chemical composition of the environment in which they are growing, and both metal sorption and subsequent mineralization will reflect solution composition of the environment (Konhauser et al., 1993; Konhauser 1998; Douglas and Beveridge, 1998). Identical minerals are found associated with a variety of physiologically diverse bacteria in the same environment (Lowenstam and Weiner, 1989; Konhauser et al., 1993). This result underscores the importance of bacterial surfaces as nucleation templates, but that system geochemistry controls the precipitates that form (Konhauser et al., 1993; Warren and Ferris, 1998). However, it is also true that system geochemistry in the microzone adjacent to bacterial cells can differ among species occurring in the same environment; leading to differential minerals being formed in the cell's vicinity. Actively metabolizing bacteria pump out protons and metabolic waste products, which can influence the pH and chemical composition of their immediate surroundings. A microenvironment directly surrounding the cell can thus be produced that may be oversaturated in some respect and may induce precipitation of specific mineral types from solution (Ferris, 1997, Fortin et al., 1997, Douglas and Beveridge, 1998).

1.6.2. Characteristics of authigenic minerals

Bacterially induced precipitates can form on the inside, outside or even some distance away from the cells (Ferris, 1997). Metal aggregates deposited within the cell wall itself are physically restricted in size by intermolecular spaces. Only fine-grained precipitates are formed, and these are not easily redissolved or replaced by protons or other metals (Beveridge et al., 1995; Konhauser 1998). In contrast, epicellular grains reaching several μm in diameter can form on the surface of bacterial cells and EPS (Beveridge 1989; Warren and Ferris, 1998). Inorganic grains that are commonly found in a variety of freshwater environments have characteristics including size, crystallinity, chemical composition, and spatial orientation that suggest that their origin was authigenic (Konhauser and Urrutia, 1999), and that bacterial mineralization is a widespread and important phenomenon. The grains tend to be amorphous, poorly structured, and small in size (< 1 μm, majority <100 nm) and thus possess high potential geochemical reactivity (Nelson et al., 1999a).

The amorphous nature of precipitates at bacterial surfaces is explained by the "Otswald Step Rule" which states that the least stable solid phase with the highest solubility will be formed first in a consecutive precipitation reaction. The nucleation of a more soluble phase is kinetically favored as it has a lower solid-solution interfacial tension compared to less soluble or more stable and often more crystalline phases

(Stumm, 1992). The initial nuclei of biological mineral precipitates are commonly amorphous or contain highly metastable ratios of both major cations and trace constituents (Mann, 1990; Stumm, 1992).

1.6.3. Bacterially-promoted mineral dissolution

Mineral dissolution can also occur as a result of microbial activity and can have important implications for trace metal cycling, as metals can be associated with the mineral phases. A number of studies have examined the reductive dissolution of minerals associated with the decomposition of organic matter by bacteria (e.g. Arnold et al. 1988; Stucki et al. 1987). Bacteria use minerals as a terminal electron acceptor and couple the oxidation of organic matter to the reduction of metal ions in the mineral structure. Reduction of the metal ion in the structure results in subsequent dissolution of the mineral. Bacteria can couple a wide array of oxidation redox half reactions to the reduction of metal ions (e.g. a wide variety of organic substrates: formate, lactate, pyruvate, butyrate, toluene, phenol; as well as H_2, and reduced S compounds; Lovley 1995; Stumm and Morgan, 1996; Morel and Hering, 1993).

1.7. Micro- and Molecular Level Approaches

Having considered the complex bio-geochemical controls on metal behaviour, one of the major challenges for environmental geochemists is accurate quantification of these processes in natural environments. The inherent complexity of natural systems and the specificity of sorbent-sorbate reactions underscore the absolute requirement for a mechanistic understanding of processes occurring at interfaces. In particular, the molecular geochemistry occurring at surfaces can neither be predicted based on macroscopic information nor understood without some identification of the controls on the processes that occur at this scale. Recently developed and increasingly applied analytical (microelectrodes), microscopic (confocal laser scanning microscopy, environmental scanning electron microscopy, and atomic force microscopy; Nealson and Stahl, 1997; Barns and Nierzwicki, 1997; Eggleston et al., 1998) and spectroscopic techniques allow for in situ quantification, mechanistic understanding and visualization of microbial-mineral-trace metal interactions at scales that are relevant to these processes. These novel in situ and nondestructive techniques are providing real insight into processes relevant at the bacterial scale and interfacial processes. Discussed further here are microelectrodes and synchrotron-based X-ray absorption spectroscopy, two techniques employed in this Ph.D. research.

Field researchers are always looking for ways to examine the microbial impact on natural environments in situ, i.e. with minimal disturbance to the system. One such technique is microelectrodes. Microsensors or microelectrodes can be used to measure in situ profiles of specific chemical species within biofilms or sediments at high spatial resolution. Revsbech (1989) developed the first microsensor for profiling of dissolved oxygen in sediments and biofilms. Microsensors now exist that measure ΣH_2S, pH, O_2, N_2O, NO_2^-, NO_3^-, NH_4^+, CH_4^+, CO_2, glucose, light, flow and diffusion (individual developers referenced in Lens et al., 1995; Santegoeds et al., 1998; de Beer and Schramm, 1999). The high spatial resolution (< 50 μm) of the microsensors is due to the

small size of the tip diameter, 1-20 μm (Santegoeds et al., 1998). The small size and analyte consumption of the microsensors allows the sample to be probed without disturbing either the structural/ecological distribution within the biofilm or the chemical gradients (Santegoeds et al., 1998). These new microsensors permit accurate characterization of geochemical conditions occurring within localized, geochemically intense zones such as redox clines in sediments and biofilms. The high spatial resolution of the geochemical information afforded by these microsensors will aid to quantitatively understand the processes involved in metal dynamics.

X-ray absorption spectroscopy (XAS) allows the in situ examination of hydrated samples and has been used extensively to look at a variety of mineral surfaces (e.g. Brown et al., 1989; Chisholm-Brause et al., 1990; Peterson et al., 1997; Parkman et al., 1998). XAS spectroscopies can provide information on the molecular processes occurring at surfaces and give quantitative insight into speciation and the types of bonds being formed. Two commonly used and complementary XAS spectroscopic techniques are Extended X-ray Absorption Fine Structure (XAFS-EXAFS) and X-ray Absorption Near-Edge Structure (XANES). Analysis of EXAFS data yields information about the coordination environments of the element being analyzed, i.e. the number and distance of nearest atomic neighbors in a structure. XANES is most often used to evaluate the oxidation state of the element being examined. Combined, these techniques represent a powerful means to assess the chemical speciation and crystal chemistries of sorbing ions. These approaches are being used with success to identify the heterogeneous nature of surfaces (e.g., Stipp et al., 1992), the types of reactions occurring between various metal and mineral or organic surfaces (e.g. Reeder et al., 1994; Sturchio et al., 1997; Xia et al., 1997a, 1997b), as well as mechanisms of mineral reductive dissolution (e.g. Eggleston et al., 1996; Nesbitt et al., 1998). EXAFS and XANES techniques are especially relevant to metal studies as they are element specific and can provide information on metal speciation, e.g. speciation of organically bound sulfur in marine sediments (Vairavamurthy et al., 1994), Pb-humic complexes (Manceau et al., 1996), and metal partitioning between solution and solid phases (O'Day et al., 1998; Carroll et al., 1998). These molecular-level techniques provide important mechanistic insight into the specificity of metal-sorbent reactions. As such, they provide information essential for accurate models of metal dynamics within natural aquatic environments.

1.8. Acid Rock Drainage Environments

Acid Rock Drainage (ARD) environments represent a uniquely suited environment for the analysis microbe-mineral-trace metal interactions. ARD environments are created by the weathering and oxidation of pyritic (sulphidic) materials exposed during the mining of base metals and coal. It is now accepted that the oxidation of sulphide materials is an abiotic process that is significantly catalyzed by iron- and sulfur-oxidizing bacteria that are either attached or in close vicinity to the sulphide minerals (Nordstrom and Southam, 1997). Important equations in this process are (Hrncir and McKnight, 1998; Seal and Hammarstrom, 2003):

$$2FeS_{2(s)} + 7O_2 + 2H_2O \rightarrow 2Fe^{2+} + 4SO_4^{2-} + 4H^+ \quad (1.14a)$$

$$Fe_{1-x}S + (2-x/2)O_2 + xH_2O \rightarrow (1-x)\,Fe^{2+} + SO_4^{2-} + 2x\,H^+ \quad (1.14b)$$

$$4\,Fe^{2+} + O_2 + 4H^+ \rightarrow 4Fe^{3+} + 2H_2O \quad (1.15)$$

$$Fe^{3+} + 3H_2O \rightarrow Fe(OH)_{3(s)} + 3H^+ \quad (1.16)$$

$$FeS_2 + 14Fe^{3+} + 8H_2O \rightarrow 15Fe^{2+} + 2SO_4^{2-} + 16H^+ \quad (1.17)$$

Eq. 1.17 gives the overall reaction stoichiometry. Both Fe^{3+} and dissolved oxygen can act as oxidizing agents in the oxidation of sulphide minerals (Eqs. 1.15 and 1.17) and the relative importance of Fe^{3+} as the oxidizing agent increases at acidic pH values (Seal and Hammarstrom, 2003). The oxidation of sulphide in pyrite and/or pyrrhotite by dissolved oxygen results in the release of sulphate, ferrous iron and acidity into solution (Eq. 1.14a and 1.14b, respectively). Oxygen acts as the electron acceptor in the oxidation of Fe^{2+} to Fe^{3+}, however, research has shown that molecular oxygen is not needed at the surface of the pyrite particle; pyrite can be oxidized in the absence of oxygen (Nordstrom and Southam, 1997). Hydrolysis and precipitation of Fe^{3+} (Eq. 1.16) produces acidity and proceeds more rapidly than oxidation of Fe^{2+} (Singer and Stumm, 1970). Thus, the rate limiting step of the overall process is thought to be the oxidation of Fe^{2+} to Fe^{3+}, and it is the rate of this reaction that is increased by approximately 5 orders of magnitude compared to the abiotic rate in the presence of Fe-oxidizing bacteria (*Acidothiobacillus ferrooxidans*, Singer and Stumm, 1970). The acidity produced by this overall process has received much attention; however, of more concern to the toxicity of higher organisms is the high concentrations of trace metals released to solution with the accelerated weathering of sulphide minerals in systems with acidic pH (Price, 2003). Dissolved concentrations of metals (Fe, Al, Mn, Cd, Ni, Cu and Zn) associated with ARD-impacted freshwaters are high, and range from 0.1-300 mg/L (e.g. Lawrence et al., 1998b; Tonkin et al., 2002).

Extensive biofilm occurrence is commonly noted in highly metal impacted, acid rock drainage (ARD) systems. Pyritic waste materials that are ground, discharged from the mill and stored on land surfaces represent optimum substrates for microbial colonization and subsequent oxidation (Southam and Beveridge, 1992; Johnson et al., 2000). Early research on microbial influence in ARD environments focussed on the iron-oxidizing acidophilic bacterium *Acidothiobacillus ferrooxidans* (Colmer and Hinkle, 1947; Leathen et al., 1953; Singer and Stumm, 1970). However, the ecology of sulphidic mine tailings are now known to be complex and unique ecosystems that include autotrophic bacteria, heterotrophic bacteria, green algae, fungi, yeasts, mycoplasmas and amoebae (Davis, 1997; Nordstrom and Southam, 1997). In addition, bacterial populations within tailings are known to vary with depth and changing physicochemical conditions, the age of the tailings, and the method in which the tailings were deposited (Davis, 1997). Microbial diversity in AMD environments is presently under scrutiny (e.g. Edwards et al., 1999; Leveille et al., 2001) specifically because the interactions between microbes and sulphide surfaces within this environment are not well understood.

As stated by Ledin and Pedersen (1996 p. 101) "a full understanding of mine waste disposal environments cannot be achieved until the microbial processes are included in models, theories and interpretation of results". Because 650 million tonnes of

tailings (sulphide-bearing mine wastes) are produced daily in Canada alone (Government of Canada, 1991), the creation of ARD environments and their remediation is of environmental significance.

1.9. Research Objectives

The objectives of this thesis were to: (1) quantitatively evaluate trace metal sequestration within naturally occurring Acid-Rock Drainage (ARD) biofilms at highly resolved spatial and temporal scales; and (2) characterize the mechanisms involved in Ni uptake by hydrous manganese oxyhydroxides (HMO) at the molecular scale, using synchrotron-based X-ray absorption spectroscopy.

As outlined above (section 1.8.), ARD-impacted environments represent a uniquely suited study site for the examination of microbe-mineral-trace metal interactions in the natural environment, as both the rate of sulphide mineral oxidation and the cycling of metals within these environments are directly influenced by the presence of a diverse community of microorganisms. The mechanisms by which these microbial-mineral interactions ultimately impact and control trace metal cycling are poorly understood andhave yet to be quantitatively determined. Biofilms are highly stratified, complex, microbial communities, exhibiting strong internal dynamic geochemical gradients. Biological reactions (e.g. photosynthesis) occurring within the biofilm can dynamically affect bulk system geochemical status, as well as solid phase metal sequestration processes at the microscale. Elucidation of the microbial – geochemical linkages influencing the nature and extent of metal partitioning within biofilms requires the synergistic use of analytical techniques spanning molecular level to bulk system characterization. Such characterization is essential if we are to ever move beyond our current limitation of site-specific descriptions of metal partitioning within natural systems, to a mechanistic model of controls for metal dynamics within ARD environments, and freshwater systems as a whole.

In order to address the outlined objectives, this thesis is presented as a collection of five chapters. Modified versions of each of the chapters are either published, or to be submitted to refereed journals (see Preface). Chapter 1 presents a review of the current literature on trace metal behaviour in freshwater environments and highlights the need for a multidisciplinary approach in understanding the processes involved in metal sequestration in freshwaters.

Chapters 2-4 present the major research findings of this thesis. Chapter 2 outlines the design and creation of an extraction scheme, using microwave digestion, for the specific analysis of the samples involved in this study. The objective was to develop a microwave digestion sequential extraction protocol that was rapid and evaluated the important sorbent phases (i.e. amorphous oxyhydroxides vs. more crystalline oxides vs. organic matter) in natural biofilms, while minimizing the introduction of artifacts in the results. Because of the dominant and complex iron mineralogy associated with ARD environments, specific objectives were to:

(1) Characterize the bulk mineralogical components of ARD biofilms and evaluate the effectiveness of published extraction techniques for the dissolution of synthetic solids relevant to the samples.
(2) Characterize the important phases for metal retention in biofilm samples and evaluate any artifacts in metal partitioning due to methodologically induced changes in solids.

Chapter 3 presents the field study results investigating metal dynamics within ARD associated biofilms. The specific objectives of this field-based research were to:
(1) Quantitatively characterize the extent of metal accumulation and the key sorbent phases within the biofilms over seasonal (June-Sept) and diel scales.
(2) Characterize the microbial-geochemical linkages involved in the key processes controlling metal sequestration within these ARD biofilms.

Chapter 4 examines the mechanisms underlying Ni uptake by HMO using EXAFS. The objective of this laboratory-based research was to identify the mechanisms underlying the observed literature discrepancies between model-predicted and experimentally observed metal (Ni) uptake to HMO.

The significant research findings of this thesis, their broader implications for both ARD remediation and mechanistic understanding of the processes involved in reactive metal transport, and future directions are presented in Chapter 5.

CHAPTER 2: ACID ROCK DRAINAGE: STUDY SITE, SAMPLING PROTOCOL, AND METHOD DEVELOPMENT

PART I: STUDY SITE AND SAMPLING PROTOCOL

2.1. Study Site

The Falconbridge Strathcona Nickel Mine and Mill are situated in Onaping, Ontario, Canada. This mine is part of the larger mining operations of the Sudbury Structure. The major ore bearing sulphides are pyrrhotite ($Fe_{(1-x)}S$), pentlandite, ($(Fe,Ni)_9S_8$), chalcopyrite ($(CuFe)S_2$) and pyrite (FeS_2; Falconbridge Ltd., 1998).

The study site of this research is part of the larger Falconbridge Strathcona Mine and Mill (Figure 2.1a) and represents the most easterly section of the Strathcona Tailings area (Lat. 46°39'18.1", Long. 81°18'58.3"; Figure 2.1b). Tailings at the study site are older and more oxidized. Active tailings slurry disposal did occur at a more elevated site to the north-west of the study site over the years spanned by this research, 2001-2002. Subsurface flow from the active tailings deposits emerges at the study site as several seepage streams (Figure 2.2). The seepage streams are shallow, acidic, generally undersaturated with respect to dissolved oxygen, and characterized by high Fe loads (Table 2.1). Discharge from the streams ultimately flows into Moose Lake. Moose Lake is both an oxidation pond and tailings deposition area (Figure 2.1).

Tailings that are actively leaching are generally characterized by three vertical zones, of distinct geochemical and mineralogical makeup (Southam et al., 1995). The first is the upper zone closest to the tailings/air interface, in which oxygenation of the tailings material has progressed and the sulphide content is depleted. This zone is visually identified by the presence of secondary iron oxyhydroxides and sulphates, including schwertmannite, goethite, lepidocrocite, and ferrihydrite (Bigham et al., 1992) which are yellow/orange and ochre in colour. Beneath this first zone is the location of acid generation. In this second zone, sulphide oxidation and precipitation of iron minerals are ongoing processes. The third, unoxidized, zone is characterized by the deep black/brown colour of sulphide minerals and begins below the depth of oxygen penetration. The depth where the third zone begins also often corresponds to the depth of saturated pore spaces in the tailings deposits (Southam et al., 1995). The tailings at this study site correspond to the upper zone; secondary iron oxyhydroxides and sulphates were evident visually (Figure 2.3).

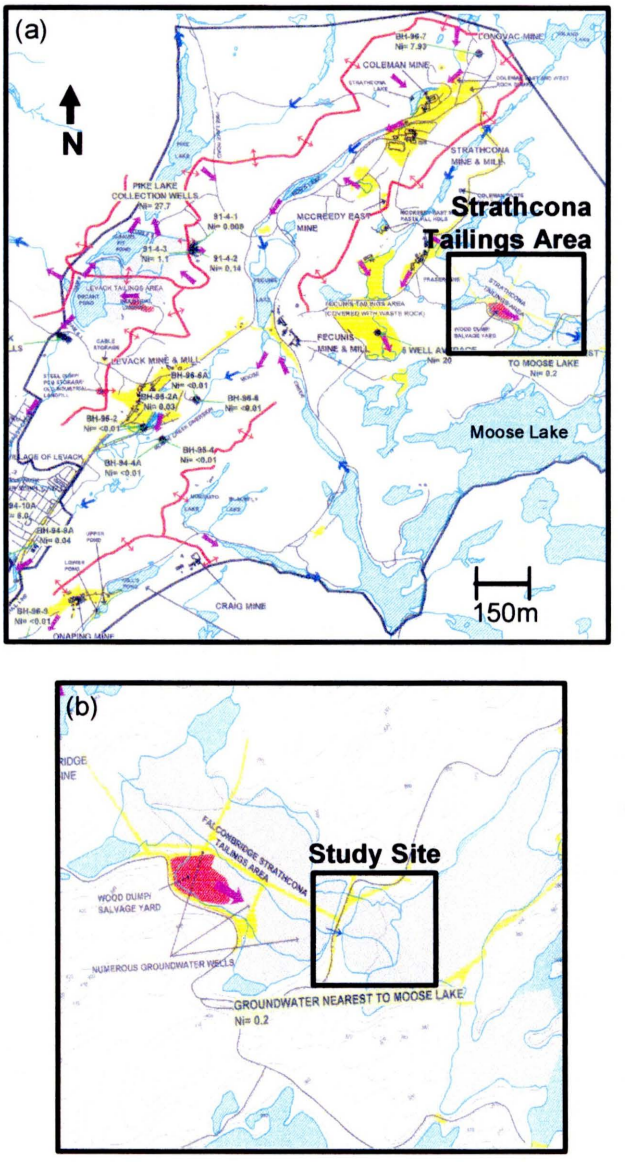

Figure 2.1. Topographic maps of the Falconbridge Strathcona Mine and Mill network in Onaping, Ontario, Canada (a) and the Strathcona Tailings Area (b; zoomed from a). The study site represents the most easterly section of the Strathcona Tailings Area (b). Tailings in this area are older and more oxidized; active slurry disposal occurred to the north-west of the study over the years spanned by this research (2001-2002). Topographic maps from Falconbridge et al. (1998).

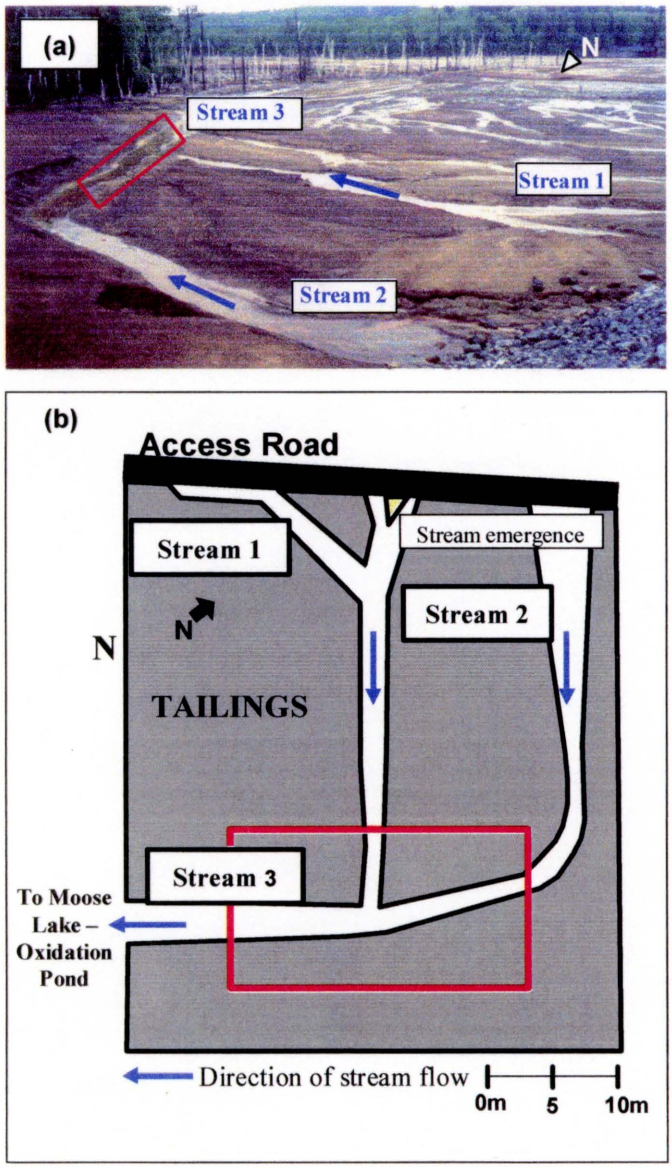

Figure 2.2. The Study Site. Photograph (a) and site schematic (b) of the study site. As shown in both (a) and (b) shallow emergent streams reflecting both surface run-off and groundwater intrusions run over the tailings; the direction of surface flow is indicated with arrows. Ultimately the discharge runs into Moose Lake (oxidation pond and tailings deposition area). The boxes in (a) and (b) indicate the streambed area where biofilm samples were collected over the sampling seasons June-Sept, 2001 and June-August 2002.

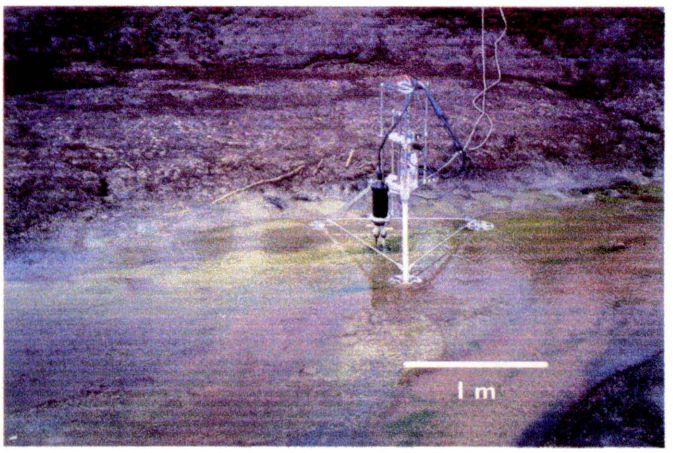

Figure 2.3. Photograph of the convergence of Streams 1 and 2 (Figure 2.2) and the microelectrode geochemical profiling system (MiniProfiler MP-4; Unisense Corp., Denmark) with pH, O_2, and reference electrodes attached. Zones of photosynthetically activity are indicated by the bright green colour. Localized differences in the iron mineralogy (secondary iron oxyhydroxides and sulphates) are evident in this image by the yellow/orange and ochre coloured streambed, and indicates small-scale variability in both microbially-induced oxidation and pH associated with biofilms within the site.

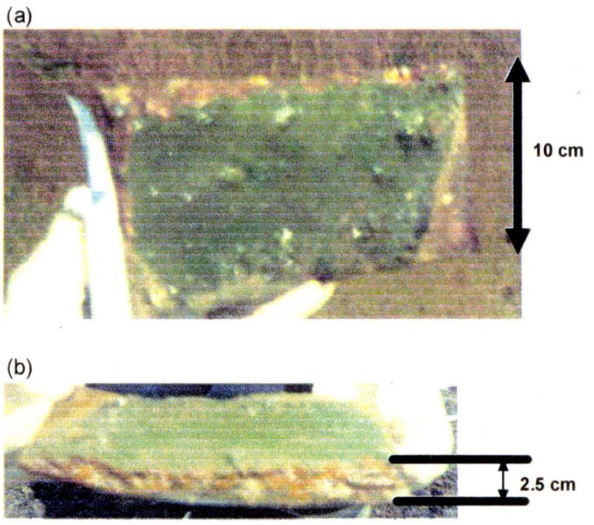

Figure 2.4. Plan view (a) and profile (b) photographs of a biofilm sample supported on a Teflon strip immediately after removal from the streambed. The bright green photosynthetic mat sits atop unconsolidated secondary iron oxyhydroxides and sulphates and represents the biofilm-water interface.

Table 2.1. Stream physico-chemical parameters and dissolved iron loading[a]

Depth (cm)	pH[b]	DO (%sat)[b]	$[Fe_{total}]$ (mM)[c]	$[Fe^{2+}]$ /$[Fe^{3+}]$[d]
5 ± 3	3.09 ± 0.32	70 ± 20	1.7 ±1.0	0.39 ± 0.35

[a] Mean values ± standard deviation for all sampling times 2001-2001 from eight sampling sites along Streams 1, 2 and 3. All Fe concentrations are dissolved (0.2 μm filtered) values.
[b] values measured in situ using a DataSonde-Surveyor 4A, Hydrolab Corporation, TX
[c] $[Fe_{total}]$: HACH Ferro Ver Method®, see section 2.5.1.
[d] [Fe2+]: 1,10 Phenanthroline Method®, HACH DR/2010, Hach Company, U.S.A.; $[Fe]^{3+} = [Fe_{total}]-[Fe^{2+}]$

2.2. Sampling Protocol

The site was viewed and preliminary water samples were taken to evaluate the pH and dissolved metals associated with the streams on July 18, 2000. A preliminary biofilm sample was collected on May 31, 2001 for analysis of the bulk mineralogy by X-ray Diffractometry (XRD). Intensive sampling began at the site in June 2001. The sampling protocol was designed to investigate diel and seasonal trends in biofilm and water column metal loads and geochemistries. In situ measurements and sample collection occurred over two open-water seasons, June-Sept 2001 and June-August 2002, over seven two-to-four day sampling periods (Table 2.2). Over each sampling period from June-Sept 2001, one or two full sets of samples (described subsequently) were collected between 15:00-21:00 of the first sampling day. The following morning, one or two full sets of samples were collected between 7:00-11:00. A full set of samples included (1) in situ profiling of geochemical conditions within the biofilm using a remotely-controlled microelectrode system (Figure 2.3), (2) characterization of overlying water column physico-chemical parameters concomitant with profiling, and (3) collection of biofilm samples for solid-phase metal analysis and water column samples for dissolved-phase metal analysis, immediately following profiling. Water column parameters measured included temperature, pH, dissolved oxygen concentrations (mg/L and % saturation), and specific conductivity (DataSonde-Surveyor 4A, Hydrolab Corporation, TX). Sampling over the period June-August 2002 was more intensive, and included between one and five complete set of samples over a twenty-four hour sampling day (Table 2.2). However, in situ profiles were not collected at each sampling time/period due to breakage of the microelectrodes (indicated in Table 2.2).

Photosynthetic mats were evident throughout the summer seasons, providing, at times, extensive coverage of the tailings surface underlying the seepage streams (Figure 2.3). Biofilm samples were collected from an area approximately 30 m downstream of the emergence of streams 1 and 2 onto the tailings, where these two streams merged to form stream 3 (Figure 2.2). The thickness of the biofilms was typically 2-3 mm, depending on time of sampling, and hereafter discussion of the biofilm refers to the top 2 mm of the sample collected. To preserve the vertical structure of the biofilm during sample collection, biofilm samples were collected on pre-etched and acid-washed Teflon sheets (double-sided ammonia etching, Enflo Canada, Ltd), measuring approximately 10x20 cm. The Teflon sheets were inserted into the streambeds horizontally, such that they were embedded below the oxic/anoxic interface in the underlying sulphidic mud, to a depth of approximately 3 cm. To remove the biofilm samples, a sterile razor blade was used to cut around the perimeter of the Teflon sheet (Figure 2.4.). The sheet and sample were then lifted carefully from the stream, and placed in acid-washed polypropylene containers on ice. The samples were stored at 4°C in the laboratory prior to analysis.

Table 2.2. Sampling Times and Dates for Sampling Seasons June-Sept 2001 and June-August 2002. Microprofiles of O_2 and pH in the biofilms were collected concurrent with sample collection on the dates indicated (Y).

Year	Date	Time	In situ Profile
2001	21-Jun	16:30	Y
	21-Jun	20:50	Y
	22-Jun	11:00	Y
	4-Jul	16:30	Y
	5-Jul	7:50	Y
	8-Aug	20:00	Y
	9-Aug	7:00	Y
	5-Sep	15:30	Y
	6-Sep	9:00	Y
	6-Sep	11:00	Y
2002	20-Jun	6:20	Y
	20-Jun	11:00	Y
	20-Jun	15:00	
	20-Jun	20:00	
	21-Jun	7:30	
	15-Jul	20:40	
	16-Jul	6:15	
	16-Jul	19:30	
	17-Jul	6:40	
	17-Jul	15:00	
	17-Jul	18:00	
	17-Jul	21:30	
	17-Jul	23:50	
	18-Jul	6:30	Y
	18-Jul	9:30	Y
	21-Aug	7:00	
	21-Aug	16:00	
	21-Aug	18:00	Y
	21-Aug	20:00	Y
	22-Aug	7:00	

PART II: DEVELOPMENT OF A MICROWAVE DIGESTION SEQUENTIAL EXTRACTION SCHEME FOR RAPID DETERMINATION OF SOLID-PHASE METAL ASSOCIATIONS IN ARD BIOFILMS

2.3. Introduction

Biofilms are highly hydrated bacterial communities of high cell density that have complex and biologically regulated architecture (Davies et al., 1998). Within the physical structure of the biofilm, microbial inhabitants are stratified with depth between the biofilm-solution and biofilm-substratum interfaces according to metabolic function. Thus, biofilms are likely to be characterized by steep, continuously shifting physico-chemical gradients (Lawrence et al., 1995). Biofilms, as geochemical entities, can be considered as intense biological reactors that create geochemical microenvironments that can differ substantially from both the overlying water column as well as the underlying substratum.

Biofilms are comprised of three major components: (1) organisms, (2) extracellular polysaccharides (EPS), and (3) authigenic minerals. A body of evidence, primarily laboratory based, now exists that has established both bacterial cells and associated EPS and authigenic minerals as highly reactive metal sorbents (e.g. Doyle et al., 1980; Beveridge, 1984; Geesey, G.G. et al., 1988; Lawerence et al., 1998). Studies on both natural and laboratory-grown biofilms indicate that within the biofilm architecture metal cations demonstrate distinct spatial patterns of sequestration that are metal-specific and reflect relative affinities for the organic and minerals components (Lünsdorf et al., 1997; Wuertz et al., 2000). A recent study found that 50-100% of the metals scavenged by a subterranean biofilm were bound specifically by biomineralized iron oxyhydroxides (Ferris et al., 1999), indicating that despite the high organic content of the biofilms metals are still selectively scavenged by associated biominerals. Thus, characterization of metal association within these live organic matrices is of utmost importance.

As with all natural samples (sediments, tills, soils), where heterogeneous multicomponent solids are the norm, quantification of whole biofilm metal concentrations is not sufficient to predict metal transport and fate (Campbell et al., 1988). Rather, it is the partitioning and the nature of the solid association (e.g. sorbed vs. precipitated) of metals to the different reactive solids within the biofilm that must be quantified. The fraction (organic versus inorganic, crystalline versus amorphous) with which the metal is associated is a defining characteristic for predicting mobility within the overall system. Further, metal sequestration in biofilms is likely a dynamic process reflecting the "live" nature of biofilms, i.e. geochemical conditions are dictated by metabolic processes, which are dynamic and shifting. Shifts in pH and pE may affect the

nature of metal sorption to the biofilm as well as mineral formation and dissolution, particularly of amorphous minerals that are sensitive to O_2 status. Thus, metals sorbed to these minerals may be more dynamically bound resulting in differential release of metals from the various biofilm solid fractions.

Quantifying metals sequestered in association with the different solid components in heterogeneous mixed-solid samples is a non-trivial task. Sequential extractions were developed from the conceptual framework that extraction of metals from the individual components in a mixed sediment sample can be achieved by the sequential application of reagents/conditions designed to attack each sediment fraction (Tessier et al., 1979). Published sequential extraction protocols are most often based on the scheme outlined by Tessier and colleagues (Tessier et al., 1979). Each extraction step in that scheme was designed to reflect a specific fraction of sediment samples known to sequester metals. These five fractions are (1) exchangeable (electrostatically associated with the sediment surface), (2) bound to carbonates, (3) bound to Fe-Mn oxyhydroxides, (4) bound to organic matter, and (5) residual, or bound within crystalline matrices. Metals associated with fractions 1-4 are interpreted as having biological or hydrogeneous origins and are typically more reactive. Metals released in the residual fraction have lithogeneous origins and are often not reactive under environmental conditions (Hall and Pelchat, 1999).

Many modifications have been made to the extraction scheme of Tessier et al. (1979) to reflect the nature of the samples being investigated in other studies. The exchangeable and carbonate fractions are commonly combined for analysis of marine sediments (Campbell et al., 1988). Other modifications have focused on differentiating between amorphous and crystalline oxyhydroxide fractions due to the recognition that a number of factors affect the extent of sorption by any one mineral sorbent type, including the degree of crystallinity, number of defect sites, impurities and/or coprecipitates, and particle size (Webster et al., 1998; Brown et al., 1999). However, while sequential extractions have been shown to have great utility for evaluating metal-sediment associations (e.g. Campbell et al., 1988; Bendell and Young; 1992; Hall and Pelchat, 1999; Filgueiras et al., 2002 and references therein) and the number of researchers using sequential extraction schemes continues to increase, there have been a number of criticisms of the technique. The criticisms have been based largely on the operationally defined nature of the schemes and their selectivity (e.g. Nirel and Morel, 1990; McCarty et al., 1998). Artefacts in the use of sequential extraction schemes have been noted in analysis of metals specifically distributed between Fe and Mn oxyhydroxides by Tiping et al. (1985). These authors evaluated a number of published reagents for extraction of Fe and Mn oxyhydroxides and found that the concentrations of trace metals extracted were not consistent with the concentrations of Fe or Mn extracted amongst reagents. Because sequential extraction schemes are a bulk technique, interpretation of the results are strengthened by evaluation of the distribution of metals between solid fractions using other analytical techniques and/or having a good understanding of the bulk solid components of the sample prior to the application of sequential extraction schemes (Hall et al., 1996; McCarty et al., 1998; Dold, 2003).

The overall objective of this study was to develop a sequential extraction scheme for the rapid and quantitative analysis of distinct (i.e. amorphous oxyhydroxides vs. more crystalline oxides vs. organic matter) metal associations within natural ARD biofilm samples. A sequential extraction protocol for analysis of solid phase metal partitioning within ARD biofilm must meet three important criteria. The first criterion is rapid analysis of the samples because of their "live" nature; cell death can cause changes in biofilm geochemical conditions and thus patterns of metal sequestration. Application of a conventional extraction scheme can take several days, dependent on the number of extraction steps used. A more rapid alternative is the use of microwave heating for extraction protocols (Nadkarni, 1984; Mahan et al., 1987; Real et al., 1994; Xing and Veneman, 1998). The second criterion is good selectivity between amorphous and crystalline Fe and Mn oxyhydroxide minerals. Biogenic Fe and Mn oxyhydroxides are typically amorphous and highly reactive for trace metals making differentiation of these phases from more crystalline phases important. The third criterion is that the extraction scheme be developed to consider the unique bulk mineralogical components of tailings environments, which differ substantially from natural soils and sediments examined routinely using conventional sequential extraction protocols.

Development of the sequential extraction technique required a number of steps, which for clarity, have been outlined in Figure 2.5. The first step was to design a Microwave Digestion Sequential Extraction Protocol (MDSEP) based on: (1) published extraction reagents and microwave protocols, and (2) consideration of the relevant solid fractions for trace metal sequestration in association with ARD biofilms. The second step was to compare the concentrations of metals extracted from a certified reference material in each fraction between the MDSEP and the Tessier method (Tessier et al., 1979), representing a conventional extraction protocol. Because tailings material was not available and because conventional sequential extraction techniques have been widely applied to sediments, a certified sediment material was used to compare the two methods. The third step was to evaluate the selectivity of the MDSEP for synthetic Fe and Mn oxyhydroxides and jarosite, a common Fe oxyhydroxysulphate mineral in ARD environments. Finally, the MDSEP was applied to natural ARD biofilms.

The organization of this chapter follows the steps outlined for the development and application of MDSEP (Figure 2.5). Materials and methods used in each step are outlined as necessary and discussion of the results follow.

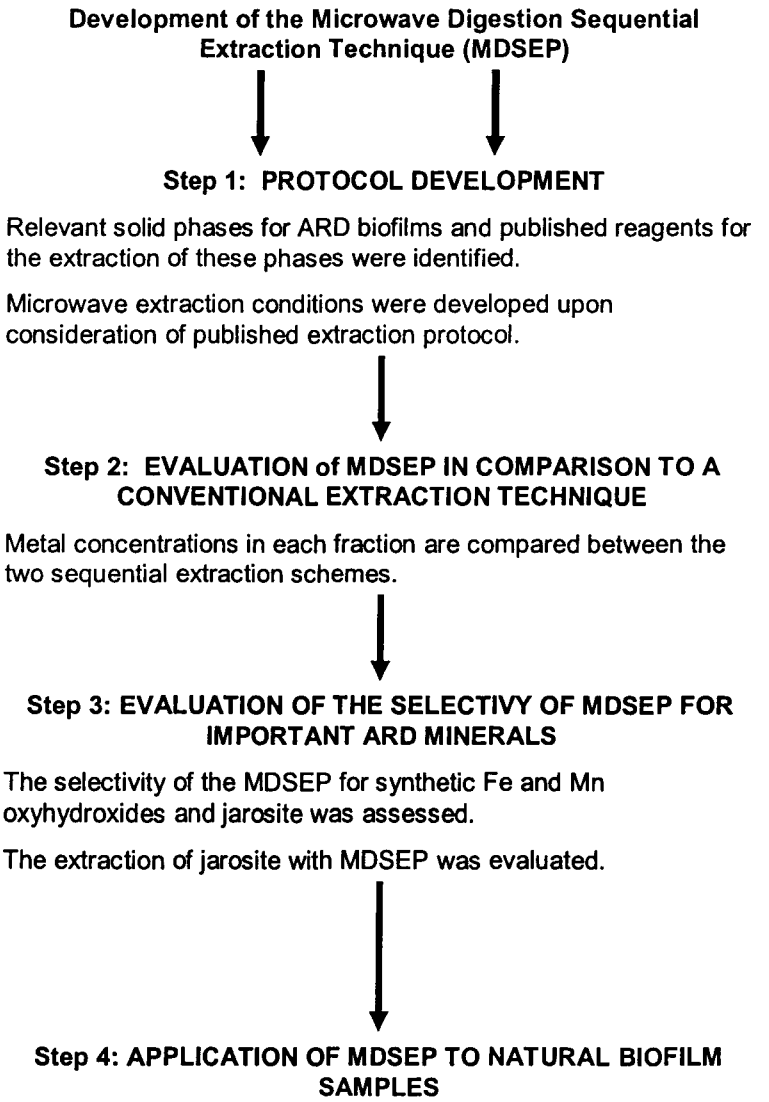

Figure 2.5. Steps in the development and evaluation of the MDSEP.

2.4. Step 1: Protocol Development

2.4.1. Selection of extractants for MDSEP from published extraction schemes.

Most published sequential extraction schemes have been based on the wet geochemical "Tessier" method (e.g. Tessier et al.; 1979, Bendell and Young; 1992, Scheckel et al; 2003). As outlined earlier, this scheme includes five extractions steps (Figure 2.6). The MDSEP developed in this study has six steps. One step was added to the conventional Tessier method to selectively extract amorphous oxyhydroxides from the larger oxyhydroxides pool (includes both amorphous and crystalline Fe/Mn oxyhydroxides). The extractions steps in MDSEP are (1) exchangeable, (2) carbonates, (3) amorphous Fe/Mn oxyhydroxides, (4) crystalline Fe/Mn oxyhydroxides, (5) organic/sulphide, and (6) residual (F1-F6; Figure 2.6). Selection of the reagents for each extraction step was made after consideration of published extraction schemes (Tessier et al., 1979; Mahan et al., 1987; Campbell et al., 1988; Real et al., 1994; Hall et al., 1996 and references therein; McCarty et al., 1998). The rationale behind the selection of each reagent is outlined below. One additional difference between the MDSEP and Tessier method is noted here. The reagent-to-dry-mass ratio applied in the MDSEP was 40:1 (20 mL reagent, 0.5g dry mass sample) while ratios varied from 8:1 to 20:1 in the Tessier scheme (1 g dry weight) depending on the extraction step (Figure 2.6). Rauret et al. (1989) indicated that the higher ratio adopted in the MDSEP is more effective for metal extraction than the conventional ratios.

F1: Exchangeable

To release metals that are most loosely bound to the solid matrix, the leaching solution applied in the exchangeable step is typically a 1.0 M solution of alkali or alkaline-earth metal salts. These solutions have relatively high ionic strength and remobilize trace metals by influencing outer-sphere complexes (Filgueiras et al., 2002). 1.0 M Na-acetate solution (adjusted to pH 8.2 with acetic acid) was chosen as the exchangeable leaching solution in MDSEP as more reproducible values have been reported for this reagent compared to a solution of $MgCl_2$ (Gulmini et al., 1994), as applied in the Tessier scheme (Figure 2.6).

F2: Carbonates

Carbonate minerals are soluble under acidic conditions and this fraction is often termed "acid-soluble" (Filgueiras et al., 2002). The reagent used in the MDSEP is that most used by other researchers: 1.0 M Na-acetate, adjusted to pH 5.0 with acetic acid.

F3: Amorphous Fe/Mn oxyhydroxides

Fe and Mn oxyhydroxides are not stable under reducing conditions. The conventional Tessier method extracts amorphous and crystalline Fe/Mn oxyhydroxides together with one leaching reagent (Figure 2.6). Because biogenic Fe and Mn oxyhydroxides are amorphous and are potentially important solid fractions for metal sequestration in natural ARD biofilms, this step was divided into two steps in the MDSEP. A number of reagents have been used with the goal of selectively extracting amorphous Fe/Mn oxyhydroxides (Hall et al., 1996; McCarty et al., 1998 and references therein). The selectivity of published reagents for amorphous and crystalline Fe oxyhydroxides phases has varied

between researchers and samples (McCarty et al., 1998). The best results for the selective extraction of amorphous Fe oxyhydroxides from natural sediments were shown by Chao and Zhou (1983). Differentiation between amorphous and crystalline Mn oxyhydroxides has not been shown. Both crystalline and Mn oxyhydroxide phases are extracted typically by the "amorphous" reagent (Tipping et al., 1985; Hall et al., 1996). Thus, the reagent of Chao and Zhou (1983) was selected for use in MDSEP, being 0.25 M hydroxylamine hydrochloride (NH_2OH-HCl) in 0.25 M HCl. The concentration of acid used in this reagent, 0.25 M HCl, has also been shown to minimize re-adsorption of trace metals to the solid residue during extraction (Sholkovitz, 1989).

F4: Crystalline Fe/Mn oxyhydroxides

The reagent used to extract crystalline Fe/Mn oxyhydroxides in the MDSEP was 0.04 M hydroxylamine hydrochloride in 25 % v/v acetic acid, as per the Tessier scheme (Figure 2.6).

F5: Organic/Sulphide

Organic matter and sulphides are decomposed under oxidizing conditions. Amongst published extraction schemes, 30% H_2O_2 in an acidic medium is typically the reagent used (Filgueiras et al., 2002). These reagents were used in the Tessier method and are also used here in the MDSEP. The volumes of H_2O_2 and 0.02M HNO_3 were increased proportionally in the MDSEP from those in the Tessier method to reflect the higher organic content of the natural biofilm samples compared to sediments. Organic matter typically makes up 5-10% of sediments by mass (Wetzel, 1983), while the organic content of the biofilm samples was 11-27% by mass (June-Sept, 2001). Biofilm organic content was determined by loss on ignition (%LOI, 550°C for 2 hours) on previously dried samples (80°C for 12 hours).

F6: Residual

Hydrofluoric acid and/or strongly oxidizing acid mixtures (HNO_3+$HClO_4$) are typically used to attack primary minerals in the samples (Tessier et al., 1979; Filgueiras et al., 2002). Trace metals associated with these fractions are held within the crystal structure of these compounds and their reactivity is not relevant under environmental conditions and time scales of interest to this study. Because of the low reactivity of trace metals associated with this fraction and the experimental hazards associated with using both HF and $HClO_4$ in conjunction with the microwave apparatus, the residual reagent applied in the MDSEP was a weaker 16.0 M HNO_3 (Figure 2.6).

2.4.2. Microwave Extraction Conditions

Conventional wet geochemical sequential extraction protocols are time consuming. Full extractions require several days. Microwave technology can significantly reduce the amount of time needed to complete extractions (e.g. on the order of hours). Four published reports of the use of microwave technology for sequential extraction were found: Mahan et al. (1987), Gulmini et al. (1994), Real et al. (1994), and Fanfani et al. (1997). The first three research groups carried out comparative studies in which the concentrations of metals extracted in each fraction were determined for both the conventional Tessier method and by microwave heating. Between the optimized microwave methods and the Tessier method, the precision, accuracy, and concentrations

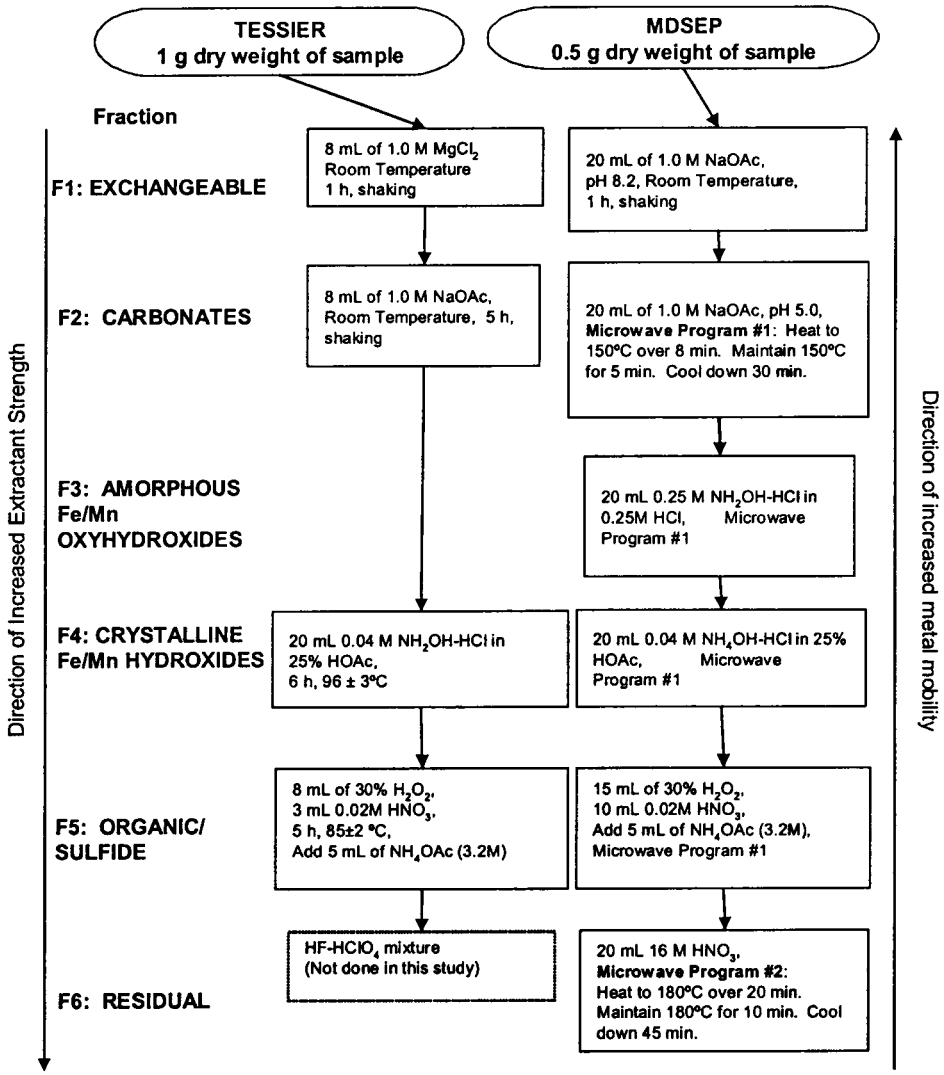

Figure 2.6. Comparison of the Tessier and MDSEP Sequential Extractions Schemes: Fractions, Reagents and Extraction Condition.

of metals extracted were comparable. Microwave heating time was optimized by analysis of the concentrations of several metals extracted with progressively longer heating periods. Plateaus in the extraction curves occurred between 4-16 minutes, depending on the element.

Fanfani et al. (1997) has the most direct relevance to this study. They used a microwave digestion protocol, modified from Mahan et al. (1987), to examine solid-phase metal associations in abandoned mine tailings. Five steps were included in their extraction scheme, as per the Tessier scheme, with the addition of a "soluble fraction" as the first step (demineralized water, 2 hours shaking, room temperature). Microwave heating times ranged from 7 minutes (exchangeable fraction) to 22 minutes (Fe/Mn oxyhydroxides). The authors noted that complete extraction of the high iron loads associated with the ARD material required 6 repetitions of 22 minute microwave heating. Unfortunately, the authors did not give any details about the microwave oven used or the number of samples run simultaneously, making it of little practical utility for establishing extraction conditions for the MDSEP.

Overall, it was difficult to use the published microwave digestion extraction protocols as a starting point in the development of the MDSEP. Mahan et al. (1987), Gulmini et al. (1994), and Real et al. (1994) used conventional microwave ovens based on power levels, whereas the microwave labstation used in this study (Ethos Plus, Milestone Inc.) is designed to control extraction conditions through direct temperature regulation. A disadvantage of using microwave systems based on power is that adjustments must be made between runs to account for differences in sample mass, reagent volume, and the number of samples between runs. Using the Ethos Plus labstation, temperature profiles can be predefined with system software (easyWAVE, version 3.2.1.0, MLS GmbH Germany). The power delivered by the microwave is automatically adjusted to heat the samples to the required temperature. Two temperature profiles were applied in the MDSEP after consideration of three factors: (1) the 4-16 minute time periods needed for extraction in Mahan et al. (1987), Gulmini et al. (1994), and Real et al. (1994), (2) the much longer microwave extraction times recommended by Fanfani et al. (1997) for tailings environments, and (3) the temperatures used in the conventional Tessier scheme (Fe/Mn Oxyhydroxide Fraction: 6 hours at 95 °C and Organic sulphide: 5 hours at 85 °C, Figure 2.6).

- Program 1: heat samples to 150°C over 8 minutes, 5 minute digestion period at 150°C, 30 minute cool-down period
- Program 2: heat samples to 180°C over 20 minutes, 10 minute digestion period at 180°C, 45 minute cool-down period.

Steps F2-F5 applied Program 1. Program 2 was applied for the residual step, F6.

The Ethos Plus labstation is equipped to run a maximum of 10 samples simultaneously. Temperature within the vessels is approximated by monitoring the temperature within one of the sample vessels with an internal probe. Sample digestions are carried out in polytetrafluoroethylene blend 50 mL sample vessels that allow for trace-metal grade analysis. The samples are positioned on a rotating tray, to allow more homogeneous heating of the sample. The sample vessels are tightly capped and have a

pressure-release mechanism, minimizing evaporation and sample loss during digestion. The maximum power of the system is 1000W. Sample vessels are acid washed by closed-vessel acid reflux with OPTIMA grade HNO_3 (Fisher Scientific). Repeated extraction steps can be run on the same day, as the microwave digestion steps, from warm up to cool down, takes at most 75 minutes.

2.4.3. Summary

The MDEST developed has 6 extraction steps: exchangeable (F1), carbonates (F2), amorphous Fe/Mn oxyhydroxide (F3), crystalline Fe/Mn oxyhydroxide (F4), organic/sulphide (F5), and residual (F6). Reagents used in each extraction step were carefully selected based on published extraction schemes. Microwave conditions were based on the conditions detailed in the limited published microwave protocols as well as to reflect the high temperatures used in the Fe/Mn oxyhydroxide and organic/sulphide fractions of the classic Tessier approach (Figure 2.6).

2.5. Step 2: Comparison of the MDSEP to the Tessier Extraction Scheme

When new sequential extraction protocols are developed the precision, accuracy, and the concentrations of metals extracted in each fraction are typically compared to the conventional Tessier method to permit calibration and to evaluate the comparability of results yielded by different protocols. Such a comparison was performed in this study using a certified reference material. A standard sediment material was chosen because the conventional Tessier method has been widely applied to sediment samples and a certified reference material is not available for ARD or biofilm samples. However, because the MDSEP does not apply HF or strongly oxidizing acid mixtures in the residual step, the total amount of metals extracted by this technique are not directly comparable to the certified reference values. The residual step in the Tessier extraction was not performed and comparison of the two methods involved examining the concentrations of Fe, Mn, Ni, Co and Cr extracted in steps F1-F5 (Figure 2.6).

2.5.1. Materials and Methods

The standard reference material used was Buffalo River Sediment (National Institute of Standards and Technology (NIST), #8704). Five replicates sample were run, using 1.0 g of sediment for the Tessier scheme and 0.5 g for the MDSEP. The conditions and reagents applied in both the Tessier scheme and the MDSEP are summarized in Figure 2.6. Extractions by the Tessier method were run in 30 mL polypropylene centrifuge tubes. Samples run by the MDSEP were digested in polytetrafluoroethylene microwave digestion vessels. Between digestion steps, the samples were transferred from the digestion vials to 30 mL centrifuge tubes for centrifugation. The supernatant was separated from the solid residue after each extraction step by centrifugation (30 minutes x 10 000 rpm, Tessier method; 20 minutes x 16 000 rpm, MDSEP).

All water used in extraction reagents and stock solutions was ultrapure (UPW; Millipore, Milli-Q, 18.2mΩ.cm). Polyethylene bottles were left overnight in a 3-5% HCl bath and subsequently rinsed seven times in UPW. All reagents used were of analytical grade or better and for the elements tested were not contaminated (with the exception of

Cr contamination of acetic acid, see 2.5.2.). Mn, Ni, Co and Cr concentrations extracted in each sediment fraction were quantified by ICP-MS. Total Fe, ($[Fe]_{total}$, extracted in each fraction was quantified by colorimetric analysis (Ultrospec 3000, Uv/Visible Spectrophotometer (Pharmacia Biotech, Cambridge, U.K.) using the Ferro Ver Total Iron HACH Method 8008 (Ferro Ver Iron Reagent Powder Pillow®; Registered Trademark of the Hach Company, Loverland, CO) adapted from Clesceri et al. (1998). Reagent blanks were included in each digestion assay. Matrix effects associated with ICP-MS were corrected by using an internal standard (Y^{89} in-line at 2 ppb) and matrix-matched standards.

2.5.2. Results and Discussion

Metal concentrations extracted in each of the fractions (F1-F6) for the Tessier and MDSEP schemes are given in Table 2.3, and shown in Figure 2.7. Concentrations of Cr in the carbonates and exchangeable fraction were not quantifiable due to high blank values in both extraction schemes (<50ppb). For subsequent analyses, an optima grade acetic acid was used to prepare reagents for the exchangeable, carbonate and crystalline reagents (OPTIMA, Fisher Scientific, Cr < 0.01ppb). Method detection limits for each element in all fractions were calculated as 3 x the standard deviation (σ) of the blanks (Bárány et al., 2002). Concentrations below the detection limits were indicated by "b.d." (Table 2.3). Total metal concentrations were determined by summing concentrations in the fractions F1-F5 (Σ Total; Table 2.3). As mentioned, because complete extractions using HF or strongly oxidizing acid mixtures were not performed in this study, total metal concentrations for each of the schemes are not directly comparable to the NIST certified values (Table 2.3). However, comparisons of the concentrations of metals extracted between the Tessier method in this study and published results and between the MDSEP and Tessier methods were possible for extraction steps F1-F5.

Fe, Ni, Mn and Co concentrations in F1-F5 of the Tessier extraction corresponded to 13%, 35%, 73% and 43% of the NIST certified values (indicated by "% certified" values in Table 2.3). These results are consistent with results from published studies for these elements. Fe, Ni, Mn and Co concentrations in steps F1-F5 reported originally by Tessier et al., (1979) for two lake sediments were approximately 17%, 33%, 50% and 61%. Hall and Pelchat (1999) also showed <15%, <40%, ~60% extracted in F1-F5 for Fe, Ni and Mn, respectively, using the Tessier method on agricultural soils.

The total amount of metal extracted in extraction steps F1-F5 by the MDSEP exceeded that extracted using the Tessier method for all elements analyzed (Σ Total; Table 2.3, Figure 2.7). While the % of the NIST certified values extracted in these extraction steps was comparable for Mn and Cr (Mn: 73% by Tessier scheme vs. 90% by MDSEP; Cr: 44% by Tessier scheme vs. 47% by MDSEP; Table 2.3), the % Fe, Ni and Co extracted was significantly higher by the MDSEP (t-test, $p<0.05$). However, in both the schemes, the same two solid fractions were important for Mn, Cr, Ni and Co sequestration in the NIST certified material. Important fractions for Mn were F2 and the Fe/Mn oxyhydroxides fractions (F3+F4 in MDSEP, F4 in Tessier scheme); together these fractions accounted for at least 70% of the total Mn extracted in both schemes (Table 2.3, Figure 2.7). The concentration of Mn extracted in F2 by the MDSEP accounted for

approximately 50% of the total Mn extracted versus ~28% by the Tessier scheme (Table 2.3, Figure 2.7). Hall and Pelchat (1999) have reported higher relative Mn concentrations in the carbonates fraction in their extraction scheme, where the F2 leach was applied twice. This result suggests that leaching of Mn in F2 may not be complete in the Tessier method. The amount of Mn extracted in the Fe/Mn oxyhydroxide fractions of MDSEP (F3+F4: 213ugg^{-1}) also exceeded that extracted in the Tessier scheme (F4: 171ugg^{-1}).

The two important solid fractions for Cr, Ni and Co sequestration were the Fe/Mn oxyhydroxide fractions (F3+F4) and the organic fraction (F5) (Table 2.3; Figure 2.7). Between schemes, the relative importance of these fractions differed. Greater amounts of Cr, Ni and Co were extracted in the Fe/Mn oxyhydroxide fractions of the MDSEP (F3+F4) compared to Tessier method (F4). The increase was due to greater concentrations of these elements in F3 by the MDSEP. Concentrations of Cr, Ni and Co extracted in F5 by the Tessier scheme significantly exceeded those extracted in that fraction by the MDSEP (t-test, $p<0.05$). For Fe, the Fe/Mn oxyhydroxides fraction was the only important fraction identified by both schemes. Fe concentrations extracted by the MDSEP in F3+F4 (17.7 mgg^{-1}) exceeded that extracted in F4 by the Tessier scheme (4.72 mgg^{-1}).

The shift in the relative proportion of trace metals (Ni, Co and Cr) between the Fe/Mn oxyhydroxide fractions and the organic fraction and the higher concentrations of Mn and Fe in F3+F4 by the MDSEP compared to the Tessier scheme could have two causes. Firstly, the Tessier method may underestimate the concentration of metals associated with the oxyhydroxides fraction because of incomplete attack of Fe/Mn oxyhydroxides. Release of metals associated with this fraction would occur in subsequent steps and result in overestimation of metal concentrations in the organic/sulphide and residual fractions. Alternatively, the observed trend could represent the attack of phases other than amorphous Fe/Mn oxyhydroxides by the F3 reagent in the MDSEP. Because there are no other reports of amorphous extractions by microwave digestion it is not possible to compare the results from this study to other studies. Both Mahan et al. (1987) and Gulmini et al. (1994) showed comparable concentrations of Ca, Fe, Mn in the crystalline fractions using 0.04 M hydroxylamine hydrochloride in 25% v/v acetic acid between microwave protocol and conventional Tessier schemes, thus, it is not inherently the microwave heating which causes the differences between MDSEP and the Tessier method. Results from other studies have indicated that the conventional Tessier technique may be attributing metals to the residual fraction that are in fact part of the reducible fraction. Hall and Pelchat (1999) found that concentrations of Ni, Cu, Fe and Zn were comparable between their amorphous Fe/Mn oxyhydroxide step (0.25M hydroxylamine hydrochloride in 0.05M HCl) and the Fe/Mn oxyhydroxide step in the conventional Tessier scheme. However, a second "reducible" fraction was included in their extraction scheme (corresponding to F4 in this study) and significant concentrations of all elements were extracted in this fraction. These additional concentrations of Zn, Cu, Ni and Fe would have been attributed to the residual fractions using the conventional Tessier scheme. Hall and Palchat (1999) caution that it may be erroneous to assume that the dominant proportion of these elements is tied up in resistant mineral structures.

Table 2.3. Metals extracted in fractions F1-F6 in the Tessier Scheme and the MDSEP

	mean and standard deviation[a]					
	Fraction	Tessier	MDSEP	Fraction	Tessier	MDSEP
	F1	b.d. (<0.01)	b.d. (<0.01)	F1	0.70 ± 0.05	0.34 ± 0.02
Fe	F2	0.34 ± 0.02	0.57 ± 0.06	**Ni** F2	1.21 ± 0.16	2.99 ± 0.08
	F3		16.2 ± 1.3	F3		24.0 ± 1.14
	F4	4.72 ± 0.29	1.54 ± 0.12	F4	7.02 ± 0.34	2.48 ± 0.31
	F5	0.58 ± 0.02	0.32± 0.06	F5	6.08 ± 0.92	2.8 ± 0.6
	F6		15.8 ± 1.1	F6		5.75 ± 0.35
	Σ Total[b] (F1-F5)	5.64 ± 0.29	34.6 ± 1.2	Σ Total (F1-F5)	14.9 ± 1.1	32.6 ± 1.1
	Certified Value	39.7 ± 1.0		Certified Value	42.9 ± 3.7	
	% of Certified[c]	13	45	% of Certified	35	76
Mn	F1	78.8 ± 9.6	33.2 ± 0.9	**Co** F1	0.35 ± 0.03	0.14 ± 0.01
	F2	108 ± 20	235 ± 7	F2	0.37 ± 0.05	1.56± 0.03
	F3		194 ± 3	F3		7.29 ± 0.25
	F4	171 ± 7	19.0 ± 0.9	F4	2.91 ± 0.11	0.73 ± 0.02
	F5	44.9 ± 7.0	5.3 ± 0.4	F5	2.22 ± 0.32	0.8 ± 0.03
	F6		53.9 ± 3.7	F6		1.42 ± 0.123
	Σ Total (F1-F5)	396 ± 19	487 ± 9	Σ Total (F1-F5)	5.83 ± 0.36	10.5 ± 0.3
	Certified Value	544 ± 21		Certified Value	13.57 ± 0.43	
	% of Certified	73	90	% of Certified	43	77
Cr	F1	b.d.	b.d.			
	F2	b.d.	b.d.			
	F3		42.6 ± 2.9			
	F4	27.5 ± 1.5	5.6 ± 1.5			
	F5	25.2 ± 3.5	10 ± 1.4			
	F6		12.5 ± 1.5			
	Σ Total (F1-F5)	50.0 ± 3.1	58.7 ± 3			
	Certified Value	121.9 ± 3.8				
	% of Certified	44	47			

[a] Concentrations of Fe (mgg^{-1}) and Mn, Ni, Co and Cr (μgg^{-1}) in extraction steps F1-F6 for the Tessier method (F3 and F6 not run) and MDSEP. Analytical precision (1σ, n=5) was generally better than 10% for MDSEP and 15% for the Tessier method.

[b] ΣTotal represents the sum of metals extracted in fractions F1-F5. Because the Tessier extraction was only run as far as F5 comparison between the two extraction schemes does not include metals extracted in F6 by MDSEP.

[c] This value is the % of the certified value extracted in F1-F5 for both extraction methods

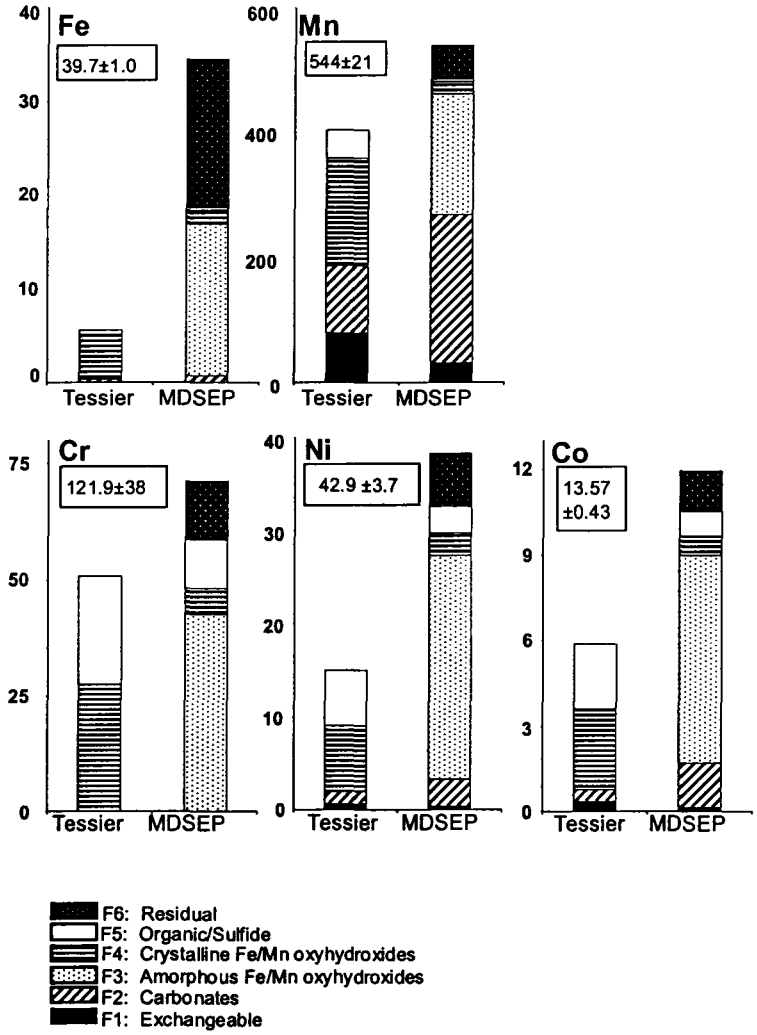

Figure 2.7. Concentrations of Fe (mgg^{-1}) and Mn, Ni, Co and Cr (μgg^{-1}) in NIST standard reference material (Buffalo River Sediment), for extraction steps F1-F6 for the Tessier method (F3 and F6 not run) and MDSEP. Certified values for total solid-associated metal concentrations are indicated (boxed value) for each element. Differences were observed between the amount of each element extracted in the Amorphous Fe/Mn oxyhydroxides fraction and the Organic/Sulphide fraction. For clarity, error associated with metal concentrations in each fraction is not shown. Coefficients of variation (1σ, n=5) was generally better than 10% for MDSEP and 15% for the Tessier method.

2.5.3. Summary

When applied to a sediment sample, the Tessier scheme and the MDSEP identified the same two important solid fractions for metal sequestration in extraction steps F1-F5. The two important solid fractions were the carbonates and Fe/Mn oxyhydroxides for Mn and the Fe/Mn oxyhydroxides and the organic fraction for Fe, Cr, Ni, and Co for the standard reference material. The relative amount of metal extracted in each of the two important fractions did differ between the two schemes, with relatively more being extracted in the amorphous Fe/Mn oxyhydroxide fraction of the MDSEP compared to the Fe/Mn oxyhydroxide step in the Tessier Scheme. Without further information about the exact mineralogical components of the standard reference material (Buffalo River sediments), it is difficult to interpret the differences between the two extraction schemes, and the results of this comparison highlights the operational nature of sequential extraction techniques. The results do suggest that interpretation of metal partitioning results by the MDESP would be made more accurate better constraining the selectivity of the extraction steps used in the scheme for Fe/Mn oxyhydroxides. Further, because the goal was to apply MDSEP to natural biofilm samples from ARD environments, it was important to determine the bulk Fe-mineralogy of these samples and evaluate the efficiency and effectiveness of extracting these phases using MDSEP.

2.6. Step 3: Evaluation of the Selectivity of MDSEP for Important ARD Minerals

ARD environments are characterized by a bulk mineralogy, which differs significantly from the mineralogy of lake sediments and natural soils that are routinely evaluated using sequential extraction schemes. At my study site, the biofilms represent the interface between waste rock tailings and the shallow overlying water (Figure 2.3). The seepage streams occur over older more oxidized tailings and thus the concentration of sulphides is expected to be low in association with the biofilms. The suite of minerals that have the potential to be important for trace metal sequestration in association with the biofilms are biogenic amorphous oxyhydroxides of Fe and Mn and abiotic Fe oxyhydroxides. These minerals, especially those catalyzed by microbes, are fine grained (Konhauser, 1998; Konhauser and Urrutia, 1999; Nelson et al., 1999a) and may only constitute a minor fraction of the overall sample by mass. Secondary oxyhydroxy sulphate minerals, jarosite and schwertmannite, likely make up the bulk Fe mineralogy in these samples (Seal and Hammarstrom, 2003). To assess the selectivity of the MDSEP protocol for amorphous vs. crystalline Fe/Mn oxyhydroxides, the extraction of synthetic amorphous and crystalline Fe/Mn oxyhydroxide phases was determined. In addition, the bulk mineralogy of the natural biofilm samples was determined and the behaviour of K-jarosite examined by MDSEP. Assessment of the selectivity occurred in two steps:

1) The reagents and conditions of F3 and F4 were applied directly to the synthetic phases to determine the percent (%) dissolution of the samples in these fractions.
2) MDSEP was applied to the synthetic analogues to determine if the first two extraction steps (F1 + F2) induced any mineral alterations, which in turn affected the selectivity of the MDSEP in steps F3 and F4.

Additionally, changes in the mineralogy of jarosite after each extraction step was analyzed using X-ray diffractometry (XRD) because jarosite has not previously been examined using sequential extraction schemes.

2.6.1. Materials and Methods

Preparation of Synthetic Compounds

Ferrihydrite (2-line), and hematite were prepared according to Cornell and Schwertmann (1996). Amorphous manganese oxyhydroxide (hydrous manganese oxyhydroxide, HMO) was prepared by the slow addition of $MnCl_2$ to alkaline $NaMnO_4$ solution, as described previously (Murray, 1974). Potassium jarosite, $KFe_3(SO_4)_2(OH)_6$, identified as the jarosite species in the biofilm samples (see 2.6.2), was prepared according to Brophy et al. (1962) and Drouet and Navrotsky (2003), with some modifications. Crystalline jarosite is formed by the co-precipitation of $Fe_2(SO4)_3$ and K_2SO_4 at 95°C for 4 hours, in acidic solution (0.1 M H_2SO_4) to avoid hydrolysis of Fe^{3+}. Attempts to precipitate jarosite under these conditions failed (initial solution pH <1) and the published technique of Drouet and Navrotsky (2003) was modified to bring the initial solution pH to values between 2 and 3. The relatively higher pH value is more consistent with the pH conditions (2-3) under which jarosite forms naturally (Bigham, 1994). The published technique was further modified by using microwave heating in contrast to conventional heating. The reaction between $KFe_3(SO_4)_2(OH)_6$ and $Fe_2(SO4)_3$ is very vigorous and boils at approximately 90°C. This reaction was traditionally run using a hotplate, but this requires careful attention to the reaction and addition of ultrapure water to the solution at regular intervals. A microwave profile was designed to bring the temperature of the solution to 95°C over 10 minutes, followed by 4 hours at 95°C, and finally a 1 hour cool-down period, with constant stirring. Synthetic K-jarosite was thus precipitated in this study by the addition of 1.64 g $Fe_2(SO4)_3$ and 0.7 g of K_2SO_4 (excess) to 40 mL of 0.05 M H_2SO_4 solution using microwave heating. The resulting precipitate was washed five times with UPW and dried overnight at 100°C. The identity of the synthetic jarosite was verified by XRD (see below).

X-ray Diffraction Analyses

Diffraction data was collected for both synthetic jarosite samples and natural ARD biofilm samples. The crystalline components of the ARD biofilm samples were identified using a Siemen's D5005 diffractometer (Cu Kα radiation, Goebbel mirrors, LiF monochromator; Falconbridge Technology Centre, Sudbury, ON). Step diffraction scans were made from 5 to 75 °2θ. The diffractometer was operated at 40kV with 40mA. Prior to XRD analysis, the whole biofilm samples were rinsed three times in UPW with centrifugation between rinses (10 minutes, 10 000 rpm) and finally air dried. Samples were homogenized and hand-ground by mortar and pestle. All samples were run in zero background holders for a 5 hour scan, to attempt to detect any crystalline phases present.

Search/match software was used with a chemical filter and the 1997 International Center for Diffraction Data (ICDD) database. Phases were identified and evaluated as major (>20%), intermediate (10-20%) or trace (5-10%), components by mass.

All XRD analysis of synthetic K-jarosite samples were recorded with a Nicolet I2 diffractometer operated at 50 kV and 30 mA and using Cu Kα radiation. Step diffraction scans were made from 10 to 70 °2θ with a 0.03 °2θ step increment and counting rate of 0.1 °2θ a minute (K-jarosite) or 0.04 °2θ step increment and a counting rate of 0.5 °2θ a minute (extracted fractions, qualitative scans; Brockhouse Institute for Materials Research, McMaster University, Hamilton, ON).

Solid-phase metal analysis

After each extraction, the supernatant was separated from the solid residue by centrifugation (16 000 rpm, 20 minutes). Dissolved Fe/Mn concentrations were determined by ICP-MS and UV-VIS spectroscopy (see 2.5.1.). In all extractions of synthetic solids, 0.5 g dry weight of the samples was used. Ferrihydrite and HMO were added as wet pastes to equivalent 0.5 g dry weight. Digestions were run in triplicate.

2.6.2. Results and Discussion

Biofilm Mineralogy

The bulk crystalline materials in the biofilm samples were jarosite, quartz, gypsum and several phyllosilicates (Table 2.4). Examination of the mineralogical content of two biofilm samples collected one month apart (May 30 and June 21, 2001) reveals that the same bulk mineralogy occurs in both samples with differences in the relative contributions of the identified minerals (Table 2.4). Jarosites are secondary weathering products of pyritic minerals and are commonly found in acidic environments (pH < 3) with high Fe^{3+} and sulphate loads (Dutrizac and Jambor, 2000). The generalized ideal formula of jarosites is $AFe_3(SO_4)_2(OH)_6$ where A is most commonly Na^+, K^+, and NH_3^+. This is an ideal formula as stoichiometric deficiencies in Fe have been reported for synthetic and natural jarosite samples (Dutrizac and Kaiman, 1976; Paktunc and Dutrizac, 2003). The subgroup of jarosites identified in the natural biofilm samples was K-jarosite. Crystalline Fe or Mn oxyhydroxides phases were not detected by XRD, even as trace components of the bulk biofilm mineral composition. The XRD analysis, however, did not identify mineral phases that comprise less than 5% of the whole sample by mass (Shirley Lalonde, Falconbridge Technology Center, personal communication)

The identification of these solid phases is important because of their potential reactivity for trace metals, and thus, for the interpretation of the MDSEP results for natural biofilm samples. The reactivity of primary minerals such as quartz and albite with regards to trace metals is thought to be low (Jenne, 1968), i.e. these bulk crystalline minerals are not likely to be important metals sorbents in this environment. In waste rock systems that are poor in carbonate minerals, biotite, $[K(Mg^{2+},Fe^{2+})_3[AlSi_3O_{10}](OH,F)_2]$, is one of the gangue minerals thought to provide a major sink for produced acidity

(Ströemberg and Banwart, 1994). The first step in the weathering process of biotite is expansion of the interlayer spacing and exchange of non-hydrated K^+ for hydrated or hydrolyzed ions (Fanning et al., 1989). Partial weathering of biotite is enhanced under low pH conditions, and is thought to be one of the primary sources of K^+ in the formation of K-jarosite in acid-rock drainage impacted environments (Acker and Bricker, 1992; Malmström and Banwart, 1997). Research examining Cu(II), Pb(II) and Cd(II) uptake to biotite under acidic conditions (pH 5.4 ± 0.2) has suggested that all three metals are sorbed, and that Cu(II) appears to exchange for K^+ in the biotite structure (Farquhar et al., 1997). Thus, there is the potential for metal release to solution upon partial dissolution of biotite.

Jarosite minerals show a limited reactivity for trace metals (Dutrizac, 1984). In fact, jarosite is becoming an important solid in the field of metallurgy precisely because precipitation of this mineral rids the system of unwanted Fe(III), alkali metals and sulphate ions, but does not scavenge significant amounts of valuable metal ions (Dutrizac and Jambor, 2000). One study has shown that divalent trace metal ions are incorporated into the crystal structure of the jarosite as a result of vacant Fe^{3+} octahedral positions. Fe^{3+} octahedral-site deficiencies can be as high as 17% in synthetic jarosites (Paktunc and Dutrizac, 2003), imparting an excess negative charge to these minerals. Amongst divalent transition metal ions, the order of metal incorporation into jarosite decreases in the order: Cu>Zn>Co~Ni~Mn>Cd (Dutrizac, 1984). The weight % of these elements incorporated into the jarosite structure increases with pH but does not exceed 2.5% in synthetic or natural samples, and is often much lower (Dutrizac, 1984). Although the reactivity of these minerals is low on a per mass basis, they may still represent an important metal sink in the ARD environment given their often substantive relative mass.

Selectivity of F3 and F4 for amorphous and crystalline Fe/Mn oxyhydroxides

Hematite and (2-line) ferrihydrite were synthesized as analogues for crystalline and amorphous Fe oxyhydroxides, respectively. Commerical pyrolusite (MnO_2, Fisher and synthetic HMO were used to similarly assess the selectivity of the MDSEP for crystalline and amorphous Mn phases. Ferrihydrite and HMO were chosen as the most appropriate analogues for biogenic Fe and Mn oxyhydroxides. K-jarosite was chosen to represent the jarosite subgroup based on the XRD results for the biofilm samples. Solubilization of each analogue was carried out to determine the weight % of the major ions, Fe or Mn, in each of the solid fractions (Table 2.5). Total digestions were carried out in 20 mL of HNO_3 using microwave heat (Profile 2; see 2.4.2).

The extent of dissolution of the synthetic solids in the MDSEP fraction F3 (amorphous oxyhydroxides; all solids) and F4 (crystalline solids: hematite, pyrolusite, and jarosite) is shown in Table 2.5. The amount of Fe/Mn leached in each of the extractions is given as a percentage of total dissolution of that phase (based on weight%). The results indicate that MDSEP in not completely selective for amorphous vs. crystalline Fe/Mn oxyhydroxide phases. Both HMO (amorphous Mn oxyhydroxides) and pyrolusite (crystalline MnO_2) were completely dissolved in F3 (Table 2.5). Ferrihydrite,

Table 2.4. Bulk crystalline mineralogical composition of two natural ARD biofilm samples[a].

Biofilm Sample	Phases Identified by XRD		
	Main (20-25%)	**Minor (10-20%)**	**Trace (> 5%)**
A (May 31, 15:00)	Jarosite, quartz, albite	Clinochlore, biotite, actinolite	Gypsum
B (June 21, 16:30)	Quartz, albite, gypsum	Jarosite, clinochlore, biotite	Actinolite

[a] XRD analysis was performed on air-dried homogenized samples

the amorphous Fe oxyhydroxide was only incompletely dissolved in F3 (~73% dissolved) and hematite, the crystalline Fe oxide, and jarosite (also crystalline, see below) were both partially leached in this extraction step (~34% and ~30% dissolved, respectively, Table 2.5). The lack of selectivity was expected for Mn oxyhydroxides; other studies have shown leaching of both amorphous and crystalline Mn oxyhydroxides by the amorphous Fe/Mn oxyhydroxides reagent (e.g. Tipping et al., 1985; Hall and Palchat, 1999). However, crystalline Mn oxides, such as pyrolusite and ramsdellite are not expected to be important solid fractions associated with ARD environments (Post, 1999). The lack of selectivity for Fe minerals was also expected. A growing number of researchers using sequential extractions have reported non-selectivity for iron minerals as well as other metals that represent major matrix elements, in modified extraction schemes (e.g. Mahan et al., 1987; Real et al., 1994; McCarty et al., 1998).

The reagent used in F4 (0.04 M hydroxylamine hydrochloride) was not selective for crystalline Fe/Mn phases: less than 15% of the sample mass was dissolved for hematite, jarosite and pyrolusite (Table 2.5). Because of the high jarosite content by mass in the biofilm samples, the concentration of reductant in this fraction was incrementally increased with constant extraction conditions to evaluate the dissolution of jarosite (0.1 M, 0.5M, 1.0 M successively; data not shown). However, even in a 1.0 M solution, synthetic jarosite was not completely dissolved (~77% dissolved, Table 2.5). The reagent used in F4 was modified in all subsequent applications of MDSEP, from 0.04 M to 1.0 M hydroxylamine hydrochloride in 25% v/v acetic acid (see Figure 3.1). Concentrations of hydroxylamine greater than 1.0 M were not assessed; values higher than 1.0 M have not been found in published reports and increasing concentration of this reagent decreases selectivity (Hall et al., 1996).

Assessing changes in mineral dissolution with sequential extraction

The second step in assessing the selectivity of MDSEP for the synthetic phases was to evaluate if any alterations in the selectivity of fractions F3 and F4 occurred when applied sequentially. Results show that, generally, application of MDSEP did not change the selectivity of F3 and F4. The dissolution of both amorphous and crystalline Fe/Mn mineral phases was negligible in F1 and F2, and comparable extraction of ferrihydrite (~72%), hematite (~31%) and jarosite (~55%) occurred whether sequentially in the MDESP or separately with F3 (Tables 2.5 and 2.6). HMO dissolution was complete in F3 whether sequentially or separately. The only change in reactivity was observed for pyrolusite, which was not completely dissolved in F3 using a sequential approach, rather than a separate F3 extraction.

A mineralogical change in the jarosite sample was visually observed both after steps F3 and F4 run independently, as well as after F2 in the sequential extraction. Synthetic K-jarosite has a bright and distinct yellow color and after these extraction steps the residue had a deep red color, suggesting the formation of an iron oxyhydroxide mineral phase. The alteration of K-jarosite through the extraction was examined further using XRD (see below).

Table 2.5. Summary of published reagent efficacy for selective dissolution of amorphous and crystalline oxyhydroxides[a].

Solid Sample	Molecular Formula	Theoretical weight % major cation (Fe or Mn)	Experimental weight% major cation (Fe or Mn) from total digestions	Reagent		
				F3[a]	F4[a]	Modified F4[a,d]
Ferrihydrite	$Fe_5HO_8 \cdot 4H_20$	0.58	0.49 ± 0.03	73 ± 4	N.A	97± 3
Hematite	Fe_2O_3	0.70	0.65 ± 0.04	34 ± 9	10 ± 2	95 ± 4
Jarosite	$KFe_3(SO_4)_2(OH)_6$	0.34[b]	0.30 ± 0.01	47 ± 5	3.2 ± 0.4	77 ± 0.4
HMO	Birnessite-like	(0.53)[c]	0.53 ± 0.03	100 ± 7	N.A.	N.A.
Pyrolusite	MnO_2	0.63	0.54 ± 0.03	97 ± 6	15 ± 3	100 ± 3

[a] The amount of solid dissolved in each fraction is given as a % of that dissolved in the total extractions (100%). Total extractions reagents were 16.0 M HNO_3.
[b] Stoichiometric deficiencies of iron in synthetic and natural jarosites have been reported (Dutrizac and Kaiman, 1976). Fe weight % of 30.00 and 29.18 have been reported (Paktunc and Dutrizac, 2003).
[c] ideal structural formula of HMO is not known. Total digestions suggest that this solid has a weight % like that for birnessite (0.528; Drits et al., 1997)
[d] The F4 reagent, 0.04M was modified to 1.0 M hydroxylamine hydrochloride in 25% v/v acetic acid.

Table 2.6: Summary of Fe and Mn released from amorphous and crystalline phases with MDSEP[a]

Solid Sample	F1	F2	F3	F4	Overall % Recovery
Ferrihydrite	b.d.[b]	<1	72 ± 4	18 ± 2	88 ± 6
Hematite	b.d.	b.d.	31 ± 10	64 ± 5	88 ± 8
Jarosite	<0.1	<0.1	55 ± 5	35 ± 2	90 ± 6
HMO	b.d.	<1	82 ± 7	N.A.	82 ± 7
Pyrolusite	<1	<1	72 ±3	6.5 ± 0.8	80 ± 3

[a] Values are given as % of the solid dissolved from total extractions (100%).
[b] indicates below detection limits
[c] The overall recovery of synthetic Fe/Mn oxyhydroxides by MDSEP was 80-90%. The MDSEP does require a number of transfer steps between microwave vessel and centrifuge tubes, contributing to the overall loss of sample.

Alterations in the mineralogy of synthetic jarosite with sequential extraction

Consistent with the visual observation, analysis of K-jarosite mineralogy by XRD indicates that jarosite partially decomposes to form hematite under the high temperature conditions of F2, F3 and F4 of MDSEP. XRD analysis of the initial precipitate verified that K-jarosite was the only crystalline phase in the synthetic jarosite sample (by comparison with JCPDS-ICDD standard #36-427; Figure 2.8a). Results indicate that the K-jarosite structure was not altered by F1 (Fig. 2.8b), but peaks consistent with hematite (Fe_2O_3: #33-664) appeared in the XRD scan of the sample following extraction F2 (Figure 2.8c, peaks due to hematite are labeled "H"). After F2, the solid residue contained K-jarosite, hematite, and trace amounts of syngenite ($K_2Ca(SO_4)_2 \cdot H_2O$: #28-739) formed as a byproduct of jarosite dissolution to hematite. Jarosite will decompose to goethite or ferrihydrite upon exposure to high temperatures and alkali conditions (Dutrizac and Jambor, 2000) and to hematite at temperatures above 100°C (Stoffregen et al., 2000). Both high temperature (above 100°C) and alkali conditions are met in the extraction scheme; during the exchangeable fraction the solution pH is adjusted to 8.2 and during the carbonates fraction the sample is heated to 150°C in a solution at pH 5.2. Thus, the alteration of jarosite results from methodological artifacts of the extraction protocol. Following F3, the residue is again composed of jarosite, with trace amounts of hematite.

These results indicate that changes in the mineralogy of the jarosite sample occur as a result of MDSEP. The hematite formed as a result of this transformation is extracted in F3. However, not all of the jarosite was transformed. This complex process may have implications for the interpretation of trace metal sequestration in samples containing this mineral, such as ARD associated samples. The final step in the development of MDSEP was thus to examine changes in the mineralogy of natural biofilm samples with the application of MDSEP and evaluate its efficacy for natural samples by determining the important solid fractions for trace metal sequestration in those solids.

2.7. Step 4: Application of MDSEP To Natural ARD Biofilms

The overall objective of this study was to develop a sequential extraction scheme for the rapid and quantitative analysis of distinct (i.e. amorphous oxyhydroxides vs. more crystalline oxyhydroxides vs. organic matter) metal associations within natural biofilm samples. Evaluation of the selectivity of the published extraction reagents for amorphous and crystalline Fe/Mn oxyhydroxides indicated that alteration of jarosite can occur, and should be considered in the application of MDSEP to natural ARD biofilms. Thus, a combined approach was taken, where solid-phase metal associations within the biofilm samples were quantified by MDSEP and the mineralogy of the sample was analyzed after relevant extraction steps by XRD.

2.7.1. Materials and Methods

MDSEP extractions were applied to natural biofilm samples collected on May 31, 2001 (15:30) and June 21, (16:30) for XRD analysis and to samples collected June 21 (16:30), June 21 (20:50) and June 22 (11:00) for analysis of metal partitioning within the

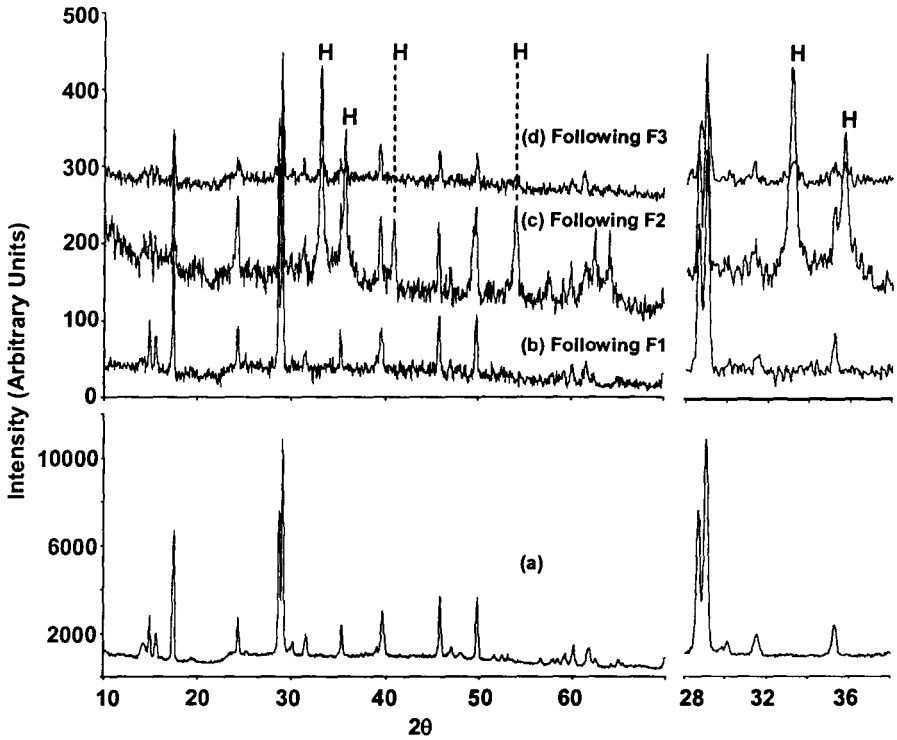

Figure 2.8. XRD analyses of synthetic K-jarosite (a) and the residue after sequential extractions steps F1 (b), F2 (c) and F3 (d). The letter H indicates peaks in the scans that are the result of hematite.

biofilm. Triplicate samples were run using approximately 1.0 g of wet unhomogenized biofilm sample. Quantification of Fe, Mn, Ni, Co and Cr in each extraction sample was performed as previously described (2.5.1). Analytical accuracy during each run was assessed by extraction of certified reference material. Because MDSEP does not fully decompose sediments samples, a biological reference sample (Bovine Liver, NIST standard reference material #1577b) was used that was fully decomposed within the extraction procedure. Use of the biological material allowed comparison between the certified values for selected elements and the total metal concentrations extracted by MDSEP (Table 2.8). XRD analysis of the extracted biofilm samples was carried out after extractions steps F1 through F4 at the Falconbridge Technology Center (see 2.7.2.).

2.7.2. Results and Discussion

XRD Analysis of Extracted Biofilm Samples

The bulk crystalline components of the biofilm samples prior to application of MDSEP were K-jarosite, quartz, gypsum, albite, chlinochlore, biotite, and actinolite, (Table 2.4). Changes to both the mineralogies of biofilms A and B after application of MDSEP were (1) the loss of gypsum, biotite, and chlinochlore after F1; (2) the appearance of Fe-minerals phases other than jarosite after F1 (hematite, magnetite, Fe-Ox-hydrate); (3) replacement of jarosite by hematite, as the main mineralogical component of the biofilms after F2; and (4) dissolution of all detectable Fe-mineral phases after F3 (Table 2.7).

The loss of gypsum, biotite and chlinochlore after F1, is consistent with the high solubility of gypsum (Morel and Hering, 1993) and the weathering of biotite and chlinochlore, $[(Mg^{2+},Fe^{2+})_5(Si_3Al)O_{10}(OH)_8]$. As introduced earlier, (see 2.6.2) trace metals can be sorbed to biotite and weathering of this mineral is a potential source for trace metals in this fraction. The appearance of hematite, magnetite and Fe-Ox-hydrate after F1 could have two sources. The first is that dissolution of gypsum results in a greater relative mass of these minerals in the biofilm sample, and detection by XRD. Decomposition of some of the natural jarosite could also have occurred. The formation of Fe-Ox-hydrate is consistent with the decomposition of jarosite at alkaline pH values (Dutrizac and Jambor, 2000). Alteration of the synthetic K-jarosite did not occur until heat was applied in F2; however, the reactivities of the natural jarosite and the synthetic K-jarosites may differ. Jarosite does remain the major crystalline Fe phase in the samples after F1, indicating that if alteration of jarosite occurs, it is not complete. Consistent with the decomposition of synthetic K-jarosite to hematite in F2, hematite becomes the main crystalline component of the natural biofilm samples following F2 (Table 2.7). After F3, all detectable Fe mineral phases in the biofilm samples were dissolved. (Fe mineral phases have to be crystalline and greater than ~5% by mass of the sample to be detected). This result further suggests that natural jarosite, as well as natural hematite may be more reactive than their synthetic analogs as neither synthetic K-jarosite nor hematite was fully dissolved by MDSEP until application of F4. Clearly, application of MDSEP to the

Table 2.7. Bulk mineralogical composition of ARD biofilms after defined extraction steps[a].

Biofilm Sample	Phases Identified by XRD[a]		
	Main	**Minor**	**Trace**
A (May 31; 15:00)			
F1	Jarosite	Albite, Quartz	Hematite
F2	Hematite	Quartz, Jarosite, Albite	Fe-Ox-hydrate
F3	Albite, Quartz	Actinolite	-
F4	Albite, Quartz	Actinolite	-
B (June 21; 16:30)			
F1	Jarosite	Albite, Quartz	Magnetite
F2	Hematite	Fe-Ox-hydrate	Quartz, Albite
F3	Albite, Quartz	Actinolite	-
F4	Albite, Quartz	-	Actinolite

[a] XRD analysis was performed on air-dried homogenized samples

natural biofilms has resulted in complex alterations to Fe minerals. It should be noted that these alterations are likely to occur with other extraction protocols also as most microwave and conventional extraction schemes apply alkaline solutions for release of exchangeable metals and heat for extraction of metals bound to Fe/Mn oxyhydroxides phases.

XRD analysis of the solid residue after extraction steps F1 through F4 of the MDSEP also indicate that synthetic minerals, precipitated under abiotic conditions, are not necessarily an accurate representation of natural mineral behaviour. Jarosite associated with the biofilm samples appears to be decomposed more easily than the synthetic K-jarosite. Sasaki and Konno (2000) examined the crystallinity and morphology of jarosite samples precipitated under both abiotic conditions and in the presence of the iron-oxidizing bacterium *Acidothiobacillus ferrooxidans*. The abiotic and authigenic minerals were both crystalline and cannot be differentiated by XRD. The morphologies of the minerals, as visualized with Scanning Electron Microscopy, did however differ. Jarosite precipitated abiotically had small (~1 μm) crystals of irregular shape while jarosite crystals formed in the presence of bacteria were submicroscopic and formed aggregates with large surface areas. The authors suggested that the organic matrix constrained the morphology of the jarosite to the smaller submicroscopic particles. The surface of a hydrated biofilm sample collected as part of this study (biofilm B, June 21, 2001; 16:30) was visualized using Environmental Scanning Electron Microscopy (ESEM; ESEM system 2020, Version 3.53, FEI company). The surface was characterized by the organic matrix and by distinct zones of mineralization (Fig 2.9a,b). Included in the elemental composition of this sample were Fe, S, O, Ni, C, P, K and Ca (Figure 2.9c, ESEM-associated Energy Dispersive X-ray Spectroscopy; PGT IMIX system, prism digital detector). The elemental distribution of Fe, S, O and K^+, and the visual similarity between the aggregates at the biofilm surface (Figure 2.9b) and those of authigenic jarosite, suggest that jarosite is being precipitated in association with the organic matrix of the biofilm at the ARD site. These aggregated particles of high surface area are likely to be more reactive than synthetic jarosite minerals. These results also make the broader point that caution must be taken when interpreting natural system behaviour based on laboratory experimentation and interpretation with synthetic analogues.

Trace Metal Partitioning in the Natural Biofilm Samples

Total metal concentrations extracted by MDSEP varied substantially between three biofilm samples collected over a 24-hour period (Table 2.8), indicating that the biofilms exhibit highly dynamic metal retention behaviour. Two important solid fractions were identified for the metals analyzed: the amorphous oxyhydroxide fraction for all elements and the organic fraction for Ni and Co. Combined, over 70% of the biofilm total trace metal content is associated with the amorphous oxyhydroxide and the organic/sulphides fractions (Table 2.9). Further discussion of these biofilm metal retention trends is part of Chapter 3 (see 3.3.1.) and will not be discussed further here.

The partial weathering of biotite was identified as a potential process for trace metal release to solution in F1. Both Co and Cr concentrations were below detection in

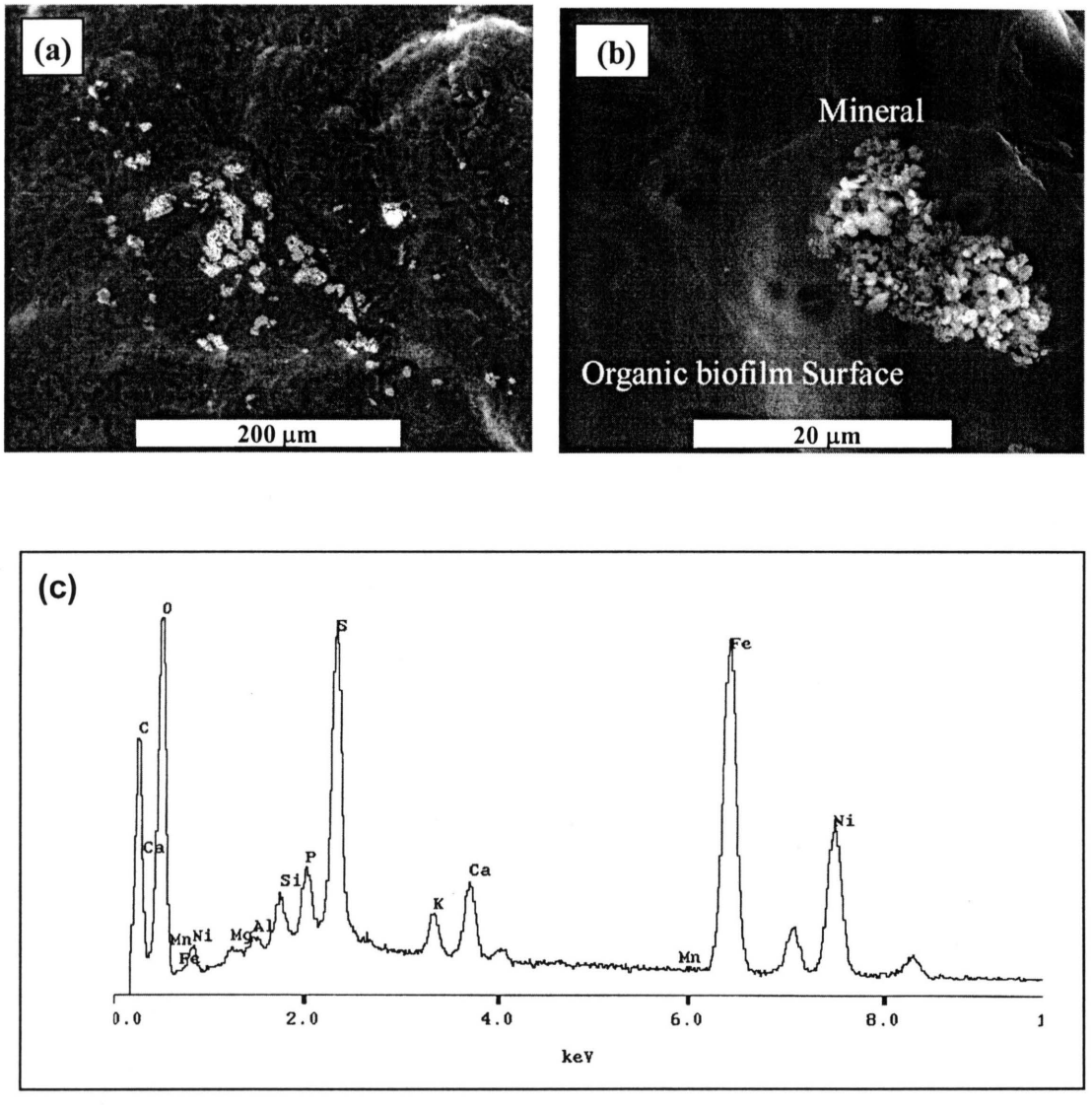

Figure 2.9: Environmental Scanning Electron Microscopic images of the hydrated biofilm surface (June 21, 2001, 16:30). Evident heterogeneity and complexity in surface structure and areas of associated minerals occurred. The microtopography of the biofilm surface revealed distinct structures and zones of mineralization (a). Typically minerals were observed to be extremely small, amorphous, and occurred in clusters in localized regions (b). ESEM-associated EDS analysis indicated that Fe, S, Ni, and O were major elements associated with the biofilm surface(c).

F1 for the biofilm samples analyzed (Table 2.9). Ni concentrations extracted in F1 corresponded to 2-16% of the total Ni extracted (Table 2.9). Partial weathering of biotite may thus be a source of Ni in these extractions; however, it is not possible to distinguish that particular mechanism from true surface exchangeable metals associated with the biofilms. This fraction was not a significant sink for any of the trace metals analyzed, as would be expected in the high ionic strength low pH conditions of the shallow ARD seepage streams.

XRD analysis of the natural biofilm samples indicated that all detectable Fe-mineral phases were dissolved in F3. Consistent with this result, between 84-93% of the total Fe extracted from the biofilms was extracted in F3 (Table 2.9). Alterations to jarosite associated with the biofilm samples began in F1 (possible formation of Fe-Ox-hydrate) and continued in F2 (decomposition to hematite). If trace metals were associated with jarosite in the natural biofilm samples, the decomposition of jarosite early in the extraction scheme would have implications for the interpretation of metal partitioning by the MDSEP. Three processes could potentially result from the alteration of jarosite: (1) release of trace metals to solution in F1 and F2, (2) re-sorption of trace metals to the Fe oxyhydroxides formed, and (3) re-sorption of trace metals to the other important solid fraction, the organic matrix. Co and Cr concentrations were below detection in F1 and F2. Quantifiable amounts of Ni were extracted in these fractions, representing as much as 24% of the Ni extracted (Table 2.9). It is possible that Ni was sorbed initially to jarosite and was released during the transformation of jarosite. However, as discussed above, there are other possible sources of Ni in these fractions (exchangeable and Ni sorbed to biotite). In F3, trace metal and Fe concentrations were not significantly correlated ($R^2 < 0.2$, $p \leq 0.05$; linear regression was done on log-transformed data using S-PLUS, MathSoft Inc., 2000). However, a strong positive correlation was observed for trace metal and Mn concentrations in F3 ($R^2>0.70$). These results suggest that Mn oxyhydroxides rather than Fe minerals are likely sequestering trace metals in these biofilms. Mn oxyhydroxides are known to be more reactive at low pH values compared to Fe oxyhydroxides (Tessier et al., 1996; Tonkin et al., 2004). An important role for biofilm-associated Mn oxyhydroxides in metal sequestration is an interesting result in this ARD system, given the highly unlikely formation of Mn oxyhydroxides at acidic pH values without microbial catalysis. These results are discussed in greater depth in Chapter 3.

Finally, trace metals could have been re-sorbed to the organic fraction (F5). Cr concentrations were below detection in this fraction and Ni and Co concentrations in F5 were not significantly correlated to Fe concentrations extracted in F3 ($R^2<0.3$). Thus, while it is impossible to rule out the possibility that metals are released in association with dissolution and alterations of Fe minerals through the extraction protocol, the lack of any trends between trace metal and Fe concentrations in any of the relevant fraction does not suggest that Fe minerals play a significant role in metal sequestration in these biofilms. Further, only the amorphous fraction (F3) and the organics/sulphides (F5) were important for metal retention in these samples. The significant correlation specifically between Mn and trace metal concentrations in the amorphous oxyhydroxides fraction

Table 2.8. Total metal concentrations in three biofilm samples and the standard reference material.

Metal Concentration ($\mu molg^{-1}$)[a]	Biofilm Material			Bovine Liver: Reference / Measured values ($\mu molg^{-1}$, as reported)
	B (June 21; 16:30)	C (June 21; 20:00)	D (June 22, 11:00)	
Fe ($mmolg^{-1}$)	3.69 ± 0.55	5.16 ± 0.40	4.10 ± 0.32	3.3 ± 0.3 / 3.1 ± 0.5
Mn ($\mu molg^{-1}$)	0.88 ± 0.04	1.85 ± 0.37	0.73 ± 0.17	0.19 ± 0.03 / 0.22 ± 0.03
Ni ($\mu molg^{-1}$)	3.48 ± 0.5	5.37 ± 0.56	1.95 ± 0.52	Not reported
Co ($\mu molg^{-1}$)	0.13 ± 0.03	0.18 ± 0.02	0.06 ± 0.01	$4.2*10^{-3}$ / $(4.4 \pm 0.3)*10^{-3}$
Cr ($\mu molg^{-1}$)	0.24 ± 0.03	0.40 ± 0.05	0.23 ± 0.02	Not reported

[a] Total metal concentrations are sums of metal concentrations in F1-F6.

Table 2.9. Percent of total metal partitioned to the biofilm in each fraction F1-F6.

Fraction	Percentage of Total Biofilm Metal Concentration				
	Fe	Mn	Ni[a]	Co[a]	Cr[a]
F1	b.d.	4-7	2-16	b.d.	b.d.
F2	b.d.	3-10	2-10	b.d.	b.d.
F3	84-93	40-49	25-52	21-43	77-87
F4	2 -8	b.d.-14	1.4-10	b.d.	b.d.
F5	<1-7	3-11	24-60	42-65	b.d.
F6	1-4	27 - 47	1-3	b.d.	12-22

[a] Trace metals (Ni, Co, Cu) were dominantly associated with two fractions, the amorphous oxyhydroxide (F3) and organic/sulphide fractions (F5).

further supports the contention that Fe mineral phases are not important for metal geochemical partitioning in this system.

2.8. Conclusions

In conclusion, this chapter outlined the development of a rapid technique for the analysis of solid-phase metal partitioning within ARD-impacted biofilms, which provides advantages in time of analyses for such sensitive organic matrices. This method, MDSEP, was determined to be suitable for the analysis of metal partitioning within natural biofilm samples examined in subsequent detail in this thesis. The MDSEP scheme developed has six extraction steps: exchangeable, carbonates, amorphous Fe/Mn oxyhydroxides, crystalline Fe/Mn oxyhydroxides, organic/sulphides and residual. These reagents and conditions used in the each of the six extraction steps were chosen on the basis of published extraction protocols and upon consideration of the likely mineralogical components of ARD biofilms.

One important conclusion from this work is that synthetic analogs of natural solids may not reflect the inherent reactivity of their natural counterparts. Thus, even the most carefully developed extraction protocol based on synthetic solids may not truly reflect the behaviour of natural solids. While there is utility in using synthetic solids for assessment of the selectivity of reagents, it should be noted that these solids represent a "conservative" estimate of the natural solids. The morphology of jarosite associated with the natural biofilms is at least visually consistent with authigenic jarosite (Sasaki and Konno, 2000) and it is the differing particle size and morphology that likely imparts different reactivities to the biofilm-associated and synthetic jarosites.

CHAPTER 3: BIOFILM HYDROUS MANGANESE OXIDE FORMATION AND ASSOCIATED METAL DYNAMICS IN ACID ROCK DRAINAGE

3.1. Introduction

Microbes have been implicated in all steps of environmental metal cycling, through both direct and indirect mechanisms, particularly through their influence on precipitation-dissolution reactions of metal reactive minerals such as hydrous Fe and Mn oxyhydroxides. Active redox cycling of Fe and Mn occurs through bacterially mediated reduction of Fe(III) and Mn(IV) hydrous oxides (HFO, HMO) by dissimilatory Fe and Mn-reducing bacteria (Nealson and Saffarini, 1994), and bacterially catalyzed oxidation of Fe(II) and Mn(II) (Nealson et al., 1989; Tebo et al., 1997). These direct mechanisms can result in both the immobilization of trace metals associated with HFO and HMO formation, well-established metal sorbents (Tessier et al., 1996; Nelson et al., 1999a; Fuller and Harvey, 2000), as well as metal release associated with the reductive dissolution of these minerals. Bacteria can also affect trace metal mobility through sorption/precipitation reactions at cell and cellular polysaccharide exudate surfaces (Fein et al., 1997; Warren and Ferris, 1998). Further, microbial metabolic activity can create geochemical microenvironments within the cell's immediate vicinity, which differ from bulk system conditions.

Biofilms are bacterial communities of high cell density that are characterized by dynamic, physico-chemical gradients resulting from stratified metabolic function. As such, they provide an ideal system in which to examine the linkages between metal behaviour and microbial activity. Within the biofilm geochemical microenvironment, conditions may be created which may immobilize trace metals through the formation of sparingly soluble precipitates and/or redox transformations (e.g. Cr(VI) to Cr(III); Smith and Gadd, 2000), or alternatively, increase their solubility. While the exact mechanisms by which specific bacterial strains influence trace metal cycling has been the subject of much laboratory based research (e.g. Kashefi and Lovley, 2000; Templeton et al., 2003), quantitative field investigations into the extent of microbial importance for metal dynamics, as well as the types of reactions and their associated controls (e.g. mineral formation and dissolution, geochemical microenvironments of pH and redox) relevant for metal fate are far fewer. Such investigations are needed to evaluate if the complex microbial communities found in natural systems can significantly impact metal behaviour, and if so, through which processes (Warren and Kaufman, 2003). Freshwaters impacted by acid-rock drainage (ARD) are ideal systems for the elucidation of microbial

impact on trace metal cycling, as they exhibit high dissolved metal loads, low pH (2-4; e.g. Bigham et al., 1992) and extant microbial communities (Stumm and Morgan, 1995; Edwards et al., 1999). Further, within ARD-impacted environments, microbial metabolic activity may particularly influence important reactive solids for metals, such as HFO and HMO, as rates of Fe(II) and especially Mn(II) oxidation are slow at low pH without microbial catalysis. While the essential role of microbially-catalyzed oxidation of Fe(II) and consequent formation of iron oxyhydroxides in ARD environments is well documented (e.g. Bigham et al., 1992), evidence consistent with biogenic formation of HMO in ARD-impacted streams is also beginning to emerge (Robbins et al., 1999; Kay et al., 2001). Associated with the formation of both HFO and HMO in these environments, has been enhanced uptake of trace metals, including Ni and Co (Lawrence et al., 1998b; Fuller and Harvey, 2000).

Our objectives in this field investigation were to quantitatively characterize: (1) biofilm metal (Fe, Mn, Ni, Co and Cr) accumulation, (2) key biofilm metal sorbents, and (3) the controls for biofilm metal sequestration processes, over seasonal and diel timescales, within shallow ARD-associated tailings stream biofilms.

3.2. Materials and Methods

3.2.1. Site Description / Sampling Protocol

The study site, located at the Falconbridge Strathcona Nickel Mine, in Onaping, Ontario, Canada (Lat. 46°39'18.1", Long. 81°18'58.3") consists of shallow seepage streams which flow over oxidized tailings deposits (See 2.1.). The sampling protocol was designed to investigate diel and seasonal trends in biofilm and water column metal loads and geochemistry. In situ measurements and sample collection occurred over four, two-day sampling periods in 2001: June 21-22, July 4-5, August 8-9, and September 5-6 (Table 2.2). Depending on the month, a minimum of one set of complete samples was collected concurrent with water and biofilm geochemical characterization between 15:00-21:00 on the first day, as well as again the following morning between 7:00-11:00. Typically two to three complete sets of samples and geochemical characterization were taken over the total twenty-four hour period. Geochemical characterization and sample collection included: 1) in situ profiling of geochemical conditions within the biofilm using microelectrodes (pH and O_2); 2) characterization of overlying water column physico-chemical parameters concomitant with profiling; and 3) collection of biofilm samples for solid-phase and water column samples for dissolved-phase metal analyses, immediately following profiling. Water column parameters measured included temperature, pH, dissolved oxygen concentrations (mg/L and % saturation), and specific conductivity (DataSonde-Surveyor 4A, Hydrolab Corporation, TX).

3.2.2. Biofilm Geochemistry

Dissolved oxygen (DO) and pH profiles were recorded in parallel using the submersible, remotely controlled MiniProfiler MP4 microelectrode system (Unisense Corp., Denmark; DO: Clark-type microelectrode; type OX-50; outer-tip dimensions 40-60 μm; 90% response time < 5s; linear response from 0-1 atm pO_2; pH: glass combination microelectrode; type PH-10, outer tip dimensions, 10-19 μm; length of

sensitive pH glass, 100-150 μm; 90% response time < 20s; linear response from pH 4-10; reference: simple Ag/AgCl open-ended electrode). Overlying water DO values were measured with the microelectrode (mA) and calibrated against those measured with the Hydrolab. The pH microelectrode was calibrated using a three-point calibration of pH 2, 4 and 7 buffers. Data collection programs were user-defined; pH and DO measurements were made on a coarse scale (≤ 1mm increments) in the overlying water and at a fine scale (25μM increments) at the biofilm-water interface and within the oxygenated zone of the biofilm. At each successive depth, ten measurements were recorded for DO and pH electrodes following a ten second microelectrode equilibration time. The coefficient of variation for each set of measurements did not exceed 10% for DO or 1% for pH. Using this collection program, each profile of geochemical conditions within the biofilm (from overlying water column to anoxic conditions) required approximately 1.5 hours. Forward and reverse profiles indicated that the electrodes did not disrupt the geochemical conditions within the biofilm, i.e. hysteresis did not occur, (data not shown). Thus, the recorded profiles can be considered as representative of in situ geochemical conditions.

Measured DO concentration profiles were interpreted using PROFILE software (version 1.0, Peter Berg, University of Virginia). This program returns the simplest set of net O_2 production/consumption zones that best reproduces the measured DO profile (lease squares fit, statistical F-testing, $P < 0.05$, vertical transport was restricted to molecular diffusion). Biofilm porosity was assigned a value of 0.9 (representing an upper porosity limit in microbial mats; Canfield and DesMarais, 1993), and was assumed constant with depth.

3.2.3. Dissolved- and solid-phase metal analyses

Overlying water samples for dissolved-phase metal analysis were collected immediately above the biofilm (1-2 cm downstream from the electrodes and 0.5 cm above the biofilm water interface). Water samples were collected using acid-washed syringes, passed serially through 0.45 and 0.2 μm syringe filters, and subsequently acidified with HNO_3 to 0.2% v/v (OPTIMA HNO_3, Seastar Chemicals Inc., PA).
Dissolved metal reagent blanks, consisting of Milli-Q water, were transported to, filtered, and acidified at the sampling site. Samples were stored in the dark at 4°C until analysis.
Dissolved metal concentrations, $[M^{z+}]_D$, were quantified either by colorimetric analysis ($[Fe]_{total}$: FerroVer Method, see 2.5.1., Ultrospec 3000, Uv/Visible Spectrophotometer, Pharmacia Biotech, Cambridge, U.K.) or by inductively coupled plasma mass spectrometry, ICP-MS
(Mn, Ni, Co, and Cr: PerkinElmer SCIEX ELAN 6100, Woodbridge, ON, Canada).
Blank analysis indicated negligible contamination for all elements analyzed. Coefficients of variation of ICP-MS analyses averaged 1.6, 1.7, 2.3, and 1.2 % for Mn, Ni, Co and Cr respectively. Measured concentrations significantly exceeded instrument detection limits (0.5 μgL^{-1}), with the exception of Cr on August 9, 2001.

Biofilm samples were collected immediately following in situ profiling (see 2.2.). Solid-phase metal analysis of the biofilms occurred within forty-eight hours of sample collection. Traditionally, multi-step sequential extraction procedures have been employed to characterize metal associations within complex natural samples (Tessier et

study, a sequential extraction technique involving microwave digestion was developed based on the same conceptual framework (MDSEP, Chapter 2). Biofilm samples were not dried or homogenized prior to digestion. Biofilm-associated metals were partitioned into six operationally defined solid matrix fractions: the exchangeable (loosely-bound); carbonate; amorphous Fe/Mn hydrous oxyhydroxides (e.g. HFO, HMO, reducible); crystalline Fe/Mn oxyhydroxides (reducible); organic/sulphide (oxidizable) and residual fractions (Table 3.1). Samples vessels were cleaned for trace metal analysis by closed vessel acid reflux with ultrapure HNO_3. Pressure-release device mechanisms minimized evaporation and sample loss during digestion.

Mn, Ni, Co and Cr concentrations extracted in each biofilm fraction were quantified by ICP-MS. Total Fe extracted in each fraction was quantified by colorimetric analysis (as for dissolved $[Fe]_{total}$). Reagent blanks were included in each digestion assay. Matrix effects associated with ICP-MS were corrected by using an internal standard (Y^{89} in-line at 2 ppb) and matrix-matched standards. Biofilm total metal concentrations, $\{M^{z+}\}_T$, were determined by summing the individual concentrations in each of the six defined fractions. These totals were verified by separate total sample digestion in concentrated HNO_3. In addition, analytical accuracy during each run was assessed by the extraction of certified reference material (Bovine Liver, NIST, Standard Reference Material 1577b). The sum of the extracted concentrations of the reference material was within the certified range for all metals analyzed.

3.2.4. Biofilm Mineralogical and Organic Composition

Mean biofilm dry weights were determined by heating of triplicate biofilm samples at 80°C to constant weight. Mean bulk organic content of the biofilm samples was then determined by loss on ignition (%LOI, 550°C for 2 hours). X-ray Diffractometry was used to determine the bulk mineralogical composition of two air dried, homogenized biofilm samples (XRD: Siemen's D5005 X-ray diffractometer).

3.2.5. Statistical Analysis

All statistical analyses were performed using S-Plus (MathSoft Inc., 2000). Multiple linear regression (MLR) analysis was performed on untransformed data to identify key influencing variables for seasonal trends in metal concentrations within the overlying water, total biofilm, and individual biofilm fractions. The relevant variable identified by the MLR to explain the most variance was subsequently used in a linear regression analysis with the dependent variable of interest. Logarithmic transformation was performed on the data prior to linear regression analysis to improve normality and homoscedasticity of the data (Tabachnick and Fidell, 1983; Devore, 1995). Unless otherwise stated: 1) the number of observations for all dissolved and solid phase metal data was thirty; 2) the total number of in situ biofilm geochemical profiles was ten; and 3) the significance level applied to all statistical tests was $\alpha = 0.05$.

Table 3.1: Reagents and conditions for the six-step microwave digestion sequential extraction technique (MDSEP; Chapter 2). Biofilm samples were run in triplicate.

(Sequence) Fraction	Reagents	Conditions[a]
F1: Exchangeable	1M sodium acetate, pH 8.2 (with HOAc)	1h shaking, room temperature
F2: Carbonates	1M sodium acetate, pH 5.0 (with HOAc)	Microwave Program 1 (MP-1): Heat to 150°C over 8 minutes. Maintain temperature for 5 minutes. 30 minute cool-down.
F3: Reducible Amorphous Fe/Mn Oxyhydroxides	0.25 M Hydroxylamine hydrochloride in 0.25 M HCl.	MP-1
F4: Reducible Crystalline Fe/Mn Oxyhydroxides	1.0 M Hydroxylamine hydrochloride in 25% (v/v) acetic acid.	MP-1
F5: Oxidizable[b] Organics and Sulphides	3:2 ratio 30% H_2O_2: 0.02M HNO_3 + 1:4 ratio 3.2 M NH_3OAc:UPW.	MP-1
F6: Residual Resistate Minerals	Concentrated HNO_3	Microwave Program 2 (MP-2): Heat to 180°C over 20 minutes. Maintain temperature for 10 minutes. 45 minute cool-down.

[a] This scheme is based on a 40:1 ratio reagents-to-dry weight biofilm sample.

[b] A precautionary note: The oxidizable fraction involves addition of 30% peroxide to the samples; a vigorous exothermic reaction can be expected for samples with high organic content. Difficulties with this reaction and microwave heating have been noted (*23*). We avoided potential problems by adding an initial 4 mL of peroxide to the samples. The sample vessels were placed on a hot plate to initiate the oxidation reaction if the reaction was not immediate and vigorous. A further 11 mL of peroxide was added gradually to the samples to maintain the reaction, again, adding heat if necessary. Such a pre-treatment of the samples allows breakdown of the more labile organic matter before microwave heating is applied to the samples.

3.3. Results and Discussion

3.3.1. Stream and Biofilm Geochemistry

Stream

Geochemical conditions and metal loads in the seepage streams over the May - September sampling season reflect the extreme nature of this sampling site. The tailings streams were shallow (1.6 ± 1.0 cm), relatively warm (18 ± 4°C) and acidic (seasonal pH range: 3.51-3.72, Table 3.2). Water column DO concentrations were generally unsaturated (82 ± 18 %) with the lowest concentration being recorded in August (August 9, DO = 3.9 mg/L, 42% saturation; Table 3.2). On a diel basis, geochemical conditions within the overlying water column were highly variable. While pH did not show a clear variation with diel cycle, minimum temperatures and maximum DO concentrations (mg/L) were typically measured before 11:00 a.m. (Table 3.2).

Seasonal, mean overlying water dissolved metal concentrations ($[M^{z+}]_D$, 0.2 μm filtered) decreased in the order: Fe_{total} (5 mM) > Ni (500 μM) > Mn (60 μM) > Co (10 μM) > Cr (0.2 μM). These values are within one order of magnitude of dissolved metal concentrations measured in other low pH ARD-impacted freshwaters (Lawrence et al., 1998b; Scott et al., 2002; Tonkin et al., 2002). Dissolved Fe_{total}, Mn and Cr concentrations showed no evident seasonal trends (Figure 3.1), while $[Ni]_D$ and $[Co]_D$ decreased over the sampling season (Figure 3.1). Dissolved Mn concentrations, $[Mn]_D$, varied consistently with diel cycle in contrast to the other elements analyzed. $[Mn]_D$ recorded during afternoon hours (June 5, 16:30; July 4, 16:30; and Sept 5, 15:30) were significantly higher than those recorded the following morning (June 6, 11:00; July 5, 7:50; and Sept 6, 9:00; Figure 3.1). Diel fluctuations in Mn concentrations have been previously reported for circumneutral ARD-impacted streams. In contrast to our results, elevated nocturnal (18:00-6:00) $[Mn]_D$ were observed by Brick and Moore (1996), which was attributed to both nocturnal reductive dissolution of Mn oxyhydroxides in the bed sediments, as well as increased influx of hyporheic water associated with decreased evapotranspiration. In another study (Scott et al., 2002) diel fluctuations in $[Mn]_D$ were observed but no consistent diel trend was reported. The observed fluctuations in $[Mn]_D$ were attributed to hydrologic and biogeochemical processes occurring upstream of the sampling site. Our results, showing consistently elevated $[Mn]_D$ during afternoon hours, will be discussed subsequently and related to biofilm HMO dynamics.

No discernable trends between dissolved metal concentrations and water physicochemical parameters (pH, DO, temperature) within the seepage streams were observed.

Biofilm

Biofilm metal dynamics were element specific. Iron was the most abundant element in the biofilm. The mean seasonal biofilm total Fe concentration, $\{Fe\}_T$, of 4.8 $mmolg^{-1}$ (Table 3.3), represented approximately 28% of the total mass of the biofilm. However, in contrast to biofilm total metal concentrations of the other elements analyzed, $\{Fe\}_T$ remained invariant over the season (Figure 3.2). Seasonal mean concentrations for

Table 3.2: Seasonal and diel overlying water column and biofilm geochemical conditions. Depth-integrated O_2 production rates were calculated to permit comparison of activity across the season, as the thickness of the surface biofilm photosynthetic layer varied.

Date	Time	Overlying water column Temperature (°C)	pH			Dissolved Oxygen (mg/L)		Depth-integrated O_2 production ($nmolcm^{-2}s^{-1}$)	Depth of oxic/anoxic boundary (mm)
			Overlying water column	Biofilm/water interface	Oxic/anoxic boundary	Overlying water column	Biofilm/ water interface		
21- Jun	16:30	19.2	3.66	3.69	3.81	10	11.0	0.71	1.33
21-Jun	20:50	15.1	3.51	3.57	3.66	8.3	8.9	0.69	1.05
22-Jun	11:00	13.5	3.58	3.65	3.72	10.2	19.1	4.52	1.63
4- Jul	16:30	22.0	3.72	3.74	4.54	8.3	11.2	1.02	1.13
5-Jul	7:50	10.3	3.65	3.68	3.75	9.8	12.6	2.80	0.95
8- Aug	20:00	20.8	3.59	3.59	3.66	6.5	5.9	1.22	0.77
9- Aug	7:00	19.0	3.62	3.59	3.58	3.9	2.7	0.43	1.05
5-Sept	15:30	25.2	3.53	3.99	4.59	6.5	4.7	0.12	2.38
6-Sept	9:00	17.1	3.66	3.83	3.86	6.7	9.4	0.58	1.33
6-Sept	11:00	21.4	3.69	3.69	3.68	7.3	13.7	1.25	1.50

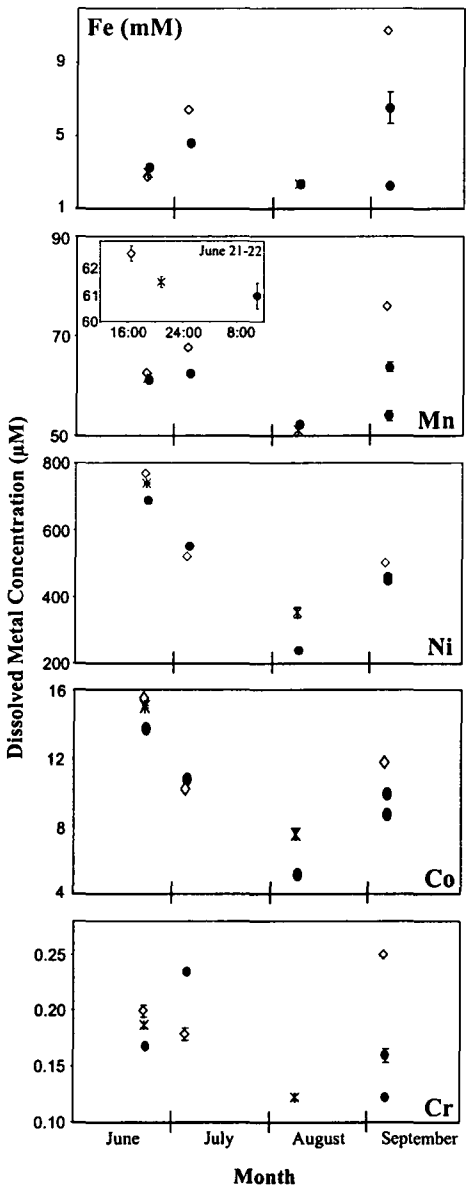

FIGURE 3.1. Seasonal (June-September 2001) dissolved metal concentrations $[M^{z+}]_D$ for the overlying water column for each of Fe, Mn, Ni, Co and Cr (elements indicated in each panel). Afternoon (15:00 – 17:00, ◊), evening (20:00 – 21:00, *), and morning (7:00 – 11:00, •) concentrations are indicated for each element for each sampling period. $[Mn]_D$ was the only metal to show a consistent diel trend of elevated afternoon concentrations compared to later evening or subsequent morning sampling (see June (inset panel), July, and September sampling periods for Mn). Mean ± standard error values are shown (n = 3).

the other elements decreased in the order: $\{Ni\}_T$ (13.5 $\mu molg^{-1}$) > $\{Mn\}_T$ (1.88 $\mu molg^{-1}$) > $\{Cr\}_T$ (0.49 $\mu molg^{-1}$) > $\{Co\}_T$ (0.37 $\mu molg^{-1}$) (Table 3.3), and increased significantly over the season (Figure 3.2). $\{Ni\}_T$ and $\{Co\}_T$ were significantly correlated (R^2 = 0.99) and both increased approximately six-fold from June to September (Ni: 3.60 to 25.70 $\mu molg^{-1}$; Co: 0.12 to 0.68 $\mu molg^{-1}$). Biofilm $\{Mn\}_T$ and $\{Cr\}_T$ were also strongly positively correlated (R^2=0.91), and doubled in their biofilm concentrations from June to September (Mn: 1.16 to 2.68 $\mu molg^{-1}$; Cr: 0.29 to 0.65 $\mu molg^{-1}$; Table 3.3). Total biofilm concentrations of all elements analyzed were not correlated with either their respective overlying water solution concentrations or with overlying water column pH. Mean seasonal distribution coefficients (K_d, Lkg^{-1}:$\{M^{z+}\}$solid / $[M^{z+}]$dissolved; 15) indicated substantive differences in relative metal affinities for the biofilm. K_d values for Fe (Log K_d 3.1) and Cr (Log K_d 3.4) were two orders of magnitude above those for Mn, Ni, and Co (Log K_d 1.4, 1.3 and 1.5, respectively; Table 3.3). A paucity of reported literature K_d values for either ARD or biofilm environments preclude direct comparison to other systems. However, the observed element trends are consistent with those reported in the literature. For instance, lower partitioning of metals between biofilms and bulk solution has been reported in acidic systems compared to circumneutral systems (Ferris et al., 1989), where K_d values of 10^2-10^3 for Mn and Cr and 10^5 for Co have been measured (Ferris et al., 1999). Further, K_d values of ~10^2 have been reported for Ni in pH 4.0 soils (Sauvé et al.; 2000).

Biofilm Reactive Solid Phases

Biofilms represent heterogeneous matrices variably composed of associated minerals and biominerals, as well as the organic constituents, i.e., bacterial cells and associated extracellular material, of the biofilm itself. These components are differentially reactive, display differing affinities for specific elements and scavenge metals through a variety of processes with differing controls. Characterizing which biofilm solid phases are involved in metal retention through sequential extraction provides insight into likely processes and associated controls. Results indicated that two biofilm solid phases were consistently important for metal retention: the amorphous oxyhydroxide fraction (all metals) and the organic/sulphides fraction (Ni and Co only) (Figure 3.3). Fe, Cr, and Mn were concentrated in the amorphous oxyhydroxide fraction (>80%, >63% and >45%, respectively), while greater than 80% of the total biofilm Ni and Co were sequestered in the amorphous oxyhydroxides and organic/sulphides fractions of the biofilm. Approximately 20-30% of total biofilm Mn and Cr concentrations were associated with the residual fraction (Figure 3.3). In both cases, residual associated concentrations were invariant over the sampling season (Mn: 0.66 ± 0.01 $\mu molg^{-1}$; Cr: 0.15 ± 0.00 $\mu molg^{-1}$), consistent with their association with refractory mineral phases that are typically not dynamic under ambient environmental conditions.

In this study, metals extracted in the organic/sulphides fraction are considered to be associated with organics rather than discrete sulphide minerals. Biofilm samples consisted of only the surficial 1-2 mm of the stream - tailings interface. Bulk XRD analysis of biofilm samples supports this contention, identifying the main crystalline components of the biofilm as silicate (quartz and albite) and oxidized sulphate minerals

Table 3.3: Biofilm total metal concentrations (Fe: $mmolg^{-1}g$; Mn, Ni, Co, Cr: $\mu molg^{-1}$), Partition Coefficients ($K_d = \{M^{z+}\}_{solid} / [M^{z+}]_{dissolved}$, Lkg^{-1}), and biofilm organic matter content (percent loss on ignition; %LOI)[a]

Period	% LOI	Fe	Mn	Ni	Co	Cr
		Biofilm Total Metal Concentration				
June	20.1 ± 5	4.3 ± 0.8	1.16 ± 0.6	3.6 ± 1.7	0.12 ± 0.1	0.29 ± 0.1
September	13.8 ± 2	4.7 ± 1.4	2.68 ± 0.6	25.7 ± 9.1	0.68 ± 0.2	0.65 ± 0.1
Seasonal	16.2 ± 4	4.8 ± 1.0	1.88 ± 0.8	13.5 ± 10.3	0.37 ± 0.3	0.49 ± 0.1
				Log K_d values		
June		3.2 ± 0.1	1.2 ± 0.2	0.7 ± 0.2	0.9 ± 0.2	3.2 ± 0.1
September		3.0 ± 0.2	1.7 ± 0.0	1.7 ± 0.1	1.8 ± 0.1	3.7 ± 0.1
Seasonal		3.1 ± 1.4	1.4 ± 0.2	1.3 ± 0.5	1.5 ± 0.4	3.4 ± 0.2

[a] Biofilm total metal concentrations and calculated K_d values increased seasonally for all elements except Fe. Values shown for June and September are means ± standard deviation (n = 9). Seasonal means are calculated from all four sampling periods (n = 30). Total concentrations were calculated by summing concentrations in each of the six sequential extraction steps.

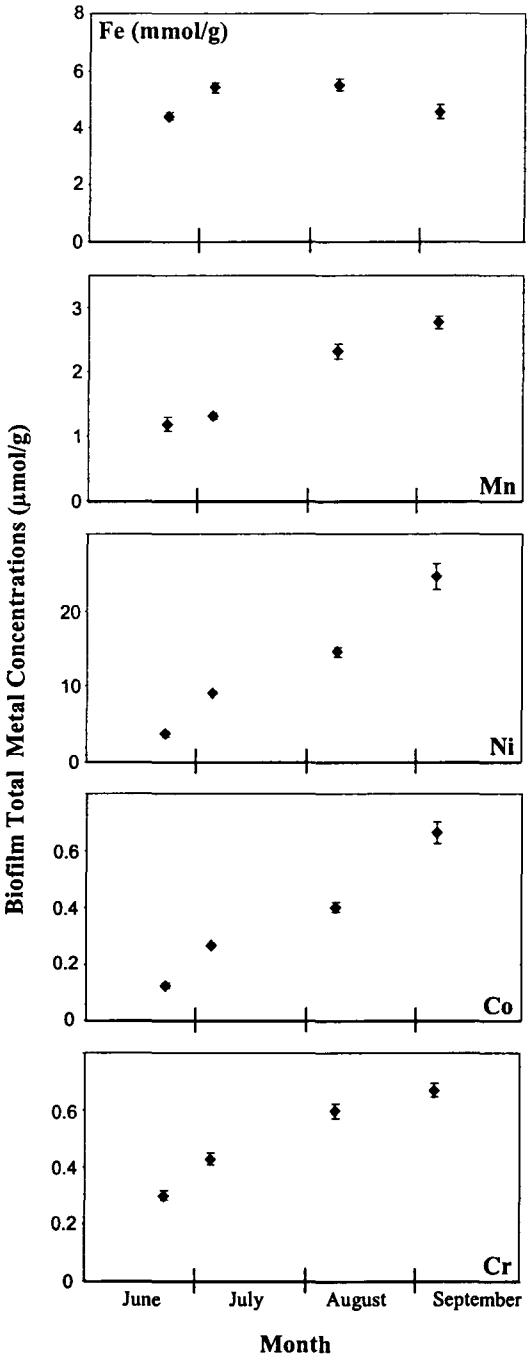

FIGURE 3.2. Biofilm total metal concentrations $\{M^{z+}\}_T$, as determined by the sum of sequential extraction steps (see Table 1) over the sampling season. A seasonal increase in biofilm total metal content was observed for all metals, except $\{Fe\}_T$. Mean monthly values ± standard error are shown (n = 6 or 9)

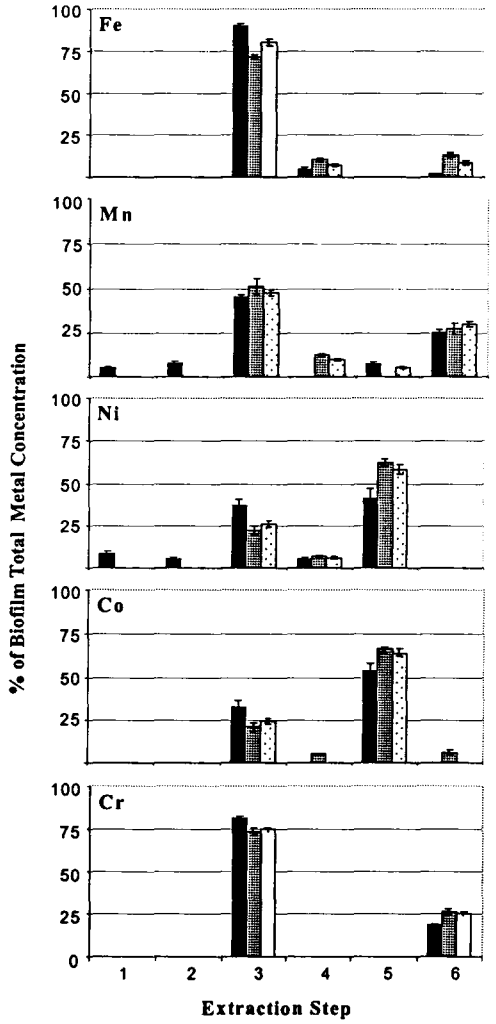

FIGURE 3.3. The relative proportion observed in each of six extraction steps of the biofilm total concentration for each metal. Mean proportions are shown for June (solid, n = 9), September (striped, n = 9), and over the sampling season (June – September, dotted, n = 30). Metals were sequentially extracted in six steps (Table 1): exchangeable (1), carbonates (2), amorphous oxyhydroxides (3), crystalline oxyhydroxides (4), organic/sulphides (5), and residual (6). For clarity, only those fractions representing more than 5% of the biofilm total metal concentration have been shown.

(jarosite, gypsum; data not shown). Ni and Co concentrations associated with the organic fraction, $\{Ni\}_{Org}$ and $\{Co\}_{Org}$, increased seasonally (Figure 3.3). However, increased $\{Ni\}_{Org}$ or $\{Co\}_{Org}$ were not correlated with bulk biofilm organic content (% LOI), which decreased over the season (Table 3.3). Hunt et al. (2001) have shown that microbial numbers, rather than organic content, correlate with biofilm-associated metals (Mn, Cr, Cd, Cu), which may explain the observed results here. However, Ni is known to sorb to both extracellular polymeric substances (EPS) as well as cell walls in biofilms (Wuertz et al., 2000), and exopolymer production is not a direct function of the cell numbers (Prochnow et al., 2001). Further, protocol for cell enumeration in heterogeneous mineral-microbe-organic matter mixtures, such as a biofilm, is not well established (dos Santos-Furtado and Casper, 2000). Quantification and characterization of those fractions of the bulk organic matter relevant for specific (Ni and Co) metal uptake were thus considered beyond the scope of this study.

3.3.2. Biofilm HMO

The amorphous oxyhydroxide fraction $\{M^{z+}\}_A$, was an important solid fraction for all elements analyzed, accounting for up to 75% of the total metal content in the biofilm (Figure 3.3). Fe concentrations in the amorphous oxyhydroxide fraction, $\{Fe\}_A$, remained relatively invariant over the sampling season, with a mean seasonal value of 3.9 $\pm$ 0.9 $mmolg^{-1}$. Trace metal concentrations associated with the amorphous oxyhydroxide fraction were highly significantly positively correlated with Mn concentrations in the amorphous oxyhydroxide fraction, $\{Mn\}_A$, ($R^2 \geq \{Fe\}_A$, Figure 3.4), but not to $\{Fe\}_A$ (data not shown). While the importance of Fe as a bulk constituent cannot be ruled out for overall reactive metal transport in this system, Fe oxyhydroxides (HFO) do not appear to play a significant role in biofilm metal scavenging. The respective surface reactivities of HFO and HMO would predict higher HMO scavenging abilities at the low pH values - MnO_2; of the biofilms. Cited pH_{zpc} values for HMO are substantially lower (e.g. ~3; Pretorius and Linder, 2001; Kennedy et al. 2004) than those for HFO (e.g. ~7.5 for ferrihydrite; Hendershot and Lavkulich, 1983).

While biofilm HMO concentrations increased seasonally, a strong diel trend in biofilm $\{Mn\}_A$ concentrations was also observed (Figure 3.5). Minimum HMO as indicated by $\{Mn\}_A$ concentrations, were recorded in late afternoon time periods (15:00-20:00) compared to other sampling times over a twenty four hour period (Figure 3.5a) while HMO maxima typically occurred in later evening or following morning sampling periods. $\{Mn\}_A$ diel trends were more readily apparent with more detailed twenty-four hour sampling carried out in June 2002, which showed rapid loss of $\{Mn\}_A$ between 11:00 and 15:00 to $\{Mn\}_A$ diel minima, and subsequent recovery to early morning maxima concentrations by 20:00 (Figure 3.5b). Daylight minima in biofilm HMO were correlated to increased water column dissolved Mn concentrations directly overlying the biofilms in the afternoon hours of June, July and September (2001, $p<0.05$, $R^2=0.78$, Figure 3.1). Under the low pH conditions of this system, these rates of HMO formation are consistent with microbial catalysis of Mn oxidation.

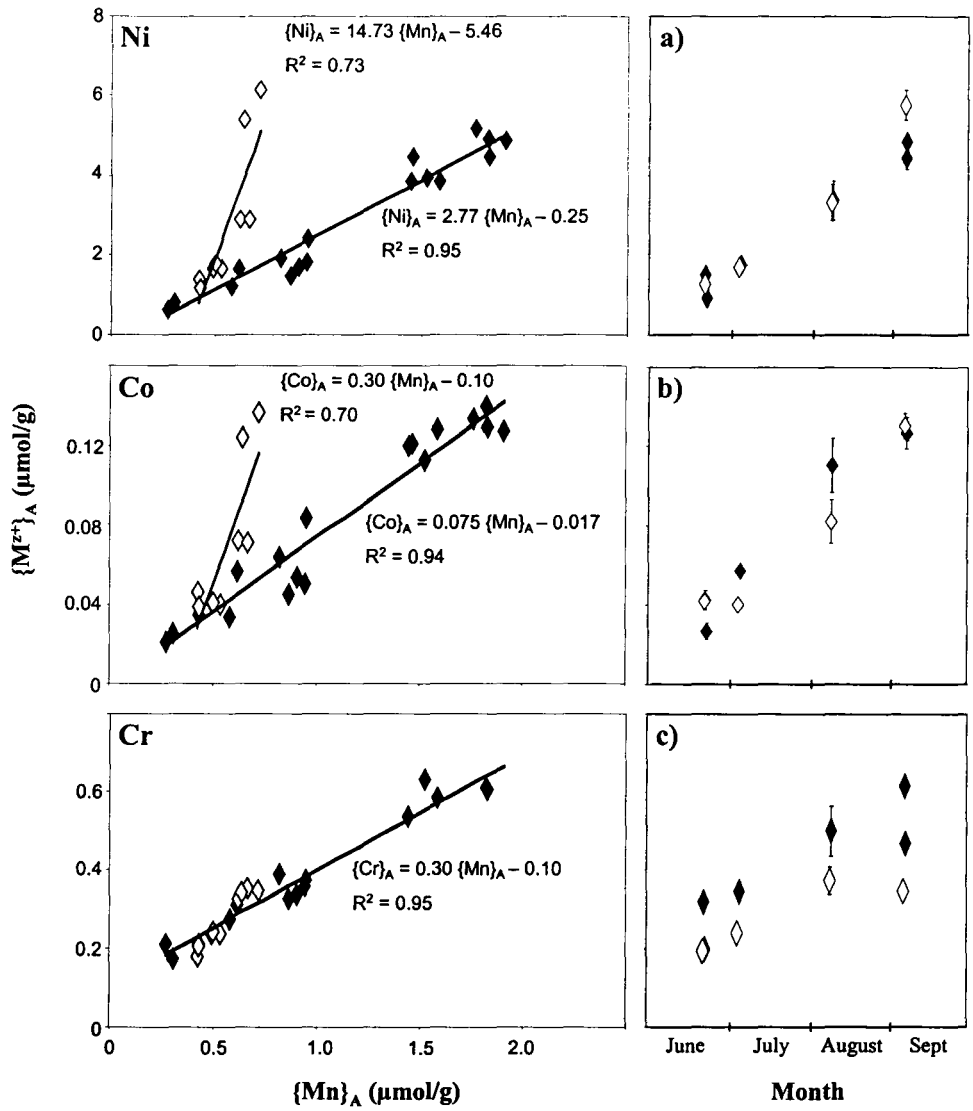

FIGURE 3.4. Biofilm $\{Ni\}_A$, $\{Co\}_A$, $\{Cr\}_A$ vs. $\{Mn\}_A$ (HMO; ◊ indicate late afternoon sampling times 15:00- 20:00; ♦ indicate either later evening or following morning sampling times). All three trace metal concentrations in the amorphous oxyhydroxide fraction were significantly positively correlated to HMO concentrations ($R^2 > 0.70$). Enriched $\{Ni\}_A$:$\{Mn\}_A$ and $\{Co\}_A$:$\{Mn\}_A$ ratios were observed for late afternoon samples (◊). Data points represent individual samples. Seasonal accumulations of Ni, Co, and Cr in the amorphous oxyhydroxide fraction for the same sampling times are shown in panels a – c, respectively. Mean ± standard error values are shown (n=3).

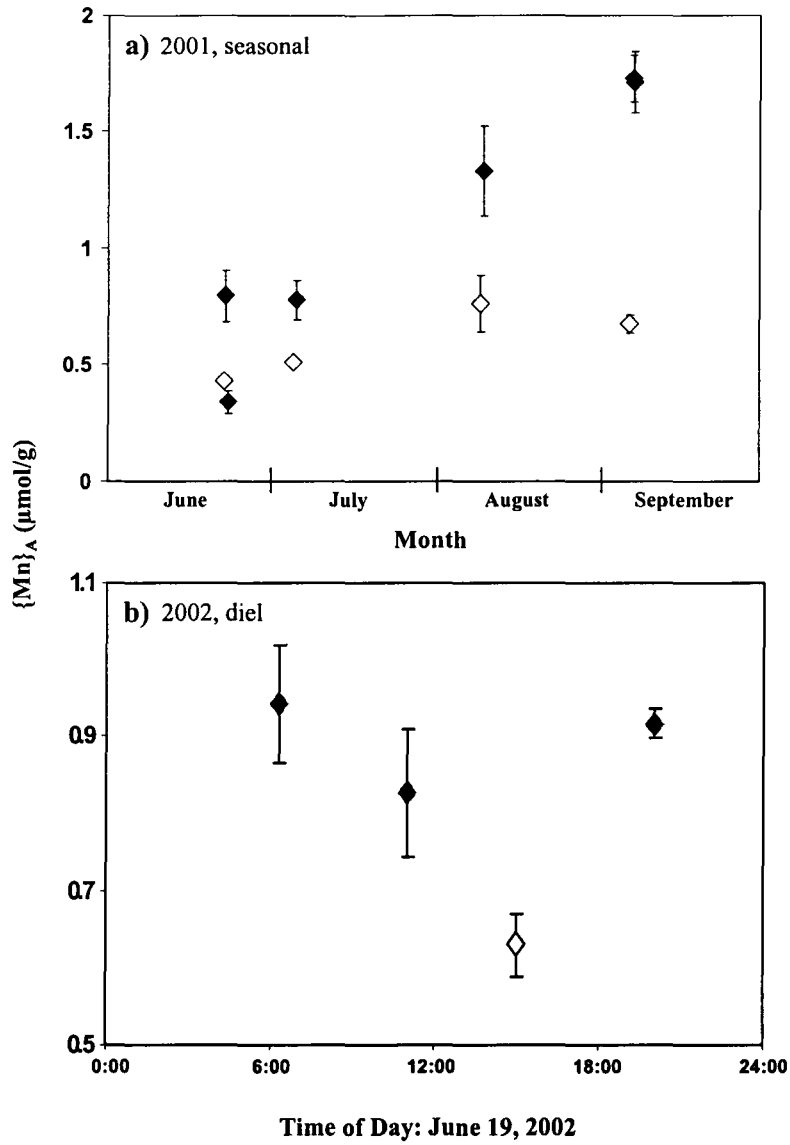

FIGURE 3.5. Biofilm HMO concentrations as estimated by $\{Mn\}_A$, for both the 2001 season (panel a) and over a diel (24 h) sampling period in 2002 (panel b). With one exception (panel A, June samples), minimum concentrations were always noted for late afternoon sampling times between 15:00 – 20:00 (◊), compared to either later evening or following morning sampling times (♦).

Biofilm O_2 and pH Dynamics

Several studies have indicated that both Mn(II) oxidation and associated precipitation of HMO, as well as reductive dissolution of HMO, occur at oxic-anoxic interfaces, reflecting the necessary redox gradients required for microbial catalysis of these reactions (Tipping, 1984; Nealson et al., 1988). Biofilm pH and O_2 profiles varied with depth within the biofilm (Figure 3.6), as well as with time (Table 3.2), reflecting a dynamic balance between oxygenic photosynthesis and respiration. Diel trends in biofilm O_2 and pH conditions are exemplified by in situ profiles measured on June 21 at 16:30 and the following morning, June 22 at 11:00 (Figure 3.6a,b). Typically oxygen production was highest before noon and decreased during afternoon periods; whilst pH typically increased from morning to afternoon sampling periods. Biofilm photosynthetic production of oxygen was observed over the entire sampling season (Table 3.2), but showed seasonal variation in activity rates. Depth integrated net oxygen production rates at the biofilm-water interface varied from 0.12 to 4.52 nmol $cm^{-2}s^{-1}$, with the highest rates recorded in June and July (Table 3.2). O_2 concentrations in the overlying water column and biofilm were also correlated (R^2=0.78), and indicated that a net O_2 flux from the biofilm to the overlying water typically occurred (Table 3.2). Associated with photosynthetic production of oxygen were elevated biofilm-water interface pH values in the afternoon (Figure 3.6a,b, Table 3.2). Whilst we have no mechanistic explanation for this time-delayed pH increase, it is consistent with other studies of microbial mats. Time-delays in photosynthesis-associated pH changes have also been noted in cyanobacterial mats from both high-iron content and hypersaline waters (Revsbech and Ward, 1984; Pierson et al., 1999).

Net oxygen production within the biofilm was generally constrained to the top 300 μm of the biofilm (Figure 3.6c,d). Below this depth, several zones of net oxygen consumption typically characterized the biofilms (Figure 3.6c,d). The magnitude of net oxygen consumption/production rates below the surficial primary production zone was depth dependent, indicating vertical variation in microbial activity and/or numbers.
Despite the temporally significant differences in the magnitude of O_2 production and consumption rates observed, anoxic conditions were always reached within 2.5 mm of the biofilm surface, and generally were reached within the first 1.6 mm (Table 3.2). Other studies of tailings environments have measured zones of greater oxic thickness below the tailings-water interface, e.g. 3-7 mm (Vigneault et al., 2001), and 11-17 mm (Holmström and Ölander, 2001), suggesting that in this system, microbial production may be more limited and/or consumption processes are of greater magnitude. On a diel basis, the vertical depth of the oxic-anoxic boundary migrated by as much as one mm (e.g. September 5th - 6th, 1.03 mm; Table 3.2). This vertical migration of the oxic/anoxic boundary creates a highly dynamic redox zone within the biofilm, where both oxic and anoxic conditions are experienced cyclically over a twenty-four hour period. Such shifts in redox conditions have the potential to impact formation and dissolution of redox sensitive minerals, as well as constraining microbial metabolic activity.

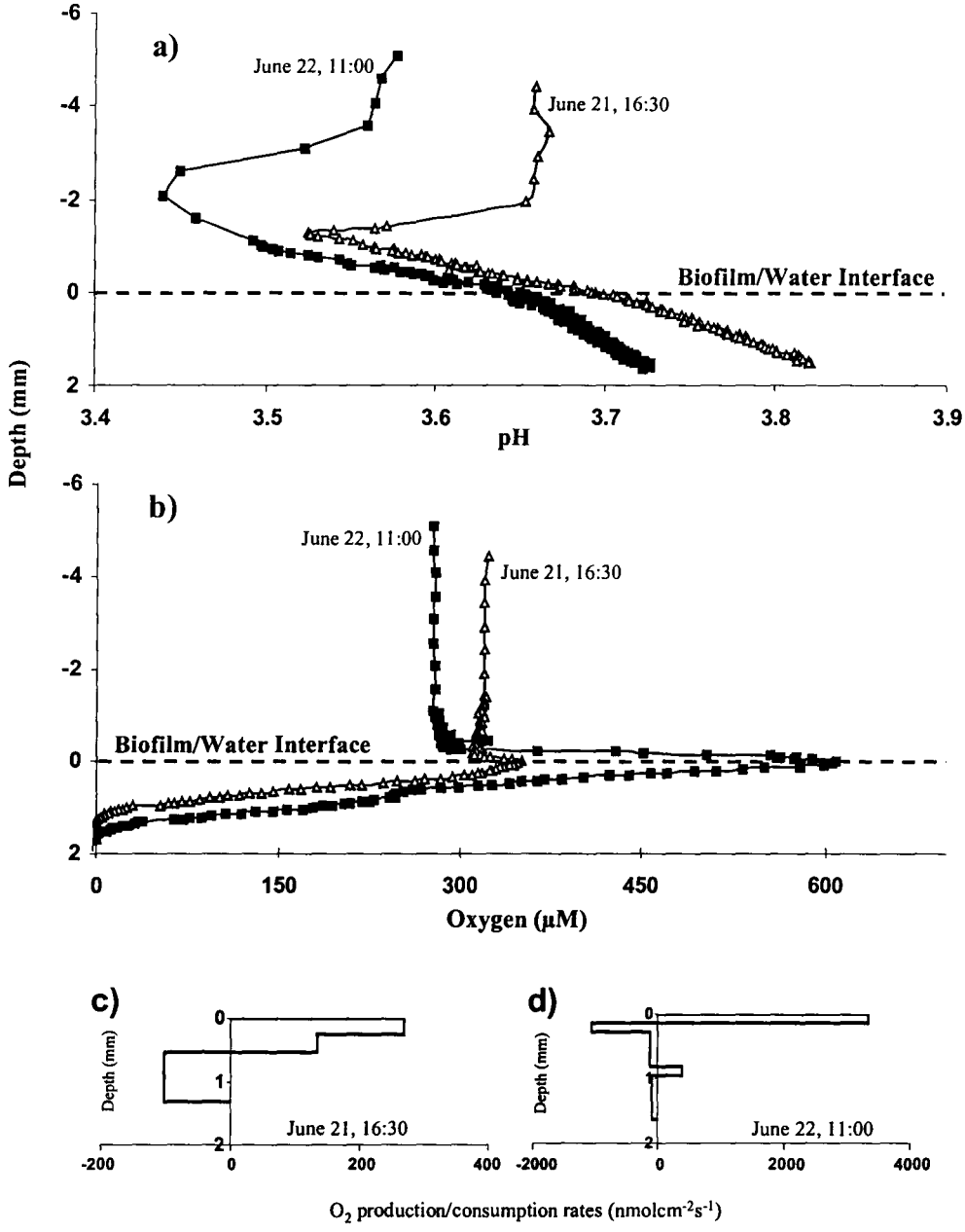

FIGURE 3.6. Representative in situ geochemical profiles of the biofilm and overlying water column (June 21, 16:30, Δ; June 22, 11:00, ■). pH (a) and DO (b) profiles indicate that: (1) biofilm geochemical conditions differ from the overlying water column; (2) geochemical depth zonation occurs within the biofilm; and (3) biofilm geochemical conditions are dynamic over short time scales. The biofilm-water interface is indicated by the dotted line. Net oxygen production (positive) and consumption (negative) rates within the biofilm (depth ≥ 0 mm) were calculated and shown for c) June 21, 16:30 and d) June 22, 11:00.

Biofilm Geochemical Dynamics and HMO Diel Cycling

Oxic conditions always extended deepest into the biofilms during afternoon sampling times (16:00-20:00, Table 3.2). The relative deepening of oxygenated conditions in the biofilm correlated positively with the relative loss of HMO observed from the biofilms (R^2=0.72). The actual depth of the oxic/anoxic boundary and absolute biofilm HMO concentrations at any given sampling time were not correlated, reflecting the longer-term seasonal buildup of HMO biominerals in the biofilm (Figure 3.5a). While biofilm HMO concentrations vary over diel timescales, seasonal biofilm-associated formation of HMO exceeds rates of HMO dissolution. The processes resulting in HMO formation dominated during non-lighted hours when biofilm oxic status was lower and the oxic-anoxic boundary was shallower; whilst processes resulting in HMO dissolution dominated during lighted hours, when the biofilm oxic status was greater and the oxic anoxic boundary extended deeper into the biofilm.

The observed formation of HMO over a period of hours at the low pH conditions of these ARD seepage streams, can only be the result of microbial catalysis of Mn(II) oxidation and associated precipitation of Mn(III/IV) oxyhydroxides (Stumm and Morgan, 1996). The build-up of HMO during non-photosynthetically-active hours may reflect a dependency of overall HMO formation rates on the status of both light and oxygen conditions in the biofilms, as indicated in the literature. The potential for Mn(II) oxidizing bacteria to be highly active under conditions of low oxygen has been shown in a hypersaline system (Tebo, 1991) as well as in laboratory studies (Vandenabeele et al., 1995). Alternatively, sunlight induced suppressed rates of Mn(II) oxidation have been reported (Sunda and Huntsman, 1987; Moffett and Ho, 1996), and attributed to photoinhibition of Mn-oxidizing bacteria.

Biofilm HMO dissolution, as evidenced by decreasing $\{Mn\}_A$, occurred during photosynthetically active daylight hours, when oxygen status of the biofilm was maximal and the oxic-anoxic boundary was deepest. This process is supported by both the observed biofilm HMO loss (Figure 3.5) and elevated dissolved Mn concentrations in the water column directly overlying the biofilms (Figure 3.1), during afternoon sampling hours. A number of processes, such as abiotic and/or biotic reductive dissolution and photoreduction may be contributing to HMO dissolution during lighted hours. Biotic dissolution of HMO has been reported in the presence of oxygen (Bratina et al., 1998; Ehrlich, 2000), and photoreductive dissolution of natural Mn oxyhydroxides has been shown in both marine (Felter and Dourson, 1997) and ARD-impacted waters (Scott et al., 2002). Further, abiotic dissolution of Mn(IV) by various reductants likely to be present in these biofilms, including Fe^{2+} (e.g. Stollenwerk, 1994), HS^- (e.g. Yao and Millero, 1993), organic compounds (e.g. algal/cyanobacterial photosynthate; Mercz and Madgwick, 1982), is well established.

3.3.3. Biofilm HMO Metal Sequestration

Total biofilm scavenging of Cr was the highest of the trace metals examined (K_D $10^{3.4}$ vs. $10^{1.3\text{-}1.5}$ for Co and Ni, Table 3.3). Cr scavenging to the amorphous oxyhydroxides fraction was highly correlated to biofilm HMO concentrations (R^2 = 0.95, Figure 3.4). $\{Cr\}_A$ showed the same diel fluctuations as $\{Mn\}_A$, with significantly lower

values being measured in the afternoon (Figure 3.4). As a result, $\{Cr\}_A$:$\{Mn\}_A$ ratios remained constant at ~0.3 on both diel and seasonal timescales, indicating that Cr loss from the biofilm oxyhydroxide fraction likely occurred during daylight-associated HMO dissolution.

Under acidic conditions, Cr(VI) occurs as $HCrO_4^-$, a highly mobile, toxic and soluble species (Felter and Dourson, 1997). Sorption-desorption reactions to positively charged surfaces are thought to control the mobility of $HCrO_4^-$ at low dissolved concentrations (e.g. 10^{-6} -10^{-7} M, consistent with this study). Given the likely negative surface charge of the HMO even under these low pH conditions (Kennedy et al., 2004), sorption of $HCrO_4^-$, is not likely (Guha et al., 2001). Furthermore, the invariant $\{Cr\}_A$:$\{Mn\}_A$ ratio and coupled Mn and Cr cycling observed in the biofilms, are more consistent with redox rather than sorption processes controlling HMO scavenging of Cr. Reduction of Cr(VI) to Cr(III) would result in immobilization of Cr, as Cr(III) precipitates are sparingly soluble (Liu et al., 2002).

Bacterially-catalyzed Cr(VI) reduction may be a process controlling Cr accumulation in the ARD biofilms during non-photosynthetic hours. Much research has focused on the indirect reduction of Cr(VI) under anaerobic conditions associated with microbial metabolism, e.g. indirect Cr(VI) reduction by H_2S produced by sulphate reducing bacteria (SRB; Smith and Gadd, 2000; Obraztsova et al., 2002). However, direct bacterially-controlled reduction of Cr(VI) has been demonstrated (Marsh et al., 2000), and a very recent study reports that direct Cr(VI) reduction occurs and is more likely to be carried out by facultative anaerobes such as *Shewanella spp.* rather than SRBs, as had previously been thought (Meriah Arias and Tebo, 2003). These studies showed inhibition of Cr(VI) reduction in the presence of oxygen.

Direct reduction of Cr coupled specifically to Mn oxidation has been shown in the chemical literature (e.g. Perez-Benito and Arias, 1998; Perez-Benito et al., 2001). These authors suggest that direct Cr(VI) reduction can be catalyzed by Mn(II) when the reductant used also acts as a stabilizing ligand for Mn(III), conditions which are likely to be met in the geochemical environment of these biofilms. This process involves a one electron transfer (Mn(II) to Mn(III)), and proceeds according to:

$$Cr\ (VI) + 3\ Mn(II) = Cr(III) + 3\ Mn\ (III) \qquad (3.1)$$

The calculated Cr:Mn ratio of 0.3 during non-photosynthetically active hours in our biofilms is close to this stoichiometric ratio.

Reductive dissolution of HMO induced by abiotic or biotic mechanisms mentioned above, could lead to loss and subsequent re-oxidation of Cr(III) at the surface of the remaining HMO pool (Manceau and Charlet, 1992; Chung et al., 1994), a process that involves the oxidation of Cr(III) to Cr(VI) paired to reduction of Mn(IV) to Mn(III) (Banerjee and Nesbitt, 1999). This coupled process could occur during daylight hours in the biofilm, enhancing HMO dissolution and loss of Cr associated with the amorphous oxyhydroxides fraction.

In contrast to $\{Cr\}_A$, $\{Ni\}_A$ and $\{Co\}_A$ did not vary over diel periods (Figure 3.4).

Thus, $\{Ni\}_A$:$\{Mn\}_A$ and $\{Co\}_A$:$\{Mn\}_A$ ratios varied with diurnal and nocturnal time periods, reflecting the dynamic diel biofilm loss and gain of HMO. The high $\{Ni\}_A$:$\{Mn\}_A$ ratios suggest coprecipitation of Ni with HMO may be occurring. In afternoon periods, $\{Ni\}_A$:$\{Mn\}_A$ and $\{Co\}_A$:$\{Mn\}_A$ when HMO concentrations were lowest, Ni:Mn and Co:Mn ratios were enriched (Figure 3.4). The magnitude of this enrichment increased linearly over the season ($\{Ni\}_A$:$\{Mn\}_A$; June: 2.97 vs. September: 8.51; $\{Co\}_A$:$\{Mn\}_A$; June: 0.098 vs. September: 0.19), reflecting a balance between the seasonal HMO accumulation of Ni and Co and the magnitude of HMO loss. Enriched Co:Mn ratios have been reported by Taillefert et al. (2002) at the oxic/anoxic boundary of a stratified lake. The authors attributed the enriched ratios to re-scavenging of Co by the remaining HMO pool upon partial reductive dissolution of HMO, consistent with the enriched $\{Co\}_A$:$\{Mn\}_A$ and $\{Ni\}_A$:$\{Mn\}_A$ ratios observed in our system.

3.4. Conclusions

Presently, we can only speculate as to the processes involved in trace metal association with these biofilm HMO. However, the results of this study are consistent with two differing processes controlling Cr and Ni/Co uptake in association with biofilm HMO biominerals. While the mechanisms controlling Ni/Co cycling in association with HMO are likely sorption and/or coprecipitation, Cr partitioning is more consistent with redox associated, immobilization of Cr(III) with the HMO. All these processes appear to be contingent on the vertical migration of the oxic/anoxic boundary within the biofilm; which is itself controlled by the balance between photosynthesis and respiration on a diel basis. Thus, the geochemical microenvironment of the biofilm, regulated largely by microbial activity and attendant ecological controls, has the potential to discernibly affect trace metal dynamics. The results of this field investigation indicate that microbial biofilms can impact metal dynamics within ARD environments, and raise new questions that need to be addressed in the development of an accurate framework of microbial-trace metal geochemistry.

CHAPTER 4: INSIGHT FROM EXAFS AND THE MUSIC MODEL INTO THE DISCREPANCY BETWEEN SCM-PREDICTED AND EXPERIMENTALLY-OBSERVED Ni SORPTION TO HMO

4.1. Introduction

4.1.1. Predictive Models

Effective remediation/bioremediation strategies for heavy-metal contaminated natural environments such as ARD, must necessarily incorporate a sound understanding of the nature of the interaction between metals ions in solution with the solid fraction, and further, how these interactions are affected by changes in geochemical conditions including pH. Fundamental to the design of effective remediation strategies is also the issue of scale; metal concentrations in natural systems are routinely determined at the macroscale (total solid and dissolved concentrations), whereas the processes that control their speciation, mobility, and transport occur at the nanoscale. Thus, predictive models are needed that relate macroscale properties of a natural system (pH, E_h, types and concentrations of sorbents and sorbates) to the mechanisms that drive contaminant sequestration on the nanoscale.

The Surface Complexation Model is a surface reaction-based chemical equilibrium model that has been applied to predict metal sorption to a number of environmental surfaces, under a wide range of geochemical conditions (Westhall and Hohl, 1980; Hayes and Leckie, 1987; Dzombak and Morel, 1990; Cox et al., 1999; Yee and Fein, 2002). Historically, the development of this model focused on describing the interaction of protons and metal ions with (hydroxide) functional groups at the surface of iron(III) oxyhydroxides because of the ubiquity of this mineral group. Many simplifying assumptions are made in using this model, to allow for consideration and mathematical computation of both the intrinsic (chemical) and electrostatic (Coulombic) components of complexation reactions between ions in solution and the variably charged solid surface (Morel and Hering, 1993). The important assumptions made are that: (1) there are a small number of types of amphoteric functional groups on the surface of the oxyhydroxide, each type displaying chemical equivalency; (2) reactions occur strictly at the surface of the particle, i.e. the oxyhydroxide particles is impenetrable and consequentially treated mathematically as an infinite plane; and (3) the position of co- and counter-ions from the interface to bulk solution can be described by various hypothetical physical representations that maintain electrical neutrality between solid and bulk solution (Westall and Hohl, 1980; Davis and Kent, 1990; Drever, 1997). The framework for SCM models is experimental acid-base titration data, from which net surface charge versus pH curves are derived. Typically, the shape of this curve is then mathematically described as the linear sum of Langmuir isotherms for individual types of

binding sites (Borkovec et al., 1996). The number of binding site types selected in the final model reflects both the minimum number of sites required for the best statistical fit, and the number of types of sites the researcher feels best describes the intrinsic heterogeneity of the solid surface.

SCM, however, is a purely macroscopic technique and some problems have been encountered in extending SCM models from the description of proton-binding curves to the prediction of metal sorption. For example, high and low affinity sites are needed to fit metal sorption data but not proton sorption data to iron oxyhydroxides (Benjamin and Leckie, 1981; Dzombak and Model, 1990; Robertson and Leckie, 1998). However, the creation of two binding site types in these models was not justified by spectroscopic evidence of functional groups on the surface of the oxyhydroxide with unique abundance and/or reactivities towards metal ions. Recently, Cd-HFO surface complexation reactions were analyzed by integrating Extended X-ray Adsorption Fine Structure Spectroscopy (EXAFS) with potentiometric titrations and knowledge of the surface site structure of HFO at the molecular level. Consistent with earlier macroscale results, good fits to Cd^{2+} sorption curves were achieved using a single type of reactive site up to a sorption density of 50%. Above this sorption density, a second, lower affinity site was required to give a good fit to the experimental sorption curves. For each type of binding site, a corresponding Cd surface complex structure was identified on each of the crystal faces of HFO where adsorption occurred. Similarly, SCM has been applied to proton and metal binding at bacterial surfaces. Typically, three types of monoprotic binding sites are required to fit proton binding curves to the surfaces of a number of bacterial species, while only two types of binding sites are required to fit metal sorption curves (Fein et al., 1997; Daughney et al., 1998). Based on pK_a values, the two types of sites required for metal sorption were inferred to be carboxyl and phosphate groups. Underestimation of uranyl (UO_2^{2+}) at low pH was attributed to sorption of uranyl to neutral phosphoryl groups. This conclusion was confirmed by analysis of uranyl sorption to bacterial cells wall with EXAFS (Kelly et al., 2002). Results indicated that at low pH uranyl was bound only by phosphoryl functional groups while at higher pH both carbonyl and phosphoryl functional groups were implicated in uranyl sorption. These two studies highlight the strength of integrating macroscopic and molecular-level analysis in predictive models for metal binding to environmental solids.

4.1.2. Manganese oxyhydroxides

Increasingly, the importance of manganese oxyhydroxides, in addition to iron oxyhydroxides, is being acknowledged for trace metal transport. Their reactivity for trace metals is potentially higher than those of Fe oxyhydroxides (Young and Harvey, 1992; Nelson et al., 1999b), even in ARD impacted environments where total solid concentrations of Fe are orders of magnitude higher than total solid Mn concentrations (Haack and Warren, 2003). Both physical and chemical heterogeneity are observed in natural Mn oxyhydroxides. Chemically, the heterogeneity arises from the three different oxidation states of Mn: Mn^{2+}, Mn^{3+} and Mn^{4+}. Average oxidation states of Mn oxyhydroxides in aquatic environments are always greater than 3, and more often range between 3.5 and 4 (Mandernack et al., 1995, and references therein). Physically, a

variety of tunnel (e.g. todorokite) and layered structures (e.g. birnessite) are formed by linking of higher valence MnO_6 octahedra by edges and corners (Post, 1999). In this chapter, the term hydrous manganese oxyhydroxide, HMO, will be used to denote all layered birnessite-like Mn oxyhydroxides (see 4.3.2.).

Specifically, it has been the structures and reactivities HMO and todorokite that have been the subject of extensive research. These Mn oxide minerals occur in marine ferromanganese nodules and terrestrial manganese deposits (Buser et al., 1954; Turner and Buseck, 1979; Usui, 1979; Dymond et al., 1984; Post and Bish, 1988; Post, 1999; Bilinski et al,. 2002), and they exhibit high ion exchange capacity (Mellin and Lei, 1993; Shen et al., 1993; Silvester et al., 1995). Buserite is also an oxidation catalyst (Fendorf and Zasoski., 1991; Manceau et al., 1997). Further, at pH values below 9 abiotic oxidation of Mn(II) is slow and rate of Mn(II) oxidation is regarded as a fingerprint of bacterial catalysis (Zhang et al., 2002). Villalobos et al. (2003) determined that biogenic HMO formed in the presence of the manganese-oxidizing bacterium *Pseudonomas putida* strain MnB1 have a layered hexagonal structure, with a bulk oxidation state of ~3.9 and approximately 5% vacant MnO_6 octahedral sites in the layer. Only one study has examined metal sorption specifically to biogenic HMO. Biogenic HMO formed in the presence of *Leptothrix discophora* SS-1 sorbed 4.0 $\mu molmg^{-1}$ of Pb (Nelson et al., 1999a). This value exceeded that measured for abiotic HMO, 1.5 $\mu molmg^{-1}$, a value consistent with other studies of Pb uptake in association with synthetic HMO (McKenzie, 1970; Matocha et al., 2001). Sorption to the biogenic HMO exceeded that to colloidal Fe oxyhydroxide under the same conditions by two orders of magnitude (Nelson et al., 1999a). Maximum sorption densities of trace metals including Pb, Ni, Co, Cu, and Zn to HMO generally range between 0.7-2.5 $\mu molmg^{-1}$ (Logonathan and Burau, 1973; Murray, 1975; Gray and Malati, 1979; Usui, 1979; Catts and Langmuir, 1986; Matocha et al., 2001; Kennedy et al., 2004), exceeding sorption densities of these same elements to iron oxyhydroxides by 1-2 orders of magnitude (Dzombak and Morel, 1990; Tamura and Furuichi, 1997) Clearly, there is a need to investigate metal sequestration specifically by HMO.

Attempts have been made to predict metal sorption to HMO using the Surface Complexation Model. Two approaches have been taken. In the first, spectroscopic evidence of functional groups associated with the HMO structure have not been explicitly considered in the development of the model. Two types of binding sites typically give the best fit to experimental acid-base titrations of the HMO in electrolyte solution. The first type of site has a pK_a value between 1.27 and 3.5 and the second site has pK_a values of -3.5 to -1.6 (corresponding to binding of H^+ to the protonated binding site) group) and 5.99-6.2 (corresponding to deprotonation of the binding site). Electrostatic interactions were represented with the triple layer model (Catts and Langmuir, 1986) and the diffuse double layer model (Pretorius and Linder, 2001; Tonkin et al., 2004). Although the models have shown some success at fitting and predicting pH-dependent metal sorption curves for a number of divalent metals, inconsistencies do occur. The inconsistencies can be attributed to the assumption that the HMO is characterized by a small number of binding sites types with chemical equivalency. For example, model fits to pH-dependent Cu^{2+} and Zn^{2+} sorption predicted rapid increase in cation sorption between pH 4 and 6,

while much more gradual uptake was observed experimentally resulting in over prediction of the amount of metal uptake at circumneutral pH values (pH 6-8) (Pretorius and Linder, 2001). Model fits frequently over- or under-predicted the amount of metal sorbed compared to experimental values from sorption isotherms (Tonkin et al., 2004). The model of Catts and Langmuir (1986) was not able to accurately model pH-dependent sorption curves when the amount of sorbent was increased at a constant concentration of sorbate. Further, plots of equilibrium binding constants versus surface coverage did not plateau at a constant value but decreased continually with increased surface coverage (Catts and Langmuir, 1986). Together, these results strongly suggest that HMO is characterized by a number of binding sites with a range of proton and metal affinities that cannot be represented by current SCM approaches.

The second approach is that of Appelo and Postma (1999), who explicitly considered the importance of layer vacancy sites for both proton and metal sorption in formulating their model. This group represented the vacancy site as doubly charged, multi oxygen adsorption site, and modeled proton, Mg, Ca, Sr, and Ba sorption to HMO using only this site. The model fits using the diprotic site only were significantly better than fits using monodentate and bidentate surface complexation reactions, even with the addition of "high" and "low" affinity sites. However, the model was not used to describe heavy metal uptake to HMO. The authors cautioned that, unlike alkaline earth metals that sorb in the interlayer at vacancy sites only, heavy metal ions can form solid solutions with HMO, and thus a surface complexation model is not appropriate.

4.1.3. Cation sorption in association with HMO

There is evidence in the literature to suggest that metal interaction with HMO may not be represented accurately by surface complexation reactions. Early studies of heavy metal ion uptake to HMO suggested that the uptake of these elements was not a result of surface complexation reactions, but rather that the cations were being incorporated into the HMO structure. The following experimental findings suggest that metals are being incorporated into the HMO structure: (1) the concentrations of electrolyte ions released to solution and heavy metals sequestered are positively correlated (Usui, 1979; Stroes-Gascoyne et al., 1987); (2) significant release of Mn from the structure occurs upon uptake of some heavy metals (e.g. Cu and Co; Usui, 1979; Logonathan and Burau 1973, Matocha et al., 2001); 3) hysteresis is observed in metal sorption curves (Murray, 1975); and (4) a maximum value for the ratio of trace element (Co, Ni, and Cu) to Mn in natural ferromanganese nodules is reported (Burns and Burns, 1978; Usui, 1979). Further, leaching experiments are consistent with the incorporation of Ni, Co and Cu associated in the structure of HMO, and surface adsorption for these same elements in association with goethite (Kumar et al., 1994).

More recently, EXAFS analysis of metal sequestration in association with HMO has indicated that vacancy sites in the MnO_6 octahedral layer are an important binding site for heavy metal ions. Manceau and colleagues have examined the local binding environment(s) of a number of divalent heavy metal ions equilibrated with HMO at acidic pH values (typically pH 4). Zn^{2+} and Cu^{2+} sorb above/below layer vacancies only, even at relatively high surface loadings (Zn: 1.23 $\mu molmg^{-1}$; Cu: 1.50 $\mu molmg^{-1}$;

Manceau et al., 2002a). Pb^{2+} also sorbs above/below layer vacancies (Matocha et al., 2001; Manceau et al., 2002a). However, there is some experimental evidence to suggest that $Pb^{2+}O_6$ octahedra share edges with layer MnO_6 octahedra to form tridentate edge sharing interlayer complexes at moderate Pb^{2+} loading (0.56 $\mu molmg^{-1}$). Uptake of Co^{2+} in association with HMO is more complex and involves the oxidation of Co^{2+} to Co^{3+} paired to the reduction of Mn^{3+} to Mn^{2+} (Manceau et al., 2000). At low Co loading, isomorphic substitution of Co^{3+} for Mn^{3+} in the octahedral layer occurs, while at higher loading (~2.3 $umolmg^{-1}$), Co^{2+} and Co^{3+} are additionally sorbed above/below layer vacancies. Manceau et al. (1997) state that it is the similarity of ionic radii between low spin Co^{3+} and Mn^{4+} (0.53 and 0.54 Å, respectively) that allows substitution of Co^{3+} into the layer. In none of these studies was there evidence of sorption at the edges of the solid or the formation of surface precipitates. Together, the results of these studies indicate the number of different mechanisms by which trace metals interact with the bulk HMO structure. The type of interaction that occurs appears to be dependent on the element itself and the sorbate/sorbent ratio. In all cases, the interactions cannot be described as adsorption; i.e. sorbate ions are not forming covalent bonds with functional groups situated strictly at the surface of the HMO particle. Thus, in this chapter the broadest definition of sorption will be used to describe the interaction of cations with HMO. "Sorption", as defined by Morel and Hering (1993), "involves the partitioning of solutes between the solution and the whole of the particulate phase".

4.1.4. Ni sorption to HMO

A number of studies have indicated that HMO is an important sorbent phase for Ni in natural environments (e.g. Usui, 1979; Fuller and Harvey, 2000; Kay et al., 2001); however, analysis of the mechanism by which Ni is sorbed to HMO has not been well-constrained. In the field-examination of ARD biofilms (Chapter 3), HMO biominerals were shown to be important for Ni, Co and Cr sequestration. The biofilm samples examine occurred in association with shallow seepage streams. The depth of these streams was observed to vary on diel timescales. As a result of this observation, the effect of periodic wetting and drying on the acid-base behaviour and the extent of Ni uptake to HMO was examined (Kennedy et al., 2004). Synthetic HMO samples were exposed to three different hydrologic regimes: (1) wet, freshly precipitated, amorphous Mn oxyhydroxides (WET); (2) dried Mn oxyhydroxides (DRY): and (3) Mn oxyhydroxides that were cyclically exposed to wet and dry conditions (CYCLE). For each sample, a pK_a spectrum and proton binding capacity were derived from experimental acid-base titration data using the Fully Optimized ContinUouS (FOCUS) pK_a model (Smith and Ferris, 2001, see 4.4.2.). Results indicated that while all three hydrologically conditioned HMO samples had amorphous structures, significant differences in the number and pK_a of proton binding sites occurred amongst samples. Batch Ni uptake experiments to the pre-conditioned HMO were run at pH values 2 and 5. Consistent with other attempts to model cation sorption to HMO, Ni uptake to all three hydrologically-conditioned HMO samples was underestimated at pH 2 and somewhat overestimated at pH 5. Thus specifically examining the local coordination of Ni in association with HMO as well as the underlying structure of this solid has relevance for

better understanding how HMO sequesters trace metals in ARD environments as well extending our modeling ability through characterization of the fundamental mechanisms involved in metal solid interactions.

To better understand the discrepancy between the model-predicted and experimentally-observed Ni sorptive capacity of HMO, sorption of Ni to HMO at the molecular level was examined and results used to constrain macroscale models of Ni sorption to HMO. This chapter is presented in two parts. In Part I, the local coordination of Ni sorbed to HMO samples that had undergone hydrological pre-treatment is examined using EXAFS. In Part II, acid-base titrations of HMO and Ni-sorbed HMO samples were performed and pK_a spectra for each experimental system were derived using the FOCUS model. Changes in the pK_a spectra amongst HMO and Ni-sorbed HMO samples were rationalized in terms of the EXAFS results and by applying the bond valence method to calculate theoretical pK_a values for functional groups associated with HMO. It is the integration of both macroscale and molecular-level techniques that allow the unique insight into the structural reactivity of HMO for Ni presented in this paper.

PART 1: SYNCROTRON X-RAY ABSORPTION SPECTROSCOPY

4.2. Materials and Methods

4.2.1. Preparation and hydrologic conditioning of HMO

All reagents and chemical used in the preparation of HMO were of analytical grade and only ultra pure water was employed (UPW, 18.2Ω). Glassware/plastic ware was acid washed in 3-5% HCl and rinsed in UPW prior to use. HMO was prepared by the "redox" method (Villalobos et al., 2003), according to:

$$2\,NaMnO_4 + 3MnCl_2 + 4NaOH \rightarrow 5MnO_2 + 6NaCl + 6H_2O \qquad (4.1)$$

$MnCl_2$ was added slowly to alkaline $NaMnO_4$ solution (Kennedy et al., 2004, Murray, 1974). Freshly precipitated HMO was washed four times by centrifugation (10 minutes at 10,000 rpm, Sorvall RC5C+ ultracentrifuge) and resuspension in UPW, and was subsequently divided into three subsamples for hydrologic conditioning. The three experimental systems from Kennedy et al. (2004) were replicated to permit comparison of the results of that study with those presented here: (1) WET: wet, freshly precipitated Mn oxyhydroxide; (2) DRY: Mn oxyhydroxide dried at 37°C for 8 days; and (3) CYCLE: Mn oxyhydroxide dried at 37°C for 24 hours, then hydrated for 24 hours, with the wetting/drying cycle repeated three times over 7 days.

4.2.2. Nickel Sorption Experiments

Sorption experiments were designed to examine the effects of both pH and hydrologic regime on Ni sorption to synthetic HMO, over a short 24 hour time period. The 24 hour time period may not represent "true equilibrium"; however, previous studies

have indicated that divalent metal ion sorption to HMO occurs rapidly, over the course of hours (Logonathan and Burau, 1973, Matocha et al., 2001). Sorption experiments were run in 250 mL acid washed polypropylene bottles and were initiated by adding $Ni(NO_3)_2$ solution to a suspension of approximately 0.25 g of hydrologically pre-conditioned HMO in 100 mL of electrolyte, to a nominal Ni^{2+} concentration of 0.1 mM. The pH of the hydrated HMO suspensions was adjusted immediately to one of the three selected pH values: 2, 4 or 6.5. Analysis of solution conditions by MINTEQL indicated that Ni^{2+} dominated (>91%) aqueous phase Ni speciation in all systems (MINTEQ, version 2.14). Blanks accounted for loss of Ni to the bottle walls (0.1 mM $Ni(NO_3)_2$; no solid) and dissolution of HMO (solid only, pH 2), which was expected to be greatest at pH 2. Reaction occurred under atmospheric conditions over 24 hours, with gentle shaking (Forma Scientific, orbital shaker, 150 rpm). The solution pH was adjusted in each bottle every 30-60 minutes for the first 8 hours, and again after 20 hours. At the end of 24-hour reaction period, the final pH was recorded without adjustment, and the samples were centrifuged immediately (Sorvall RC-5C$^+$ ultracentrifuge, 30 minutes at 10,000 rpm). Following centrifugation, the supernatant was removed, passed sequentially through 0.45 and 0.2 μm filters (Nucleopore Acrodisc® 25mm syringe filter, Pall Gelman Laboratory, MI), and acidified to 0.2% HNO_3 v/v (Fisher Scientific OPTIMA HNO_3, Seastar Chemicals Inc., PA). The pelleted solid samples were stored moist at 4°C in tightly sealed containers for XAFS analysis; storage time prior to analysis varied from 48 hours to a maximum of 4 days.

The extent of Ni uptake to each HMO sample was quantified from dissolved Ni concentrations in the supernatant. The difference between the initial and equilibrium Ni concentrations in each bottle represents the amount of Ni sequestered, after correction is made for loss of Ni to the bottle walls (<6% of the nominal concentration). Dissolved Mn concentrations were also measured since increased Mn in solution after the 24-hour equilibration time could indicate both dissolution of the solid or exchange of Ni with interlayer Mn cations. Dissolved Mn concentrations always represented less than 1% of the Ni sequestered, and less than 0.01% of the HMO added, indicating that both processes were negligible. Dissolved-phase Ni and Mn were quantified by ICP-MS. (PerkinElmer SCIEX ELAN 6100, Woodbridge, ON, Canada). Coefficients of variation of ICP-MS (calculated as the relative standard deviation of blanks) averaged 1.6 and 1.7% for Mn and Ni, respectively.

4.2.3. XAFS Data Collection and Analysis

X-ray absorption fine structure spectra (XAFS) were collected on bending magnet 13-BM at the Advanced Photon Source (APS), Argonne, Illinois. The electron beam energy and maximum beam current were 7 GeV and 100 mA, respectively. A water-cooled Si(111) double-crystal monochrometer was used and higher order harmonics rejected by detuning the second crystal to roughly 25% of the maximum intensity. Prior to data collection, the monochrometer was calibrated using the first inflection points in the absorption edges for Mn and Ni foils, at 8333 eV and 6539 eV, respectively. All XAFS spectra were collected under ambient conditions. Ambient conditions are more reflective of natural environmental conditions and other studies have shown that while

spectra collected at 77 K allow improved signal-to-noise ratios, there is no structural information missing from spectra recorded at higher temperature (Pandya et al., 1990; Charlet and Manceau, 1992, Scheidegger et al., 1996).

Mn K-edge XAFS spectra of the pristine hydrollogically-conditioned HMO samples (WET, DRY, CYCLE) were collected in transmission mode (using N_2 filled ionization detectors) over the energy range 6345-7095 eV. "Pristine" will henceforth be used to denote HMO that had undergone hydrological conditioning, but was not equilibrated at acidic pH values for electrolyte solution or reacted with Ni, i.e. represents the starting material for the sorption experiments. Ni K-edge XAS spectra of Ni-sorbed HMO samples were collected in fluorescence mode using a Ge detector (16 element Ge detector, Canberra) over the energy range 8140-8890 eV. Sample holders consisted of 4 x 15 mm slots cut into 2 mm thick Teflon blocks, sealed on both sides with Kapton tape. A minimum of 10 successive scans were averaged together to improve the signal to noise ratio.

Mn and Ni K-edge XAFS spectra were collected in transmission mode for synthetic Na-birnessite and commercial model compounds: $MnCO_3$, Mn_2O_3, MnO_2 and β-$Ni(OH)_2$. Model compounds were crushed to powders with a mortar and pestle and applied as a thin layer to transparent tape. Several one-layer thicknesses were stacked to make a suitable sample density. Mn K-edge XAFS spectra were collected over the energy 6345-7095 eV for Na-birnessite and 6439-6676 for $MnCO_3$, Mn_2O_3, and MnO_2. Synthetic Na-birnessite was prepared by the oxidation-deprotonation reaction method, as per Yang and Wang (2002). Structures of the model compounds $Ni(OH)_2$ and Na-birnessite were verified by XRD (Siemen's D5005, Falconbridge Technology Centre; data not shown).

Data processing and analysis were done using ATHENA (version 0.8.013, Bruce Ravel, University of Washington) and IFEFFIT (Newville et al., 2001). The raw XAS data was pre-edge subtracted and normalized using the autoback algorithm. The resulting Extended X-ray Absorption Fine Structure (EXAFS) functions were converted from energy to k($Å^{-1}$) after specifying the values of E_0 as the inflection point of the relevant K absorption edge. Unsmoothed EXAFS spectra were k^2-weighted and fit in R space using a non-linear least-squares procedure, typically over the k-range of 3.2 – 10.9 $Å^{-1}$ and R-range of 0.8-3.8 Å. Structural fitting was done by first Fourier filtering the EXAFS spectra to isolate scattering contributions from the first two shells of backscattering neighbors. Fits to the filtered data provided likely chemical identities of the atoms in the first and second shells surrounding the central atom, and initial values of interatomic distances and number of atoms in each shell for the final fitting procedure. All shells were fit simultaneously in the final fitting procedure and ΔR, the change in path distance, E_0, the energy shift (relative to the theoretical standard), σ^2, the mean-square displacement of the bond (Debye-Waller factor), and N, the coordination number were allowed to vary in the fits. The value of E_0 was constrained to a single value for all shells. The EXAFS amplitude reduction factor, s_0^2, was set to a constant value after fitting the experimental EXAFS spectra for model compounds with theoretically-generated functions.

Ab initio amplitude and phase functions for the model compounds Na birnessite and β-$Ni(OH)_2$ were calculated with FEFF6 (Rehr et al., 1992) using crystallographic

data (Na birnessite: Post and Veblen, 1990, corrected as outlined in Ressler et al., 1999; β-$Ni(OH)_2$: McEwen, 1971). Fits to both model compounds involved two single-scattering paths, Mn-O and Mn-Mn, and Ni-O and Ni-Ni, respectively. Based on these fits, the value of s_0^2 was set at 0.71 for Mn samples and 0.97 for Ni samples. The number of parameters varied in the fitting procedure never exceed the number of independent degrees of freedom, according to $N_{max} = [(2\Delta k \Delta R/\pi)] + 2$, (Stern, 1993) where Δk ($Å^{-1}$) is the k region of the spectrum that was Fourier transformed and ΔR (Å) the region of the data that was Fourier filtered. For all fits, the "goodness of fit" is expressed with the *R*-factor, which gives the absolute misfit between theory and the experimental data (Ravel, 2000).

$$R = \sum_{i=1}^{N_{pts}} \frac{[\mathrm{Im}(\chi_{dat}(R_i)-\chi_{th}(R_i))]^2 + [\mathrm{Re}(\chi_{dat}(Ri) - \chi_{th}(R_i))]^2}{[\mathrm{Im}(\chi_{dat}(R_i)]^2 + [\mathrm{Re}(\chi_{dat}(R_i))]^2} \qquad (4.2)$$

where N_{pts} is the number of points in the fitting range of the data, and Im and Re are the real and imaginary parts of the complex Fourier transforms of the data (χ_{dat}) and theory (χ_{th}), respectively.

The FEFF-derived amplitude and phase function for Ni-O derived from β-$Ni(OH)_2$ was used to fit first-shell backscattering contributions in the Ni-HMO sorption samples and for the hydrated Ni^{2+} ion (0.01 M $Ni(NO_3)_2$). Fitting of the sorption samples required two (pH 2 and 4) or three (pH 6.5) single scattering paths. Single scattering Ni-cation (Ni-Mn and Ni-Ni) paths at interatomic distances of 2.9 and 3.5 Å were created using SIXPACK (version 0.35, Samuel Webb, 2002, Stanford Synchrotron Research Laboratory) and used as input files for FEFF6.0. Ni-HMO samples at pH 2 and 4 required only one cation scattering path, at a distance of 3.5 Å. During the initial fits, the Debye-Waller factors, σ^2, for the Ni-cation shell was allowed to vary; the fitted values ranged from 0.005 and 0.014 $Å^2$. In the final fitting procedure, the value of σ^2 was fixed at the mean value of 0.009 $Å^2$ to reduce the number of degrees of freedom in the fitting procedure. Fitting of the Ni-HMO samples at pH 6.5 required two single scattering Ni-cation paths. These shells were fit simultaneously in the initial fits due to the overlap between corresponding peaks in the Fourier transform. The EXAFS for these samples represented a linear combination of two Ni binding environments. In all EXAFS, the coordination numbers, $N_{observed}$, returned in the fit are a weighted average of the different crystallographic environments (Manceau et al., 1997). Thus, to determine the "true" coordination number, N, of the two Ni-cation shells, $N_{observed}$ (returned by IFEFFIT) for both shells need to be corrected for the mole fraction of Ni in each of the two coordination environments. For the longer Ni-cation shell, at interatomic distance of 3.5 Å, N was set to a constant value and adjusted in the fits by a floating parameter α, such that $N_{observed} = N \times \alpha$. For the shorter Ni-cation path (2.9 Å), $N_{observed}$ was allowed to vary and was expressed $N_{observed} = N \times (1-\alpha)$. In the final fits, N and σ^2 values for the Ni-O and Ni-cation path at 3.5 Å were constrained to their mean values from the fits for samples at pH 2 and 4 and σ^2 for the Ni-cation path at 2.9 Å at 0.09 $Å^2$ (for the reasons

given above). ΔE_0, α, N and R for the Ni-cation shell at 2.9 Å were allowed to vary in the final fits of the Ni-HMO samples at pH 6.5.

4.3. Results and Discussion

4.3.1. Mn K-edge EXAFS

Mn K-edge EXAFS analysis indicates that the pristine HMO samples have a local structure very similar to that of Na-birnessite. Hydrologic conditioning did not alter the local structure of the pristine HMO. Normalized, background subtracted and k^2 weighted XAFS spectra of Na-birnessite, WET, DRY and CYCLE samples are shown in Figure 4.1a, and Fourier transforms are shown in Figure 4.1b. Fourier transforms of all samples are not corrected for phase shift (ncps). Thus, compared to true interatomic distances, the position of peaks in the Fourier transforms are shifted to a lower distance by approximately 0.3-0.4 Å.

Fourier transforms for Na-birnessite and the HMO samples show two strong peaks, at ncps distances of ~1.3 Å, and ~ 2.5 Å. The first shell peak corresponds to the Mn-O single scattering path and the second peak corresponds to Mn-Mn cations across the edge of Mn edge-sharing octahedra. Interatomic Mn-Mn distances are typically 2.8-2.9 Å for edge-sharing Mn octahedra (Manceau and Combes, 1988). Peaks appearing at higher R(Å) (~5.1 Å) in the Fourier transform arise from single and multiple scattering between first and second shell Mn cations, and potentially more distant shells. Due to the number of single and multiple scattering paths that must be considered for EXAFS analysis at longer distances (e.g. Ressler et al., 1999), peaks beyond ~3Å are not explicitly considered here.

The best two-shell fit to Na-birnessite using theoretically-derived EXAFS phases and amplitudes gave 6.0 oxygen atoms at 1.89 ± 0.01 Å and 5.6 Mn at 2.86 ± 0.03 Å (Table 4.1). These values compare well with Mn-O and first-neighbor Mn-Mn interatomic distances determined in other EXAFS studies of Na-birnessite (e.g. McKeown and Post, 2001). The best two-shell fits for WET, DRY and CYCLE gave between 5.8-6.3 nearest O atoms at 1.89 ± 0.01 Å, and 5.2-5.6 nearest Mn neighbors at 2.86 (± 0.03) Å (Table 4.1). Best fits to the experimental EXAFS spectra are indicated by the dashed lines in Figure 4.1a-b.

There was no evidence for a second Mn metal neighbor in either the HMO samples or the Na-birnessite sample; EXAFS fits were not significantly improved with the addition of a Mn backscattering shell at ~3.4 Å (ncps), corresponding to Mn corner sharing octahedra. This result was expected for Na-birnessite. A lack of corner-sharing Mn-Mn interactions has been noted in the literature for light cation (e.g. Na, Ca, Mg)-birnessite samples (Manceau et al., 1992, Silvester et al., 1997). The EXAFS analyses indicate that the hydrologically conditioned HMO samples have a 2-D layered and not a 3-D tunnel structure. In contrast, a weak but significant contribution from corner-sharing Mn atoms has been observed for HMO, as for todorokite (Manceau et al., 1992). Thus, it was suggested that HMO be considered a solid solution intermediate between a phyllomanganate with 2-D structure and todorokite with 3-D structure (Manceau et al., 1992). Differences between the results of this study and those of Manceau et al., (1992)

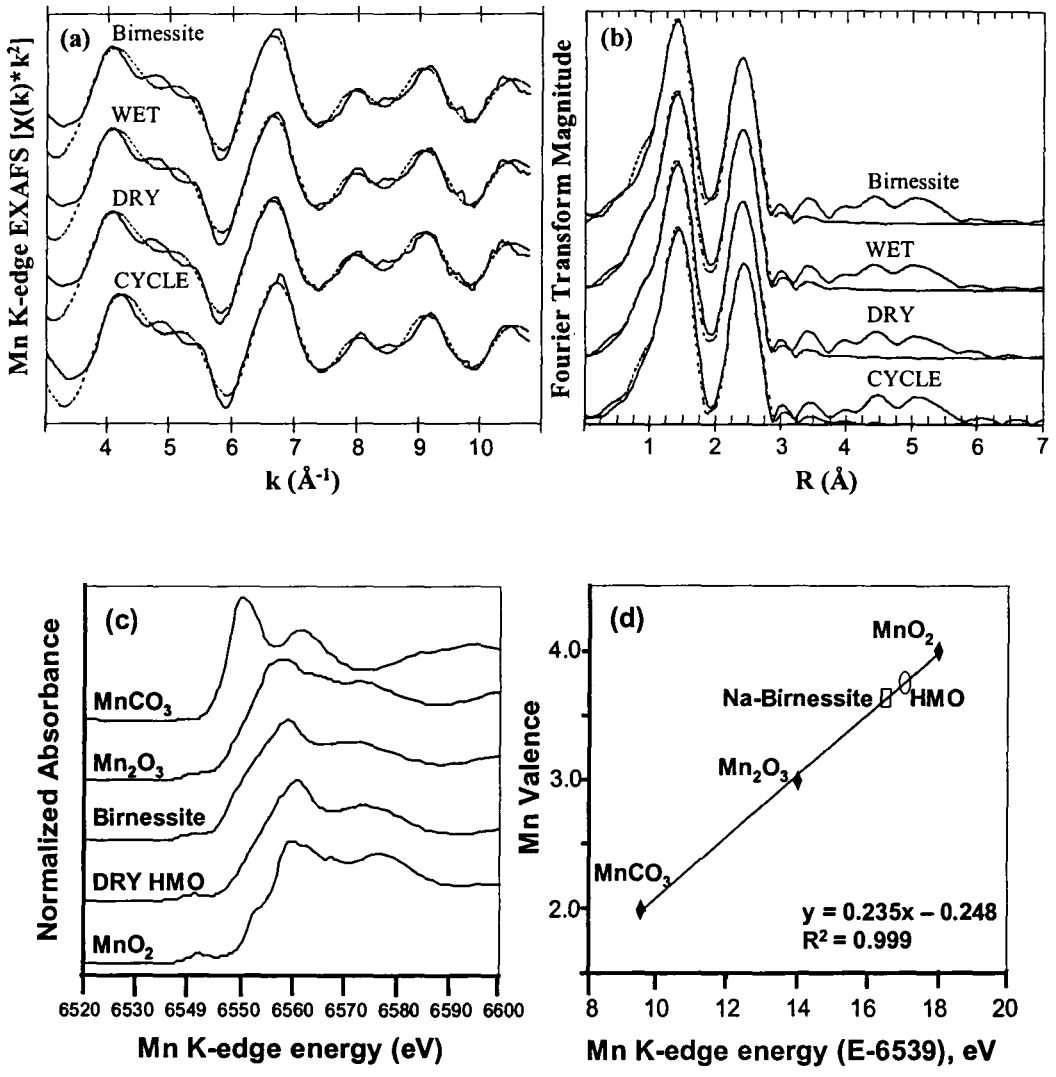

Figure 4.1: Mn K-edge $\mathbf{k}^2$-weighted EXAFS spectra (a) and Fourier transforms (b) of hydrologically conditioned HMO and birnessite. In both (a) and (b), dashed lines indicate best least-squares fit to the $\mathbf{k}^2$-weighted EXAFS spectra. Normalized Mn K-edge XANES spectra of DRY HMO and Na-birnessite, compared to selected manganese model compounds (c). The XANES spectra for the DRY HMO sample is representative of all hydrologic conditions. All spectra were collected at 298 K. Bulk oxidation state of Mn was determined using a calibration curve (d) derived from the edge position of the first inflection point of the main edge (measured on smoothed first derivative spectrum). The valence of Mn in the model compounds was assumed to be representative of a single oxidation state.

Table 4.1: Results of least-squares analysis of Mn K-edge EXAFS spectra. R= interatomic distance, σ^2 = the Debye-Waller mean-square disorder parameter, and N= coordination number. Shown in parentheses following each value is the estimated standard deviation, given as 3σ (Foster et al., 2003). These values refer to the estimated error in the last decimal place unless otherwise indicated.

		EXAFS least -squares fits results						
EXAFS Sample	ΔE_o (eV)	Mn-O			Mn-Mn (edge sharing)			
		R(Å)	σ^2 (Å^2)	N	R(Å)	σ^2 (Å^2)	N	r-factor
Na-Birnessite	-7.7 (3.3)	1.89(1)	0.004(3)	6.0 (2.0)	2.86 (3)	0.007(5)	5.6 (3.1)	0.010
WET	-7.9 (3.3)	1.89(1)	0.004(3)	6.3 (2.0)	2.86 (3)	0.007(4)	5.6 (2.7)	0.006
DRY	-7.7 (3.3)	1.89(1)	0.005(3)	6.2 (1.9)	2.86 (2)	0.006 (4)	5.2 (2.5)	0.009
CYCLE	-3.3 (3.5)	1.89(1)	0.004(4)	5.8 (2.1)	2.86 (3)	0.007(5)	5.4 (3.0)	0.008

[a] s_0^2 fixed at 0.71.
[b] r_factor gives an estimate of the relative misfit; it is misfit scaled to the data (as outlined in 4.2.3)

may be a result of sample preparation protocol. A small number of corner sharing Mn octahedra can not be excluded from the structure of the hydrologically conditioned HMO samples as the detection limit for corner-sharing octahedra has been reported as <8% (Manceau and Combes, 1988).

4.3.2. Structure of Na-birnessite and HMO

HMO has well documented ion exchange capacity (e.g. Golden et al., 1986; Le Goff et al., 1996) and metal sorptive capacity (e.g. Murray, 1975; Nelson et al., 1999a). However, comparison of results amongst studies and disciplines has been hampered somewhat by the varied nomenclature in the literature and the number of protocols for layered Mn oxyhydroxide synthesis. To simplify further discussion of the structure and reactivity of the layered Mn oxyhydroxide phases, commonly used nomenclature will be briefly outlined here. The marine literature has favored the terms 7 Å and 10 Å manganates, terms that reflect the approximate d-spacings associated with these phases. Synthetic 7Å Na-manganate is prepared via a hydrated 10 Å precursor, by oxidation of Mn(II) by O_2 in alkaline solution (Stähli, 1968; Golden et al., 1986; Usui, 1979; Kuma et al., 1994). In the terrestrial literature, the layered Mn oxyhydroxide phase made by the same synthesis method is called Na-birnessite and the hydrated precursor is Na-buserite (e.g. Post and Veblen, 1990; Drits et al., 1997). Na-buserite has approximately 10Å d-spacing and two layers of water molecules between MnO_6 octahedral layers. The structure of Na-buserite is not stable at ambient temperature and pressure and contracts to Na-birnessite (7Å d-spacing) (Usui, 1979; Kuma et al., 1994). Na-birnessite is also commonly prepared via the "redox" method (Villalobos et al., 2003 and references therein). The product yielded is sensitive to both the molar ratio of oxidant/reductant (Eq. 4.1) and the sequence in which they are added. Crystalline Na-birnessite with an oxidation state of 3.67-3.88 is yielded (always through a hydrated precursor) when the oxidatant/reductant molar ratio is 0.3-0.4 (Shen et al., 1993). The terms δ-MnO_2 and HMO have been used to describe the poorly crystalline solid with bulk oxidation state closer to 4.0 (although values as low as 3.1 have been reported by Foster et al., 2003) yielded when stoichiometric ratios of oxidant/reductant are used (Murray, 1974, 1975; Catts and Langmuir, 1988; Trivedi et al., 2001, Villalobos et al., 2003; Kennedy et al., 2004). Although there is the potential for structural variability in the layered Mn oxyhydroxide phases, the extent of cation uptake in association with the different phases is surprisingly constant. As introduced earlier, maximum sorption capacities of layered Mn oxyhydroxides for Ni, Co, Cu, Pb, and Zn typically range from 0.7 and 2.5 μmol M^{z+} mg^{-1}. For generalization, the term HMO is used in here to describe all amorphous layered birnessite-like Mn oxyhydroxides. The term Na-birnessite will only be used when referring to the work of Manceau and colleagues (Silvester et al., 1997; Drits et al., 1997; Lanson et al., 2002) that observed a transformation in the structure of triclinic Na-birnessite with pH (so as to be consistent with their terminology when referring directly to their findings).

Structurally, all HMO are composed of layers of MnO_6 octahedra that are separated by one (7Å d-spacing) or two (10Å d-spacing) layers of water molecules, which are the predominant interlayer species. Alkali, alkaline earth, and transition metal

cations are also positioned in the interlayer. As outline above, HMO is most often synthesized with Na^+ as the interlayer cation. Na^+ is easily exchanged for other cations. Na^+ exchange efficiencies are generally greater than 80% with uptake of Ni, Co, and Cu, and 100% with Ca and Mg (Usui, 1979), but are interestingly never exceeded. Examination of the interlayer positions of Na^+, K^+ and Mg^{2+} by the powder XRD (Post and Veblen, 1990; Kuma et al., 1994) indicated that Na^+ and K^+ were positioned approximately equidistant between the MnO_6 layers, in positions similar to those occupied by water molecules. In contrast, Post and Veblen (1990) reported that Mg^{2+} was more closely associated with the MnO_6 layers, and was sorbed above/below layer vacancies. However, not consistent with positioning of Mg^{2+} above/below layers, the 2authors reported that their HMO were free of vacancies, suggesting that perhaps a transformation in the structure of HMO (i.e. the creation of layer vacancies) occurs with uptake of Mg. Kuma et al., (1994) found that the exchange of Ni^{2+}, Ba^{2+}, Ca^{2+} and Mg^{2+} for Na^+ stabilized the 10Å d-spacing of HMO and that these ions were sorbed above/below layer vacancies. Their results were consistent with a linear arrangement of the layer vacancies, such that vacancy-rich rows occur every third row parallel to the *b* axis. Thus, it appears that the structural framework of HMO is flexible and that transformation of the bulk structure occurs with exchange of divalent ions for Na^+ (and K^+).

The number of cations exchanged in the HMO structure has been linked suggestively to the number and distribution of lower valence Mn ions in the bulk structure (Shen et al., 1993). Evidence for this comes from the structural change observed for Na-birnessite with acidic pH values. Protons thus become the ions exchanging for Na^+. Using XRD, Lanson et al. (2000) determined that synthetic Na-birnessite has a one-layer triclinic structure where Mn^{3+} rich rows (that can also contain Mn^{2+}) alternate regularly with Mn^{4+} rows along the *a* axis, according to the sequence $Mn^{3+}Mn^{4+}Mn^{4+}Mn^{3+}$ (Drits et al., 1997; Figure 4.2). Two Na-birnessite microcrystals with different structural formula were identified: (1) the more abundant Type II microcrystals with structural formula $Na^+_{0.333}(Mn^{4+}_{0.722}Mn^{3+}_{0.222}Mn^{2+}_{0.055})O_2$, and (2) Type I microcrystals with structural formulae ranging from $Na^+_{0.167}(Mn^{4+}_{0.833}Mn^{3+}_{0.167})O_2$ to $Na^+_{0.25}(Mn^{4+}_{0.75}Mn^{3+}_{0.25})O_2$. Na^+ in the Na-rich birnessite structure exchanges for H^+ in solution and at pH values ≤ 5, triclinic Na-rich birnessite transforms to hexagonal birnessite (Figure 4.2). The transformation occurs by a two-step process (Silvester et al., 1997). First, a rapid (within minutes) exchange of some of the Na^+ with H^+ from solution occurs followed by the slower disproportionation of one-third of the Mn^{3+} according to:

$$2Mn^{3+} \rightarrow Mn^{2+} + Mn^{4+} + \square \qquad (4.3)$$

where □ is a layer vacancy. Mn^{2+} cations formed by the disproportionation reaction migrate into solution, leaving the layer enriched in Mn^{4+} and layer vacancies. The second step of the transformation involves complete exchange of H^+ for Na^+ and the slow migration of Mn^{3+} into the interlayer, where it sorbs above/below layer vacancies. Overall, the process results in rows with the number of vacancies representing 50% of the initial Mn^{3+} in the layer, and the spatial distribution of the vacancies reflecting the initial distribution of lower valence Mn ions in the structure (Figure 4.2). At pH values of 5 and

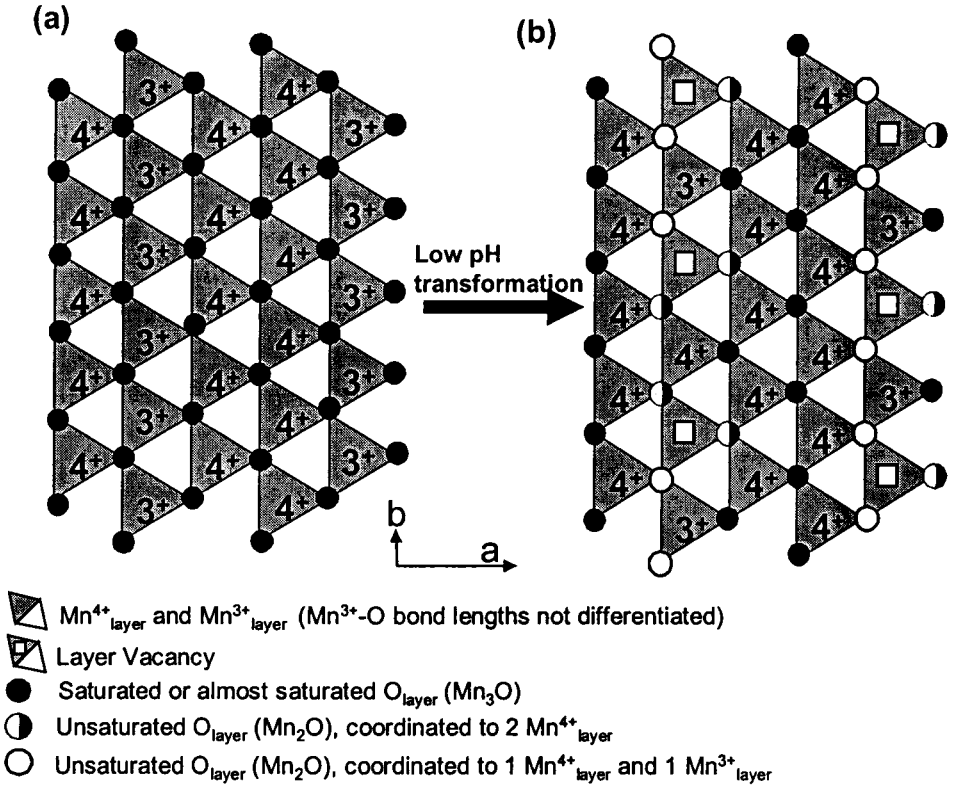

Figure 4.2: Idealized structural model for Na-birnessite (a) and H-Birnessite (b), modified from Lanson et al., (2000). The distribution of oxygens are shown within the upper surface upper surface of the lower layer (grey triangles) in projection on the *ab* plane. With the low pH transformation of Na-birnessite to H-birnessite, layer vacancies are formed by both the disproportionation and associated release of Mn(II) to solution and the migration of Mn^{3+}_{layer} to the interlayer. Mn^{4+}, Mn^{3+} and layer vacancies are shown as 4^+, 3^+ and open squares, respectively. Oxygen atoms forming the upper surface of the lower layer are shown by large circles. Solid circles = saturated or almost saturated O_{layer} atoms; Split circles = unsaturated O_{layer} atoms coordinated to two Mn^{4+} layer cations; Open circles = most undersaturated O_{layer} atoms coordinated to one Mn^{4+}_{layer} cation and one Mn^{3+}_{layer} cation.

below, H-birnessite is composed per octahedron of : 1) 0.722 Mn(IV) cations and 0.111 Mn(III) cations in the layer; 2) 0.167 layer vacancy sites; and 3) a total of 0.167 interlayer Mn cations (Mn(III) and Mn(II)) adsorbed above/below vacancy sites (Lanson et al., 2002).

The low pH transformation of Na-birnessite has two important implications. The first is that the transformation in the structure affects only the rows rich in Mn(III); rows of $Mn(IV)O_6$ octahedra are not affected by changes in pH. The driving force behind the transformation was proposed to be destabilization of the Mn(III)-rich rows at acidic pH values (Drits et al., 1997). Thus, the reactivity of the Na-birnessite structure is a function of the presence of lower valence Mn ions in the structure. The second is that the linear spatial distribution and abundance of vacancy sites created in the Na-birnessite structure at acidic pH values matches those reported by Kuma et al. (1994) for Ni, Ca, Mg, and Ba-sorbed HMO. Thus, it appears that the sorption of Ni, Ca, Mg and Ba may have the same effect on HMO structure that H^+ has on the structure of Na-birnessite, and again, may be linked to the presence of lower valence Mn ions in the bulk HMO structure.

The pre-conditioned HMO samples in this study had a bulk oxidation state of 3.72 ± 0.02 by the oxalate method (following Freeman and Chapman, 1971; and Silvester et al., 1997). Briefly, HMO was digested in excess oxalate and the back-titrated with hot potassium permanganate. Results from the oxalate method compared well with the bulk oxidation state of the HMO of 3.74 ± 0.05 determined from a calibration curve calculated by using the energy position of the first inflection point of the main edge from XANES spectra of model compounds $MnCO_3$ (MnII), Mn_2O_3 (MnIII), and MnO_2 (MnIV) (Figure 4.1cd). Thus, as much as 27% of the Mn present in the MnO_6 layer structure could be Mn(III) or ~13 % Mn(II) (or a combination thereof). A certain degree of ordering in the distribution of lower valence Mn atoms is expected in all HMO; due to the Jahn-Teller distortion of $Mn(III)O_6$ octahedra a random distribution of Mn(III) would results in high steric strain on the structure (Ressler et al., 1999). Using multi-scattering EXAFS analysis, Ressler et al. (1999) proposed a 2-D structure for HMO with average valence of 3.67, whereby Mn(III) atoms clustered amid rows rich in Mn(IV). The distribution of Mn(III) in the Mn(IV)-rich rows was such that the number of collinear Mn(III) triplets was optimized. Thus, it is likely that there is some form of clustering of lower valence Mn atoms in the HMO and that the reactivity of this structure for Ni will reflect the spatial distribution of the Mn(III)/Mn(II) in the bulk MnO_6 layer structure.

Implications of these results are profound for modeling attempts as they clearly show that structural changes occur as a function of pH, and potentially in solutions of divalent cations. These structural changes are not currently included in our quantitative assessment of HMO uptake of metals.

4.3.3. Ni Uptake and K-edge EXAFS

Ni uptake to all three hydrologically conditioned HMO samples increased with increasing pH, on a per-weight basis. As would be expected from classic theory underlying surface complexation reactions, higher Ni uptake was observed at pH 4 compared to pH 2 for all three HMO treatments (t-test). Between pH 2 and 4 the amount of Ni sorbed to HMO increased from ~ 0.028 to 0.035 $\mu molmg^{-1}$ (Table 4.2),

corresponding to an increase in the relative removal of Ni^{2+} from solution of >75% at pH 2.0 to >96% at pH 4.0. As approximately 100% of the Ni was sorbed at pH 4, differences in the amount of Ni sorbed were not observed between pH 4 and 6.5 (Table 4.2). Hydrologic conditioning did affect the amount of Ni sorbed; significantly more Ni was sequestered by the DRY samples at pH 4 and 6.5. Whilst differences were observed amongst treatments at pH 2, they were not statistically significant.

The local coordination environment of Ni sorbed to the three hydrologically pre-conditioned HMO samples was determined using synchrotron-based X-ray absorption spectroscopy. Ni K-edge EXAFS spectra and Fourier transforms of β-$Ni(OH)_2$ of all experimental Ni-HMO systems are shown in Figure 4.3. Best two-shell fit for β-$Ni(OH)_2$ to 3.2 Å resulted in 5.8 ± 1.3 O at 2.06 ± 0.01 Å and 5.7 ± 2.3 Ni at 3.12 ± 0.01 Å (Table 4.3). The structural parameters determined for β-$NiOH_2$ in this study compare well with XRD- and XAFS-derived values reported in the literature (Pandya et al., 1990, Scheidegger et al., 1998 and references therein). Further, the fitted values of 6.1 ± 1.5 O atoms at an interatomic distance of 2.05 ± 0.02 Å for the Ni^{2+} ion ($Ni(NO_3)_{2\ (aq)}$) also compare well with values found in the literature (Magini et al., 1988; Table 4.3).

Fourier transforms of all Ni-sorbed HMO samples show a dominant peak at ~1.6 Å (ncps) corresponding to the first coordination shell of Ni. Scattering contributions from the first shell were fit with 5.9-6.8 O atoms at a distance of 2.03-2.04 Å from the central Ni atom (Table 4.3), indicating that Ni is octahedrally coordinated in all samples. The Ni-O bond distance in the samples is slightly shorter than in the aqueous solution. Fourier transforms of the Ni-HMO samples at pH 2.0 and 4.0 show a second peak at (ncps) ~3.1 Å, while at pH 6.5, two peaks appear at (ncps) distance of ~2.5 and ~3.1 Å.

The intensity of the second and third peaks in the Fourier-transforms suggests the presence of heavy backscattering elements such as Ni and Mn. In fitting the EXAFS spectra for our samples, three reported coordination environments for Ni in association with natural Mn oxide phases were considered. The first coordination environment considered for Ni sorption to HMO was sorption above/below layer vacancies, consistent with the XRD and SAED results of Kuma et al., (1994) and with naturally-occurring Erninickelite. Erninickelite is a natural analog to the phyllomanganate chalcophanite (Grice et al., 1994). In chalcophanite, pairs of Zn^{2+} are located above and below vacancy sites in the $Mn(IV)O_6$ layer. Each Zn^{2+} ion is bound to three oxygen atoms from the layer and three oxygen atoms from water molecules positioned in the interlayer. As such, Zn^{2+} forms a tridentate corner-sharing complex with the MnO_6 layer and is most closely surrounded by 6 Mn ions from the layer. The second coordination environment considered for Ni in association with HMO was substitution of Ni for Mn in the MnO_6 layer. Substitution of Ni for Mn in the MnO_6 octahedral layer of lithiophiorite has been reported (Manceau et al., 2002b). Lastly, precipitation of $Ni(OH)_2$ in a discrete layer, as in natural asbolane (Manceau et al., 1987) was considered.

Reported Zn-Mn corner-sharing interatomic distances in chalcophanite derived from EXAFS analysis are 3.5 Å (Manceau et al., 2002a). This distance was used to create a single-scattering Ni-Mn path in the fitting procedure for Ni-HMO samples at pH 2.0 and 4.0. Structural parameters derived for the final multishell fitting procedure are summarized in Table 4.3. The best two-shell fits to the experimental EXAFS spectra for

Table 4.2: Ni sorptive capacity in batch experiments to hydrologically pre-conditioned HMO samples.

Sample	pH	Ni^{2+} added (μmol)	Mass HMO (g)	WET	DRY	CYCLE
				Ni^{2+} sorption density ($\mu molmg^{-1}$)		
Batch Experiment (this study)	2	10	0.25	0.0288 ± 0.0012	0.0286 ± 0.0004	0.283 ± 0.007
	4	10	0.25	0.0326 ± 0.0006	0.0372 ± 0.0002	0.0363 ± 0.018
	6.5	10	0.25	0.0331 ± 0.0014	0.0381± 0.001	0.0370 ± 0.004
Kennedy et al., (2004)	2	1000	0.08	0.42 ± 0.01	0.43±0.01	0.48 ± 0.02
	5	1000	0.08	0.90 ± 0.04	0.79±0.01	0.83 ± 0.04
				Chemical Properties[a]		
			pH_{zpc}	6.82 ± 0.06	3.2 ± 0.3	5.05 ± 0.05
			Total Proton binding Capacity ($\mu molmg^{-1}$)	3.4 ± 0.2	0.96 ± 0.04	1.8 ± 0.2
			Proton binding Capacity at pH 2 ($\mu molmg^{-1}$)	0.0068±0.0007	0	0.005±0.003

[a] Chemical Properties of the three hydrologically conditioned HMO samples were reported in Kennedy et al. (2004).

the pH 2.0 and pH 4.0 Ni-HMO samples show 6.3-7.3 Mn atoms surrounding the central Ni ion at a distance of 3.49-3.50 Å (Table 4.3). These results are consistent with Ni sorbing above a layer/below a layer vacancy. In this position each NiO_6 octahedra would theoretically be most closely surrounded by 6 Mn atoms in the MnO_6 layer.

At pH 6.5, two cation backscattering peaks at (ncps) distances of approximately 2.4 and 3.2 Å were observed in the Ni-HMO samples. The appearance of an additional cation backscattering shell in these spectra indicates a change in the local Ni coordination environment at pH 6.5 compared to the more acidic pH values examined. The EXAFS spectra for the Ni-HMO samples at 6.5 were fit by assuming that the peak at (ncps) 3.2 Å was the result of Ni sorption as a tridentate corner-sharing complex, as for the Ni-HMO samples at pH values 2 and 4. Edge-sharing Ni-Mn pairs were additionally considered, based on the reported Ni-Mn edge-sharing distance of 2.91 Å reported by Manceau et al. (2002b) for natural ferromanganese nodules. The best three-shell fits to the Ni-HMO samples at pH 6.5 were achieved by constraining the coordination numbers and Debye Waller factors for the Ni-O and corner-sharing Ni-Mn shells to their mean values from the Ni-sorbed HMO samples at pH 2.0 and 4.0 (indicated in Table 4.3). Additionally, the Debye-Waller factor for the edge-sharing Ni-Mn was constrained after determining the mean value from previous fits. Results indicated that Ni shares edges with 4.4-5.4 Mn atoms at an interatomic distance of 2.88-2.90 Å (Table 4.3), and suggests that Ni is substituting for Mn in the MnO_6 octahedral layer.

Amongst hydrologic conditions there was some variation in the fitted parameters for the Ni-Mn edge-sharing path (Table 4.3). The mole fraction term indicates the amount of the total Ni sorbed that is represented by tridentate corner-sharing complexes (Table 4.3). The percent of Ni sorbed above/below layer vacancies increased from approximately 56% of the total Ni sorbed in the WET sample to 65% in the DRY and CYCLE samples. Even after considering that the Ni uptake to DRY and CYCLE samples on a per-weight basis was higher than to the WET samples (Table 4.2), more Ni was sequestered in edge-sharing positions by WET-HMO.

It is important that it be stressed here that the structural parameters reported in Table 4.3 represent the best fits; i.e. the residuals are minimized when Ni-Mn pairs are assumed for both cation shells. However, due to the similarity in phase shifts and amplitudes between Ni and Mn, the identity of the heavy backscattering ion as either Ni or Mn cannot be resolved unambiguously in this study. The possibility of discrete $Ni(OH)_2$ precipitation was examined in each sample; reasonable fits to the isolated shells were not achieved using Ni-Ni distances (~3.12 Å) from β-$Ni(OH)_2$ for any of the samples. However, Ni-Ni distances shorter than those reported for $Ni(OH)_2$ have been reported for Ni in solid solutions; Ni-Ni interatomic distance of 3.05-3.06 have been reported for Ni solid solutions with clay and aluminum oxide minerals (Scheidegger et al., 1998). Attempts were made to fit this shorter Ni-Ni distance in the pH 6.5 Ni-sorbed HMO samples, where there was evidence of a shorter cation-cation interatomic distance. In all fits the Ni-Ni distance was constrained to 3.06 Å. Reasonable fits were not obtained using this Ni-Ni shell.

Together, the Ni K-edge EXAFS results for Ni sorption to HMO are consistent with two processes: 1) sorption of Ni above/below layer vacancies at all pH values

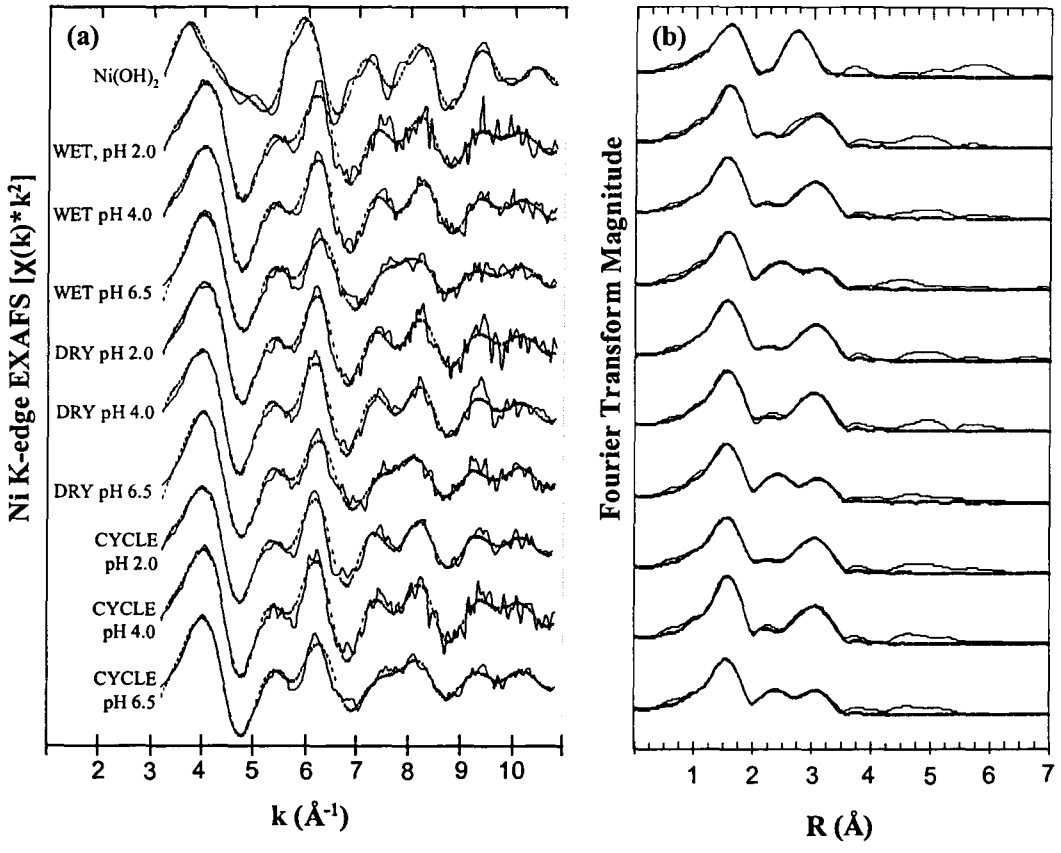

Figure 4.3: Ni K-edge $\mathbf{k}^2$-weighted EXAFS spectra (a) and Fourier transforms (b) of Ni-sorbed HMO samples and β-$Ni(OH)_2$. In both (a) and (b), dashed lined indicate best least-squares fit to the $\mathbf{k}^2$-weighted EXAFS spectra.

Table 4.3. Results of least-squares analysis of Ni K-edge EXAFS spectra. R = interatomic distance, σ^2 = the Debye-Waller mean-square disorder parameter, and N= coordination number. Shown in parentheses following each value is the estimated standard deviation, given as 3σ. These values refer to the estimated error in the last decimal place unless otherwise indicated.

EXAFS least -squares fits results												
Sample	ΔEo (eV)	Ni-O			Ni-Ni							r_factor
		R(Å)	σ^2 (Å^2)	N	R(Å)	σ^2 (Å^2)	N					
β-Ni(OH)$_2$	-5.7(1.1)	2.06 (1)	0.006 (3)	5.8 (1.3)	3.12 (1)	0.007(4)	5.7 (2.3)					0.006
Ni(NO3)$_2$	-6.3 (1.2)	2.05 (2)	0.008 (5)	6.1(1.5)								0.005
		Ni-O			Ni-Mn (Edge Sharing)			Ni-Mn (Corner Sharing)				
		R(Å)	σ^2 (Å^2)	N	R(Å)	σ^2 (Å^2)	N	R(Å)	σ^2 (Å^2)	N	mole fraction	
W 2	-5.1(1.8)	2.04 (3)	0.006(4)	5.9(2.2)				3.50(4)	0.009*	6.3(1.8)		0.017
D 2	-5.6(1.9)	2.04(2)	0.007(3)	6.5(1.6)				3.50(3)		6.7(1.2)		0.007
C 2	-6.3(1.9)	2.04(2)	0.008(3)	6.3(1.5)				3.50(2)		6.7(1.1)		0.006
W 4	-6.4 (2.0)	2.03(2)	0.007(3)	6.7(1.2)				3.49 (2)		6.9 (8)		0.003
D 4	-6.6 (2.9)	2.04(2)	0.007(4)	6.8(2.6)				3.50 (4)		7.3 (1.9)		0.015
C 4	-5.2 (1.3)	2.04(2)	0.005(3)	6.1(1.9)				3.50 (4)		7.3 (1.7)		0.015
W 6.5	-4.5 (2.9)	2.03(3)	0.007*	6.4*	2.90 (5)	0.009*	4.4 (2.7)	3.50 (4)		6.9*	0.56 (0.22)	0.002
D 6.5	-4.8 (2.3)	2.04(2)			2.89 (4)		5.4 (3.2)	3.51 (3)			0.63 (0.19)	0.010
C 6.5	-5.6 (2.6)	2.03(2)			2.88 (5)		4.7 (3.2)	3.49 (3)			0.65 (0.19)	0.011

[a] The asterisk indicates that this value was fixed in the fit.
[b] s_0^2 fixed at 0.97.
[c] r_factor gives an estimate of the relative misfit (see 4.2.3)

examined; and 2) substitution of Ni for Mn in the MnO_6 octahedral layer at circumneutral pH.

4.3.4. Ni Uptake and Local Coordination Environment

The Ni K-edge EXAFS are consistent with two types of binding environments for Ni in association with the layered HMO at low nominal Ni^{2+} concentrations (0.1mM $Ni(NO_3)_2$, 2.5 g HMO L^{-1}). At all pH values examined (2, 4 and 6.5) Ni is sorbed as a tridentate corner-sharing complex above/below vacancy sites in the MnO_6 octahedral layer. Additionally, at pH 6.5 our results suggest isomorphic substitution of Ni for Mn in the MnO_6 octahedral layer. Isomorphic substitution indicates that Ni substitutes for Mn without a change in the bulk HMO structure. Hydrologic pre-conditioning of the HMO samples did not affect the Ni binding environment(s) at the pH values examined nor did it affect the shift in binding environment with pH.

The pH-dependence of the local Ni coordination environment associated with HMO is an important finding. Between pH 2 and 4, the amount of Ni sequestered above/below layer vacancies increased significantly for all HMO treatments (Table 4.2). Increased uptake at one type of binding site with increased pH is consistent with a sorption process, whereby Coulombic forces drive the initial interaction between the hydrated Ni^{2+} ion in solution and the HMO surface (Trivedi and Axe, 2001). Between pH 4.0 and 6.5, the extent of Ni sorption increased by less than 3%, as approximately all $Ni^{2+}_{(aq)}$ (0.1 mM) added to the system had been sorbed by HMO at pH 4. However, between these two pH values, the crystal chemistry of Ni shifted dramatically for all hydrological treatments. The shift in local Ni coordination cannot be ascribed to increased sorption density. EXAFS results indicated that at pH 6.5, Ni sorbed as a corner sharing complex accounted for between 56-65% of the total Ni sequestered (Table 4.3); the remaining 35-44% of the total Ni sequestered substituted for Mn in the MnO_6 octahedral layer. Thus, these results show that a fundamental change in the process that drives Ni association with HMO occurs with pH; at higher pH values the process of Ni substitution for Mn in the layer competes with sorption of Ni above/below vacancy sites. Further, these results are consistent with sorption of Co by HMO. Manceau et al. (1997) found that isomorphic substitution of Co^{3+} for Mn^{3+} occurred at relatively low sorption densities. It was only at higher sorption densities that Co^{2+} and Co^{3+} were also sorbed above/below layer vacancies. The relative dominance of substitution versus sorption above/below layer vacancies thus appears to be element-dependent.

A change in the local coordination environment of Ni clearly occurs with increasing pH. It is suggested here that the mechanism underlying the change in Ni coordination environment is structural transformation of the bulk HMO solid due to changes in pH and divalent ion concentration (as outlined in 4.3.2.). Specifically, it is likely changes in the spatial distribution of Mn(III) within the bulk HMO structure that are key to understanding Ni uptake in association with HMO. Manceau et al. (2002b) postulated Ni^{2+} was replacing Mn^{3+} in the MnO_6 octahedral layer of lithiophiorite, based on the similarity in their atomic radii (0.69 and 0.645 Å respectively), compared to the much smaller ionic radius of Mn^{4+} (0.53 Å). Further, the crystal field stabilization energies of Ni^{2+} in an octahedral field (29.6 kcal/mol) and Mn^{3+} are comparable, while

both exceed that of Mn^{2+} (0 kcal/mol; Logonathan and Burau, 1973). Manceau et al. (1997) observed Co^{3+} exchange for Mn^{3+} in the layer of birnessite and attributed the exchange both to the similarity in ionic radii of Co^{3+} and Mn^{4+}, and the fact that Co^{3+}does not undergo Jahn-Teller distortion. Like Co^{3+}, Ni^{2+} does not undergo Jahn-Taller distortion and the driving force behind isomorphic substitution is likely to be the resulting increase in structural order in the $Mn(IV)O_6$ octahedral layer.

Ni sorption to HMO has only been examined once previously using EXAFS (Trivedi et al., 2001). Trivedi and co-authors concluded that both Ni and Zn maintained their hydration sphere (5.4-8.9 oxygen atoms as next-nearest neighbors to both cations) and were sorbed as outer-sphere complexes. Their Ni K-edge EXAFS spectra did not show any changes with time (4 hours-110 days), pH (5 and 7) or sorption density (10^{-3} to 10^{-2} mol Ni g^{-1} HMO). Interestingly, the Ni-O interatomic distance for the next-nearest oxygen neighbor was 2.34Å, the arithmetic mean of the two Ni-Mn distances reported in this study. It is proposed that the Ni K-edge results of Trivedi et al. (2001) are more consistent with the incorporation of NiO_6 into the structure of HMO as both corner-sharing and edge-sharing complexes, rather than sorption of Ni to HMO as an outer-sphere complex.

4.3.5. Discrepancy identified by the hydrologic pre-treatment of HMO.

Although hydrologic treatment did not affect the local chemistry of Ni in any of the samples, the effects of hydrologic conditioning of HMO on the relative amount of Ni sorbed at constant pH did reveal an important discrepancy that needed to be addressed.

In both our batch experiments and those of Kennedy et al. (2004), the extent of Ni uptake was very consistent amongst hydrologic conditions at pH 2 (Table 4.2). The nominal concentration of $Ni^{2+}_{(aq)}$ was much higher in Kennedy et al. (2004) and the Ni sorption densities they reported represent maximum Ni sorption capacity for the HMO samples at both pH 2 and 5. The consistency in Ni uptake between hydrologically-conditioned HMO samples at pH 2.0 in both that study and this one could not be rationalized in light of both the widely-different proton binding capacities and apparent pH_{zpc} values determined for each of the three hydrologically-conditioned HMO samples (Table 4.2).

At pH 2.0, the proton binding capacities of the samples decreased in the order of WET > CYCLE > DRY (Kennedy et al., 2004; Table 4.2). The proton binding capacity was derived from the acid-base titration curves using the FOCUS model, as introduced earlier (4.1.4.). Typically, in extending SCM models such as the FOCUS model to include metal binding to a surface, proton and metal binding are considered to be competitive processes; i.e. protons and metals are assumed to bind at the same sites (Warren and Haack, 2001). If Ni and proton binding to HMO are assumed to be competitive processes, the maximum proton sorption at a given pH value represents the upper limit for Ni sorption capacity (as all protons may not be displaced and Ni binding may be multidentate). Results from our batch experiments and those of Kennedy et al. (2004) clearly demonstrate that this relationship is not upheld. Ni sorptive capacities exceeded proton binding capacities by 1-2 order of magnitude in Kennedy et al. (2004) (Table 4.2). Using the same values for proton binding capacity, Ni sorption capacity in

our batch experiments still exceeded the model-derived proton-binding capacity by a factor of > 5.

The EXAFS results presented here show that Ni binds above/below layer vacancies at pH 2.0. Thus, the discrepancy between model-derived proton binding capacities and experimental Ni sorption capacities can not be attributed to precipitation of Ni as a separate solid phase. Rather, the results suggest that the binding environment relevant for Ni sorption at low pH, being vacancy sites in the MnO_6 layer, is not being accurately quantified using acid-base potentiometric titrations. Part II of this study further addresses this discrepancy by examining the proton affinities of sites associated with HMO structure, using both acid-base titration and a theoretical model, by examining changes in the bulk structure of HMO itself with Ni sorption.

PART II: CHARACTERIZATION OF HMO REACTIVITY FOR Ni USING POTENTIOMETRIC TITRATION AND A THEORETICAL MODEL

4.4. Materials and Methods

4.4.1. Titration Method

All titrations were performed at room temperature (25°C) in a plastic titrator cup as part of the automatic Mettler Toledo DL70 unit interfaced to DLWin software. The titrator, set in dynamic mode, was programmed to maintain approximately equal pH intervals (~ 0.2 pH units) by delivering variable amount of titrant. Equilibrium was operationally defined in the titration scheme; additional titrant was added only after the potential of the solution being titrated changed by less than 0.3 mV in 150s, reflecting the sensitivity of the electrode. All titrations were run using identical titration parameters, making comparisons between samples valid.

DRY HMO samples were used for all titrations. The DRY sample was chosen to minimize the uncertainty associated with measuring the sample mass (i.e. no wet/dry conversion required). Approximately 0.125 g of DRY HMO and 50 mL of electrolyte solution, 0.1 M KNO_3, were added to a titrator cup under N_2 conditions in an anaerobic chamber. For titrations of the DRY HMO alone (i.e. without Ni added), the pH of the solution was brought to a start point of approximately pH 10 with standard NaOH. The cup was removed from the chamber and immediately transferred to the titrator, where the DRY HMO was allowed to hydrate with stirring, for one hour under N_2 atmosphere. Ascarite towers were used to prevent any contamination of the sample by CO_2. After hydration, the sample was titrated down to the preset end point, approximately pH 4.0 using standardized 0.1M HNO_3, stirring throughout with a Teflon paddle attached to the titrator unit. Prior to starting titrations, blank titrations of 0.1 M KNO_3 and NaOH were run to calibrate the electrode directly from activity units to concentrations units, thus pH = -log[H^+], not activity. Additionally, an internal calibration was performed after each titration to account for electrode fouling.

Titrations with Ni^{2+} added as $Ni(NO_3)_2$ were run at two nominal Ni^{2+} concentrations, 0.2 mM (to represent low Ni loading) and 10 mM (to represent maximum Ni loading)(Table 4.4). DRY HMO samples were hydrated as described above, however, the initial pH of the solution was not raised above pH 8.0 to avoid precipitation of $Ni(OH)_2$ upon addition of Ni^{2+} to the solution. Immediately following the hydration period, the appropriate aliquot of $Ni(NO_3)_2$ was added manually to the solution. All titrations were run in triplicate. A separate series of titrations were run at the highest nominal Ni^{2+} concentration (10 mM; Table 4.4) with the end point set to pH 6.5. Following each titration, 10 mL of the suspension was removed from the titrator cup using an acid-washed syringe. Dissolved Ni and Mn concentrations were quantified as outlined above (see 4.2.2.).

Table 4.4: Ni sorption densities measured in the Ni-sorbed HMO acid-base titrations[a]

Ni^{2+} (mM)	pH	Ni^{2+} sorption density ($\mu molmg^{-1}$)
0.2	4	0.083 ± 0.010
10	4	0.88 ± 0.11
10	6.5	1.7 ± 0.1

[a] All titrations were run in 50 mL 0.1 M KNO_3 with 0.125 g of HMO.

4.4.2. The FOCUS Model: Titration Data Processing and Representation

The experimental acid-base titration data were fit to a smooth continuous pK_a spectra using the FOCUS pK_a spectrum method, which optimizes for both goodness-of-fit and smoothness. Detailed discussions of the FOCUS model are given elsewhere (Smith and Ferris, 2001), but a brief outline of the method has been included below. A continuous model was most appropriate for our purposes. By using a continuous model, the proton binding characteristics of a solid can be represented by a continuous pK_a spectrum. Continuous models have been applied to describe the proton binding characteristics of polyeletrolytes (Nederlof et al., 1994; Plette et al., 1995), and they are thought to better represent solids with multiple functional group types. The pK_a spectra derived with the FOCUS method are apparent spectra, as electrostatic effects and site-site interactions are not considered. All data were analyzed using Matlab™ (The MathWorks Inc., Mass, US). Parameter fitting was performed using the Optimization Toolbox within Matlab.

Experimental acid-base titration data are fit by assuming equilibrium and that the solid can be represented as a sum of monoprotic sites with monoprotic dissociation reactions. First the data are transformed to the charge excess expression, then the charge excess data are fit to a model for the proton-interface system. The charge excess from the data for the i^{th} addition of titrant is shown on the left below ($b_{i,meas}$) and the model that is fit to the data ($b_{i,calc}$) is shown on the right:

$$b_{i,meas} = \frac{Cb_i - Ca_i + [H^+]_i - [OH^-]_i}{C_s}; b_{i,calc} = \sum_{j=1}^{m} \frac{K_j L_{T\,j}}{K_j + [H^+]_i} + S_0 \qquad (4.4)$$

where $b_{i,meas}$ is the charge excess in $\mu molmg^{-1}$ of solid, Cb_i, and Ca_i are the concentrations of base and acid added respectively and the final two terms in the numerator are the proton and hydroxyl concentrations in solution, determined using the glass electrode. Finally, C_s is the solid concentration in mgL^{-1}.

A pK_a spectrum represents the overall proton binding of the surface as a summation of monoprotic dissassociation reactions, each reaction being defined by a unique pK_a value (K_j in Eq. 4.4) and a corresponding site concentration (L_{Tj} in Eq. 4.4). To determine a pK_a spectrum, first the pK_a values are defined on a sequence from some minimum to some maximum value at fixed step sizes. Thus, the pK_a values are fixed and what remains is to assign concentrations to each of m sites such that the data is described as follows for n titration points:

$$\mathbf{Ax} = \mathbf{b}$$

$$\text{where } \mathbf{A}(i,j) = \frac{K_j}{K_j + [H^+]_i} \text{ for } i = 1 \ldots n \text{ and } j = 1 \ldots m \qquad (4.5)$$

$$\text{and } \mathbf{A}(i,j) = 1 \text{ for } i = 1 \ldots n \text{ and } j = m+1$$

There is an $n\times(m+1)$ matrix **A** of alpha terms, an $(m+1)\times 1$ vector of site concentrations, **x** where the final entry is a constant offset term S_0 (see Eq. 4.4). The stability constants K_j are defined from the disassociation reaction of each monoprotic site with corresponding $pK_a = 10^{-Kj}$. The $n\times 1$ vector of measured charge excess terms is defined as **b**. A traditional least-squares approach to this problem would vary the parameters in **x** in order to minimize the sum of the squares of the difference between the calculated and measured value for **b**. However, mathematically the problem is ill-posed (Press et al., 1992). This is because many solutions can describe the data equivalently well and a slight change in the data results in a large change in the fitted parameters. Černík et al., (1995) have applied a regularization method of solving ill-posed problems to acid-base titration data. Regularization involves using some *a priori* information about the system to further constrain the results; reducing the sensitivity to data changes. One constraint imposed by the nature of the system is that all of the ligand concentrations must be positive. Further, the results can be regularized for a few discrete sites or for smoothness depending on if a discrete or continuous result is desired. Here, regularization for smoothness is applied. This a priori assumption about the nature of the final result makes it possible to formulate the regularized least-squares optimization problem for n titration points as:

$$\begin{gathered}\text{minimize } SS + \lambda R \\ \text{where } SS = \sum_{i=1}^{n} (b_{calc,i}(\mathbf{x}) - b_{meas,i})^2 \\ \text{and } R(x_1,\ldots,x_m) = \sum_{j=2}^{m-1} (x_{j-1} - 2x_j + x_{j+1})^2 \\ \text{and } \mathbf{x} \geq 0\end{gathered} \tag{4.6}$$

The SS term is the usual sum of squares term for nonlinear regression; without regularization only this term would be minimized. The regularization term is also dependent on the values of the parameter vector and the regularization power is controlled by the constant λ. The R function corresponds to the sum of squares of finite difference approximation of the second derivatives. This function is small for smoothly varying values of **x** and large if the values of **x** oscillate.

There are two values to optimize for the minimization problem defined in Eq. 4.6, both the smoothness and the goodness of fit. Theoretically, there is an optimal answer that satisfies both criteria with a minimum of compromise in the other (Press et al., 1992). Determining this optimal solution depends on the regularization strength given by the parameter λ. Smith and Ferris (2001) present a method to optimize the parameter λ such that both the goodness of fit and regularization are best satisfied. This method involves defining two axes, one for SS and one for λR values. In this space the origin is defined as the optimal answer to the sum of squares problem and the regularization problem independent of the other problem. The optimal answer is determined by varying λ, and calculating new values of SS and λR, in order to minimize the distance from this new

point to the origin, and in this way, optimally satisfying both criteria. Because both goodness-of-fit and smoothness are optimized, this is termed the Fully Optimized ContinUouS (FOCUS) pK_a spectrum method.

An important consideration in determining pK_a spectra is the influence of proton binding sites outside the analytical window of the experimental data. Potentiometric data is fundamentally restricted by the pH range of glass electrodes; thus, sites with very high proton affinity (high pK_a values) and very low proton affinity (low pK_a values) are not quantifiable. The influence of these sites is included in the constant offset parameter, S_0 (Eq. 4.4). This term corresponds to how much the titration curve has to be shifted so that the changes in shape can be represented as a sum of monoprotic negatively charged sites; i.e. to the acid neutralizing capacity (Brassard et al., 1990). Alternatively, it can be thought of as the difference between the proton binding sites that are always saturated and those that are always empty over the titration range. If sites outside the experimental window are not constrained during optimization, very large concentrations of strong or weak sites may be included at the edges of the pK_a spectrum. To avoid this, and because the S_0 term already includes average information about these sites, the pK_a outside the experimental window is forced to zero (Nederlof et al., 1994; Černik et al., 1995).

4.4.3. The Multi-Site Complexation Model (MUSIC)

The multi-site complexation model (MUSIC), developed and refined by Hiemstra et al., (1989; 1996) applies Pauling's definition of bond valence (Pauling, 1929) to calculate the theoretical proton affinities of functional groups associated with metal oxides from their crystal structures. Within the oxide structure, the bond valence is simply the mean charge per bond, or, the charge z of a cation (M^{z+}) divided by the number of bonds it shares with surrounding oxygen atoms (Hiemstra et al., 1996). The MUSIC model predicts that the intrinsic proton affinities of individual surface groups will differ as a result of the number of metal ions coordinated to the oxygen atoms being considered. The model also predicts a difference of approximately 14 log K units between the first and second dissociation constants for the same oxygen. In this study, the MUSIC model is used to calculate the proton affinities of functional groups associated with the HMO structure. The surface step-wise dissociation reactions can be written in generalized form (charges are omitted for simplicity) for HMO as:

$$MnOH_2 = MnOH + H \quad (4.7)$$
$$MnOH = MnO + H \quad (4.8)$$

The first step in calculating theoretical pKa using the MUSIC model is to calculate the actual bond valence, s, after Hiemstra et al., (1996):

$$s = \exp[(R-R_0)/b] \quad (4.9)$$

where b is a constant (0.37 Å; Brown and Altermatt, 1985). The value of R_0 is element-specific and represents an average cation-oxygen bond length for the material being considered, calculated using known cation-oxygen distances, R, in the structure and equating the sum of all bond valences around the oxygen to a value of -2 (the valence of

oxygen). The R_0 value of 1.806 used in this study was calculated using an average bulk oxygen sorbed to three Mn with three different bond distances (after Lanson et al., 2002). For a given oxygen sorbed to p manganese and a hydrogen bond valence of 0.2, the expression for the theoretical pK_a is:

$$pK_a = -19.8(-2 + 0.8m + 0.2n + {}^{p}\Sigma_{i=1}\, s_{me}) \quad (4.10)$$

Both m and n are integers in Eq. 4.10, and their values are dependent on the type of surface reaction and represent the number of orbitals available for proton interaction with singly, doubly and triply coordinated surface functional groups (Hiemstra et al., 1996). Thus, if the reaction forms a singly protonated oxygen (Eq. 4.7) then n=1 and m=1, and if a completely deprotonated surface oxygen is formed (Eq. 4.8) then n=2 and m=0.

4.5. Results and Discussion

4.5.1. Extent of Ni Uptake

The Ni uptake to HMO at pH 4 for all titrations and at pH 6.5 for the highest nominal $Ni(NO_3)_2$ concentration are shown in Table 4.4. Maximum uptake of Ni to HMO at pH 4 and 6.5 was 0.88 ± 0.11 $\mu molmg^{-1}$ and 1.7 ± 0.1 $\mu molmg^{-1}$, respectively (Table 4.4). The maximum measured sorption densities compare very well with those measured by Murray (1975), who reported the pH-dependent sorption of Ni (and other cations) to HMO. The experimental conditions in that study were similar to those used here: ionic strength of 0.1M (NaCl), HMO $1gL^{-1}$, and nominal $Ni(NO_3)_2$ of 0.001M. Maximum Ni sorption densities were approximately 0.9 $\mu molmg^{-1}$ at pH 4 and 1.5 $\mu molmg^{-1}$ at pH 6. The similarity between our values and those reported by Murray (1975) is encouraging as Murray showed considerable hysterisis in divalent cation sorption between forward (incremental increases in pH from acidic to basic values) and reverse titrations (incremental decreases in pH from basic to acidic values). The values reported above for Murray (1975) reflect a forward titration, while here a reverse titration was performed. Because the extent of Ni sorption is comparable between the two set of results, the titration results in this study do not appear to be affected by hysteresis. Reverse titrations were run here to better reflect the experimental conditions of the batch experiments where Ni^{2+} was added to solution followed by a pH adjustment. Further, Na-birnessite does undergo structural transformation at acidic pH values (Silvester et al., 1997). While Manceau et al. (1997) have shown that the addition of Co^{2+} in solution did not affect the low-pH transformation of birnessite, the reversibility of this process has not been examined. Thus, to best reflect known transformation processes, titrations were run in reverse.

4.5.2. Acid-Base behaviour of HMO and Ni-substituted HMO

The transformed data from each titration were fit individually using the FOCUS pK_a spectrum method. From the replicate FOCUS spectra a best-fit mean spectrum was calculated and the confidence interval about the results was approximated using the standard deviation of the replicated spectra (Figure 4.4). Results are shown for the

pristine HMO (HMO 2.5gL^{-1}), low Ni loading (0.2mM Ni, HMO 2.5gL^{-1}), and maximum Ni loading (10mM Ni, HMO 2.5gl^{-1}). It is apparent that the residuals are mostly randomly distributed about the best-fit lines. Larger errors are associated with the acid and basic ends of the titrations, consistent with the error function determined by Monte Carlo simulations by Smith et al. (1999), that showed larger errors at the ends of the titration. The range of the pK_a values in the spectra was restricted to 2-8 because of the precipitation of $Ni(OH)_2$ above pH 8.

The pK_a spectra for the pristine HMO sample and low Ni loading (Ni_{low}-HMO) showed 4 peaks within the range of pK_a values. In contrast, with maximum Ni loading (Ni_{max}-HMO), only three peaks were observed in the pK_a range. In order to allow more quantitative comparison between the pK_a spectrum for HMO alone and the spectra for Ni-sorbed HMO, all pK_a spectra were divided into intervals of integer pK_a values (i.e. 2-3, 3-4, 4-5, etc.) and the area beneath the curves integrated to yield the abundance of proton-bindings sites over the defined intervals (Table 4.7). The choice of interval was arbitrary, but was thought to best encompass the four peaks in the pK_a spectrum of pristine HMO without showing bias to any one of the pK_a spectra. Overall, two trends were observed in the pK_a spectra with Ni loading: (1) the number of binding sites at both the lowest (2-3) and highest (7-8) pK_a ranges decreased; and (2) the pK_a values for peaks in the intermediate pK_a intervals shifted towards higher pK_a values and the abundance of sites associated with these peaks increased. These results are discussed further below and rationalized using our EXAFS results and the MUSIC Model.

4.5.3. Considerations and Calculation of Theoretical pK_a values

The MUSIC model has, until now, only been applied to well-characterized oxides. For example, it was used to show that experimental and theoretical pH_{zpc} values for rutile and goethite compared very well (Hiemstra et al., 1996). This comparison was possible because both the dominant faces in solution and the number and relative abundance of surface functional groups were well known for both minerals. Such information is not presently available for HMO. Thus, to identify functional groups associated with HMO, synthetic triclinic Na-birnessite was chosen as a model compound. This decision was made for two reasons: (1) EXAFS result indicated that the pristine HMO had a birnessite-like layered structure; and (2) the crystalline structure of Na-birnessite has been well characterized using powder X-ray diffraction (Post and Veblen, 1990; Drits et al., 1997; Lanson et al., 2002). In adopting Na-birnessite as the model compound, one important assumption was made with regards to the azimuthal orientation of $Mn(III)O_6$ octahedra in the layer structure. $Mn(III)O_6$ octahedra are distorted due to the Jahn-Taller effect; the length of the axial Mn(III)-O bonds (2.26Å) are greater than the equatorial Mn(III)-O bonds (1.93Å). Lanson et al. (2002) reported an elongation of the triclinic Na-birnessite structure along the *a* axis. The elongation was accounted for by assigning the same azimuthal orientation to all Mn(III) octahedra, with the long Mn(III)-O bond in the *ac* plane. The azimuthal orientation of the $Mn(III)O_6$ octahedra associate was not similarly constrained in this study, i.e. a more random orientation of the $Mn(III)O_6$ octahedra was allowed when identifying functional groups. Since, the structure of HMO is amorphous (Kennedy et al., 2004) it is likely to be more disordered than crystalline Na-birnessite.

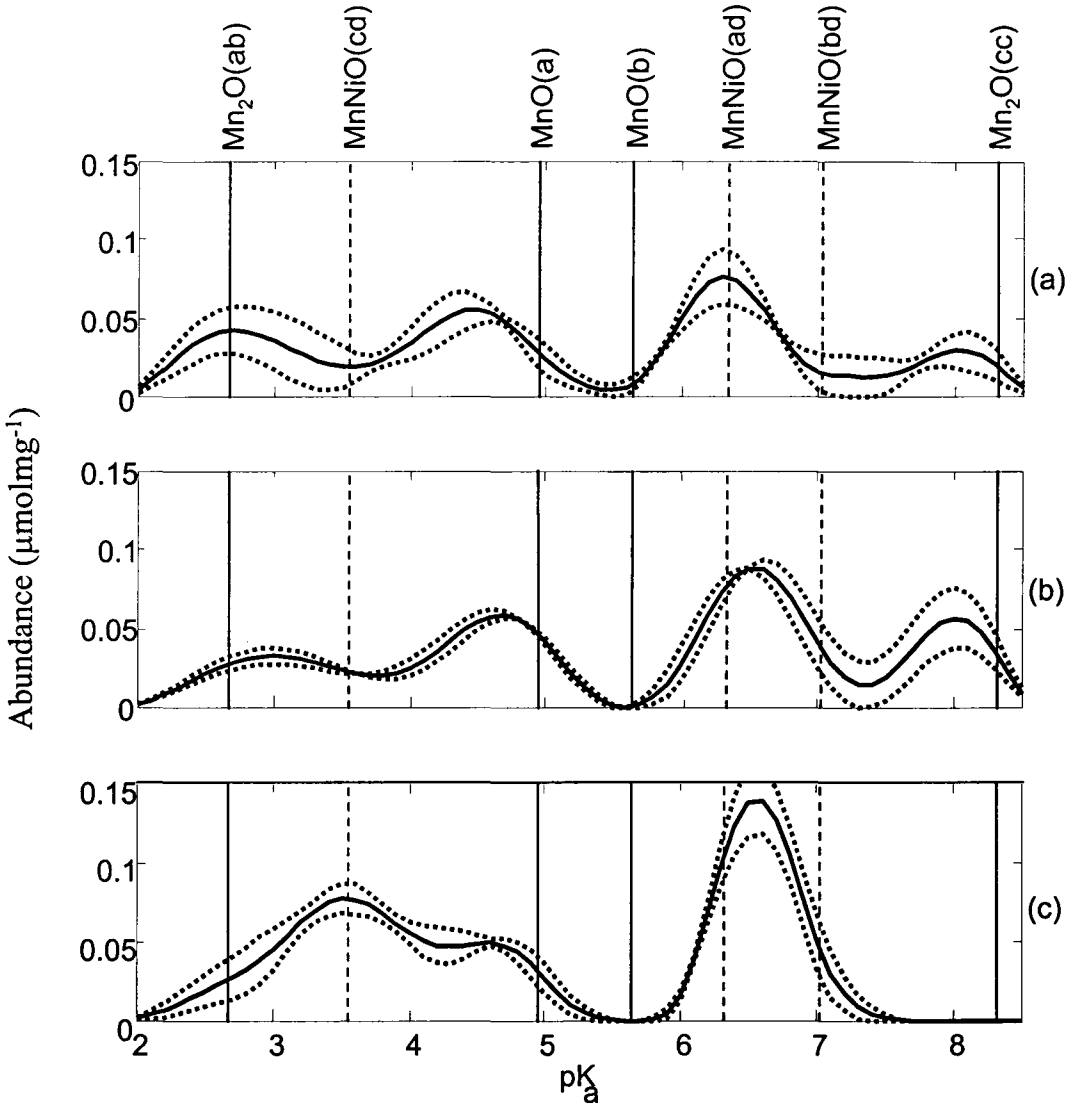

Figure 4.4: pK_a spectra for pristine HMO (a) Ni_{low}-HMO (b) and Ni_{max}-HMO (c). Functional groups assigned to the pristine HMO using the MUSIC model are shown with solid lines, and are labeled above the spectra according to convention. Dashed lines indicate functional groups that are created by isomorphic substitution of Ni for Mn in the MnO_6 octahedral layer, and are similarly labeled.

A number of factors complicate the task of identifying potential functional groups and interpreting the pK_a spectra. The first is that, as mentioned above, the dominant crystal face(s) of birnessite in solution have not been reported. Thus, functional groups associated with different crystal faces of Na-birnessite were identified visually using graphical representation of the crystal structure (Mercury 1.1.2, http://www.ccdc.cam.ac.uk/mercury). It was hypothesized that the dominant face is [010], which runs parallel to the MnO_6 octahedral layer (Figure 4.2a) but functional groups identified here were not limited to that crystal face. The second complicating factor is that the bulk structure of triclinic Na-birnessite transforms to hexagonal H-birnessite at acidic values (Silvester et al., 1997). Experimentally, this means that the acid-base titrations not only reflect the heterogeneity of sites associated with HMO, but will reflect changes in the structure itself. At circumneutral to alkaline pH values (~6-8), the acid-base titration curve will reflect the proton affinities of surface sites that correspond to the structure of triclinic Na-birnessite, i.e. rows of Mn^{3+} and Mn^{4+} that alternate regularly along the *a* axis, according to the sequence $Mn^{3+}Mn^{4+}Mn^{4+}Mn^{3+}$, and do not contain significant layer vacancies (Lanson et al., 2002; Figure 4.2a). Under these conditions, all oxygen atoms on the [010] face are triply coordinated unless they lie in edge positions. In contrast, at acidic pH values, the shape of the acid-base titration curve will reflect the structure of H-birnessite which, compared to Na-birnessite, is characterized by rows depleted in Mn(III), and rich in layer vacancies (Figure 4.2b). The third complicating factor is that the effect(s) of Ni^{2+} on the structure of HMO at all pH values is not definitively known. The EXAFS results of this study suggest that there are multiple sites of Ni uptake in association with HMO. However, the relative importance of each type of site is likely to shift with pH and Ni loading.

Vacancy sites created in the structure of Na-birnessite at acidic values represent a unique set of functional groups on the [010] face. Three undersaturated doubly coordinated oxygen atoms surrounding the vacancy site are left sticking up and down from the layer, into the interlayer. The doubly coordinated oxygens can be (Figure 4.2b): (1) coordinated to two Mn(IV) atoms with identical Mn(IV)-O bond lengths; (2) coordinated to one Mn(III) atom with an equatorial Mn(III)-O bond length and one Mn(IV) atom; and (3) coordinated to one Mn(III) atom with an axial Mn(III)-O bond length and one Mn(IV) atom (if the azimuthal orientation of $Mn(III)O_6$ octahedra is not constrained). The MUSIC model predicts that the latter functional group will be the weakest acid (highest pK_a) as the undersaturation of oxygen valence increases with Mn-O bond lengths. The relative abundance of these different functional groups is not presently resolvable for HMO.

Bond valence values were calculated using published Mn-O bond lengths and the Ni-O bond length measured in this study (Table 4.3). By convention, Mn-oxygen bond distances are represented by small case letters in parentheses. For example, (a) always designates the short 1.91Å Mn(IV) bond length (Table 4.5). Theoretical pK_a values for functional groups associated with Na-birnessite and Ni-sorbed Table 4.6; pK_{a1} and pK_{a2} values reflect the acidity constants for reactions (4.7) and (4.8), respectively. All pK_a values within the range of potentiometric titrations are bolded. Again, by convention, functional groups are represented by the number and type of M^{z+} ions coordinating the

oxygen atom and the M^{z+}-O bond distance(s). For example, the notation $Mn_2O(ab)$ indicates that the oxygen is coordinated by two Mn atoms, one Mn(IV) with bond length (a), and one Mn(III) atom with short bond length (b).

4.5.4. Assigning functional groups to experimentally-derived proton binding sites associated with HMO

The pristine HMO spectrum showed four peaks (Figure 4.4a). The most acidic peak, with a pK_a of ~ 2.7, corresponds to the pK_{a2} for the theoretical site $Mn_2O(ab)$, which has a theoretical pK_{a2} of 2.7 (Figure 4.4a, Table 4.6). Assuming a ± 0.01 Å error in the Mn-O bond lengths, the theoretical pK_a values for this site will range from 1.8 to 3.4 (Errors associated with pK_a values based on this assumption will henceforth follow the theoretical pK_a value in parentheses). This functional group occurs both in association with vacancy sites (as outlined above) and at edge sites. This is the only configuration of doubly-coordinated oxygen atoms at vacancy sites that could be quantified in this study, due to the pH range of the potentiometric titrations (pH ~4-8). The other doubly coordinated oxygen configurations, $Mn_2O(aa)$ and $Mn_2O(ac)$, have theoretical pK_a values below and above the quantifiable range, 2.0 and 11, respectively.

The next two peaks in the experimental pK_a spectrum are inferred to be edge sites MnO(a) and MnO(b), where oxygen is singly coordinated (Figure 4.4a, Table 4.6). These sites have theoretical pKa_1 values of 5.0 (4.5-5.3) and 5.6 (5.2- 6.0), respectively, and are protonated over the entire range of the potentiometric titrations. The most basic peak in the HMO pK_a spectrum is inferred to be the functional group $Mn_2O(cc)$, with theoretical pK_a value of 8.3 (7.9-8.5). This functional group would not occur if Mn(III) octahedra in HMO have constant azimuthal orientation, as was proposed for birnessite. The presence of this functional group suggests that HMO is characterized by a greater degree of disorder than Na-birnessite.

The total number of quantifiable proton binding sites for the pristine HMO was approximately 2.0 $\mu molmg^{-1}$. The two most abundant bindings sites were those assigned to the functional groups MnO(a) and MnO(b); these edge sites represent ~22 and ~27% of the total number of sites, respectively.

4.5.5. Changes in the pKa spectra with Ni^{2+} loading

Ni loading affected both the types and abundance of proton binding sites associated with the HMO (Figure 4.4, Table 4.7). The Ni K-edge EXAFS results of this study served as the foundation in rationalizing these changes. When Ni is sorbed above/below a vacancy site in the MnO_6 octahedral layer, it shares bonds with the three undersaturated doubly coordinated oxygens associated with the vacancy site and three oxygens from water molecules in the interlayer. Oxygens associated with the layer vacancies thus become triply coordinated and are no longer proton reactive under the experimental conditions (e.g. Mn_2NiO (aad); Table 4.6). Thus, with increasing Ni^{2+} loading, a decrease in the number of proton active functional groups associated with layer vacancies was expected. $Mn_2O(ab)$ sites (theoretical pK_a value 2.7) are the only functional group associated with layer vacancies that can be quantified in this study.

Table 4.5: Mn-O and Ni-O interatomic distances and related bond valences (s_{Mn}) for Na-Birnessite, and Ni-sorbed HMO

Mineral	Group	Distance	s_{Mn}
Na-Birnessite	Mn(IV)O(a)	1.91[a]	0.75
	Mn(III)O(b)	1.93[b]	0.72
	Mn(III)O(c)	2.26[b]	0.29
Ni-sorbed HMO	Ni(II)O(d)	2.04[c]	0.53

[a] From Thackeray et al. (1993)
[b] From Töpfer et al. (1995)
[c] This study

Table 4.6: Theoretical pK_a values calculated for functional groups associated with Na-birnessite and Ni-sorbed HMO. pK_a values within the titration range are bolded.

Label	pK_{a1}, pK_{a2} values	Location
MnO(a)	**4.9**, 16.8	edge
MnO(b)	**5.6**, 17.5	edge
MnO(c)	14.1, 25.9	edge
NiO(d)	**9.3**, 21.2	edge
Mn_2O(aa)	-9.9, **2.0**	[010]surface[a], adjacent to vacancy
Mn_2O(bb)	-8.51, **3.4**	edge
Mn_2O(cc)	**8.3**, 20.2	edge
Mn_2O(ab)	-9.2, **2.7**	[010] surface adjacent to vacancy
Mn_2O(ac)	-0.79, **11.1**	[010] surface adjacent to vacancy
Mn_2O(bc)	-0.10, **11.8**	edge
MnNiO(ad)	-5.5, **6.3**	Ni replaces Mn(III), interior or edge
MnNiO(bd)	-4.9, **7.0**	Ni replaces Mn(III), edge
MnNiO(cd)	**3.5**, 15.4	Ni replaces Mn(III), edge
Mn_3O(abc)	N.A., -3.2	[010] surface
Mn_3O(aaa)	N.A., -12.9	[010] surface
Mn_3O(aab)	N.A., -12.3	[010] surface
Mn_3O(abb)	N.A., -9.7	[010] surface
Mn_3O(aac)	N.A., -3.8	[010] surface
Mn_3O(acc)	N.A., **5.3**	[010] surface
Mn_2NiO(aad)	N.A., -8.5	Ni sorbed at vacancy
Mn_2NiO(abd)	N.A., -7.9	Ni sorbed at vacancy
Mn_2NiO(acd)	N.A., 0.59	Ni sorbed at vacancy

[a] [010] surface designates the crystal face running parallel to the MnO_6 octahedral layer, not the "surface" of the HMO particle

Although not statistically significant, a decrease in the number of Mn_2O(ab) sites with Ni loading was observed, as indicated by a decrease in the abundance of sites in the pK_a 2-3 range from 0.31±0.12 $\mu molmg^{-1}$ for the pristine HMO to 0.20 ± 0.09 $\mu molmg^{-1}$ for Ni_{max}-HMO (Table 4.7).

For pK_a values above 3, three trends were observed with increased Ni loading: 1) the appearance of a peak in the pK_a interval 3-4 at maximum Ni loading; 2) the consistency in the abundance of sites and pK_a value of the peak in the pK_a interval 4-5 amongst all pKa spectra; and 3) an increase in the abundance of binding sites in pK_a interval 7-8 and an associated shift of the peak to more alkaline values with increasing Ni loading (Figures 4.4 and 4.5). The first and third trends observed are due to isomorphic substitution of Ni for Mn(III) in the MnO_6 octahedral layer. The type of binding site with pK_a value between 3 and 4 corresponds to the edge site MnNiO(cd), with theoretical pKa_1 value of 3.6 (3.0-3.9). The oxygen atom in this functional group is coordinated to one Mn(III) atom (axial Mn-O interatomic distance) and one Ni atom. The creation of MnNiO(cd) is also consistent with the disappearance of Mn_2O(cc) edge sites in the pKa spectrum for Ni_{max}-HMO. As suggested earlier, the presence of Mn_2O(cc) sites suggests that HMO is a more disordered solid than Na-birnessite. It is likely that the substitution of a NiO_6 octahedron for a distorted $Mn(III)O_6$ octahedron lessens steric strain on the solid and may be the driving force for Ni substitution for Mn in the solid structure.

The peak in the pK_a interval 4-5 was attributed to the edge site MnO(a) for the pristine HMO sample. The number of sites in this pK_a interval remained very consistent amongst titrations (~0.46 $\mu molmg^{-1}$), indicating that neither increased concentrations of Ni in solution nor increased Ni loading in association with the bulk solid affected proton interactions with this type of edge site. This functional group can thus be considered "proton-active" but not "Ni-active". The larger implications of this will be discussed further below.

Finally, the increase in the number of binding sites between pK_a interval 6-7 and the associated shift in this peak to more alkaline pK_a values with increased Ni^{2+} loading is ascribed to: (1) the creation of functional groups MnNiO(ad) and MnNiO(bd), with theoretical pK_a values of 6.3 (5.6-7.0) and 7.0 (6.3-7.6), respectively (Figure 4.4, Table 4.6); and (2) a decrease in the total number of MnO(b) sites. MnNiO(ad) functional groups are created if Ni replaces an Mn(III) adjacent to a layer vacancy or replaces an Mn(III) adjacent to an Mn(IV) at an edge position. The creation of MnNiO(ad) edge sites results in a decrease in the number of MnO(b) sites, and a corresponding increase in the number of NiO(d) sites. An increase in the number of NiO(d) sites is not quantifiable in this study (theoretical pK_{a1} is 9.3; Table 4.6). MnNiO(bd) sites can be created by the substitution of Ni for an Mn(III) at an edge position that is adjacent to another Mn(III) or a vacancy site. Overall, all three functional groups, MnO(b), MnNiO(ad), and MnNiO(bd), likely contribute to the abundance of sites that have pK_a values between 6 and 7 and can not be differentiated in this study.

Table 4.7: Abundance of sites with pK_a values between integer values and the total number of sites over the pK_a spectrum for each set of experimental acid-base titration curves. Sites were quantified by integrating the area beneath the pKa spectrum curve over the defined ranges. Mean values (n=3) ± standard deviation are given.

	Abundance		
pK_a range	Pristine HMO	Ni_{low}-HMO (0.2 mM $Ni(NO_3)_2$)	Ni_{max}HMO (10 mM $Ni(NO_3)_2$)
2 to 3	0.31 ± 0.12	0.20 ± 0.03	0.20 ± 0.09
3 to 4	0.25 ± 0.13	0.25 ± 0.03	0.67 ± 0.08
4 to 5	0.45 ± 0.10	0.46 ± 0.04	0.46 ± 0.07
5 to 6	0.15 ± 0.05	0.13 ± 0.04	0.08 ± 0.03
6 to 7	0.53 ± 0.11	0.68 ± 0.09	0.95 ± 0.15
7 to 8	0.17 ± 0.10	0.31 ± 0.16	0.09 ± 0.05
8 to 9	0.10 ± 0.05	0.20 ± 0.06	0.00 ± 0.00
ΣTotal	2.0 ± 1.2	2.2 ± 0.7	2.4 ± 0.9

4.5.6. Discussion of titration and modeling results

The results from the geochemical and theoretical modeling efforts, although more qualitative than quantitative, do allow some unique insights into the reactivity of HMO for Ni. The first important insight is that HMO is characterized by an edge site, MnO(a) (pK_{a1} 4.5-5.3), that binds protons but does not bind Ni, even at elevated Ni^{2+} solution concentrations. A model that assumed a competitive process for H^+ and Ni^{2+} sorption at this type of site would be erroneous, and would result in over-prediction of the extent of Ni^{2+} at circumneutral pH.

The second important insight is into the 2-D distribution of Mn(III) in the MnO_6 octahedral layer. Several results from our interpretations of the pK_a spectra of pristine HMO and Ni-sorbed HMO suggest that layers rich in Mn(III) are positioned along the edges of the MnO_6 octahedral layers. The first piece of evidence for this is that mean values for site abundance of MnO(a) (pK_a range 4-5) and MnO(b) sites (pK_a range 6-7) for pristine HMO are not significantly different (0.45 ± 0.10 and 0.53 ± 11 $\mu molmg^{-1}$, respectively; Table 4.7). Considering the ideal distribution of Mn(III) in Na-birnessite (Figure 4.2), the abundance of MnO(a) edge sites exceeds that of MnO(b) edge sites along the *a* axis. Additionally, if, rows rich in $Mn(IV)O_6$ represented edge sites parallel to the *b* axis, the ratio of MnO(a) sites to MnO(b) would increase further. However, a high ratio of MnO(a) sites to MnO(b) sites is not observed in the pristine HMO. The second piece of evidence is the presence of MnO(cc) edge sites. The presence of this functional group requires that two $Mn(III)O_6$ octahedra be positioned adjacent to one another at the edge of an MnO_6 octahedral layer. The third piece of evidence is that Ni is substituted for Mn(III) in the MnO_6 octahedral layer largely at edge sites, including MnNiO(ad), MnNiO(bd) and MnNiO(cd). This last piece of evidence requires further clarification.

Substitution of Ni for Mn(III) at edge sites and the creation of functional sites MnNiO (bd) and MnNiO(cd) increases the abundance of sites in the pK_a ranges 6-7 and 3-4, respectively. The abundance of sites in the pK_a range 3-4 increased from a mean value of 0.25 ± 0.013 $\mu molmg^{-1}$ for both the pristine HMO and Ni_{low}-HMO to a mean value of 0.67 ± 0.08 $\mu molmg^{-1}$ for Ni_{max}-HMO. Thus, the upper limit for the abundance of MnNiO(cd) functional groups created is ~0.4 $\mu molmg^{-1}$. Considering that the maximum Ni sorption density measured at pH 4.0 was 0.80 ± 0.11 $\mu molmg^{-1}$, isomorphic substitution of Ni for Mn(III) at edge sites could account for as much as 50% of the total Ni sorbed at pH 4. At higher pH values (6.5), it is more difficult to even estimate the percentage of the total Ni sorbed that is accounted for by Ni substitution for Mn(III) at edge sites. This is because multiple functional groups (MnO(b), MnNiO(ad) and MnNiO(bd)) potentially contribute to the peak in pK_a interval 6-7. However, while MnNiO(ad) sites can occur both in the bulk of the HMO structure (adjacent to vacancy sites), the presence of MnNiO(bd) sites is consistent with substitution of Ni for Mn(III) located at edges. Further, consistent with the substitution of Ni for Mn(III) positioned at edge sites are our EXAFS results for the Ni-sorbed DRY HMO, in which the coordination number for Ni-Mn edge sharing pairs was 5.4 ± 3.2 (Table 4.3). While the error associated with the coordination number for the Ni-Mn edge-sharing path is quite

large, and is correlated to the value of the fixed value of the Debye-Waller factor (σ^2), it does suggest that Ni is being substituted adjacent to vacancy sites in the bulk structure (theoretical coordination number of 5) and at edge sites (theoretical coordination number of 4).

Although speculative, one other insight into the structure of HMO can be drawn from the integration of the modeling and EXAFS results. Earlier it was suggested that Ni may substitute for Mn(III) to lessen steric strain on the MnO_6 octahedral layer. At the low Ni sorption density of our batch experiments, Ni was sorbed above/below layer vacancies at both pH 4 and 6.5, and was substituted for Mn only at the higher pH value. Consistent with this, the pK_a spectrum for Ni_{low}-HMO does show an increase in the abundance of sites in the pK_a 6-7 interval due to substitution of Ni for Mn(III), from 0.53 $\pm$ 0.11 to 0.68 $\pm$ 0.09 $\mu molmg^{-1}$ while is does not show increased site abundance in the pK_a interval 3-4 (Table 4.7). Further, as Ni loading increases, the peak in the pK_a interval 6-7 increases in abundance and a shift in the peak to a higher pK_a value is observed. Functional groups that have pK_a values in this range are MnO(b), MnNiO(ad) and MnNiO(bd). The theoretical pK_a values of the functional groups MnNiO(ad) and MnNiO(bd) are approximately 6.4 and 7.0, respectively. A shift in the peak in this interval to higher pK_a values with increased Ni loading suggests that MnNiO(ad) functional groups are created first, followed by the creation of MnNiO(bd) functional groups. Simply stated, Ni may be substituting for Mn(III) adjacent to Mn(IV) ion in the HMO structure before it replaces Mn(III) positioned adjacent to another Mn(III) ion. Further, MnNiO(ad) functional groups can be created at edge sites but can also occur within the bulk structure of the HMO material, if Ni substitutes for Mn(III) adjacent to a vacancy site. Thus, isomorphic substitution of Ni for Mn(III) may be preferred at sites within the bulk structure where strain on the layer is maximized due to Jahn-Teller distortion of $Mn(III)O_6$ octahedra. Consistent with this contention is that the edge functional group MnNiO(cd) (pK_a 3-4 interval) appears only at maximum Ni loading (Ni_{max}-HMO; Figure 4.4, Table 4.7).

Finally, the creation of the MnNiO(cd) functional group at maximum Ni sorption density (Figure 4.4), indicates that Ni substitution for Mn in the MnO_6 octahedral layer occurs at pH values below 6.5 at higher Ni loadings. This result appears to contradict our EXAFS results, in which Ni is exclusively adsorbed above/below layer vacancies at pH 4. However, the Ni sorption density at pH 4 in the batch experiments was low (Table 4.2) and substitution of Ni in the layer at acidic pH values at higher sorption densities likely reflects the strong relative affinity of functional groups at vacancy sites for Ni.

4.6. Conclusions and Implications

Integration of our EXAFS results with potentiometric titrations and the MUSIC model has enabled a much more in-depth analysis of the reactivity of HMO and the 2-D distribution and nature of Ni sorption to HMO.

1. HMO is an amorphous solid (Kennedy et al., 2004) and this study indicates that the structure of this solid is more disordered than that of crystalline Na-birnessite,

with Mn(III) atoms having unconstrained azimuthal orientation and occupying edge positions.

2. HMO has ion exchange properties and Ni is sorbed above/below layer vacancies in the bulk structure of this solid. However, the number of type of functional groups associated with vacancy sites can not be quantified accurately in this study due to their high (MnO(aa)) and low (MnO(ac)) proton affinities. There is a competing process that becomes increasingly important with increased pH and surface loading, which is the isomorphic substitution of Ni for Mn in the MnO_6 layer. The driving force for this substitution is likely the stability imparted to the overall bulk structure.
3. Both a geochemical and a theoretical model were used and confirmed that sorption of Ni in association with HMO was not the result of "surface complexation". Monodentate proton binding sites do occur at the edges of the bulk HMO solid (MnO(a)) but there is not evidence in this study of Ni binding to these sites. Inclusion of these sites in model of metal binding to HMO will result in over-prediction of metal sorption at circumneutral pH, which has been shown both by Kennedy et al. (2004), and by others.
4. Beyond the results of this study, these findings have important implications for sorption of trace metals to HMO occurring in natural environments, and specifically to biogenic Mn oxyhydroxides. The distribution of lower valence Mn ions in these structures has not been determined. In situ analysis of Mn(II) oxidation by *Bacillus sp.* strain SG-1 did not show any evidence of intermediary Mn(III) phases (Bargar et al., 2001), however, intermediate Mn(III) ions can not be excluded. Rothe et al., (1999) showed local variability in Mn(II) and Mn (III) associated with natural biogenic HMO agglomerates and no evidence of Mn(III) as a reaction intermediate, while Pecher et al. (2003) did observe Mn(III) at the microscale associated with biogenic HMO nodules. Our results indicate that the distribution of lower valence Mn is of utmost importance, and because biogenic Mn oxyhydroxides have been shown to have such a high sorption capacity for Pb (Nelson et al., 1999a), future research should be focused on determining the spatial distribution of lower valence Mn ions within these amorphous structures.

CHAPTER 5: SUMMARY, SIGNIFICANT FINDINGS, AND FUTURE WORK

The research carried out and presented in this thesis has advanced our understanding of how microbial activity influences trace metal dynamics in Acid Rock Drainage (ARD) and has demonstrated why current surface complexation models (SCM) do not accurately represent metal sorption to hydrous manganese oxyhydroxide (HMO). Additionally, this research has indicated potential methodological artifacts associated with common sequential extraction techniques for Fe minerals. Specifically, the results and significant findings of this thesis and future work are summarized under: (1) sequential extraction method development and evaluation for ARD solid matrices; (2) in situ investigation of metal sequestration by ARD biofilms; and (3) laboratory investigation of the HMO sorption mechanisms for Ni.

5.1. Sequential Extraction Method Development and Evaluation

A rapid, microwave based, extraction scheme for determination of metals associated with ARD biofilm solid samples was developed to minimize sample degradation associated with live organic material. The results indicate that a microwave based extraction protocol provides a rapid and robust approach for determining metal concentrations within this complex matrix, which is advantageous over more traditional wet geochemical methodology.

The selectivity of the extractants used in the developed microwave digestion sequential extraction protocol (MDSEP) was evaluated for the specific bulk crystalline mineralogy of the biofilms. Jarosite was one of the major crystalline components of the samples from the ARD environment, and this study is the first to examine the dissolution of jarosite in published extraction reagents. X-ray diffraction (XRD) analysis was used to monitor changes in the mineralogy of synthetic K-jarosite with extraction step. Jarosite was partially decomposed early in the extraction scheme and hematite was formed. Subsequent application of the MDSEP to natural biofilm samples was also examined by XRD. The reactivity of the natural jarosite for the extraction reagents differed from that of synthetic K-jarosite. The natural jarosite appears to have been more extensively altered earlier in the extraction sequence and there was evidence for the formation of hydrous ferric oxide in the transformation in addition to hematite.

The important finding of this work was that the transformation of jarosite did not impact trace metal (Ni, Co, Cr) partitioning results as determined by analyses of Fe and metal concentrations within the relevant extraction steps. This result may reflect the nature of metal sorption within the sample site biofilms. Biofilm Mn oxyhydroxides exclusively controlled levels of Co, Ni, and Cr in the amorphous oxyhydroxide fraction. These results reflect the ARD conditions of the study site where low pH would limit the

efficacy of Fe oxide sorptive abilities (i.e. higher pH_{zpc} of Fe oxides compared to HMO). However, the results of this thesis suggest artifacts in metal extraction may occur. The potential for methodological artifacts and associated shifts in metal partitioning should thus be carefully considered for systems at more circumneutral pH values where metal sorption to Fe minerals can be significant.

Analysis of solid-phase metal partitioning is of utmost importance as it has implications for the long-term sequestration of a metal, as well as its bioavailability and toxicity. The issue of detection limits in complex media has long plagued quantification of metals partitioned within natural solids; metals are often associated with fine-grained reactive particles that do not represent the bulk mineralogical or organic components of the sample by mass. Sequential extraction techniques serve an important role (globally) in assessing the relative importance of sorbent phases for metals in numerous natural and extreme environments, including ARD. The utility of this analytical method is not in question; however, the results of this thesis highlight the need for examination of natural samples prior to the application of any given extraction scheme. Extraction techniques also are limited in their selectivity for iron minerals, and thus in environments where sorption to iron oxides is the dominant control on trace metal cycling, these schemes may have more limited utility.

5.2. In Situ Investigation of Metal Sequestration by ARD Biofilms

The results of this field-based research are the first to quantitatively examine metal dynamics within ARD biofilms using geochemical techniques at both diel and seasonal timescales. They provide strong evidence for the significant role that microbial activity can play in metal geochemistry in ARD environments.

The sampling protocol of this study was designed to link the patterns of solid-phase metal speciation to the dynamic microbially-driven geochemical conditions measured at the microscale within biofilms on diel, and seasonal time scales (June-Sept, 2001 and June – August 2002). The results show that biofilms in shallow, tailings associated streams accumulated metals over the sampling season, indicating that metal scavenging by these biological solids is stable over a seasonal time frame. Total biofilm-associated Mn and Co doubled over the sampling season while Ni and Co concentrations increased by over 6-fold. Biofilm oxygen and pH gradients measured over diel time scales with microelectrodes were observed to be temporally variable, suggesting highly dynamic geochemical gradients within biofilms.

Biofilm metal retention and affinities were element specific indicating that different processes control their sequestration. Metals were specifically scavenged by the organic constituents of the biofilm itself (Ni, Co) and/or associated biominerals of amorphous Mn oxyhydroxides (HMO; Ni, Co and Cr). Results are consistent with sorption and co-precipitation processes controlling Ni and Co biofilm association, while Cr dynamics appear linked to those of Mn through redox processes. Biofilm HMO concentrations increased seasonally but showed significant diel fluctuations, indicating that both formation and dissolution processes occurred over rapid time scales in these biofilms. Biofilm HMO concentrations increased nocturnally, but decreased during

daylight hours to late afternoon minima. Under the geochemical conditions of the streams, observed HMO formation rates can only be explained by microbial catalysis.

The results from this work challenge a number of traditionally held beliefs in geochemistry; primarily that trace metal solid sequestration can be predicted by solution pH and dissolved metal concentrations. Total metal uptake in the biofilms was independent of either water column solution metal concentrations (0.2 μm filtered) or pH. Rather, biofilm metal uptake was related more to the dynamic geochemical conditions created within the biofilm by shifts in the relative dominance of photosynthetic and respirative metabolic activity over diel timescales. The findings of this study indicate that microbial ecology and activity can drive metal behaviour in ways not predicted by abiotic models.

The importance of HMO for trace metal sequestration in the ARD biofilms also underscores the relevance of small, fine-grained and reactive particles within a larger bulk sample for trace metal behaviour. In the ARD system, the bulk crystalline component of the biofilms was jarosite. The results of this study indicate that jarosite is not an important solid fraction for the sequestration of trace metals in ARD biofilms (see section 5.3). The ultimate relevance of these findings is their potential to serve as a foundation for the future development of bioremedation strategies in ARD environments. Effective remediation strategies must incorporate a sound understanding of the processes that control trace metal behaviour. The results presented here clearly demonstrate that future effort should not be directed towards elucidating those processes controlling Fe concentrations in these natural biofilm systems, but, rather should be directed at harnessing the microbially-controlled processes that impact biofilm-associated Mn concentrations.

Future work on ARD biofilms should focus on determining the exact mechanisms of trace metal-HMO associations. Metal partitioning within the biofilm was determined at the macroscale in this work, using sequential extraction. The results of this field study could be furthered by analysis of the association of Ni, Co, and Cr with HMO at the micro and molecular level. Microscale maps of elemental distribution within the biofilm structure and analysis of the local coordination environment of metals is possible using synchrotron-based micro X-ray fluorescence (μ-XRF) and EXAFS, respectively. However, this task is a challenge analytically because of the organic nature of the biofilms (photooxidation of organic matter by the beam can induce reduction of Mn oxides; Dr. K. Kemner, personal communication, Advanced Photon Source, Argonne, IL, U.S.A.), and because the overwhelming fluorescence signal from Fe in the biofilm samples at wavelengths above the Fe K-edge renders detection of Ni and Co very difficult by these techniques. The analytical challenges associated with these techniques for analysis of metal partitioning again highlights the challenge of linking metal behaviour to the small reactive particles important for their sequestration in heterogeneous mixed-solid matrices.

5.3. Laboratory investigation of the HMO sorption mechanisms for Ni

Investigation of Ni sorption to HMO in this thesis provides new insight into the mechanisms by which HMO "sorbs" Ni, which are not currently addressed by surface

complexation models (SCMs). HMO is increasingly receiving attention as an important sorbent for trace metals in a number of natural environments including ARD-impacted freshwaters, underscoring the substantive significance of these findings. Prediction of metal sorption to a wide array of mineral surfaces by SCMs is predicated on the assumptions that: (1) metal uptake or "sorption" to functional groups occurs strictly at the surface of the solid particle; and (2) metal sorption and proton binding are competitive processes. SCMs have historically been developed around the mechanisms of proton and metal sorption to iron oxides and have been extended to mineral surfaces in general.

The study of Ni sorption to HMO presented in this thesis was designed to build upon the results of an earlier study in which the Ni sorptive capacity to HMO was determined. The HMO samples were hydrologically conditioned prior to sorption experiments to reflect wetting and drying cycles in natural environments, which may impact the reactivity of minerals for metals (Kennedy et al. 2004). The extent of Ni uptake observed to the hydrologically pre-conditioned HMO samples could not be rationalized in light of the widely differing pH_{zpc} and proton binding capacities of the pre-conditioned HMO samples determined using a bulk geochemical model. Simply stated, metal sorption to HMO was not accurately predicted from the model-derived proton binding capacity of the solid.

The present study was designed to move beyond bulk geochemical interpretation of Ni sorption to HMO. Analysis of Ni-sorbed HMO samples at the molecular level indicated that the discrepancy between the observed extent of Ni sorption to HMO and that predicted could not be attributed to the formation of a separate Ni solid phase. At all pH values examined, (2, 4 and 6.5), EXAFS results were consistent with sorption of Ni above/below layer vacancies in the MnO_6 octahedral layer and with isomorphic substitution of Ni for Mn at circumneutral pH (pH 6.5). The HMO samples were shown to have birnessite-like layered structures with bulk oxidation state of ~3.7, indicating the presence of lower valence Mn ions in the bulk structure (Mn(II) and/or Mn(III)). The spatial distribution of lower valence Mn ions has been implicated in the reactivity of HMO for trace metal ions by other authors (e.g. Shen et al., 1993; Manceau et al., 1997). The results of this thesis move beyond implication and are the first to mechanistically explain observed pH-dependent local Ni coordination environment in terms of the spatial distribution of Mn(III) in the HMO structure. This was possible only through the integration of results from acid-base titration, EXAFS, and a theoretical model. Together these experimental and theoretical techniques allowed identification of functional groups important for Ni sorption within the bulk HMO structure.

A number of unique insights can be drawn from this study regarding the reactivity of HMO for Ni and are the direct result of the synergistic use of molecular-level and macroscale techniques. The first is with regards to the fundamental assumptions made in predicting metal sorption using SCM. As opposed to Ni complexing with functional groups at strictly surface sites, Ni is sorbed within the bulk structure (at vacancy sites) and is isomorphically substituted within the MnO_6 octahedral layers. The process of isomorphic substitution can not be described by the forces driving the exchange of ions at the surface or adsorption. The second insight afforded by the integration of macro- and molecular-level techniques is that Ni and proton uptake sites are independent in some

instances; i.e. there are proton exchange sites associated with the HMO structure that will not bind Ni, even at elevated solution concentrations. Additionally, HMO layer vacancy sites have a high affinity for Ni, but the number and type of functional groups associated with these sites cannot be accurately predicted (due to very high and low proton affinities).

More novel are the insights this study gives into the spatial distribution of lower valence Mn ions in the bulk structure of HMO. HMO is an amorphous phase (Kennedy et al., 2004) and the azimuthal orientation of Mn(III) in this solid appears to be more random than in crystalline triclinic Na-birnessite. The spatial distribution of Mn(III) within the HMO structure results in strain on the MnO_6 octahedral layer due to Jahn-Taller distortion of $Mn(III)O_6$ octahedra. The results of this study are consistent with substitution of Ni into octahedral positions in the MnO_6 octahedral layer that impart greater structural stability to the overall structure, i.e. Ni will substitute first for Mn(III) ions positioned adjacent to Mn(IV) ions within the bulk structure, followed by substitution at sites of adjacent Mn(III) ions at edges. The driving force for the substitution of Ni within the bulk HMO structure is not currently being addressed in models of Ni (and other divalent cations) sorption to HMO. Further, the results of this study indicate that pH and $Ni^{2+}_{(aq)}$ concentration impacts the relative amount of the Ni substituted in the layer, warranting more analysis of this process for Ni and other metal cations.

Only Ni sorption to HMO was examined here. However, sorption of various other divalent cations to HMO has been examined at the molecular level by other researchers. Pb, Zn, Cu and Co, Ca and Mg sorb above/below layer vacancies (Kuma et al., 1994; Manceau et al., 2002a) and Co is also substituted in the MnO_6 octahedral layer (Manceau et al., 1997). Thus, the mechanisms identified here for Ni sorption to HMO are consistent with the body of literature on cation sorption to HMO, and together these studies represent a pool of data sufficient to further the development of an improved model. Present limitations to the development of this model are the pH range of the glass electrodes (~ pH 4-10, Smith et al., 1999) as functional groups characterized by very high and very low proton affinities can not be quantified.

Future research on metal sorption to HMO should focus on: (1) the structure and reactivity of biogenic HMO, and (2) the extent of metal sorption from multi-element solutions. Elucidation of the structure and reactivity of HMO formed by microbial catalysis is of utmost importance as the presence of HMO in most natural environments is thought to be the result of microbial oxidation of Mn(II). The reactivity of these biogenic HMO for metal cations is likely to be higher than synthetic abiotic analogs, as shown by Nelson et al. (1999a) for Pb. The distribution of lower valence Mn ions within these structures has not been elucidated and is currently under debate. There would be great utility in applying the integrated approach used in this thesis (i.e. integration of EXFAS, and the FOCUS and MUSIC models) to the analysis of metal sorption to biogenic HMO. Further, the extent of metal uptake from multi-element solutions in association with both synthetic HMO (for purposes of comparison with the existing literature) and biogenic HMO is necessary for the development of an accurate predictive model for this solid. Analysis of trace metal concentrations in association with natural oceanic

ferromanganese nodules suggests that the total uptake of metals from a multi-element solution (natural ocean water) is limited to concentrations no greater than the maximum uptake of one individual element (i.e. ~0.17 $\mu molmg^{-1}$; Usui, 1979). In contrast, Catts and Langmuir (1986) indicated that sorption from a multi-element solution was additive; i.e. the total metal sorption was equivalent to the sum of metal uptake for each individual element (~0.5 $\mu molmg^{-1}$). As freshwaters and oceans are naturally multi-element solutions, these conflicting results indicate that further research into the reactivity of HMO for trace metals is needed.

REFERENCES

Acker, J.G. and Bricker, O.P., 1992. The influence of pH on biotite dissolution and alteration kinetics at low temperature. *Geochimica et Cosmochimica Acta*, 56: 3073-3092.

Ahmann, D., Krumholz, L.R., Hermond, H.F., Lovley, D.R. and Morel, F.M.M., 1997. Microbial mobilization from sediments of the Aberjona watershed. *Environmental Science & Technology*, 31: 2923-2930.

Allard, B., Hakansson, K. and Karlsson, S., 1987. The importance of sorption phenomena in relation to trace element speciation and mobility. In: L. Landner (Ed.), *Speciation of Metals in Water, Sediment and Soil Systems*. Lecture Notes in Earth Sciences No. 11, Springer Berlin. pp. 99-112.

Appello, C.A.J. and Postma, D., 1999. A consistent model for surface complexation on birnessite (-MnO_2) and its application to a column experiment. *Geochimica et Cosmochimica Acta*, 63: 3039-3048.

Arnold, R.G., Dichristina, T.J. and Hoffman, M.R., 1988. Reductive dissolution of Fe (III) oxides by *Pseudomonas* sp. 200. *Biotechnology and Bioengineering*, 32: 1081-1096.

Balikungeri, A. and Haerdi, W., 1988. Complexing abilities of hydrous manganese oxide surfaces and their role in the speciation of heavy metals. *International Journal of Environmental and Analytical Chemistry*, 34: 215-225.

Banerjee, D. and Nesbitt, H.W., 1999. Oxidation of aqueous Cr(III) at birnessite surfaces: Constraints and mechanism. *Geochimica et Cosmochimica Acta*, 63: 1671-1687.

Banfield, J.F. and Hamers, R.J., 1997. Processes at minerals and surfaces with relevance to microorganisms and prebiotic synthesis. In: J.F. Banfield, K.H. Nealson (Eds.), *Geomicrobiology: Interactions Between Microbes and Minerals*. Reviews in Mineralogy, 35: 81-117.

Bárány, E., Bergdahl, I.A., Bratterby, L.E., Lundh, T., Samuelson, G., Schütz, A., Skerfving, S. and Oskarsson, A., 2002. Trace elements in whole blood serum from Swedish Adolescents. *Science of the Total Environment*, 286: 129-141.

Bargar, J.G., Tebo, B.M. and Villinsky, J.E., 2001. In situ characterization of Mn(II) oxidation by spores of the marine Bacillus sp. Strain SG-1. *Geochimica et Cosmochimica Acta*, 64:2775-2778.

Barns, S.M. and Nierzwicki-Bauer, S.A., 1997. Microbial diversity in modern subsurface, ocean, surface environments. In: J.F. Banfield, K.H. Nealson (Eds.), *Geomicrobiology: Interactions Between Microbes and Minerals*. Reviews in Mineralogy, 35: 35-80.

Bartlett, R.J., 1991. Chromium cycling in soils and water: Links gaps and methods.

Environmental Health Perspectectives, 92: 17-24.

Bartschat, B.M., Cabaniss, S.E. and Morel, F.M.M., 1992. Oligeoelectrolyte model for cation binding by humic substances. *Environmental Science & Technology*, 26: 284-294.

Baruthio, F., 1992. Toxic effects of chromium and its compounds. *Biological Trace Element Research*, 32: 145-153.

Bazylinski, D.A. and Moskowitz, B.M., 1997. Microbial biomineralization of magnetic iron minerals: microbiology, magnetism, and environmental significance. In: J. F. Banfield, K. H. Nealson (Eds.), *Geomicrobiology: Interactions between Microbes and Minerals*. Reviews in Mineraology, 35: 181-223.

Beard, B.L. and Johnson, C.M., 1999. High precision iron isotope measurements of terrestrial and lunar materials. *Geochimica et Cosmochimica Acta*, 63: 1653-1660.

Bendell-Young, L.I. and Harvey, H.H., 1992. The relative importance of manganese and iron oxides and organic matter in the sorption of trace metals by surficial lake sediments. *Geochimica et Cosmochimica Acta*, 56: 1175-1186.

Benjamin, M.M. and Leckie, J.O., 1981. Multiple-site adsorption of Cd, Cu, Zn and Pb on amorphous iron oxyhydroxide. *Journal of Colloid and Interface Science*, 79: 209-221.

Bennett, P.C., Hiebert, F.K. and Rogers, J.A., 2000. Microbial control of mineral-groundwater equilibria: Macroscale to microscale. *Hydrogeology Journal*, 8:47-62.

Beveridge, T.J., 1978. The response of cell walls of *Bacillus subtilis* to metals and to electron microscopic stains. *Canadian Journal of Microbiology*, 24: 89-104.

Beveridge, T.J., 1984. Bioconversion of inorganic materials. In: M.J. Klug and C.A. Reddy (Eds.), *Current Perspectives in Microbial Ecology*. American Society for Microbiology, Washington D.C. pp.601-607.

Beveridge, T.J., 1989. Role of cellular design in bacterial metal accumulation and mineralization. *Annual Reviews in Microbiology*, 43: 147-171.

Beveridge, T.J. and Murray, R.G.E., 1980. Sites of metal deposition in the cell wall of *Bacillus subtilis*. *Journal of Bacteriology*, 141: 876-887.

Beveridge, T.J., Schultze-Lam, S. and Thompson, J.B., 1995. Detection of anionic sites on bacterial walls their ability to bind toxic heavy metals and form sedimentable flocs and their contribution to mineralization in natural freshwater environments. In: H. Allen, C.P. Huang, G.W. Bailey and A.R. Bowers (Eds.), *Metal Speciation and Contamination of Soil*. CRC Press Inc. Boca Raton, pp. 183-205.

Bigham, J.M., 1994. Mineralogy of ochre deposits formed by sulfide oxidation. In: J.L. Jambor and D.W. Blowes, (Eds.), *Environmental Geochemistry of Sulfide Mine-Wastes*. Mineralogical Association of Canada, Short Course, 22: 103-132.

Bigham, J.M., Schwertmann, U. and Carlson, L., 1992. Mineralogy of precipitates formed by the biogeochemical oxidation of Fe(II) in mine drainage. In: H.W.C. Skinner and R.W. Fitzpatrick, (Eds.), *Biomineralization Processes of Iron and Manganese*. Catena Verlag, Germany, pp 219-232.

Borkovek, M., Rusch, U., Černík, M., Koper, G.J.M. and Westall, J.C., 1996. Affinity distributions and acid-base properties of homogeneous and heterogeneous sorbents: exact results versus experimental data inversion. *Colloids and Surfaces*, 107: 285-296.

Brassard, P., Kramer, J.R. and Collins, P.V., 1990. Binding site analysis using linear programming. *Environmental Science & Technology*, 24: 195-201.

Bratina, B.J., Stevenson, B.S., Green, W.J. and Schmidt, T.M. 1998. Manganese reduction by microbes from oxic regions of the Lake Vanda (Antarctica) water column. *Applied and Environmental Microbiology*, 64: 3791-3797.

Brick, C.M. and Moore, J.N., 1996. Diel Variation of Trace Metals in the Upper Clark Fork River, Montanta. *Environmental Science & Technology*, 30: 1953-1959.

Brock, T.I., 1984. *Biology of Microorganisms. 4th Ed.* Prentice-Hall, Inc. Englewood Cliffs, N.J. U.S.A.

Brophy, G.P., Scott, E.S. and Snellgrove, R.A., 1962. Sulfate studies II: Solid solution between alunite and jaosite. *American Mineralogist*, 22: 773-784.

Brown, G.E. Jr., Parks, G.A. and Chisholm-Brause, C.J., 1989. In situ x-ray absorption spectroscopic studies of ions at oxide-water interfaces. *Chimia*, 43: 248-256.

Brown, G.E., Henrich, V.E., Casey, W.H., Clark, D.L., Eggleston, C., Felmy, A., Goodman, D.W., Gratzel, M., Maciel, G., McCarthy, M.I., Nealson, K.H., Sverjensky, D.A., Toney, M.F. and Zachara, J.M., 1999. Metal Oxide Surfaces and their interactions with aqueous solutions and microbial organisms. *Chemical Reviews*, 99: 77-174.

Brown, I.D. and Altermatt, K.K., 1985. Bond Valence parameters obtained from a systematic analyis of the Inorganic Crystal Structure Database. *Acta Crystallographica*, B41: 244-247.

Buffle, J., 1988. *Complexation reactions in aquatic systems: an analytical approach.* Ellis Horwood, Chichester.

Burns, V.M. and Burns, R.G., 1978. Diagenetic features observed inside deep-sea manganese nodules from the north equatorial Pacific. *Scanning Electron Microscopy*, 1: 245-52.

Buser, W., Graf, P. and Feitnecht, W., 1954. *Helvetica Chimica Acta*, 37: 2322-33.

Campbell, P.C.G., 1995. Interactions between trace metals and aquatic organisms: a critique of the free-ion activity model. In: A.Tessier and D. Turner (Eds), *Metal Speciation and Bioavailability in Aquatic Systems.* IUPAC Series on Analytical and Physical Chemistry of Environmental Systems. John Wiley, Chichester, pp. 45-102.

Campbell, P.G.C., Lewis, A.G., Chapman, P.M., Crowder, A.A., Fletcher, W.K., Inber, B., Luoma, S.N., Stokes, P.M. and Winfrey, M., 1988. *Panel on Biologically Available Metals in Sediments*; Pub. No. NRCC27694. National Research Council of Canada, Ottawa. 3-27.

Campbell, P.G.C. and Tessier, A., 1989. Geochemistry and bioavailability of trace metals in sediments. In: A. Boudou, F. Ribeyre (Eds.), *Aquatic Ecotoxicology.* CRC Press Boca Raton. pp. 125-148.

Canfield, D.E. and Des Marais, D.J. 1993. Biogeochemical cycles of carbon, sulfur and

free oxygen in a microbial mat. *Geochimica et Cosmochimica Acta*, 57: 3971-3984.

Carroll, S.A., O'Day, P.A. and Piechowski, M., 1998. Rock-water interactions controlling zinc, cadmium and lead concentrations in surface waters and sediments. U.S. Tri-State Mining District, II, Geochemical Interpretation. *Environmental Science & Technology*, 32: 956-965.

Catts, J.G. and Langmuir, D. 1986. Adsorption of Cu, Pb, and Zn by δMnO_2: applicability of the site-binding surface complexation model. *Applied Geochemistry*, 1: 255-264.

Černik, M., Borkovek, M. and Westall, J.C., 1995. Regularized least-squares methods for the calculation of discrete and continuous affinity distributions for heterogeneous sorbents. *Environmental Science & Technology*, 29: 413-425.

Chao T.T. and Zhou, L., 1983. Extraction techniques for selective dissolution of amorphous iron oxides from soils and sediments. *Journal of Soil Science Society of America Proceedings*, 47: 225-232.

Chapnick, S.D., Moore, W.S. and Nealson, K.H., 1982. Microbially mediated manganese oxidation in a freshwater lake. *Limnology and Oceanography*, 27: 669-677.

Characklis, W.G., 1990. Laboratory Biofilm Reactors. In: G.W. Characklis and K.C. Marshall (Eds.), *Biofilms*. Wiley, New York. pp 55-89.

Charlet L. and Manceau A., 1992. X-ray absorption spectroscopic study of the sorption of Cr(III) at the oxide/water interface. II Adsorption, coprecipitation and surface precipitation on ferric hydrous oxides. *Journal of Colloid and Interface Science*, 148: 425-442.

Chisholm-Brause, C.J., Hayes, K.F., Roe, A.L., Brown, G.E. Jr., Parks, G.A. and Leckie, J.O., 1990. Spectroscopic investigation of Pb(II) complexes at the (-Al_2O_3/water interface. *Geochimica et Cosmochimica Acta*, 54: 1897-1909.

Chung, J., Zasoski, R.J. and Lim, S., 1994. Kinetics of chromium (III) oxidation by various manganese oxides. *Agricultural Chemistry and Biotechnology*, 37: 414-420.

Clesceri, L.S., Greenberg, A.E. and Eaton, A.D. (Eds.), 1998. *Standard Methods for the Examination of Water and Wastewater.* 20th Ed. American Public Health Association. Washington D.C.

Colmer, A.R. and Hinkle, M.E., 1947. The role of microorganisms in acid mine drainage. *Science*, 106: 253-256.

Cornell, R.M. and Schwertmann, U., 1996. *The Iron Oxides. Structure, Properties, Reactions, Occurrence and Uses.* VCH. New York.

Coston, J.A., Fuller, C.C. and Davis, J.A., 1995. Pb^{2+} and Zn^{2+} adsorption by a natural aluminum- and iron-bearing surface coating on an aquifer sand. *Geochimica et Cosmochimica Acta*, 59: 3535-3547.

Cox, J.S., Smith, D.S., Warren, L.A. and Ferris, F.G., 1999. Characterizing heterogeneous bacterial surface functional groups using discrete affinity spectra for proton binding. *Environmental Science & Technology*, 33: 4514-4521.

Daughney, C.J., Fein, J.B., Yee, N., 1998. A comparison of the thermodynamics of metal

adsorption onto two common bacteria. *Chemical Geology*, 144:151-176.

Davies, D.G., Parsek, M.R., Pearson, J.P., Iglewski, B.H., Costerton, J.W. and Greenberg, E.P., 1998. The involvement of cell-to-cell signals in the development of a bacterial biofilm. *Science*, 280: 295-298.

Davis, B.S., 1997. Geomicrobiology of the oxic zone of sulfidic mine tailings. In: J.M. McIntosh and L.A. Groat (Eds.), *Biological-Mineralogical Interactions*. Mineral Association of Canada Short Course Series, 25: 93-112.

Davis, J.A. and Kent, D.B., 1990. Surface complexation modelling in aqueous geochemistry. In: M. F. Hochella Jr., A.F. White, (Eds.), Mineral-Water Interface Geochemistry. *Reviews in Mineralogy* 23: 177-260.

Davison, W., 1993. Iron and Manganese in lakes. *Earth-Science Reviews*, 34: 119-163.

De Beer, D. and Schramm, A., 1999. Micro-environments and mass transfer phenomena in biofilms studied with microsensors. *Water Science and Technology*, 39: 173-178.

Devore, J., 1995. *Probability and Statistics for Engineers and the Sciences. 4th Ed.* Duxbury Press. Pacific Grove, Calif.

Diem, D. and Stumm, W., 1984. Is dissolved Mn^{2+} being oxidized by O2 in absence of Mn-bacteria or surface catalysts? *Geochimica et Cosmochimica Acta*, 48: 1571-1573.

Dold, B., 2003. Speciation of the most soluble phases in a sequential extraction procedure adapted for geochemical studies of copper sulfide mine wastes. *Journal of Geochemical exploration*, 80: 55-68.

dos Santos Furtado, A.L. and Casper, P., 2000. Different methods for extracting bacteria from freshwater sediment and a simple method to measure bacterial production in sediment samples. *Journal of Microbiological Method*, 41: 249-257.

Douglas, S. and Beveridge, T.J., 1998. Mineral formation by bacteria in natural microbial communities. *FEMS Microbiology Ecology*, 26: 79-88.

Doyle, R.J., Matthews, T.H. and Streips, U.N., 1980. Chemical basis for selectivity of metal ions by the *Bacillus subtilis* cell wall. *Journal of Bacteriology*, 143: 471-480.

Drever, J.I., 1997. *The Geochemistry of Natural Waters. Surface and Groundwater Environments.* 3rd Ed. Prentice Hall, London.

Drits, V.A., Silvester, E., Manceau, A. and Gorskhov, A.I., 1997. The Structure of Monoclinic Na-Exchanged Birnessite and Hexagonal H-Birnessite. Part 1. Results from X-ray Diffraction and Selected Area Electron Diffraction. *American Mineralogist*, 82: 946-961.

Drouet, D. and Navrotsky, A., 2003. Synthesis, characterization, and thermochemistry of K-Na-H_3O jarosites. *Geochimica et Cosmochimica Acta*, 67: 2063-2076.

Dutrizac, J.E., 1984. The behaviour of impurities during jarosite precipitation. In: R. G. Bautista (ed). Hydrometallurgical Process Fundamentals. Plenum Press, New York, pp 125-169.

Dutrizac, J.E. and Kaiman, S., 1976. Synthesis and properties of jarosite-type compounds. *Canadian Mineralogist*, 142: 151-8.

Dutrizac, J.E. and Jambor, J.L., 2000. Jarosites and their application in Hydrometallurgy. In: Sulfate Minerals: Crystallography, Geochemistry, and Environmental Significance. *Reviews in Mineralogy and Geochemistry*. 40: 405-452.

Dymond, J., Lyle, M., Finney, B., Piper, D.Z., Murphy, K., Conard, R. and Pisias, N., 1984. Ferromanganese nodules from MANOP Sites H, S, and R - control of mineralogical and chemical composition by multiple accretionary processes. *Geochimica et Cosmochimica Acta*, 48: 931-49.

Dzombak, D.A., Morel, F.M.M., 1990. *Surface Complexation Modelling. Hydrous Ferric Oxide*. Wiley. New York.

Edwards, K.J., Gihring, T.M. and Banfield, J.F., 1999. Seasonal variations in microbial populations and environmental conditions in an extreme acid mine drainage environment. *Applied and environmental microbiology*, 65: 3627-3632.

Eggleston, C.M., Ehrhardt, J.-J. and Stumm, W., 1996. Surface structural controls on pyrite oxidation kinetics: An XPS-UPS, STM and modelling study. *American Mineraogist*, 81: 1036-1056.

Eggleston, C.M., Higgins, S.R. and Maurice, P.A., 1998. Scanning probe microscopy of environmental interfaces. *Environmental Science & Technology*, 32: 456A-459A.

Ehrlich, H.L., 2000. Ocean manganese nodules: biogenesis and bioleaching possibilities. *Minerals & Metallurgical Processing*, 17: 121-128.

Emerson, D., 2000. Microbial oxidation of Fe(II) and Mn(II) at circumneutral pH. In: D. R. Lovley, (Ed.) *Environmental Microbe-Metal Interactions*. ASM Press, Washington. pp. 31-52.

Falconbridge Ltd., 1998. INCO/Falconbridge Levack/Onaping Closure Plan Part 1, Falconbridge version. Prepared by: SENES Consultants Ltd., November 1998.

Fanfani, L., Zuddas, P. and Chessa, A., 1997. Heavy metals speciation as a tool for studying mine tailings weathering. *Journal of Geochemical Exploration*, 58: 241-248.

Fanning, D., Keramidas, V. and El-Desoky, M., 1989. Micas. In: J. Dixon and S. Weed, (Eds.), *Minerals in Soil Environments*. Soil Science Sociert of America, pp. 551-634.

Farquhar, M.L., Vaughan, D.J., Hughes, C.R.; Charnock, J.M.; England and Katharine E. R., 1997. Experimental studies of the interaction of aqueous metal cations with mineral substrates: lead, cadmium, and copper with perthitic feldspar, muscovite, and biotite. *Geochimica et Cosmochimica Acta*, 61: 3051-3064.

Fein, J.B., Daughney, C.J., Yee, N. and Davis, T.A., 1997. A chemical equilibrium model for metal adsorption onto bacterial surfaces. *Geochimica et Cosmochimica Acta*, 61: 3319-3328.

Felter, S.P. and Dourson, M.L., 1997. Hexavalent chromium-contaminated soils: options for risk assessment and risk management. *Regulatory Toxicology and Pharmacology*, 25: 43-59.

Fendorf, S.E. and Zasoski, R., 1991. Chromium(III) Oxidation by δ-MnO_2. *Environmental Science & Technology*, 26: 79-85.

Ferris, F.G., 1997. Formation of authigenic minerals by bacteria. In: J. M. McIntosh, L. A. Groat, (Eds.), Biological-Mineralogical Interactions. *Mineralogical*

Association of Canada Short Course Series, 25: 187-208.

Ferris, F.G., Konhauser, J.O., Lyvén, B. and Pedersen, K., 1999. Accumulation of metals by bacteriogenic iron oxides in a subterranean environment. *Geomicrobiology Journal*, 16: 181-192.

Ferris, F.G., Schultze, S., Witten, T.C., Fyfe, W.S. and Beveridge, T.J., 1989. Metal interactions with microbial biofilms in acidic and neutral pH environments. *Applied and Environmental Microbiology*, 55: 1249-1257.

Filgueiras, A.V., Lavilla, I. And Bendicho, C., 2002. Chemical extractions for metal partioning in environmental solid samples. *Journal of Enviornmental Monitoring*, 4, 823-857.

Fortin, D., Ferris, F.G. and Beveridge, T.J., 1997. Surface-mediated mineral development. In: J. F. Banfield, K. H. Nealson, (Eds.), *Geomicrobiology: Interactions between Microbes and Minerals.* Reviews in Mineralogy, 35: 161-180.

Fortin, D., Leppard, G.G. and Tessier, A., 1993. Characteristics of lacustrine diagenetic iron oxyhydroxides. *Geochimica et Cosmochimica Acta*, 57: 4391-4404.

Foster, A.L., Brown, G.E. and Parks, G.A., 2003. X-ray absorption fine structure study of As(V) and Se(IV) sorption complexes on hydrous Mn oxides. *Geochimica et Cosmochimica Acta*, 67: 1937-1953.

Fuller, C.C. and Harvey, J.R., 2000. Reactive uptake of trace metals in the hyporheic zone of a mining-contaminated stream, Pinal Creek, Arizona. *Environmental Science & Technology*, 34: 1150-1155.

Geesey, G.G., Jang, L., Jolley, J.G., Hankins, M.R., Iwaoka, T. and Griffiths, P.R., 1988. Binding of metal ions by extracellular polymers of biofilm bacteria. *Water Science and Technology*. 20: 161-165.

Ghiorse, W.C. and Ehrlich, H.L., 1992. Microbial biomineralization of iron and manganese. CATENA Supplement 21:75-99.

Goldberg, S., 1992. Use of surface complexation models in soil chemical systems. *Advances in Agronomy*, 47: 233-239.

Golden, D.C., Dixon, J.B. and Chen, C.C. 1986. Ion Exchange, thermal transformations, and oxidizing properties of birnessite. *Clays and Clay minerals*. 34: 511-520.

Government of Canada, 1991. The State of Canada's Environment. *Ministry of Supply and Services, Ottawa*, pp 11-19.

Gray, M.J. and Malati, M.A., 1979. Adsorption from aqueous solution by δ-Manganese dioxide. II. Adsorption of some heavy metal cations. *Journal of Chemical Technology and Biotechnology*, 29: 135-144.

Grice, J.D., Gartrell, B., Gault, R.A. and Van Velthuizen, J., 1994. Erninickelite, $NiMn_3O_7 \cdot 3H_2O$, A new mineral species from the Siberia Complex, Western Australia: Comments on the crystallography of the chalcophanite group. *Canadian Mineralogist*, 32: 333-337.

Guha, H., Saiers, J.E., Brooks, S., Jardine, P. and Jayachandran, K., 2001. Chromium transport, oxidation, and adsorption in manganese-coated sand. *Journal of Contaminant Hydrology*, 49: 311-334.

Gulmini, M; Ostocoli, G., Zelano, V. and Torazzo, A. 1994. Comparison between microwave and conventional heating procedures in Tessier's extraction of Calcium, Copper, Iron and Manganese in Lagoon Sediment. *Analyst*, 119:2075-2080.

Hall, G.E.M. and Pelchat, P. 1999. Comparability of results obtained by thte use of different selective extraction schemes for the determination of element forms in soils. *Water, Air, and Soil Pollution*. 112, 41-53.

Hall, G.E.M., Vaive, J.M., Beer, R. and Hoashi, M., 1996. Selective leaches revisited, with emphasis on the amorphous Fe oxyhydroxide phase extraction. *Journal of Geochemical Exploration*, 56: 59-78.

Hare, L., 1992. Aquatic insects and trace metals: bioavailability, bioaccumulation and toxicity. *Critical Reviews in Toxicology*, 22: 327-369.

Hayes, K.F. and Leckie, J.O., 1987. Modelling ionic strength effects on cation adsorption at hydrous oxide/solution interfaces. *Journal of Colloid Interface Science*, 115:564-572.

Hendershot, W.H. and Lavkulich, L.M., 1983. Effect of sesquioxide coatings on surface charge of standard mineral and soil samples. *Soil Science Society of America Journal*, 47: 1252-1256.

Helios-Rybicka, E. and Forstner, U., 1986. Effect of oxyhydrate coatings on the binding energy of metals by clay minerals. In: P. G. Sly (Ed.), *Sediments and Water Interactions*. Springer, Berlin, pp. 381-385.

Hiemstra, T., Venema, P. and Van Riemsdjik, W.H. 1996. Intrinsic Proton Affinity of Reactive Surface Groups of Metal (Hydr)oxides: The Bond Valence Principle. *Journal of Colloid and Interface Science*, 184: 680-692

Hiemstra, T., Van Riemsdijk, W. H. and Bolt G. H., 1989. Multisite Proton Adsoption Modeling at the Solid/Solution Interface of (Hydr)oxides: A New Approach I. Model Description and Evaluation of Intrinsic Reaction Constants. *Journal of Colloid Interface Science*, 133: 91-104.

Holmström, H. and Öhlander, B., 2001. Layers rich in Fe- and Mn-oxyhydroxides formed at the tailings-water interface, a possible trap for trace metals in flooded mine tailings. *Applied Geochemistry*, 74: 189-203.

Hunt, A.P., Hamilton-Taylor, J. and Parry, J.D., 2001. Trace metal interactions with epilithic biofilms in small acidic mountain streams. *Archiv fur Hydrobiologie*. 153: 155-176.

Honeyman, B.D. and Santschi, P.H. 1988. Metals in aquatic systems. *Environmental Science & Technology*, 22:862-871.

Ingebritsen, S.E., Sanford and W.E., Toth, J., 2000. Recent studies on bacterial populations and processes in subseafloor sediments: a review. *Hydrogeology Journal*, 8: 11-28.

Jenne, E.A., 1968. Controls on Mn, Fe, Co, Ni, Cu and Zn concentrations in soils and water: the significant role of hydrous Mn and Fe oxides. In: R. A. Baker, (Ed.), *Trace Inorganics in Water*. American Chemical Society, 73: 337-387.

Johnson, B.B., 1990. Effect of pH, temperature and concentration on the adsorption of cadmium on goethite. *Environmental Science & Technology*, 24: 112-118.

Johnson, R.H., Blowes, D.W., Robertson, W.D. and Jambor, J.L., 2000. The hydrogeochemisty of the Nickel Rim mine tailings impoundment, Sudbury, Ontario. *Journal of Contaminant Hydrogeology*, 41: 49-80.

Kashefi, K. and Lovley, D.R., 2000. Reduction of Fe(III), Mn(IV), and toxic metals at 100°C by Pyrobaculum islandicum. *Applied and Environmental* Microbiology, 66: 1050-1056.

Kay, J.T., Conklin, M.H., Fuller, C.C. and O'Day, P.A., 2001. Processes of nickel and cobalt uptake by a manganese oxide forming sediment in Pinal Creek, Globe mining district, Arizona. *Environmental Science & Technology*, 35: 4719-4725.

Kelly, S.D., Fowle, D.A., Boyanov, M.I., Bunker, B.A., Yee, N., Kemner, K.M. and Fein, J.B., 2002. X-ray absorption fine structure determination of pH-dependent U-bacterial cell wall interactions. *Geochimica et Cosmochimica Acta*, 22:3855-3871.

Kennedy, C., Smith, D. S. and Warren, L.A., 2004. Surface chemistry and relative Ni sorptive capacities of synthetic hydrous Mn oxyhydroxides under variable wetting and drying regimes. *Geochimica et Cosmochimica Acta*, 68: 443-454.

Kinniburgh, D.G., Barker, J.A. and Whitfield, M., 1983. A comparison of some simple adsorption isotherms for describing divalent cation adsorption by ferrihydrite. *Journal of Colloid and Interface Science*, 95: 370-384.

Kinniburgh, D.G., van Riemsdijk, W.H., Koopal, L.K. and Benedetti M.F., 1998. Ion binding to humic substances: measurements, models and mechanisms. In: E.A . Jenne (Ed.), *Adsorption of Metals by Geomedia: Variables, Mechanisms and Model Applications*. Academic Press, San Diego. pp.467-482.

Kinniburgh, D.G., van Riemsdijk, W.H., Koopal, L.K., Borkovec, M., Benedetti, M.F. and Avena, M.J., 1999. Ion binding to natural organic matter: Competition heterogeneity stoichiometry and thermodynamic consistency. *Colloids and Surface, A: Physicochemical and Engineering Aspects*, 151: 147-166.

Kinniburgh, D.G., Milne, C.J., Benedetti, M.F., Pinheiro, J.P., Filius, J., Koopal, L.K. and van Riemsdijk, W.H., 1996. Metal ion binding by humic acid: Application of the NICA-Donnan Model. *Environmental Science & Technology*, 30: 1687-1698.

Konhauser, K.O., 1998. Diversity of bacterial iron mineralization. *Earth-Science Reviews*, 43: 91-121.

Konhauser, K.O. and Urrutia, M.M., 1999. Bacterial clay authigenesis: a common biogeochemical process. *Chemical Geology*, 161:399-413.

Konhauser, K.O., Fyfe, W.S., Ferris, G. and Beveridge T.J., 1993. Metal sorption and mineral precipitation by bacteria in two Amazonian river systems: Rio Solimões and Rio Negro Brazil. *Geology*, 21: 1103-1106.

Kuma, K., Usui, A., Paplawsky, W., Gedulin, B. and Arrhenius, G. 1994. Crystal structure of synthetic 7 Å and 10 Å manganates substituted by mono- and divalent cations. *Mineralogical Magazine*, 58: 425-447.

Kumar, R., 1994. Leaching Charateristics of Disordered Birnessite and Goethite doped with Ni, Co and Cu in Sorption mode. *Materials Transactions, JIM.* 35: 27-34.

Lanson, B., Drits, V.A., Feng, Q. and Manceau, A. 2002. Structure of synthetic Na-birnessite: Evidence for a triclinic one-layer unit cell. *American Mineralogist*, 87: 1662-1671.

Lanson, B., Drits, V.A., Silvester, E. and Manceau, A. 2000. Structure of H-exchanged hexagonal birnessite and its mechanism of formation from Na-rich monoclinic buserite at low pH. *American Mineralogist*, 85: 826-838.

Lawrence, J.R., Korber, D.R., Wolfaardt, G.M., Caldwell, D.E., 1995. Behavioural strategies of surface-colonizing bacteria. In: G. Jones (Ed.), *Advances in Microbiology Ecology*. Plenum Press, New York, 14: 1-75.

Lawrence, J.R., Neu, T.R., Swerhone, G.D.W., 1998a. Application of multiple parameter imaging for the quantification of algal bacterial and exponents of microbial biofilms. *Journal of Microbiological* Methods, 32: 253-261.

Lawrence, J. R., Swerhone, G. D. W. and Kwong, Y. T. J., 1998b. Natural attenuation of aqueous metal contamination by an algal mat. *Canadian Journal of Microbiology*, 44: 825-832.

Le Goff, P., Baffier, N., Bach, S. and Pereira-Ramos, J.P., 1996. Synthesis, ion exchange and electrochemical properties of lamellar phyllomanganates of the birnessite group. *Materials Research Bulletin*. 31: 63-775.

Leathen, W.W., Braley, S.A. and McIntyre, L.E., 1953. The role of bacteria in the formation of acid form certain sulfuric constituents associated with butuminous coal. II. Ferrous iron-oxidizing bacteria. *Applied Microbiology*, 1:65-68.

Ledin, M. and Pedersen, K., 1996. The environmental impact of mine wastes - Roles of microorganisms and their significance in treatment of mine wastes. *Earth-Science Reviews*, 41: 67-108.

Lens, P., de Beer, D., Cronenberg, C., Ottengraf, S. and Verstraete, W., 1995. The use of microsensors to determine population distributions in UASB aggregates. *Water Science and Technology*, 31: 273-280.

Leveille, S.A., Leduc, L.G., Ferroni, G.D., Telang, A.J. and Voordouw, G., 2001. Monitoring of bacteria in acid mine environments by reverse sample genome probing. *Canadian Journal of Microbiology*, 47: 431-442.

Little, B.J., Wagner, P.A., Lewandowski, Z., 1997. Spatial Relationships between bacteria and mineral surfaces. In: J. F. Banfield, K. H. Nealson, (Eds.), *Geomicrobiology: Interactions between Microbes and Minerals*. Reviews in Mineralogy, 35: 123-159.

Liu C.X., Y.A. Gorby; Zachara J.M., Brown C.F., 2002. Reduction kinetics of Fe(III), Co(III), U(VI), Cr(VI), and Tc(VII) in cultures of dissimilatory metal-reducing bacteria *Biotechnology and Bioengineering*, 80: 637-649.

Loganathan, P. and Burau, R.G., 1973. Sorption of heavy metals by hydrous manganese oxide. *Geochimica et Cosmochimimica Acta*, 37: 1277-1293.

Lores, E.M. and Pennock, J.R., 1998. The effect of salinity on binding of Cd, Cr, Cu and Zn to dissolved organic matter. *Chemosphere*, 37: 861-874.

Losi, M.E. and Frankenberger, W.T. Jr., 1997. Bioremediation of selenium in soil and water. *Soil Science*, 162: 692-702.

Lovley, D.R., 1995. Microbial reduction of iron and manganese, and other metals. In: D. L. Sparks (Ed.), *Advances in Agronomy*. Academic Press, New York. pp. 175-230.

Lovley, D.R. and Phillips, E.J.P., 1992. Reduction of uranium by Desulfovibrio

desulfuricans. *Applied and Environmental Microbiology*, 58: 850-856.

Lovley, D.R. and Anderson, R.T., 2000. Influence of dissimilatory metal reduction on fate of organic and metal contaminants in the subsurface. *Hydrogeological Journal*, 8: 77-88.

Lowenstam, H.A., 1981. Minerals formed by organisms. *Science*, 221:1126- 131.

Lowenstam, H.A. and Weiner, S., 1989. *On Biomineralization*. Oxford University Press, New York.

Luenberger, B. and Schindler, P.W., 1986. Application of integral pK spectrometry to the titration curve of fulvic acid. *Analytical Chemistry*, 58: 1471-1474.

Lünsdorf, H., Bummer, I., Timmis, K.N. and Wagner-Döbler, I., 1997. Metal selectivity of *in situ* microcolonies in biofilms of the Elbe River. *Journal of Bacteriology*, 179: 31-40.

Magini, M., Licheri, G., Paschina, G., and Piccaluga, P., 1988. *X-Ray Diffraction of Ions in Aqueous Solution: Hydration and Complex Formation*. CRC Press Inc., Boca Raton, FL.

Mahan, K.I., Foderaro, T.A., Garza, T.L., Martinez, R.M., Maroney, G.A., Trivisonno, M.R. and Wilging, E.M., 1987. Microwave Digestion Techniques in the Sequential Extraction of calcium, iron, chromium, manganese, lead and zinc in sediments. *Analytical Chemistry*, 59: 938-945.

Malmström, M. and Banwart, S., 1997. Biotite dissolution at 25°C: The pH dependence of dissolution rate and stoichiometry. *Geochimica et Cosmochimica Acta*, 61: 2779-2799.

Manceau, A. and Combes, J.M. 1988. Structure of the Mn and Fe oxides and oxyhydroxides: a topographical approach by EXAFS. *Physics and Chemistry of Minerals*, 15: 283-295.

Manceau, A., Boisset, M.C., Sarret, G., Hazemann, J.L., Mench, M., Cambier, P. and Prost, R., 1996. Direct determination of lead speciation in contaminated soils by EXAFS spectroscopy. *Environmental Science & Technology*, 30: 1540-1552.

Manceau, A. and Charlet, L., 1992. X-ray absorption spectroscopic study of the sorption of Cr(III) at the oxide/water interface: I. Molecular mechanism of Cr(III) oxidation on Mn oxides. *Journal of Colloid and Interface Science*, 148: 443-458.

Manceau, A., Drits, V.A., Silvester, E., Bartoli, C. and Lanson, B., 1997. Sturctural mechanism of Co(II) oxidation by the phyllomanganate, Na-buserite. *American Mineralogist*. 82: 1150-1175.

Manceau, A., Gorshkov, A.I. and Drits, V.A., 1992. Structural chemistry of Mn, Fe, Co, and Ni manganese hydrous oxides: Part II. Information from EXAFS spectroscopy and electron and X-Ray diffraction. *American Mineralogist*. 77: 1144-1157.

Manceau, A., Lanson, B. and Drits, V.A., 2002a. Structure of heavy-metal sorbed birnessite. Part III: Results from powder and polarized extended X-ray adsorption fine structure spectroscopy. *Geochimica et Cosmochimica Acta*, 66: 2639-2663.

Manceau, A., Llorca, S. and Calas, G., 1987. Crystal chemistry of cobalt and nickel in lithiophorite and asbolane from New Caledonia. *Geochimica et Cosmochimica Acta*, 51: 105-113.

Manceau, A., Tamura, N., Marcus, M.A., MacDowell, A.A., Celestre, R.S., Sublett, R.E., Sposito, G. and Padmore, H.A., 2002b. Deciphering Ni sequestration in soil ferromanganese nodules by combining X-Ray fluorescence, absorption, and diffraction at micrometer scales of resolution. *American Mineralogist*, 87: 1494-1499.

Mandernack, K.W., Post, J., Tebo, B.M., 1995. Manganese mineral formation by bacterial spores of a marine Bacillus strain SG-1: Evidence for the direct oxidation of Mn(II) to Mn(IV). *Geochimica et Cosmochimica Acta*, 59: 4393-4408.

Mann, H., 1990. Biosorption of Heavy Metals by Bacterial Biomass. In: B. Volesky (Ed.), *Biosorption of Heavy Metals*. CRC Press Inc. Boca Raton. pp. 94-137.

Mann, S., 1983. Mineralization in biological systems. *Structure and Bonding*, 54: 125-174.

Marsh, T.L., Leon, N.M. and McInerney, M.J., 2000. Physicochemical factors affecting chromate reduction by aquifer materials. *Geomicrobiology Journal*, 17: 291-303.

Martell A.E., Motekaitis, R.J. and Smith, R.M., 1988. Structure-stability relationships of metal complexes and metal speciation in environmental aqueous solutions. *Environmental Toxicology and Chemistry*. 7: 414-434.

Martinez, C.E. and McBride, M.B., 1998. Solubility of Cd^{2+}, Cu^{2+}, Pb^{2+}, and Zn^{2+} in aged coprecipitates with amorphous iron hydroxides. *Environmental Science & Technology*, 32: 743-748.

Martínez, G.A., Traina, S.J. and Logan, T.J., 1998. Characterization of proton affinity reactions in polyelectrolytes: Discrete vs continuous distribution of sites approach. *Journal of Colloid and Interface* Science, 199: 53-62.

Matocha, C.J., Elzinga, E.J. and Sparks, D.L. 2001. Reactivity of Pb(II) at the Mn(III,IV) (oxyhydr)oxide-water interface. *Environmental Science and Technology*, 35: 2967-2972.

McCarty, D.K., Moore, J.N. and Marcus, W.A., 1998. Mineralogy of trace element association in an acid mine drainage iron oxide precipitate; comparison of selective extractions. *Applied Geochemistry*, 13: 165-176.

McEwen, R.S., 1971. Crystallographic studies on nickel hydroxide and the higher nickel oxides. *Journal of Physical Chemistry*, 75: 1982-1989.

McKenzie, R.M. 1970. The reaction of cobalt with manganese dioxide minerals. *Australian Journal of Soil Research*, 8: 97-106.

McKeown, D.A. and Post, J.E., 2001 Characterization of manganese oxide mineralogy in rock varnish and dendrites using X-ray absorption spectroscopy. *American Mineralogist*, 86: 701-713.

McLean, R.J.C., Fortin, D. and Brown, D.A., 1996. Microbial metal-binding mechanisms and their relation to nuclear waste disposal. *Canadian Journal of Microbiology*, 42: 392-400.

Mellin, T.A. and Lei, G., 1993. Stabilization of 10Å-manganates by interlayer cations and hydrothermal treatment: Implications for the mineralogy of marine manganese concretions. *Marine Geology*, 115: 67-83.

Mercz, T.I. and Madgwick, J.C., 1982. Enhancement of bacterial manganese leaching by microalgal growth products. *Australian Institute of Mining and Metallurgy*, 283:43-6.

Meriah Arias, Y. and Tebo B.M., 2003. Cr(VI) reduction by sulfidogenic and nonsulfidogenic microbial consortia. *Applied and Environmental Microbiology*, 69: 1847-1853.

Milne, C.J., Kinniburgh, D.G., de Wit, J.C.M., van Riemsdijk, W.H. and Koopal, L.K., 1995. Analysis of proton binding by a peat humic acid using a simple electrostatic model. *Geochimica et Cosmochimica Acta*, 59: 1101-1112.

Moffett, J.W. and Ho, J., 1996. Oxidation of cobalt and manganese in seawater via a common microbially catalyzed pathwa. *Geochimica et Cosmoshimica Acta*, 60: 3415-3424.

Mojzsis, S.J., Arrhenius, G., McKeegan, K.D., Harrison, T.M., Nutman, A.P. and Friend C.R.L., 1996. Evidence for life on earth before 3,800 million years ago. *Nature*, 384: 55-59.

Morel, F.M.M. and Hering, J.G., 1993. *Principles and Applications of Aquatic Chemistry.* Wiley Interscience. London.

Morel, F.M.M., Yeasted, J.G. and Westall, J.C., 1981. Adsorption models: a mathematical analysis of the framework of general equilibrium calculations. In: A.R. Anderson (Ed.), *Adsorption of Inorganics at Solid-Liquid Interfaces.* Ann Arbour Science Publishers Inc. pp. 263-294.

Murray, J.W., 1975. The interaction of metal ions at the manganese dioxide-solution interface. *Geochimica et Cosmochimica Acta*, 39: 505-519.

Murray, J., 1974. The Surface Chemistry of Hydrous Manganese Dioxide. *Journal of Colloid and Interface Science*, 46: 357-371.

Nadkarni, R.A., 1984. Applications of microwave oven sample dissolution in analysis. *Analytical* Chemistry, 56: 2233-2237.

Nealson, K.H. and Saffarini, D., 1994. Iron and Manganese in anaerobic respiration: environmental significance physiology and regulation. *Annual Reviews in Microbioogy*, 48: 311-43.

Nealson, K.H. and Stahl, D.H., 1997. Microorganisms and biogeochemical cycles: what can we learn from stratified communities? In: J.F. Banfield, K.H. Nealson (Eds.), Geomicrobiology: Interactions between Microbes and Minerals. *Reviews in Mineralogy*. 35: 5-34.

Nealson, K.H., Rosson, R.A., Myers, C.R., 1989. Mechanisms of oxidation and reduction of manganese. In: T.J. Beveridge, R.J. Doyle, (Eds), *Metal Ions and Bacteria.* Wiley and Sons. New York. pp. 383-411.

Nealson, K.H., Tebo, B.M. and Rosson, R.A., 1988.Occurrence and mechanisms of microbial oxidation of manganese. *Advances in Applied Microbiology,* 33: 279-318.

Nederlof, M.M., van Riemsdijk, W.H. and Koopal, L.K., 1994. Heterogeneity Analysis for Binding Data Using an Adapted Smoothing Spline Technique. *Environmental Science & Technology*, 28: 1037-1047.

Nelson, Y.M., Lion, L.W., Ghiorse, W.C. and Shuler, M.L., 1999a. Production of

biogenic Mn oxides by *Leptothrix discophora* S-1 in a chemically defined growth medium and evaluation of their Pb adsorption characteristics. *Applied and Environmental Microbiology*, 65: 175-180.

Nelson, Y.M., Lion, L.W., Shuler, M.L. and Ghiorse, W.C., 1999b. Lead binding to metal oxide and organic phases of natural aquatic biofilms. *Limnology and Oceanography*, 44: 1715-1729.

Nelson, Y.M., Lo, W., Lion, L.W., Shuler, M.L. and Ghiorse, W.C., 1995. Lead distribution in a simulated aquatic environment: effects of bacterial biofilms and iron oxide. *Water Research*, 29: 1934-1944.

Nesbitt, H.W., Canning, G.W. and Bancroft, G.M., 1998. XPS study of reductive dissolution of 7Å-birnessite by H_3AsO_3 with constraints on reaction mechanism. *Geochimica et Cosmochimica Acta*, 62: 2097-2110.

Neu, T.R. and Lawrence, J.R., 1997. Development and structure of microbial biofilms in river water studied by confocal laser scanning microscopy. *FEMS Microbiology Ecology*, 24: 11-25.

Newman, D.K., Ahmann, D. and Morel, F.M.M., 1998. A brief review of dissimilatory arsenate reduction. *Geomicrobiology Journal*, 15: 255-268.

Newville, M., 2001. IFEFFIT: interactive XAFS analysis and FEFF fitting. *Journal of Synchrotron Radiation*, 8: 322-4.

Nirel, P.M.V. and Morel, F.M.M., 1990. Pitfalls of sequential extractions. *Water Research*, 24: 1055-6.

Nordstrom, D.K. and Southam, G., 1997. Geomicrobiology of sulfide mineral oxidation. In: J.F. Banfield, K.H. Nealson (Eds), Geomicrobiology: Interactions between Microbes and Minerals. *Reviews in Mineralogy* 35: 361-390.

Obraztsova, A.Y., Francis, C.A. and Tebo, B.M., 2002. Sulfur disproportionation by the falcultative anaerobe Pantoea agglomerans SP1 as a mechanism for chromium (VI) reduction. *Geomicrobiology Journal*, 19: 121-132.

O'Day, P.A., Carroll, S.A. and Waychunas, G.A., 1998. Rock-water interactions controlling zinc, cadmium and lead concentrations in surface waters and sediments. U.S. Tri-State Mining District. I. Molecular identification using X-ray absorption spectroscopy. *Environmental Science & Technology*, 32: 943-955.

Ogunseitan, O.A. and Olson, B.H., 1991. Potential for genetic enhancement of bacterial detoxification of mercury waste. In: R.W.S.A.M. Misra, (Ed.), Mineral Bioprocessing, *The Minerals, Metals and Materials Society*, pp. 325-337.

Paktunc, D. and Dutrizac, J.E., 2003. Characterization of arsenate-for-sulfate substitution in synthetic jarosite using X-ray diffraction and X-ray Absorption Spectroscopy. *Canadian Mineralogist*, 41: 905-919.

Pandya, K. I., O'Grady, W. E., Corrigan, D. A., McBreen, J. and Hoffman, R. W., 1990. Extended x-ray absorption fine structure investigations of nickel hydroxides. *Journal of Physical Chemistry*, 94: 21-6.

Parkman, R.J., Charnock, J.M., Livens, F.R. and Vaughan, D.J., 1998. A study of the interaction of strontium ions in aqueous solution with the surfaces of calcite and kaolinite. *Geochimica et Cosmochimica* Acta, 62: 1481-1492.

Parks, G.A., 1990. Surface energy and adsorption at mineral/water interfaces: an

introduction. In: M. F. Hochella Jr., A. F. White (Eds.), Mineral-Water Interface Geochemistry. *Reviews in Mineralogy*, 23: 133-176.

Parmar, N., Warren, L.A., Roden, E.E. and Ferris, F.G., 2000. Solid phase capture of strontium by the iron reducing bacteria *Shewanella alga* strain BrY. *Chemical* Geology, 169: 281-288.

Pauling, L., 1929. The principles determining the structure of complex ionic crystals. *Journal of the American Chemical Society*, 51: 1010-1026.

Pecher, K., Bargar, J., Meigs, G., Cox, L., Nealson, K., Tonner, B., McCubbery, D., Kneedler, E. and Rothe, J., 2003. Quantitative charge state analysis of manganese biominerals in aqueous suspension using scanning transmission X-ray microscopy (STXM). *Geochimica et Cosmoshimica Acta*, 67: 1089-1098.

Perez-Benito, J.F., Arias, C., Rodriguez R.M. and Ros, M., 1998. Kinetics and mechanism of the reduction of chromium(VI) by D-ribose. *New Journal of Chemistry*, 22: 1445-1451.

Perez-Benito, J.F. and Arias, C., 2001. The pyrophosphate-assisted reduction of chromium(VI) by manganese(II) and its reverse reaction. *New Journal of Chemistry*, 25: 1438-1446.

Peterson, M.L., Brown, G.E. Jr., Parks, G.A. and Stein, C.L., 1997. Differential redox and sorption of Cr(III/IV) on natural silicate and oxide minerals: EXAFS and XANES results. *Geochimica et Cosmochimica Acta*, 61: 3399-3412.

Pierson, B.K., Parenteau, M.N. and Griffin, B.M., 1999. Phototrophs in high-iron-concentration microbial mats: physiological ecology of phototrophs in an iron-depositing hot spring. *Applied and Environmental Microbiology*, 65: 5474-5783.

Post, J.E., 1999. Manganese oxide minerals: Crystal structures and economic and environmental significance. *Proceedings of the National Academy of Science, U.S.A.*, 96: 3447-3454.

Post, J.E. and Bish, L., 1988. Rietveld refinement of the todorokite structure. *American Mineralogist*, 73:7-8.

Post, J.E. and Veblen, D.R., 1990. Crystal structure determination of synthetic sodium, magnesium, and potassium birnessite using TEM and the Rietveld method. *American Mineralogist*, 75: 477-489.

Press, W.H., Teukolsky, S.A., Vetterling, W.T., Flannery B., 1992. *Numerical Recipes in FORTRAN, 2nd ed.*, Cambridge University Press, Cambridge.

Pretorius, P.J. and Linder, P.W., 2001. The adsorption characteristics of d-manganese dioxide: a collection of diffuse double layer constants for the adsorption of H+, Cu2+, Ni2+, Zn2+, Cd2+ and Pb2+. *Applied Geochemistry,* 16: 1067-1082.

Price, W.A. 2003. Challenges posed by metal leaching and acid rock drainage, and approaches to address them. In: J.L. Jambor, D.W. Blowes, A.I.M. Ritchie (Eds.), *Environmental Aspects of Mine Wastes*. Mineraogists Assocation of Canada Short Course, 31: 11-50.

Prochnow, J.V., Schweim, C., Spork, V. and Jahnke, J., 2001. Using dissolved and particulate carbon for prediction. *Physics and Chemistry of the Earth, Part B: Hydrology, Oceans and Atmosphere.* 26: 53-57.

Puls, R.W., Powell, R.M., Clark, D. and Eldred, C.J., 1991. Effects of pH, solid/solution

ratio, ionic strength, and organic acids on Pb and Cd sorption to kaolinite. *Water, Air, and Soil Pollution*, 57-58: 423-430.

Puranik, P.R. and Paknikar, K.M., 1999. Biosorption of lead, cadmium, and zinc by *Citrobacter* strain MCM B-181: characterization studies. *Biotechnology Progress*, 15: 228-237.

Rauret, G., Rublo, R. and López-Sánchez, J.F., 1989. Optimization of Tessier procedure for metal solid speciation in river sediments. *International Journal of Environmental and Analytical Chemistry*, 36: 69-83.

Ravel, B., 2000. EXAFS analysis with FEFF and FEFFIT, Part 2: Commentary. Version 0.05, April 12, 2001. ravel@phys.washington.edu.

Real, C., Barreiro, R. and Carballeira, A. 1994. The application of microwave heating in sequential extractions of heavy metals in estuarine sediments. *Science of the Total Environment*, 152: 135-142.

Reeder, R.J., Lamble, G.M., Lee, J.-F. and Stadut, W.J., 1994. Mechanism of SeO_4^{2-} substitution in calcite: an XAFS study. *Geochimica et Cosmochimica Acta*, 58: 5639-5646.

Rehr, J.J., Zabinsky, S.I. and Albers, R.C., 1992. High-order multiple scattering calculations of X-Ray-adsorption fine structure. *Physics Reviews Letters*, 69: 3397.

Ressler, T., Brock, S.L., Wong, J. and Suib, S.L., 1999. Multiple-scattering EXAFS Analysis of Tetraalkylammonium Manganese oxide colloids. *Journal of Physical Chemistry B*, 103: 6407-6420.

Revsbech, 1989. An oxygen mivroelectrode with a guard cathode. *Limnology and Oceanography*, 34: 474-478.

Revsbech, N.P. and Ward, D.M., 1984. Microelectrode studies of interstitial water chemistry and photosynthetic activity in a hot spring microbial mat. *Applied and Environmental* Microbiology, 48: 270-275.

Richard, F.C. and Bourg, C.M., 1991. Aqueous geochemistry of chromium: A Review. *Water* Research, 25:807-816.

Robbins, E., Corley, T.L. and Conklin, M.H., 1999. Manganese Removal by the epilithic microbial consortium at Pinal Creek near Globe, Arizona. In: *USGS Toxic Substances Hydrology Program*; vol. 1.

Rothe, J., Kneedler, E., Pecher, K., Tonner, T., Nealson, K.H., Grundl, T., Meyer-Ilse, W. and Warwick, T., 1999. Spectromicroscopy of Mn distributions in micronodules produced by biomineralization. *Journal of Synchrotron Radiation*, 6: 359-361.

Robertson, A.P. and Leckie, J.O., 1998. Acid/Base, copper binding, and Cu^{2+}/H^{+} exchange properties of goethite and experimental and modelling study. *Environmental Science & Technology*, 32: 2519-2530.

Santegoeds, C.M., Schramm, A. and de Beer, D., 1998. Microsensors as a tool to determine chemical microgradients and bacterial activity in wastewater biofilms and flocs. *Biodegradation*, 9: 159-167.

Saouter, E., Turner, R. and Barkay, T., 1994. Microbial reduction of ionic mercury for the removal of mercury from contaminated environments. *Annals of the New York Academy of Sciences,* 721: 423-427.

Sasaki, K. and Konno, H., 2000. Morphology of Jarosite-group compounds precipitated from biologically and chemically oxidized Fe ions. *Canadian Mineralogist.* 38: 45-56.

Sauvé, S., Hendershot, H. and Allen, H.E., 2000. Solid-solution partitioning of metals in contaminated soils: dependence on pH total metal burden and organic matter. *Environmental Science & Technology* 34 :1125-1131.

Schekel, K.G., Impellitteri, C.A. Ryan, J.A. and McEvoy, T., 2003. Assessment of a Sequential Extraction Procedure for Perturbed Lead-Contaminated Samples with and without Phosphorus Amendments. *Environmental Science & Technology*, 37: 1892-1898.

Seal R.R. and Hammarstrom, J.M., 2003. Geoenvironmental models of mineral deposits: examples from massive sulfide and gold deposits. In: J.L. Jambor, D.W. Blowes, A.I.M. Ritchie (Eds.), *Environmental Aspects of Mine Wastes.* Mineralogists Assocation of Canada Short Course, 31: 11-50.

Scheidegger, A.M., Lamble, G.M. and Sparks, D.L., 1996. Investigation of Ni Sorption on Pyrophyllite: An XAFS study. *Environmental Science & Technology*, 30: 548-554.

Scheidegger, A.M., Sparks, D.L., Strawn, D.G. and Lamble, G.M., 1998. The kinetics of mixed Ni-Al hydroxide formation on clay and aluminium oxide minerals: A time-resolved XAFS study. *Geochemica et Cosmochimica Acta*, 62: 2233-2245.

Schiewer, S. and Volesky, B., 2000. Biosorption processes for heavy metal removal. In: D. Lovley (Ed.), *Environmental Microbe Metal Interactions.* ASM Press, Washington. pp. 329-362.

Schorer, M. and Eisele, M., 1997. Accumulation of inorganic and organic pollutants by biofilms in the aquatic environment. *Water, Air, and Soil Polluion* 99: 651-659.

Scott, D.T., McKnight, D.M., Volker, B.M. and Hrncir, D.C. 2002. Redox Processes Controlling Manganese Fate and Transport in a Mountain Stream *Environmental Science & Technology*, 36: 453-459.

Sheintuch, M. and Rebhun, M., 1988. Adsorption isotherms for multisolute systems with known and unknown composition. *Water Research,* 22: 421-430.

Shen, Y.F., Zerger, R.P., DeGuzman, R.N., Suib, S.L., McCurdy, L., Potter, D.I. and O'Young, C.L, 1993. Manganese Oxide octahedral molecular sieves: Preparation, Characterization, and Applications. *Science*, 260: 511-515.

Sholkovitz, E.R., 1989. Artifacts associated with the chemical leaching of sediments for rare earth elements. *Chemical Geology*,77: 47-51.

Shuttleworth, K.L. and Unz, R.F., 1991. Influence of metals and metal speciation on the growth of filamentous bacteria. *Water Research,* 10: 1177-1186.

Sigg, L., Goss, K-U., Haderlein, S., Harms, H., Hug and S.J., Ludwig C., 1997. Sorption phenomena at environmental solid surfaces. *Chimia*,51: 893-899.

Silvester, E., Charlet, L. and Manceau, A., 1995. Mechanism of chromium(III) oxidation by Na-buserite. *Journal of Physical Chemistry*, 99: 16662-16669.

Silvester, E., Manceau, A. and Drits, V.A., 1997. Stucture of synthetic monoclinic Na-rich birnessite and hexagonal birnessite: II. Results from chemical studies and EXAFS spectroscopy. *American Mineralologist*, 82: 962-978.

Singer, P.C. and Stumm, W., 1970. Acid mine drainage: the rate determining step. *Science*. 167: 1121-1123.

Small, T.D., Warren, L.A., and Ferris, F.G., 2000. Ionic strength effects for Sr sorption to bacterial, Fe oxide, and composite bacteria - Fe-oxide surfaces. *Applied Geochemistry,* 16: 939-946.

Small, T.D., Warren, L.A., Roden, E.E. and Ferris, F.G., 1999. Sorption of strontium by bacteria, Fe (III) oxide and bacteria - Fe (III) oxide composites. *Environmental Science & Technology,* 33: 4465-4470.

Smith, D.S. and Ferris, F.G., 2001. Proton binding by hydrous ferric oxide and aluminum oxide surfaces interpreted using fully optimized continuous pK_a spectra. *Environmental Science & Technology,* 35: 4637-4632.

Smith, D.S., Nicholas, W.H. and Kramer, J.R., 1999. Resolving uncertainty in chemical speciation determinations. *Geochimica et Cosmochimica Acta.,* 63: 3337-3347.

Smith, W.L. and Gadd, G.M., 2000. Reduction and precipitation of chromate by mixed culture sulphate-reducing bacterial biofilms. *Journal of Applied Microbiology*, 88: 983.

Southam, G. and Beveridge, T.J., 1992. Enumeration of *thiobacilli* from pH-neutral and acidic mine tailings and their role in the development of secondary mineral soil. *Applied and Environmental Microbiology,* 58: 1904-1912.

Southam, G., Ferris, F.G. and Beveridge, T.J., 1995. Mineralized bacterial biofilms in sulfide tailings and in acid mine drainage systems. In: H.M. Lappin-Scott, J.W. Costerton (Eds), *Microbial Biofilms*. Cambridge University Press, Cambridge U.K. 138-170.

Stähli, E. 1968. Über Manganate (IV) met Schichten-Stuktur. Ph.D. dissertation, University of Bern, Bern Switzerland.

Steinuch, M. and Rechun, M., 1988. Adsorption isotherms for multisolute systems with known and unknown composition. *Water Research*, 22: 421-30

Stern, E.A., 1993. Number of relevant independent points in X-ray adsorption fine structure spectra. *Physical Review B*, 48: 9825-9827.

Stipp, S.L.S., Hochella, Jr., M.F., Parks, G.A. and Leckie, J.O., 1992. Cd^{2+} uptake by calcite, solid-state diffusion, and the formation of solid-solution: interface processes observed with near-surface sensitive techniques (XPS, LEED, and AES). *Geochimica et Cosmochimica Acta,* 56: 1941-1954.

Stroes-Gascoyne, S., Kramer, J.R. and Snodgrass, W.J., 1987. Preparation, characterization and ageing of δ-MnO2, for use in trace metal speciation studies. *Applied Geochemistry*, 2: 217-226.

Stoffregen, R. E., Alpers, C. N. and Jambor, J. L., 2000. Alunite-jarosite crystallography, thermodynamics, and geochronology. *Reviews in Mineralogy & Geochemistry*, 40: 453-479.

Ströemberg, B. and Banwart, S., 1994. Kinetic Modelling of geochemical processes at the Atik mining waste rocksite in Northern Sweden. *Applied Geochemistry*, 9: 583-595.

Stumm, W., 1992. *Chemistry of the solid-water interface: processes at the mineral-water and particle-water interface in natural systems*. Wiley and Sons. New York.

Stumm, W. and Morgan, J.J., 1996. A*quatic Chemistry. Chemical Equilibria and Rates in Natural Waters. 3rd Ed.* Wiley and Sons. New York.

Stucki, J.R., Komadel, P., Wilkinson H.T., 1987. Microbial reduction of structural Iron (III) in Smectites. *Soil Science Society of America Journal,* 51: 1663-1665.

Sturchio, N.C., Chiarello, R.P., Cheng, L.W., Lyman, P.F., Bedzyk, M.J., Qian, Y.L., Yu, H.D., Yee, D., Geissbuhler, P., Sorensen, L.B., Liang, Y. and Baer, D.R., 1997. Lead adsorption at the calcite-water interface: synchrotron X-ray standing wave and X-ray reflectivity studies. *Geochimica et Cosmochimica Acta,* 61: 251-263.

Sunda, W.G. and Lewis, J.M., 1978. Effect of complexation by natural organic ligands on the toxicity of copper to a unicellular alga, *Monochrysis lutheri. Limnology and Oceanography,* 23: 870-876.

Sunda, W.G. and Huntsman, S.A., 1987. Microbial oxidation of manganese in a North Carolina estuary. *Limnoogy and Oceanograph,* 32: 552-564.

Sunda, W.G. and Keiber, D.J., 1994. Oxidation of humic substances by manganese oxides yields low-molecular-weight organic substrates. *Nature,* 367: 62-64.

Tabachnick, B. and Fidell, L., 1983. *Using Multivariate Statistics.* Harper and Row. New York.

Taillefert, M., MacGregor, B.J., Gaillard, J-F., Lienemann, C-P., Perret, D. and Stahl, D.A., 2002. *Environmental Science & Technology* 36:468.

Tamura, H. and Furuichi, R., 1997. Adsorption affinity of divalent heavy metal ions for metal oxides evaluated by modeling with the Frumkin isotherm. *Journal of Colloid and Interface Science,* 195: 241-249.

Tebo, B.M. 1991. Manganese (II) oxidation in the suboxic zone of the Black Sea. *Deep-Sea Research, Part A,* 38: S883-S905.

Tebo, B.M., Ghiorse, W.C., van Waasbergen, L.G., Siering, P.L. and Caspi, R., 1997. Bacterially mediated mineral formation: insights into manganese(II) oxidation from molecular genetic and biochemical studies. In: J. F. Banfield, K. H. Nealson (Eds.), *Geomicrobiology: Interactions between Microbes and Minerals.* Reviews in Mineraology, 35: 225-266.

Templeton, A.S., Trainor, T.P., Spormann, A.M., Newville, M., Sutton, S.R., Dohnalkova, A., Gorby, Y. and Brown, G.E. Jr., 2003. Sorption versus Biomineralization of Pb(II) within *Burkholderia cepacia* Biofilms *Environmental Science and Technology,* 37: 300.

Tessier, A., Campbell, P.G.C. and Bisson, M., 1979. Sequential extraction procedure for the speciation of particulate trace metals. *Analytical Chemistry,* 51: 844-851.

Tessier, A., Carignan, R., Dubreuil, B. and Rapin, F., 1989. Partitioning of zinc between the water column and the oxic sediments of lakes. *Geochimica et Cosmochimica Acta,* 53: 1511-1522.

Tessier, A., Fortin, D., Belzile, N. and DeVitre, R.R., 1996. Metal sorption to diagenetic iron and manganese oxyhydroxides and associated organic matter: narrowing the gap between field and laboratory measurements. *Geochimica et Cosmochimica Acta,* 60: 387-404.

Thackeray, M.M., de Kock, A. and David, W.I.F., 1993. Synthesis and structural characterisation of defect spinels in the lithium-manganese-oxide system. *Materials-Research Bulletin*, 28: 1041-1049.

Thompson, J.B., Ferris, F.G. and Smith, D.A., 1990. Geomicrobiology and sedimentology of the mixolimnion and chemocline in Fayetteville Green Lake, New York, USA. *Palaios* 5:52-75.

Tipping, E., 1984. Temperature dependence of manganese(II) oxidation in lakewaters: a test of biological involvement. *Geochimica et Cosmochimica Acta* , 48: 1353-1356.

Tipping, E., Thompson, D.W. and Davidson, W., 1984. Oxidation products of Mn(II) in lake waters. *Chemical Geology*, 44: 359-383.

Tipping, E., Thompson, D.W. and Woof, C., 1989. Iron oxide particles formed by the oxygenation of natural and model lakewaters containing Fe(II). *Archiv fur Hydrobiologie*, 115: 59-70.

Tipping, E., Hetherington, N.B., Hilton, J., Thompson, D.W., Bowles, E. and Hamilton-Taylor, J., 1985. Artifacts in the use of selective chemical extraction to determine distributions of metals between oxides of manganese and iron. *Analytical Chemistry*, 57: 1944-1946.

Tonkin, J.W., Balistrieri, L.S. and Murray, J.W., 2002. Modeling metal removal onto natural particles formed during mixing of acid rock drainage with ambient surface water. *Environmental Science & Technology*, 36: 484-492.

Tonkin, J.W., Balistrieri, L.S. and Murray, M., 2004. Modeling sorption of divalent metal cations on hydrous manganese oxide using the diffuse double layer model. *Applied Geochemistry*, 19: 29-53.

Töpfer, J., Trari, M., Gravereau, P., Chaminade, J.P. and Doumerc, J.P., 1995. Crystal growth and reinvestigation of the crystal structure of credenite, $CuMnO_2$. *Zeitschrift für Kristallographie*, 210: 184-187.

Trivedi, P. and Axe, L., 2001. Predicting divalent metal sorption to hydrous Al, Fe, and Mn oxides. *Environmental Science & Technology,* 35: 1779-1784.

Trivedi, P., Axe, L. and Tyson, T.A., 2001. XAS studies of Ni and Zn sorbed to hydrous Manganese oxide. *Environmental Science and Technology,* 35: 4515-4521.

Turner, S. and Buseck, P.R., 1979. Manganese oxide tunnel structures and their intergrowths. *Science*, 203: 456-8.

Usui, A., 1979. Nickel and copper accumulation as essential elements in 10-Å manganite of deep-sea manganese nodules. *Nature*, 279: 411-413.

Vairavamurthy, A., Zhou, W., Eglinton, T. and Manowitz, B., 1994. Sulfonates: A novel class of organic sulfur compounds in marine sediments. *Geochimica et Cosmochimica Acta,* 58: 4681-4687.

Vandenabeele, J., Vandesande, D., Verstraete, W., Vande Woestyne, M., Houwen, F. and Germonpre, R., 1995. Role of autotrophic nitrifiers in biological manganese removal from groundwater containing manganese and ammonium. *Microbial Ecology,* 29: 83.

Venema, P., Hiemstra, T. and van Riemsdijk, W.H., 1996. Comparison of different site binding models for cation sorption: Description of pH dependency, salt

concentration and cation-proton exchange. *Journal of Colloid and Interface Science,* 181: 45-59.

Vigneault, B., Campbell, P.G.C., Tessier, A. and DeVitre, R., 2001. Geochemical changes in sulfidic mine tailings stored under a shallow water cover. *Water Research,* 35: 1066-1076.

Villalobos, M., Toner, B., Barjar, J. and Sposito, G., 2003. Characterization of manganese oxide produced by Pseudomonas putida strain MnB1. *Geochimica et Cosmochimica Acta*, 67: 2649-2662.

Volesky, B., 1990. Removal and recovery of heavy metals by biosorption. In: B. Volesky (Ed.), *Biosorption of Heavy Metals.* CRC press Inc. Boca Raton, FL. pp. 7-43.

Volesky, B. and Holan, Z.R., 1995. Biosorption of heavy metals. *Biotechnoogy Progress,* 11: 235-250.

Wang, Y.-T., 2000. Microbial reduction of Chromate. In: D. R. Lovley (Ed.), *Environmental Microbe-Metal Interactions*. ASM Press, Washington. pp. 225-235.

Warren, L.A. and Zimmerman, A.P., 1993. Trace metal/SPM associations in a fluvial system: physical and chemical influences. In: S. Rao, (Ed.), *Particulate Matter and Aquatic Contaminants*. CRC Press Boca Raton Florida, pp.127-155.

Warren, L.A. and Zimmerman, A.P., 1994a. Suspended particulate oxides and organic matter interactions in trace metal sorption reactions in a small urban river. *Biogeochemistry,* 23: 21-34.

Warren, L.A. and Zimmerman, A.P., 1994b. The influence of temperature and NaCl on cadmium, copper and zinc partitioning among suspended particulate and dissolved phases in an urban river. *Water Research,* 28: 1921-1931.

Warren, L.A. and Zimmerman, A.P., 1994c. The importance of surface area in metal sorption by oxides and organic matter in a heterogeneous natural sediment. *Applied Geochemistry,* 9: 245-254.

Warren, L.A. and Ferris, F.G., 1998. Continuum between sorption and precipitation of Fe (III) on microbial surfaces. *Environmental Science & Technology,* 32: 2331-2337.

Warren, L.A., Tessier, A. and Hare, L., 1998. Modelling cadmium accumulation by benthic invertebrates in situ: the relative contributions of sediment and overlying water compartments to organism cadmium concentrations. *Limnology & Oceanography,* 43: 1442-1454.

Warren, L. A. and Haack, E. A., 2001. Biogeochemical controls on metal behavior in freshwater environments. *Earth-Science Reviews,* 54: 261-320.

Warren L.A. and Kauffman, M.E., 2003. Microbial Engineers. *Science*, 299: 1027-1029.

Warren, L.A., Maurice, P.A., Parmar, N. and Ferris, F.G., 2000. Microbially mediated calcium carbonate precipitation: implications for interpreting calcite precipitation and for solid phase capture of inorganic contaminants. *Chemical Geology*, 169: 281-288.

Webster, J.G., Swedlund, P.J. and Webster, K.S., 1998. Trace metal adsorption onto an acid mine drainage Iron (III) oxyhydroxy sulfate. *Environmental Science &*

Technology, 32: 1361-1368.

Westall, J.C., 1987. Adsorption mechanisms in aquatic surface chemistry. In: W. Stumm (Ed.), *Aquatic Surface Chemistry.* Wiley New York. pp. 3-32.

Westall, J. and Hohl, H., 1980. A comparison of electrostatic models for the oxide/solution interface. *Advances in Colloid and Interface Science,* 13: 265-294.

Wetzel, R.G., 1983. *Limnology, 2nd Ed.* Saunders College Publishing, Fort Worth, U.S.A.

Whitney, P.R., 1975. Relationship of manganese-iron oxides and associated heavy metals to grain size in stream sediments. *Journal of Geochimical Exploration,* 4: 251-263.

Wuertz, S., Müller, E., Spaeth, R., Pfleiderer, P. and Flemming, H-C., 2000. Detection of heavy metals in bacterial biofilms and microbial flocs with the fluorescent complexing agent Newport Green. *Journal of Industrial Microbiology and Biotechnology,* 24: 116-123.

Xia, K., Bleam, W. and Helmke, P.A., 1997a. Studies of the nature of Cu^{2+} and Pb^{2+} binding sites in soil humic substances using X-ray absorption spectroscopy. *Geochimica et Cosmochimica Acta,* 61: 2211-2221.

Xia, K., Bleam, W. and Helmke, P.A., 1997b. Studies of the nature of binding sites of first row transition elements bound to aquatic and soil humic substances using X-ray absorption spectroscopy. *Geochimica et Cosmochimica Acta,* 61: 2223-2235.

Xing, B. and Veneman, P.L.M., 1998. Microwave digestion for analysis of metals in soils. *Communications in Soil Science and Plant Analysis,* 29: 923-930.

Yang, D.S. and Wang, M.K., 2002. Syntheses and characterization of birnessite by oxidizing pyrochroite in alkaline conditions. *Clays and Clay Minerals,* 50: 63-39.

Yao, W. and Millero, F.J., 1993. The rate of sulphide oxidation by δ-MnO_2 in seawater. *Geochimica et Cosmoschica Acta,* 57:3359-3365.

Young, L.B. and Harvey, H., 1992. The relative importance of manganese and iron oxides and organic matter in the sorption of trace metals by surficial lake sediments. *Geochimica et Cosmochimica Acta,* 56: 1175-1186.